MEMORIAL UNIVERSITY OF NEWFOUNDLAND

A Geophysical Study of the Valentine Gold Project, West-Central Newfoundland

by

Stephanie M. Abbott

A thesis submitted to the Department of Earth Sciences in partial fulfillment of the requirements for the degree of Master of Science (Geophysics)

FACULTY OF SCIENCE
Department of Earth Sciences

September 2021

ABSTRACT

The Valentine Lake Property is located in the west-central region of the island of Newfoundland and comprises five significant structurally controlled, orogenic gold deposits. These deposits, which have proven challenging targets for geophysics, occur proximal to a major thrust faulted contact between the Precambrian Valentine Lake Intrusive Complex (VLIC), which houses the majority of gold mineralization, and the Silurian Rogerson Lake Conglomerate (RLC). Hosted within the silicic quartz-eye porphyry and trondhjemite phases of the VLIC, the gold concentrations are associated with extensional and shear parallel quartz-tourmaline-pyrite (QTP) veining. While geophysical techniques, such as induced polarization (IP), magnetics and seismic, are commonly used to detect mineral prospects, their ability to delineate the ore zone at the Valentine Gold Project (VGP) has been largely unsuccessful, primarily because the gold is scattered throughout veins within the resistive, silicic host rocks. Consequently, to date the most successful methods for locating the ore have been prospecting, soil sampling and drilling. This study employs two fresh geophysical techniques, gravity and ground-penetrating radar (GPR), supplemented by sonar surveys, in an effort to map the subsurface extent of the gold-bearing alteration zone and assess the depth of overburden and water reserves for future mine development. Throughout 2019 and 2020, a 22 line-kilometre broad-scale gravity survey, comprising 252 stations was completed, targeting the slightly less dense altered host rock. GPR data acquired over 8 priority bogs and small ponds helped define the irregular overburden to aid in gravity corrections. Combined GPR and sonar bathymetry surveys of Valentine and Victoria Lakes covering 10 and 32 square kilometres, respectively, were completed to further assist with the gravity corrections and to ascertain water resources for mining. The resulting residual Bouguer gravity map revealed a -1.7 mGal thin linear anomaly corresponding partially to the alteration zone and the bog hypsometry maps yielded overburden thicknesses up to 4.8 metres.

GENERAL SUMMARY

Over the course of four field seasons, a broad-scale gravity survey was conducted throughout the Valentine Lake Property, along with combined GPR and sonar surveys over the surrounding Valentine Lake and Victoria Lake. In addition, GPR data was acquired over 8 bogs and ponds in areas considered for mine infrastructure. Situated within one of the top mining jurisdictions in the world, the Valentine Gold Project is advancing toward production in west-central Newfoundland. Upon completion, the VGP will be the leading gold mine in Atlantic Canada and a major contributor to Newfoundland and Labrador's economy, given the proposed thirteen-year open pit and conventional milling operation. The Valentine Gold Project contains a series of mineralized deposits along a 20-kilometre northeast-southwest trend, where the gold is hosted predominantly within quartz-tourmaline pyrite veins. The goals of this study are to define the subsurface extent of the gold-hosting region using the gravity method and use ground-penetrating radar, supplemented by sonar, to determine overburden thickness and water reserves to aid with the location planning of future mining infrastructure. The acquired gravity, GPR and sonar data was organized, corrected, and additionally processed using specialized software. The resulting gravity map detected the subsurface alteration zone and the bathymetry and hypsometry maps provided insight on the water reserves and confirmed that bog thicknesses in most areas of interest were moderate and would not pose a significant obstacle to infrastructure development. Overall, this study has proven gravity, GPR and sonar as effective techniques for mineral exploration and geotechnical mining applications.

ACKNOWLEDGEMENTS

I would like to extend a sincere thank you to my supervisor, Dr. Alison Leitch, for the endless support, knowledge, and encouragement she has shown me throughout this project. She is a passionate teacher with commendable patience who believes that *we learn by experience*, and I feel honoured and privileged to have completed my research under her tutelage.

A special thanks to my supervisory committee members, Dr. Colin Farquharson and Adam Wall, for their time and commitment to this project. I am extremely fortunate to have such easy going and respectful mentors who keep morale high and drive me to succeed.

I must also acknowledge the incredibly hard work and dedication of my field assistants, Andrew Blagdon and Marie Flanagan, who set aside their own work to help me accomplish mine. Inclement weather and all, they remained positive and motivated as we push through many long and exhausting days in the field. Additional thanks are due to Josh Sellars and Ph.D. candidate Michael King for their extensive involvement in computing the gravity terrain corrections.

Thank you to the *Memorial* Technical Services team for their continued assistance with equipment repairs and modifications. Sincere gratitude towards David Snook and his skilled crew in the Mechanical Division who saw no job as too big or too small and Bill Maloney of the Electronics Division for his electrical expertise.

This project would not have been possible without the financial support from the School of Graduate Studies and a Collaborative Research and Development (CRD) grant between *NSERC* and *Marathon Gold Corporation*. An additional thank you to *Marathon Gold* for providing access to the property, logistical support, and supplementary data. A sincere appreciation to the incredibly welcoming and kind-hearted staff at the Valentine Gold camp whose hospitality goes unmatched.

Finally, I would like to say a heartfelt thank you to my family, who have taught me to always be kind, respect others and put my best foot forward. I am very fortunate to have such incredible parents who boundlessly support my desire to learn and grow as both an academic and an individual. To my selfless partner, Matthew, thank you for being my shining light through the many long nights and stressful days. The overwhelming love, reassurance, and optimism I have felt throughout this project has truly been unparalleled.

"No one who achieves success does so without acknowledging the help of others."

Alfred North Whitehead

TABLE OF CONTENTS

LIST OF TABLES

LIST OF FIGURES

LIST OF ABBREVIATIONS

BDS	BeiDou Navigation Satellite System
BGI	International Gravimetric Bureau
CGSN	Canadian Gravity Standardization Network
DEM	Digital Elevation Model
DCR-IP	Direct Current Resistivity – Induced Polarization
EM	Electromagnetic
GNSS	Global Navigation Satellite Systems
GPR	Ground-Penetrating Radar
GPS	Global Positioning System
IAG	International Association of Geodesy
IGSN	International Gravity Standardization Network
IRNSS	Indian Regional Navigation Satellite System
MASL	Metres Above Sea Level
MUN	Memorial University of Newfoundland
PPP	Precise Point Positioning
PRN	Pseudorandom Noise
QTP	Quartz-Tourmaline-Pyrite
RLC	Rogerson Lake Conglomerate
RTK	Real-Time Kinematics
TWT	Two-Way Travel Time
UHF	Ultra-High Frequency
VLIC	Valentine Lake Intrusive Complex
VGP	Valentine Gold Project
VLS	Victoria Lake Supergroup
WGM	World Gravity Map
WGS	World Geodetic System

LIST OF SYMBOLS

$\boldsymbol{a}$	Acceleration (Newton's Second Law)	$\mathbf{m/s^2}$
$\boldsymbol{a}_g$	Acceleration of Mass m_2 due to Mass m_1	$\mathbf{N/kg}$
B	Magnetic Flux Density	**T**
D	Electric Displacement Field	$\mathbf{C/m^2}$
E	Electric Field Strength	$\mathbf{V/m}$
$\boldsymbol{F}$	Force	**N**
$\boldsymbol{g}$	Gravitational Acceleration	$\mathbf{m/s^2}$
$\boldsymbol{g}_0$	Theoretical or Normal Gravity	**mGal**
$\boldsymbol{g}_{cb}$	Complete Bouguer Gravity	**mGal**
$\boldsymbol{g}_{fa}$	Free-Air Gravity	**mGal**
$\boldsymbol{g}_{obs}$	Observed Gravity	**mGal**
$\boldsymbol{g}_{sb}$	Simple Bouguer Gravity	**mGal**
$\boldsymbol{g}_t$	Terrain Gravity	**mGal**
H	Magnetic Field Intensity	$\mathbf{A/m}$
$\boldsymbol{h}$	Height	**m**
J	Total Electric Current Density	$\mathbf{A/m^2}$
$\boldsymbol{k_s}$	Spring Constant	$\mathbf{N/m}$
$\boldsymbol{m}$	Mass	**kg**
$\boldsymbol{M_e}$	Mass of the Earth	**kg**
$\boldsymbol{r}$	Distance	**m**
$\hat{\boldsymbol{r}}$	Unit (Directional) Vector	
$\boldsymbol{r_e}$	Radius of the Earth	**km**
$\boldsymbol{R}$	Range	**m**
$\boldsymbol{t}$	Time	**s**

$\boldsymbol{x}$	Displacement	$\mathbf{m}$
$\boldsymbol{v}$	Velocity	$\mathbf{m/ns}$
$\frac{\partial \mathbf{D}}{\partial t}$	Displacement Current Density	$\mathbf{A/m^2}$
$\nabla \cdot$	Divergence Operator	
$\nabla \times$	Curl Operator	
Δ	Gradient Operator	
$\boldsymbol{\alpha}$	Attenuation	$\mathbf{dB/m}$
$\boldsymbol{\sigma}$	Electrical Conductivity	$\mathbf{S/m}$
$\boldsymbol{\varepsilon}$	Dielectric Permittivity	$\mathbf{F/m}$
$\boldsymbol{\varepsilon_0}$	Permittivity of Free Space	$8.854\ x\ 10^{-12}$ $\mathbf{F/m}$
$\boldsymbol{\mu}$	Magnetic Permeability	$\mathbf{H/m}$
$\boldsymbol{\kappa}$	Dielectric Constant	
$\boldsymbol{\gamma}$	Universal Gravitational Constant	$\mathbf{Nm^2/kg^2}$
$\boldsymbol{\lambda}$	Latitude	**Rad**
$\boldsymbol{\pi}$	Pi	3.14159
$\boldsymbol{\rho}$	Density	$\mathbf{kg/m^3}$ **or** $\mathbf{g/cm^3}$

LIST OF APPENDICES

1 INTRODUCTION

1.1 GOALS AND RATIONALE

The Valentine Lake Property in west-central Newfoundland, encompasses five significant gold deposits, which are structurally controlled and of orogenic origin. These deposits have proven to be tough targets for geophysical exploration (Section 2.3). This research utilizes two geophysical techniques that have not previously been used over the property, namely gravity, and ground penetrating radar to assist with mineral exploration and geotechnical demands associated with near future mine development at the Valentine Gold Project (VGP).

One objective of this study is to map the subsurface extent of hydrothermal alteration zones associated with dense packages of gold-bearing veins by conducting a broad-scale gravity survey over the property. From this survey, a residual Bouguer anomaly map [Fig. 4.11] was generated. This map shows that density decreases (i.e., low gravity anomalies) with the silicic alteration and subsequently, gold mineralization. The second aim of this project was to determine the thicknesses of bogs which may accommodate future mine infrastructure (e.g., processing plant, tailings facility, lodgings) by conducting ground-penetrating radar surveys and producing corresponding hypsometry maps [Fig. 5.7 and Appendix F]. This information will help determine the excavation requirements, which may vary depending on the thicknesses and the foundation requirements of the infrastructure. The GPR surveys were supplemented by a third method, sonar, to achieve a secondary goal of assessing water resources for drilling and mine operation and to make corrections in processing of the gravity data (Section 4.2), through the production of bathymetry maps of Valentine Lake [Fig. 5.8] and Victoria Lake [Fig. 5.9]. Further details explaining the rationale for these methods are described below.

Although gravity methods are commonly used to detect ore deposits, they are not typically applied to the type of gold deposits present at the Valentine Lake Property, where the density contrast between lithologies is small [Fig. 2.4, Tbl. 2.1], topography is rough, and overburden is thick and irregular. Conversely, while GPR is a preferred method for shallow freshwater bathymetry studies and has had recent advances for soil and bog studies, it is not commonly employed for geotechnical mining applications. Considering this, proof-of-concept gravity and GPR surveys (Appendix A) were carried out on the property in 2018, to determine the feasibility of these methods at the VGP. The preliminary gravity survey over the alteration zone revealed a small (~1.6 mGal) but measurable negative gravity anomaly [Fig. 2.8], suggesting that gravity would be a suitable method moving forward. Similarly, the single-line ground-penetrating radar bog survey was successful in resolving the bottom of the bog and accurately measuring its depth.

The gold deposits exist along the Valentine Lake Shear Zone, a major thrust faulted contact between the Precambrian Valentine Lake Intrusive Complex (VLIC), the primary host of gold mineralization, and the Silurian Rogerson Lake Conglomerate (Tettelaar and Dunsworth, 2015). Housed within the silicic quartz-eye porphyry and trondhjemite phases of the VLIC, the gold mineralization is associated with extensional and shear parallel quartz-tourmaline-pyrite (QTP) veining. The VGP has experienced many complex stages of deformation and contains several generations of mafic dykes (Lincoln et al., 2018).

Historical exploration of the property dates back to the early 1960s, including various ground and airborne geophysical surveys, particularly magnetics, electromagnetics (EM), direct current resistivity–induced polarization (DCR-IP) and seismic. Although geophysical techniques are commonly used for investigating mineral prospects, their use to delineate the ore zone at the VGP has met with little success. Magnetic surveys delineate the mafic dykes and electromagnetic techniques detect conductive bodies, but given the nature of the gold within the resistive, siliceous host rocks (Section 2.2), both methods have been largely unsuccessful. Recognized as an effective tool for identifying disseminated ore concentrations, particularly in other parts of Newfoundland, the DCR-IP method was ineffective at the Valentine Lake Property. Similarly, seismic proved to be a nonviable technique given the small scale of the veins, the lack of contrast in the physical properties between the quartz veins and the quartz rich host rock and the nearly vertical shear zone (A. Wall, pers. comm., 2021). Therefore, to date the primary methods for locating the ore have been soil sampling and drilling.

The fieldwork component of this research was carried out using equipment available from *Memorial University*'s modern geophysical equipment pool. The gravity surveys were conducted using a *Scintrex* CG-5 Autograv gravimeter and accompanying *Topcon* Real-Time-Kinematics (RTK) GPS system. The ground-penetrating radar surveys utilized a pulseEKKO Pro system by *Sensors and Software* and the sonar method exploited a *Garmin* GPSMAP 527xs system. Additional equipment including ATV's, snowmobiles and boats were provided by *Marathon Gold Corporation*. The collected data was analyzed, processed, and mapped using various software including EKKO_Project, Oasis Montaj, Microsoft Excel, HomePort and ArcMap.

This research will test the usefulness of these non-invasive, relatively inexpensive, and straight-forward techniques over a future mine site and therefore, potentially other prospective sites within Canada which contain structurally complex ore deposits and are often overlain by bogs, ponds and till.

1.2 STUDY AREA

1.2.1 Location and Access

The Valentine Lake Property is located in the west-central region of the island of Newfoundland, southwest of the mining communities of Buchans and Millertown [Fig. 1.1]. Housing five major gold deposits and several other gold occurrences within a 20-kilometre-long northeast trending zone, the Valentine Lake Property consists of 14 adjoining mineral licenses, totalling 240 square kilometres of land. The southeastern segment of the property features a year-round exploration camp, contiguous to the shoreline of Victoria Lake (Lincoln et al., 2018). The camp, along with the respective mineral licenses, are owned entirely by *Marathon Gold Corporation* [Fig. 1.1].

Millertown is situated approximately 10 kilometres southwest of the Trans-Canada Highway turnoff onto Route 370 - the Buchans Highway (Lincoln et al., 2018). From Millertown, the 86-kilometre well-kept gravel property access road parallels the south shore of Red Indian Lake, and then travels east and south from a position 11 kilometres northeast of the southwest end of Red Indian Lake (Tettelaar and Dunsworth, 2015). A network of supplementary access roads from the camp to the various deposits and showings within the property have been developed and maintained by past and present property owners (see Section 1.2.3).

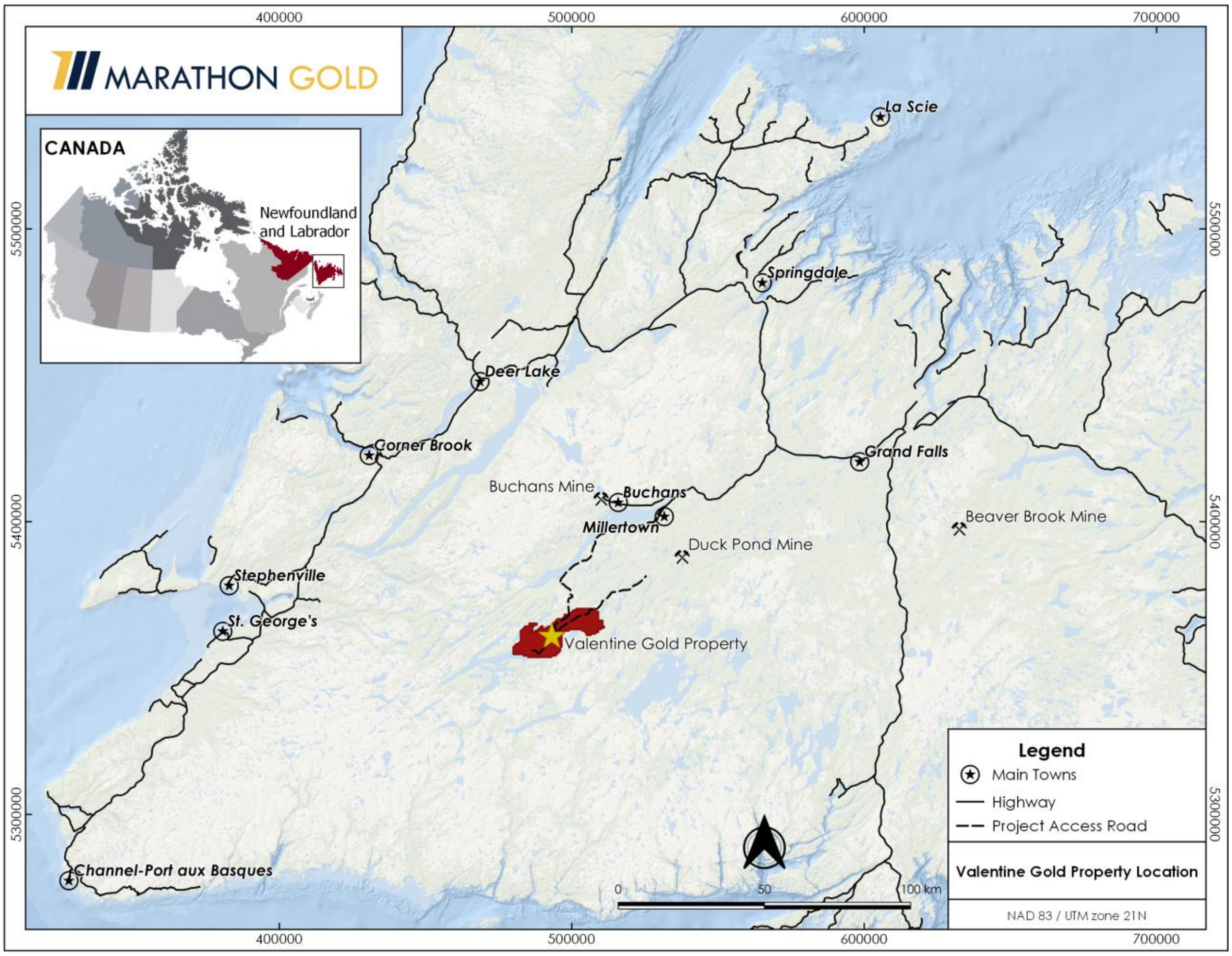

Figure 1.1: Map showing the location and access to the Valentine Lake Property (from Marathon Gold Corporation, 2021).

1.2.2 Physiography

Located within the central Uplands of Newfoundland, the Valentine Lake Property sits at the northeast end of Victoria Lake [Fig. 1.1]. Dominated by hummocky terrain, the property contains moderate slopes and elevation contrasts up to 100 metres (Tettelaar and Dunsworth, 2015). Several small lakes occur throughout the property, in addition to a well-defined northeast trending ridge that is divided by shallow cutting transitory streams [Fig. 1.2]. The central ridgeline is characterized by a combined spruce and fir forest and grassy clearings, with the peak defined by boggy ground. To the northeast of the ridge, the terrain is largely boggy [Fig. 1.2], while the southern extension is shaped by the Victoria River valley. The southwestern portion of the property is occupied by the Victoria Lake hydroelectric reservoir and has the lowest elevation on the property – 320 metres above sea level (MASL). Maximum elevation within the study area is 480 masl. Vegetation throughout the property constitutes barrens and stunted growth forests, and outcrop exposure is limited (Lincoln et al., 2018).

Figure 1.2: Perspective looking northeast along the central ridge of the Valentine Lake Property (from Lincoln et al., 2018).

1.2.3 Property History

Exploration at the Valentine Lake Property has been ongoing since the 1960s, comprising a variety of soil and channel sampling, drilling and geological mapping, as well as ground and airborne magnetics and electromagnetics, gamma-ray spectrometry, induced polarization and seismic surveys (Tettelaar and Dunsworth, 2015).

Early reconnaissance of the property by ASARCO Inc. and Hudson's Bay Oil and Gas Company was focused on base metal exploration. Gold prospecting began in 1983 when the property was acquired by Abitibi Price Inc., who forwarded ownership to BP Canada Inc. in 1985. Noranda obtained the property in 1992 and entered into a joint venture with Mountain Lake Resources in 1998. Gold exploration continued as joint ventures and property tenure progressed. *Marathon Gold Corporation* (formerly Marathon PGM) became the operator in 2010 and acquired 100% ownership of the VGP in 2012 (Murahwi, 2017). A summary of land tenure is presented below in Table 1.1.

Table 1.1: Summary of ownership of the Valentine Gold prospect.

Date	Owner/Operator
1960s	*ASARCO Inc.*
1970s – 1983	*Hudson's Bay Oil and Gas Company*
1983 – 1985	*Abitibi Price Inc.*
1985 – 1992	*BP Canada Inc.*
1992 – 1998	*Noranda Inc.*
1998 – 2003	*Mountain Lake Resources Inc.*
2003 – 2007	*Richmont Mines Inc.*
2007 – 2010	*Mountain Lake Resources Inc.*
2010 – 2011	*Marathon PGM Corporation*
2011 – present	*Marathon Gold Corporation*

2 GEOLOGICAL SETTING AND PRIOR WORK

2.1 REGIONAL GEOLOGY

The island of Newfoundland constitutes the northeastern extent of the Appalachian mountain chain and is divided into four main tectonostratigraphic zones, which are separated structurally and contrast in stratigraphy. These subzones are the Humber, Dunnage, Gander and Avalon Zones (Valverde-Vaquero et al., 2001). The Dunnage zone is divided into the Notre Dame and Exploits Subzones.

The Valentine Lake Property exists within the Exploits Subzone of the Dunnage Cambro-Ordovician mobile belt and is composed primarily of arc-related rocks of the Victoria Lake Supergroup (VLS). The VLS is a structurally complex assemblage of volcanic and epiclastic rocks with small granitoid and gabbroic intrusions (Pollock et al., 2002). The volcano-sedimentary sequence trends northeast, dips sub-vertically and exhibits a regional lower to upper greenschist metamorphic assemblage (Lincoln et al., 2018). The major lithological contacts within the VGP are primarily faulted and parallel to the regional subzone boundaries (Evans et al., 1990).

The study area centres upon the extensive multiphase Precambrian Valentine Lake Intrusive Complex (VLIC), a structural inlier of the VLS (Evans and Wilson, 1994). U-Pb zircon dated at 563 ± 2 Ma (Evans et al., 1990), the VLIC lies along the contact between the clastic sedimentary rocks of the VLS to the northwest and the Silurian Rogerson Lake Conglomerate (RLC) to the southeast [Fig. 2.1] (Gowans et al., 2012). This contact is the northeast-southwest trending, regional lithospheric-scale, subvertical to steeply northwest dipping Valentine Lake Shear Zone (Lincoln et al., 2018).

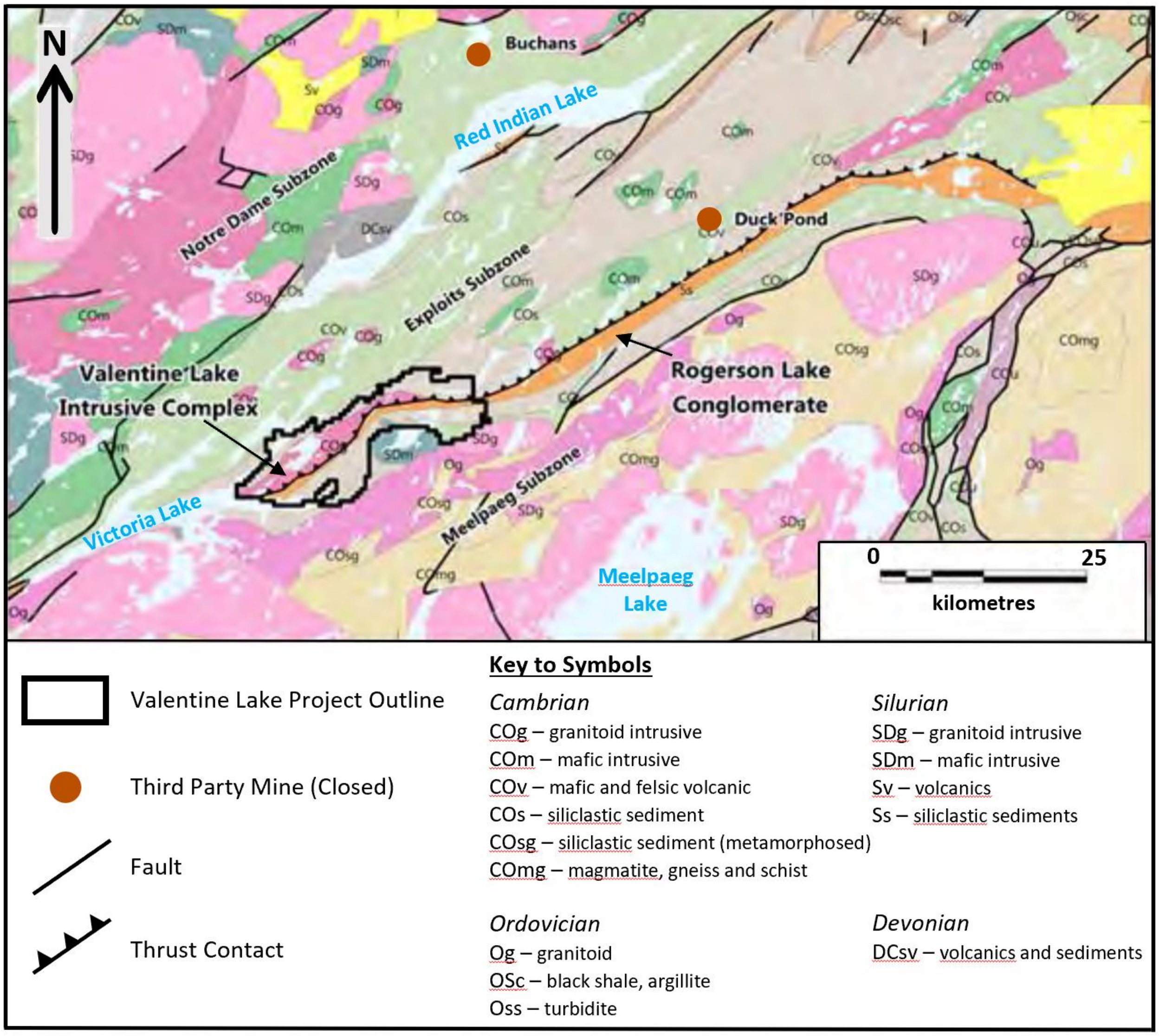

Figure 2.1: Regional geology map of the Dunnage Zone and the Valentine Gold Project, which contains the thrust faulted contact between the Valentine Lake Intrusive Complex (VLIC) and the Rogerson Lake Conglomorate (RLC) (modified from Tettelaar and Dunsworth, 2015; after Newfoundland and Labrador Geoscience Atlas Online and Piercey et al., 2014).

2.2 LOCAL GEOLOGY AND MINERALIZATION

As described by Woods (2009), the Valentine Lake Property is underlain by five major lithological units [Fig. 2.2]. From northwest to southeast, these assemblages are:

1. Cambrian-Ordovician bimodal volcanic rocks, volcanogenic and siliciclastic sedimentary units of the VLS (green and beige units)

2. The Precambrian Valentine Lake Intrusive Complex (VLIC – pink and magenta units)
3. The Silurian Rogerson Lake Conglomerate (RLC – orange unit)
4. Mixed sedimentary units and lesser gabbroic and mafic volcanic rocks of the VLS (beige unit)
5. The Silurian-Devonian Red Cross Lake Intrusion (light purple unit)

Recent findings by *Terrane Geoscience Inc.* indicate that the history of the Valentine Shear Zone is kinematically complex, extending over three Appalachian orogenies. The Valentine Gold Project has undergone five generations of deformation. Ground development prior to mineralization began during a D_2 period of tectonic relaxation, which initiated the emplacement of mafic dykes in and near the shear zone. The subsequent emplacement of mineralized quartz-tourmaline pyrite (QTP) veining occurred during D_3 shortening, as zones of contrasting competency, particularly at mafic dyke contacts developed. This promoted brittle fracturing in the host rock which allowed gold bearing fluids to enter and deposit (Kruse, 2020).

The primary host to gold mineralization at the Valentine Gold Project is the VLIC [Fig. 2.2], an extensive 22-kilometre-long, 4.5-kilometre-wide intrusive body incised within the Victoria Lake Supergroup. This intrusive suite is dominated by quartz porphyry monzonite and trondhjemite, with lesser gabbro and diorite phases present throughout the northwest extent of the property. The VLIC is crosscut by a complex assemblage of mafic dykes and unconformably overlies the younger, Rogerson Lake Conglomerate, which houses minor amounts of mineralized veining proximal to the overturned contact with the Valentine Lake Intrusive Complex (Lincoln et al., 2018). Locally, the study area is blanketed by glacial till up to several metres thick, deep bogs and ponds; occasional outcrop exposure exists along the ridge and in stream beds (Tettelaar and Dunsworth, 2015).

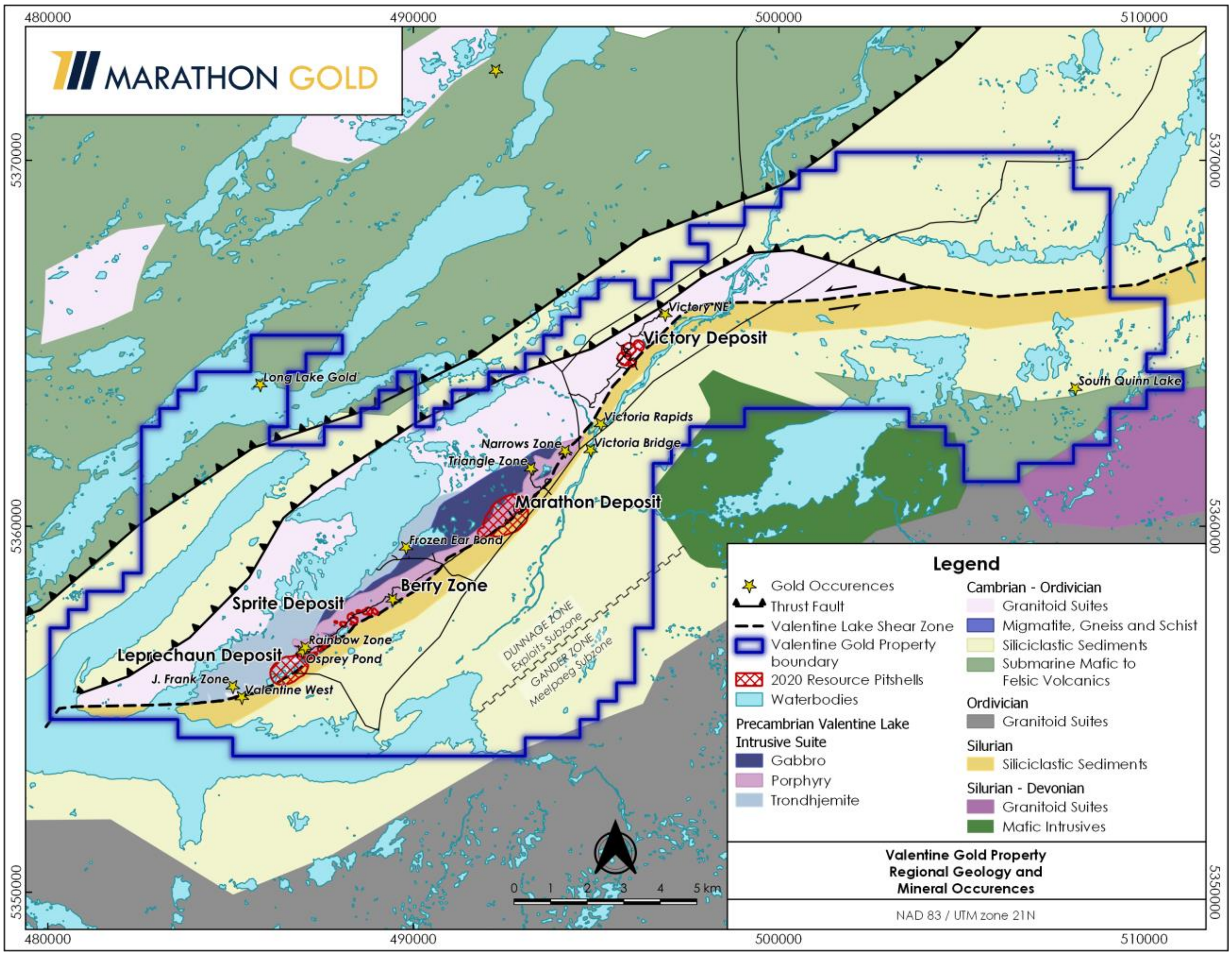

Figure 2.2: Local geology map of the Valentine Gold Project, including major gold deposits and occurrences (from Marathon Gold Corporation, 2021).

The Valentine Gold Project contains five major structurally controlled, mesothermal vein style gold deposits and numerous early stage prospects and occurrences [Fig. 2.2]. The gold is affiliated with principally shallow southwest dipping, stacked en-echelon extensional and lesser shear-parallel steeply dipping quartz-tourmaline-pyrite (QTP) veining [Fig. 2.3a]. These veins range in average thickness from 2 to 30 centimetres but can be several metres wide [Fig. 2.3b], with visible gold existing as sub-millimetre to millimetre size grains within or alongside coarse cubic pyrite [Fig 2.3c]. The highest ore grades are typically associated with extensive (1 to 3 centimetres) cubic pyrite [Fig. 2.3d] within the QTP veins (Marathon Gold Corporation, 2020).

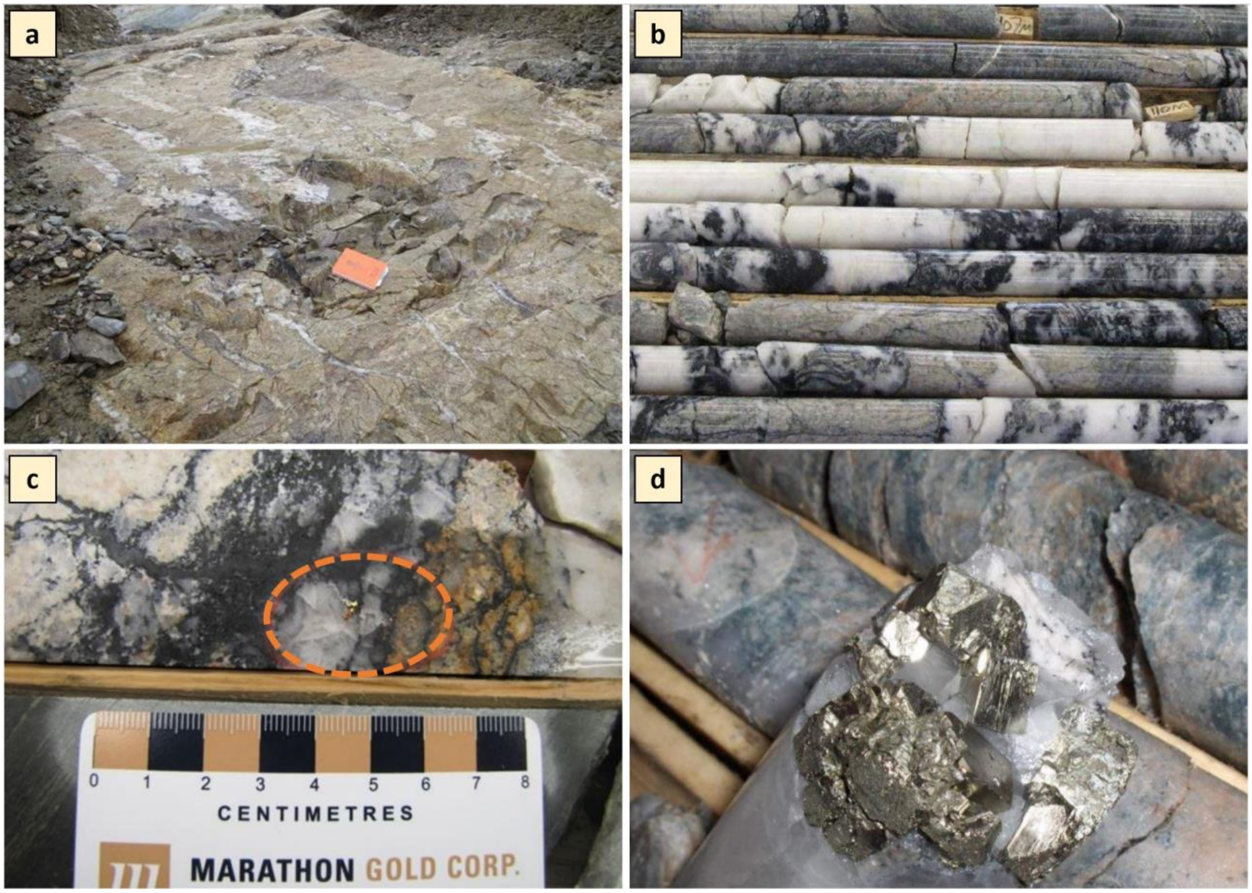

Figure 2.3: Valentine Gold Project mineralization. a) A trenched outcrop within the Marathon deposit revealing a sheeted, shallow dipping QTP veining system. b) Drill core with large pervasive QT±P veins. c). Visible gold within a QTP vein. Tourmaline bleeders and offshoots penetrate the silicic upper (left) alteration halo and the lower (right) margin is mildly oxidized. d) QTP vein with coarse cubic pyrite that intrudes the altered host rock (modified from Marathon Gold Corporation, 2020).

2.2.1 Lithological Densities

In general, the density contrasts between lithologies at the Valentine Gold Project are small, however, through density measurements obtained on a number of samples of different lithological units at the VGP [Fig. 2.4 below], it is observed that the associated QTP mineralization reduces the overall density of the hosting rock unit (i.e., QEP and trondhjemite), revealed to be enough of a contrast to be detected by the gravity method (see Section 2.3.4; Fig. 2.8).

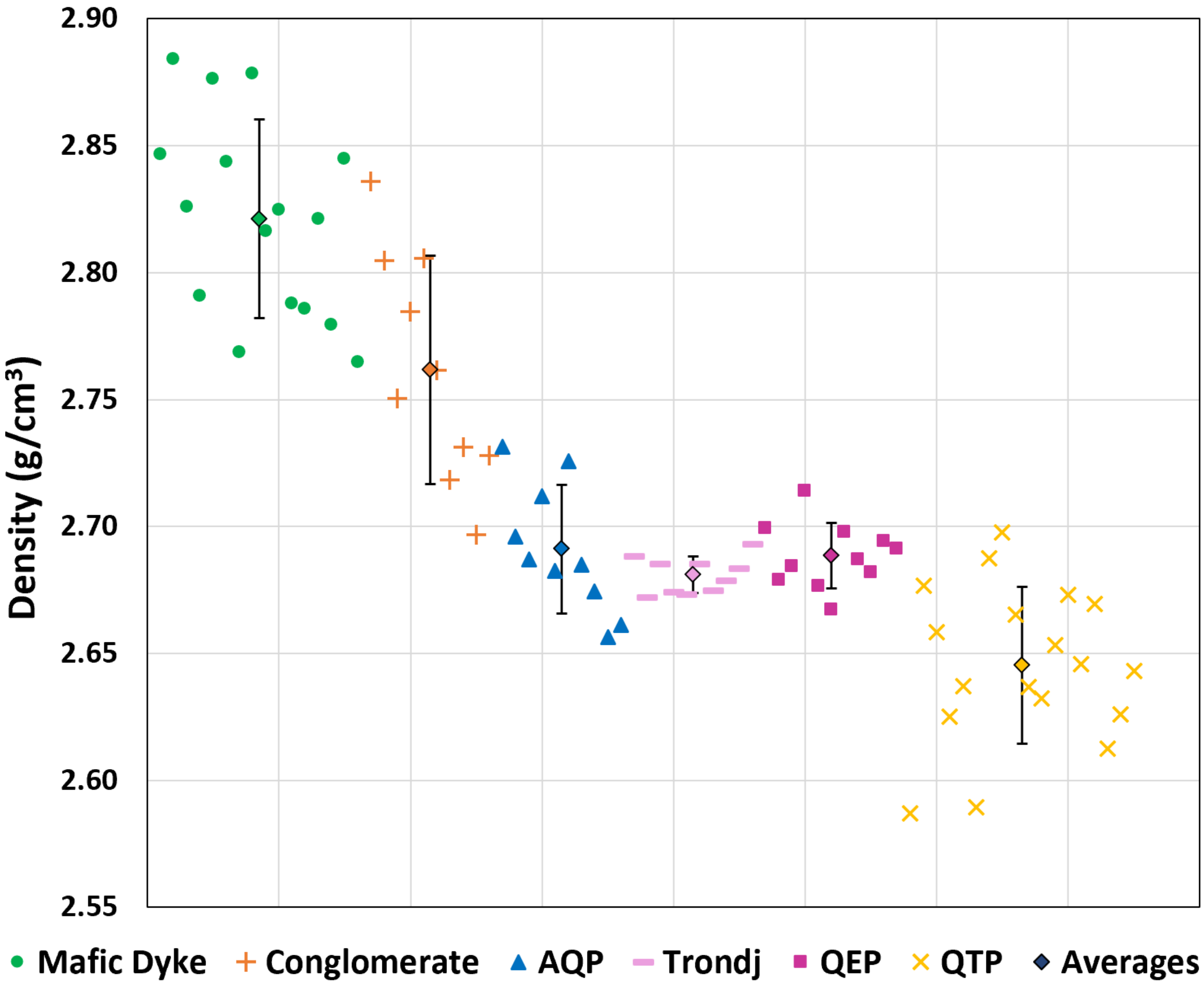

Figure 2.4: Sample densities of the main lithological units at the VGP, provided by Project Manager, Adam Wall. Error bars indicate standard deviations and the QTP (mineralized) unit is hosted within samples of QEP or trondhjemite (i.e., QEP+QTP and trondj + QTP).

Table 2.1: Average densities and standard deviations of VGP unit samples shown in Figure 2.4.

Lithological Unit	Symbol Colour	Number of Samples	Density (g/cm^3)	Standard Deviation
Mafic Dyke	Green	16	2.82	0.04
Conglomerate	Orange	10	2.76	0.05
Aphanitic Quartz Porphyry	Blue	10	2.69	0.03
Trondhjemite	Pink	10	2.68	0.01
Quartz Eye Porphyry	Purple	11	2.69	0.01
Quartz-Tourmaline-Pyrite	Yellow	18	2.65	0.03

As indicated by Figure 2.4, there is a considerable difference in the average densities of the VGP lithologies, in addition to scatter. Often, the units are intermingled within the drill cores, such that the alteration zone includes mafic dykes and unmineralized quartz porphyrys. Thus, the average density of rocks within the alteration zone may not be quite as low as the QTP (altered and mineralized unit) average, and the density contrast with surrounding units not as ideal. Nonetheless, the density differences in Figure 2.4 and Table 2.1 provide useful information for determining which geophysical methods may be appropriate to apply. The greatest density difference observed between the densest mafic dyke and the least dense QTP sample is 0.29 g/cm^3. The difference between the average conglomerate samples and the QEP is 0.07 g/cm^3 and between the average QTP and the unmineralized quartz porphyry units (QEP and AQP) is 0.04 g/cm^3.

2.3 PREVIOUS GEOPHYSICAL SURVEYS

Several geophysical surveys, including induced polarization (IP), ground magnetics, aeromagnetics and seismic, were carried out at the Valentine Lake Property between 2007 and 2017 [Fig. 2.5]. Details of these surveys are described below in Sections [2.3.1 – 2.3.3].

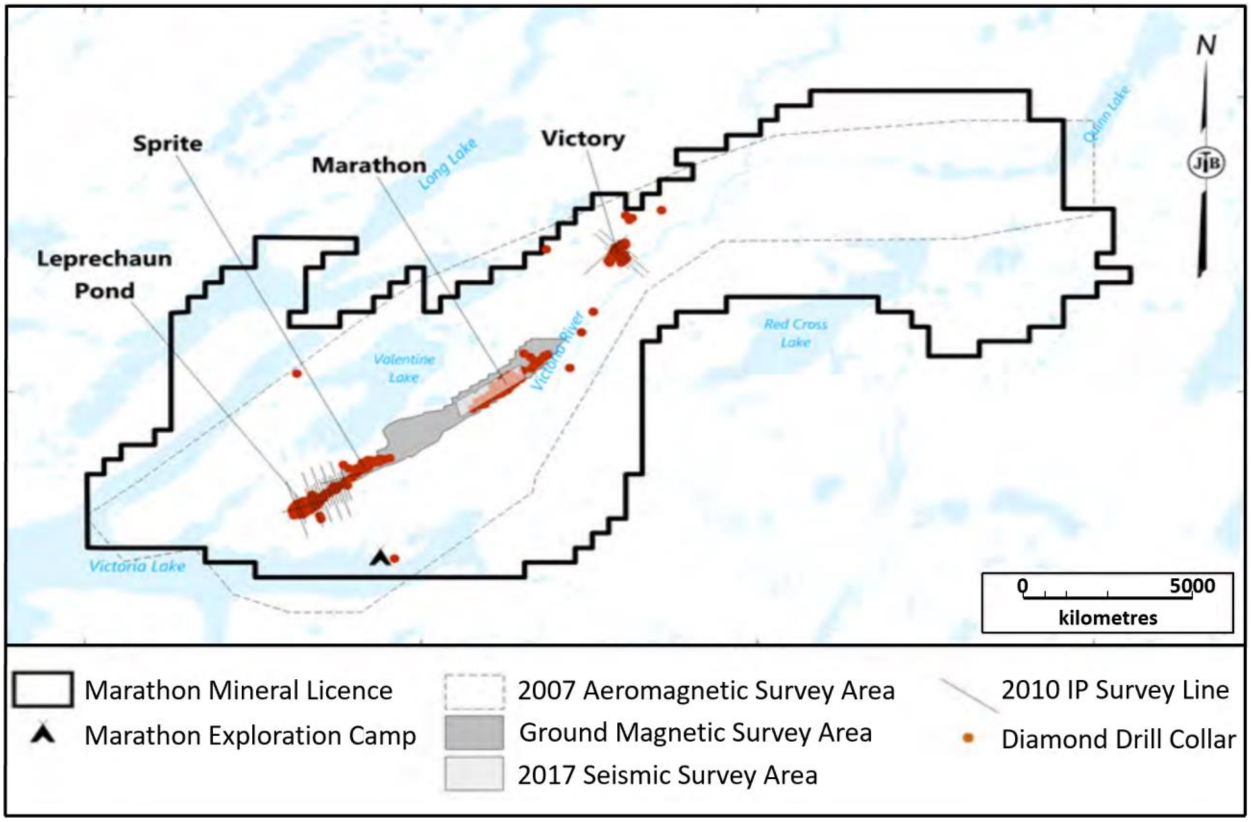

Figure 2.5: Locations of the various geophysical surveys previously carried out at the Valentine Lake Property (modified from Lincoln et al., 2018).

2.3.1 Induced Polarization (IP)

Induced polarization surveys are commonly utilized (including in Newfoundland) to locate disseminated mineralization, where valuable minerals are associated with scattered conductive grains, such as pyrite. Orogenic gold may be hosted in resistive rocks (i.e., not a low resistivity target) but the scattered associated conductors can produce a strong IP signal as they charge and discharge, making IP a preferred method for gold deposit exploration.

In 2010, *Insight Geophysics Inc*. carried out time-domain IP and resistivity surveys at the Leprechaun and Victory deposits [short grey lines in Fig. 2.5], using a transmitter spacing of 200 to 3000 metres and a receiver spacing of 12.5 metres and 25 metres. Sample intervals were 12.5 metres and 25 metres, and the lines were oriented perpendicular to the northeast-southwest trend of mineralization (Pawluk, 2010). In 2012, *JVX Ltd*. completed downhole surveys on 21 drill holes, with the intent of mapping high grade lenses, in addition to the mineralized corridor at the Leprechaun deposit (Webster and Jelenic, 2012).

The survey results revealed anomalies with potential for gold mineralization, however, later drill testing in these prospective areas by *Marathon Gold Corporation* yielded no significant results. To date, ground and downhole IP surveys have proven ineffective at identifying new mineralized zones at the Valentine Gold Project (Dunsworth et al., 2017).

2.3.2 Magnetics

Former operator, *Richmont Mines Inc.*, performed a detailed property-scale aeromagnetic survey in 2007 [Fig. 2.5]. The results [Fig. 2.6] exposed a profound structural geological relationship at the deposit locations, showcasing well-defined magnetic splays extending from the regional structure (Murahwi, 2017). A structural investigation by *SRK Consulting (Canada) Inc*., indicates the regional aeromagnetic data suggests that splays, duplexes and fault bends exist along D_1 in the nearby region, which may signify zones of increased permeability and possibly gold mineralization (Hrabi, 2014).

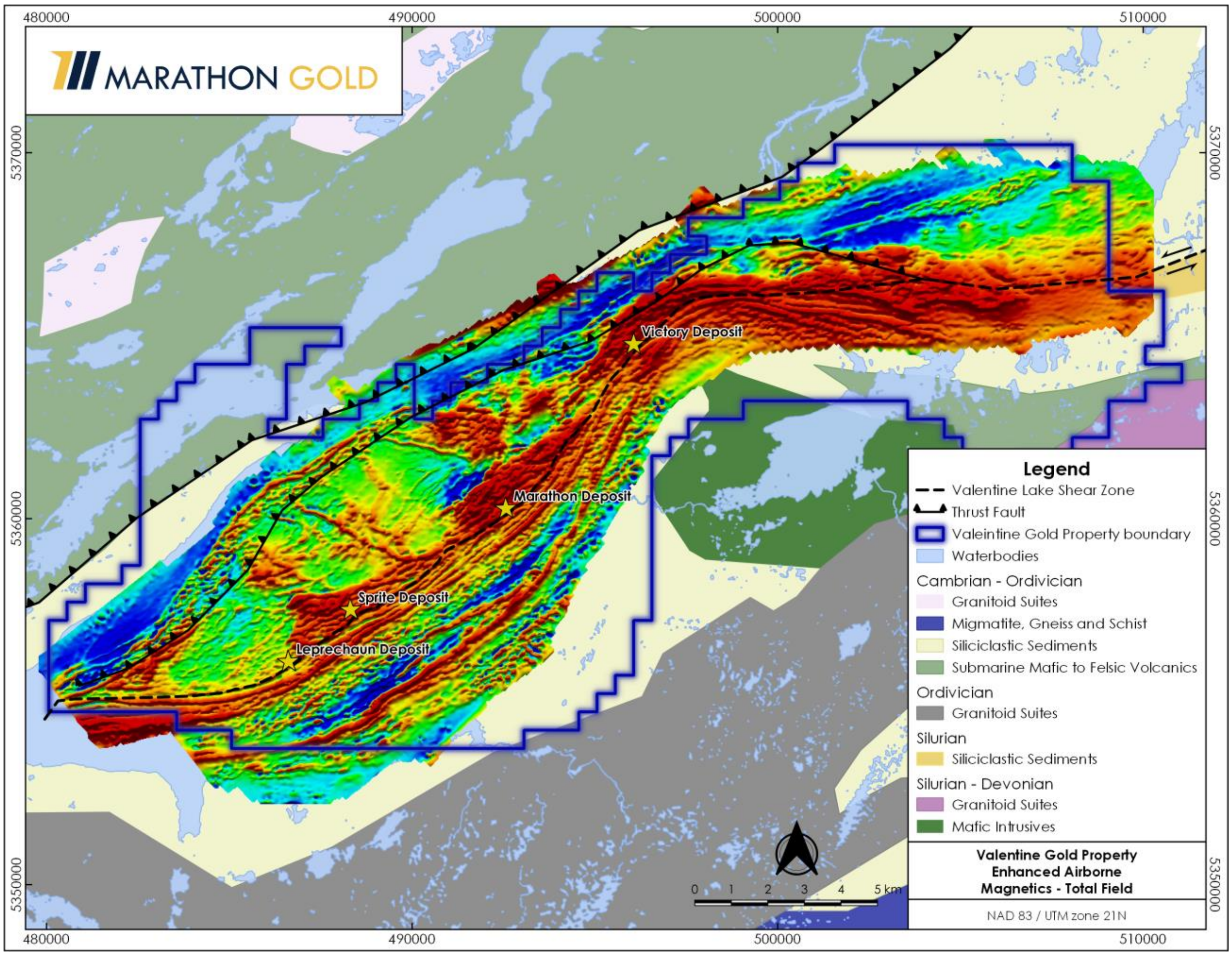

Figure 2.6: Airborne total magnetic field (reduced to pole) data revealing magnetic splays (from Marathon Gold Corporation, 2021).

Follow-up ground magnetic surveys at the Marathon and Sprite deposits were conducted by *Marathon Gold Corporation*, between 2014 and 2017 [Fig. 2.7]. The surveys were performed using an Overhauser magnetometer, comprising a total of 38.9 line-kilometres at 50-metre spacing. The significance of the results have been heavily debated and no definite correlation has yet to be made. Therefore, the magnetics data has been primarily used as an exploration tool to trace out the mafic dykes since the mineralization often intensifies along the margin (A. Wall, pers. comm., 2020).

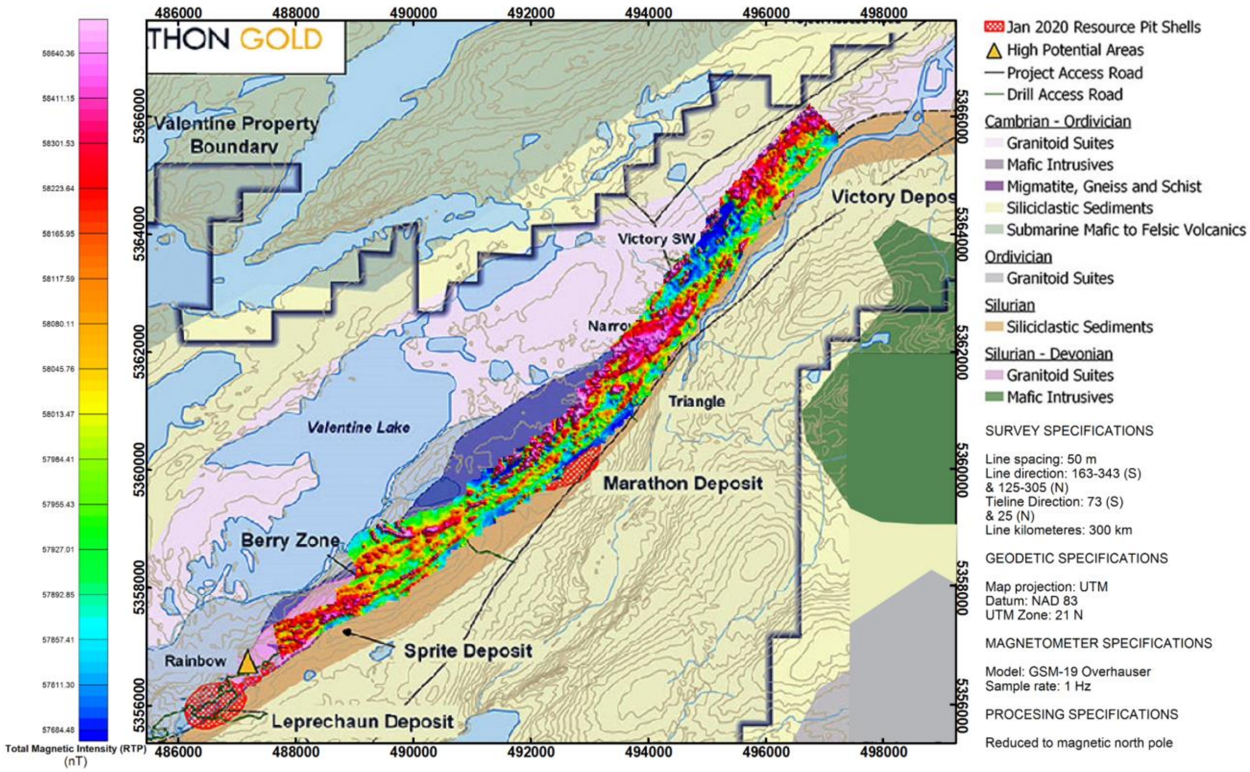

Figure 2.7: Ground magnetic field (RTP) data collected at the Valentine Lake Property.

2.3.3 Seismic

During the winter of 2017, *Acoustic Zoom Inc.* completed a seismic survey over a 2-kilometre-long, 500-metre-wide, southwest oriented zone within the property [Fig. 2.5], in an effort to delineate local geological structures, particularly, quartz-veining systems. The survey comprised of 89, 500-metre-long receiver lines at 25-metre spacing and 44 coinciding source lines at 50-metre spacing (Dunsworth et al., 2017). The 44 source lines, subsequently referred to as "mulch lines" were lines cut through thick forested areas by *Marathon Gold Corporation*, in preparation for these seismic surveys. Ground cover on the mulch lines consisted of moss, tree fragments and small boulders and rocks. Preliminary results from the seismic surveys indicated that seismic was not a suitable method of exploration at the VGP because the scale of the veins was much too small for the method to detect along with the nearly vertical orientation of the shear zone and identifying large vein “packages” proved difficult since the attempt was to highlight a series of quartz veins in a quartz rich host rock (A. Wall, pers. comm., 2021)

2.3.4 Preliminary Proof-of-Concept Gravity and Ground-Penetrating Radar

Given that ore concentrations at the VGP have proven difficult targets for previous geophysical exploration, Dr. Leitch and the author conducted a preliminary proof-of-concept gravity survey at the property in June 2018 to assess the feasibility of this technique on this style of deposits. The gravity survey was designed to transect the gold-bearing alteration zone to ascertain whether or not it would produce a measurable signature.

A nearly 3-kilometre gravity survey along Frozen Ear Road [Fig. 2.2], was performed using a *Scintrex* CG-5 gravimeter and 100-metre spacing. The resulting across-strike gravity profile revealed that the gold affiliated zone of hydrothermal alteration yielded a small (~1.6 mGal), but measurable negative gravity anomaly [Fig. 2.8], signifying that the gravity method is capable of detecting subsurface density variations and that a broad-scale survey could be useful in mapping the extent of the potentially gold-bearing alteration zone.

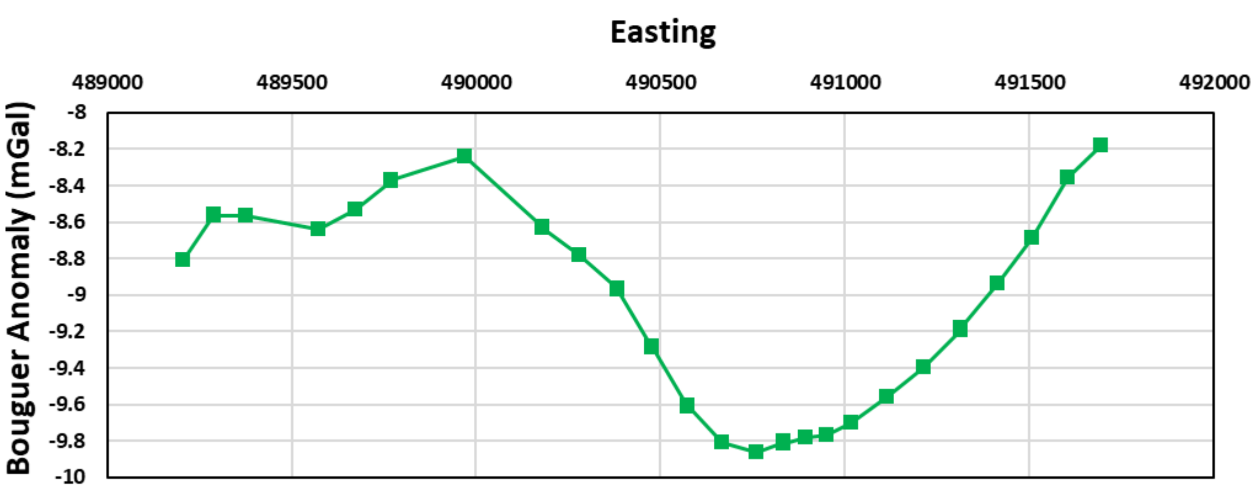

Figure 2.8: The complete Bouguer anomaly along Frozen Ear Road. The 1.6 mGal anomaly exceeds the ~0.1 mGal uncertainty threshold.

Additionally, a preliminary GPR survey was carried out over a bog in an attempt to map bog thickness as a means of determining suitable locations for future mining infrastructure. A single-line, 100 MHz GPR survey was completed using a pulseEKKO Pro GPR system by *Sensors and Software*. The 300-metre transect extended across Berry Zone and was marked at 50-metre intervals. Bog samples were collected and measured for water content since this is a major control on the radar wave velocity, which is required for depth calibration of the radar signals. From the water content analysis, a velocity of *0.035 m/ns* was chosen, which was proven accurate through testing with a bog probe. The resultant GPR profile [Fig. 2.9], proved successful at resolving the bottom of the bog, indicating that ground penetrating radar is an effective tool for determining the hypsometry of the local bogs. A detailed preliminary report of these proof-of-concept surveys and results, as well as a ground conductivity survey, is provided in Appendix A.

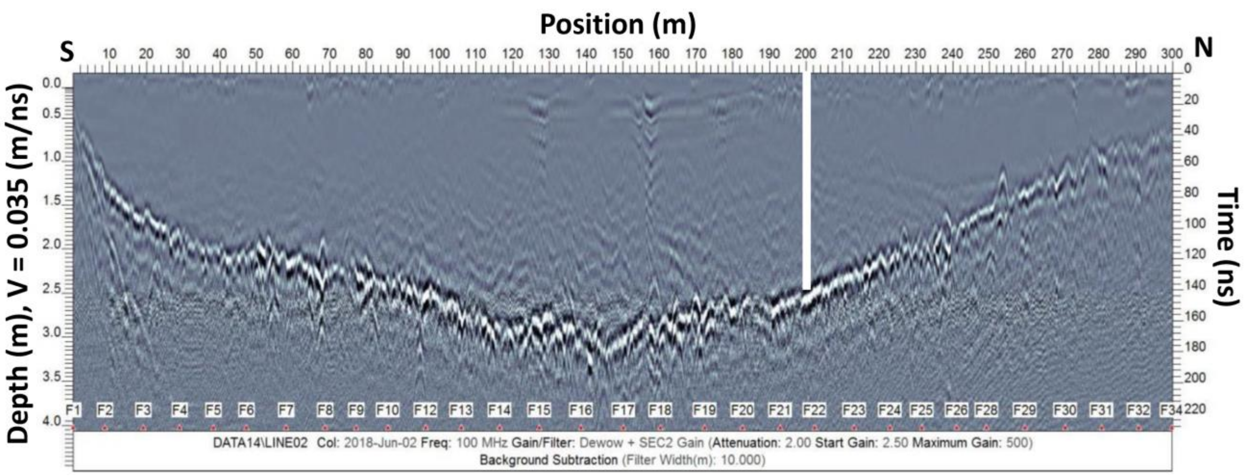

Figure 2.8: GPR profile over the 300m line across Berry Zone. Depth scale is based on a wave velocity of 0.035 m/ns, obtained by measuring the bog's water content (Appendix A).

3 BACKGROUND THEORY AND METHODS

3.1 BASIC GRAVITATIONAL THEORY

In contrast to other naturally occurring force fields in the Earth, including the magnetic field, gravity is a phenomenon which humans encounter every day: *objects when dropped fall towards the ground* (Gibson et al., 2003). Exploiting the Earth's gravitational field to investigate its internal structure has proven to be an effective method for probing large scale physical and structural variations within the subsurface. As a result, gravity has become a valuable method for discovering and assessing mineral prospects and deposits (*e.g*., Dentith and Mudge, 2014).

In geophysical exploration, gravity surveys are employed to locate bodies of contrasting density, since variations in the density of the subsurface lead to small changes in the gravity measured on the surface. Specifically, a rock body whose density differs from its surrounding medium (*i.e*., geological anomaly) generates an analogous disturbance (*i.e*., gravity anomaly) in the Earth's gravitational field (Alsadi et al., 2014). These fluctuations in gravity are measured using a device known as a gravimeter. Certain gravimeters are designed to measure absolute gravity, while others focus on relative gravity measurements. Most often, as applied to geophysical surveys, relative gravity determinations are exploited (Speight, 2015), while absolute gravimeters are used in geodesy.

At any particular location on Earth, there are numerous factors that contribute to the magnitude of gravity in addition to the crustal sources of interest. These include elevation, latitude, and surrounding topography, as well as Earth and ocean tides (Telford et al., 1990). In addition, target density anomalies in the upper crust are often superimposed onto anomalies due to deeper structures in the lower crust or mantle lithosphere, which can generate a smooth, long wavelength *"regional field"*, which can obscure the target. Therefore, as the primary interest in geophysical exploration is the contribution from subsurface density variations, the effects from these other factors must be removed before any interpretations can be made. In order to isolate gravitational signatures caused by local density variations, several corrections must be applied to the collected data. These constitute the *latitude correction*, *free-air correction*, *simple Bouguer correction*, *terrain correction*, *Earth tide correction* (Telford et al., 1990) and instrument drift. With these corrections and the *"regional"* field contributions removed, the remaining "*residual"* signal reveals the local density variations in the subsurface. This allows for accurate interpretation of the data in terms of the structures that produce them (Blakely, 1995). Gravity interpretation is a pinnacle endeavour in the geological and geophysical quest to understand the Earth and its subsurface and is the primary objective of any gravity survey.

The Earth's gravitational field is one of the fundamental potential fields existing in nature. To competently interpret variations within this field first requires an understanding of gravitational potential and acceleration. Within the gravity field, there exists an attraction force between any two masses present in nature (Alsadi et al., 2014). The following Sections [3.1.1 – 3.1.2] introduce the basic physical principles and subsequent mathematic laws that characterize this phenomenon.

3.1.1 Newton's Law of Gravitation

In 1687, English mathematician Sir Isaac Newton established the universal law of gravitation: *the gravitational force between two masses is directly proportional to the product of the masses and inversely proportional to the square of their separation* (Telford et al., 1990).

Expressed in mathematical form, *Newton's Law of Gravitation* is:

$$\boldsymbol{F} = \gamma \frac{m_1 m_2}{r^2} \hat{\boldsymbol{r}} \tag{3.1}$$

where,

$\boldsymbol{F}$ is the *force exerted on mass* m_2*, by mass* m_1;
γ is the *universal gravitational constant* $\mathbf{6.672} \times \mathbf{10^{-11}} \boldsymbol{Nm^2/kg^2}$;
r is the *distance between masses* m_1 *and* m_2;
$\hat{\boldsymbol{r}}$ is the *unit vector directed from mass* m_2 *towards mass* m_1;

The gravitational attraction force between two masses, m_1 and m_2, separated by a distance, r is illustrated in [Fig. 3.1] below.

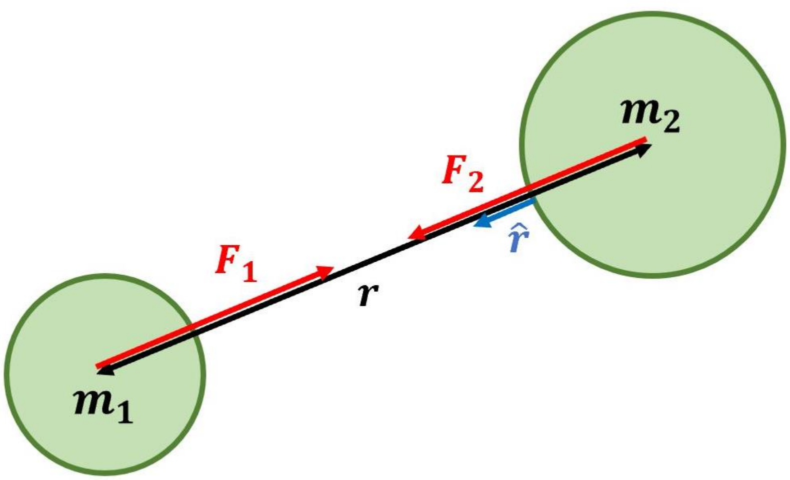

Figure 3.1: Gravitational force between two masses, m_1 *and* m_2*, separated by a distance,* r*.*

3.1.2 Acceleration due to Gravity

Newton's second law of motion states that any mass, m, that experiences a force, $\boldsymbol{F}$, will move with an acceleration, $\boldsymbol{a}$:

$$\boldsymbol{F} = m\boldsymbol{a} \tag{3.2}$$

Therefore, the acceleration of mass m_2 due to mass m_1 can be obtained by dividing the force $\boldsymbol{F}$ by mass m_2 in [Eqn. 3.1]:

$$\boldsymbol{a}_g = \gamma \frac{m_1}{r^2} \hat{\boldsymbol{r}} \tag{3.3}$$

The acceleration $\boldsymbol{a}_g$ is equivalent to the gravitational force per unit mass [Eqn. 3.2], thus if m_1 represents the mass of the Earth, M_e (5.97219×10^{24} kg), then $\boldsymbol{g}$ denotes the *acceleration due to gravity*, given by:

$$\boldsymbol{g} = \gamma \frac{M_e}{{r_e}^2} \hat{\boldsymbol{r}} \tag{3.4}$$

where,

r_e is the radius of the Earth (~ 6,371 km), which varies with latitude, and $\hat{\boldsymbol{r}}$ is directed towards the centre of the Earth (Telford et al., 1990).

3.2 MEASURING GRAVITY

A *gravimeter* is used to measure the gravitational field at specific locations on Earth. These instruments detect differences in gravity and provide an indication of the location and density of underground rock formations (Speight, 2015). There are two types of gravimeters: those that measure absolute gravity and those that measure relative gravity. In geophysical exploration, relative gravimeters are more commonly employed as absolute gravimeters are impractical and time-consuming for field operations (Alsadi et al., 2014).

Relative gravimeters quantify changes in gravity between two locations, or between two different times at the same location. Absolute gravimeters are used to determine absolute values of gravity at select locations around the world, with extreme precision. These locations constitute the *International Gravity Standardization Network* (IGSN) and serve as base stations for relative gravity surveys (Gibson et al., 2003). Establishing base stations where the absolute gravity is precisely known, allows relative gravity measurements to be determined with respect to the known absolute value at that base station.

Relative gravimeters measure gravity variations in milligals (mGal). In SI units, one mGal equals 0.00001 m/s^2. The average gravitational acceleration on the Earth's surface is approximately 981000 mGal, varying from 978100 mGal to 983200 mGal from the equator to the poles due to the Earth's flattening and rotation (ESA, 2021). Anomalies which gravimeters are employed to detect are typically on the order of a few mGal to a few tens of mGal. Small-scale geological anomalies resulting from deep structures such as ore deposits or salt domes can generate gravity anomalies as small as 0.1 mGal or less. Therefore, it is imperative that gravimeters are designed to measure gravity changes with tremendous precision. Most relative gravimeters today operate with a measurement error of 0.01 mGal and are portable, stable and fast to operate (Alsadi et al., 2014).

3.2.1 Absolute Gravity

Absolute gravimeters or "*free-fall*" gravimeters determine the constant downward acceleration of gravity by directly measuring the acceleration of a mass during free fall in a vacuum (Speight, 2015).

The time required for a free-falling mass to travel a known distance in a vacuum can be determined according to the following equation:

$$h = \frac{1}{2}\boldsymbol{g}t^2 \tag{3.5}$$

where,

h is the *height of initial resting position of the mass*;
$\boldsymbol{g}$ is the *acceleration due to gravity*;
t is the *time required for the mass to fall the distance h*;

While the physical concept of this method is straight-forward; in practice, achieving the necessary degree of accuracy can pose a challenge. It is suggested that for a one-metre fall, the distance, h, and time, t, require an accuracy within 10^{-5} centimetres and 10^{-8} seconds respectively (Alsadi et al., 2014). To achieve such accuracy, laser-interference devices are employed. This instrument, based on the falling-mass principle, comprises two corner-cube prisms and a laser-light source. It uses the interference of reflected light beams from the two prisms to determine the time, t, required for the upper prism to fall the pre-defined height, h [Fig. 3.2] (Brown, 2012). Although these devices are highly accurate, they are not very portable, and are better suited for geophysical observatories than field operations.

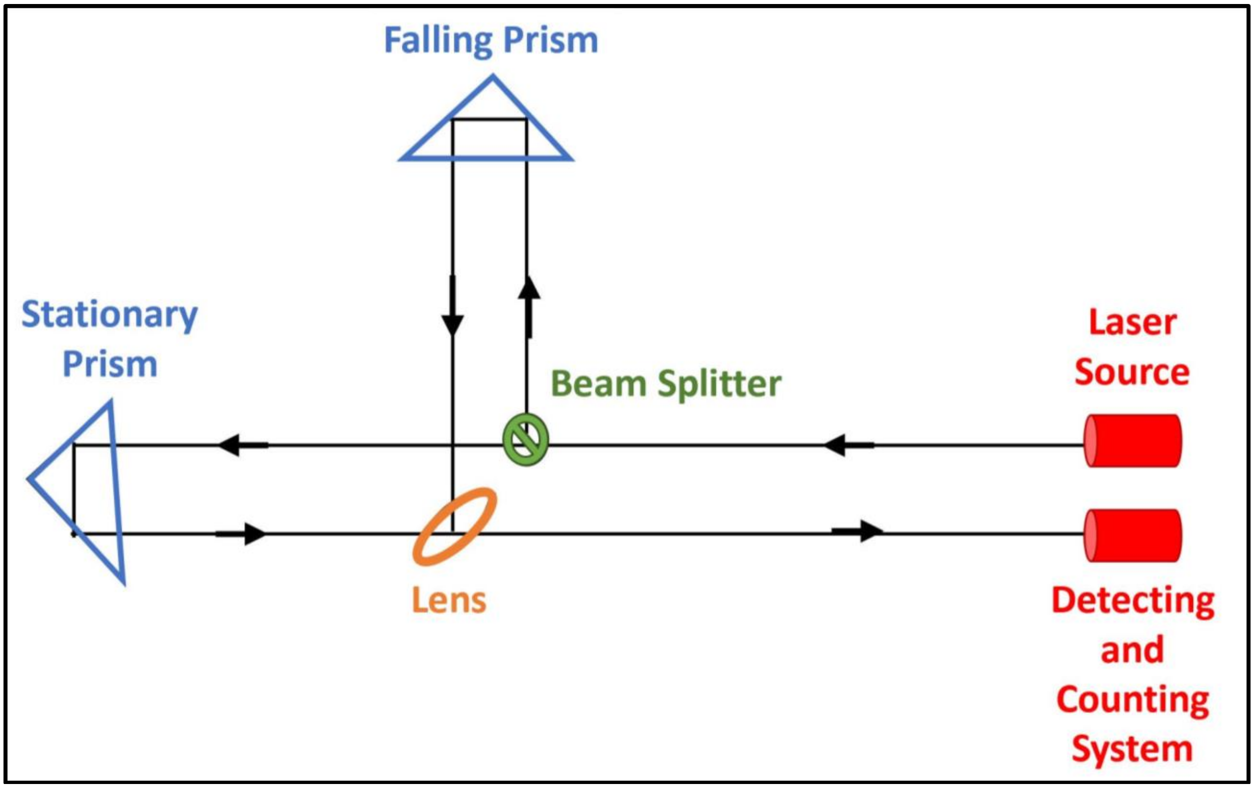

Figure 3.2: Schematic diagram of the falling-prism device for measuring absolute gravity.

3.2.2 Relative Gravity

Relative gravimeters are the dominant instrument used in today's geophysical field operations. Unlike the falling-mass device, relative or "*spring*" gravimeters measure changes in gravity rather than absolute gravity values. Simply explained, spring-based gravimeters consist of a weight suspended from a spring, where the extension of the spring depends on the pulling force. However, in reality the internal geometry of practical relative gravimeters such as the CG-5 Autograv system employed in this study (Section 4.1) are more complex than this (Scintrex, 2009). The principle is that variations in gravity will cause a change in weight of the fixed mass, which will generate fluctuations in the length of the spring (Speight, 2015).

This behaviour is based on *Hooke's law*:

$$\boldsymbol{F} = -k_s x = m\boldsymbol{g} \tag{3.6}$$

where,

$\boldsymbol{F}$ is the *force applied to the spring*;
k_s is the *spring constant*;
x is the *displacement or change in length of spring;*
m is the *mass*;
$\boldsymbol{g}$ is the *acceleration due to gravity*;

As illustrated in [Fig. 3.3], the gravitational force, $m\boldsymbol{g}$, is balanced by the upward spring force, $k_s x$. This suggests that any variation in gravity, $\Delta\boldsymbol{g}$, will yield a corresponding change, Δx, in the length of the spring, as:

$$m\Delta\boldsymbol{g} = -\,k_s\Delta x \tag{3.7}$$

Hence, from direct measurement of the change in spring length, Δx, inside the gravimeter, the change in gravity, $\Delta\boldsymbol{g}$, can be determined from:

$$\Delta\boldsymbol{g} = -\,k_s\frac{\Delta x}{m} \tag{3.8}$$

So, if a "*spring*" gravimeter is employed at a site where gravity, $\boldsymbol{g}$, is known, then the gravity at other locations can be determined by observing how the length of the spring varies between locations. The spring extension is recorded using high precision optical, electrical or mechanical amplification techniques. As the elasticity of the spring can vary over time, resulting in instrument drift, the gravimeter is calibrated at regular intervals at a base station where the absolute gravity is known (Alsadi et al., 2014).

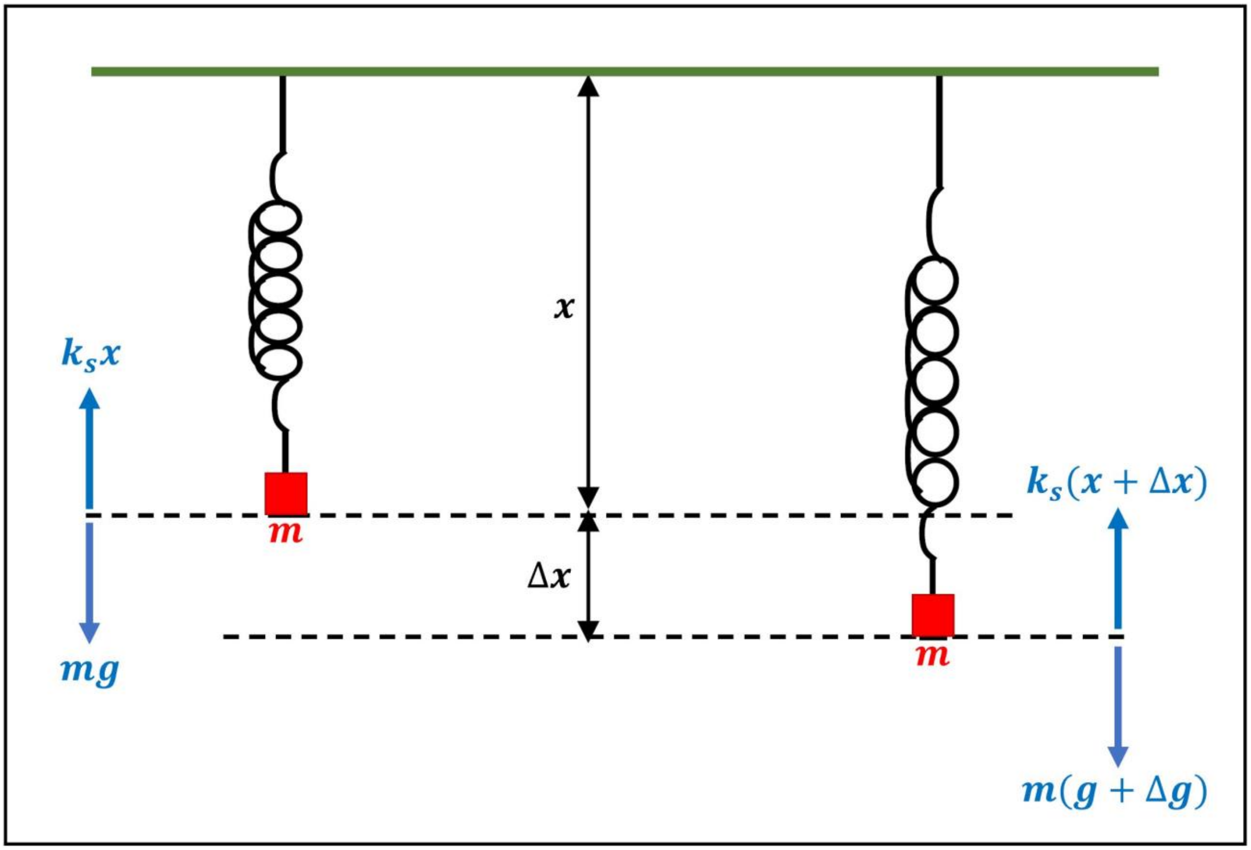

Figure 3.3: Visual representation of the principle of the spring balance, based on Hooke's law (modified from Alsadi et al., 2014).

3.3 GRAVITY CORRECTIONS AND ANOMALIES

Gravity contributions exist everywhere on Earth and result from a variety of different factors. Field gravity measurements are the combined effect of the geological structure beneath the observation location ("*residual*" field) and the gravity signatures from other sources. These contributions include the effects of the reference ellipsoid, elevation, nearby topography, and Earth and ocean tides caused by the Sun and the Moon (Blakely, 1995).

As the objective of the exploration geophysicist is to isolate the gravity anomalies due to the crustal sources of interest, all contributions apart from those due to density variations must be removed. For a ground based stationary gravimeter this is achieved by applying a series of "*corrections"* to the field data, which consist of *latitude correction, free-air correction, simple Bouguer correction*, *Earth tide correction* and *terrain correction* (Telford et al., 1990).

The process of eliminating all non-geological effects from the field data is referred to as *data reduction*. The remaining "*residual*" signal known as the *complete Bouguer anomaly* reveals the subsurface density changes with respect to the spheroidal surface that best represents the *geoid*, which is the surface defined by sea level (see below). Thus, processing of the observed gravity data is effectively removing all gravity signatures caused by time-variant changes and material located above sea level [Fig. 3.4]. The gravity corrections that contribute to the production of the *complete Bouguer anomaly* will be further discussed in Sections [3.3.1 – 3.3.5] below.

3.3.1 The Geoid, Reference Ellipsoid and Latitude Correction

The *geoid* is the surface described by sea level, excluding the effects of ocean currents, weather and tides, on which the gravitational potential is constant. On land, the geoid is analogous to what the level of water in a canal would be if either end were connected to an ocean. The shape of the geoid is affected by local mass anomalies; it swells over mountain ranges or dense buried ore deposits and depresses over valleys or low-density bodies, resulting in complex spatial variation. Consequently, a simpler, smoother surface is often used as a reference for gravity measurements; the spheroid that best approximates the geoid [Fig. 3.4]. Due to the balance between gravity and rotation, the reference spheroid is an oblate ellipsoid of revolution, known as the *reference ellipsoid* (Blakely, 1995).

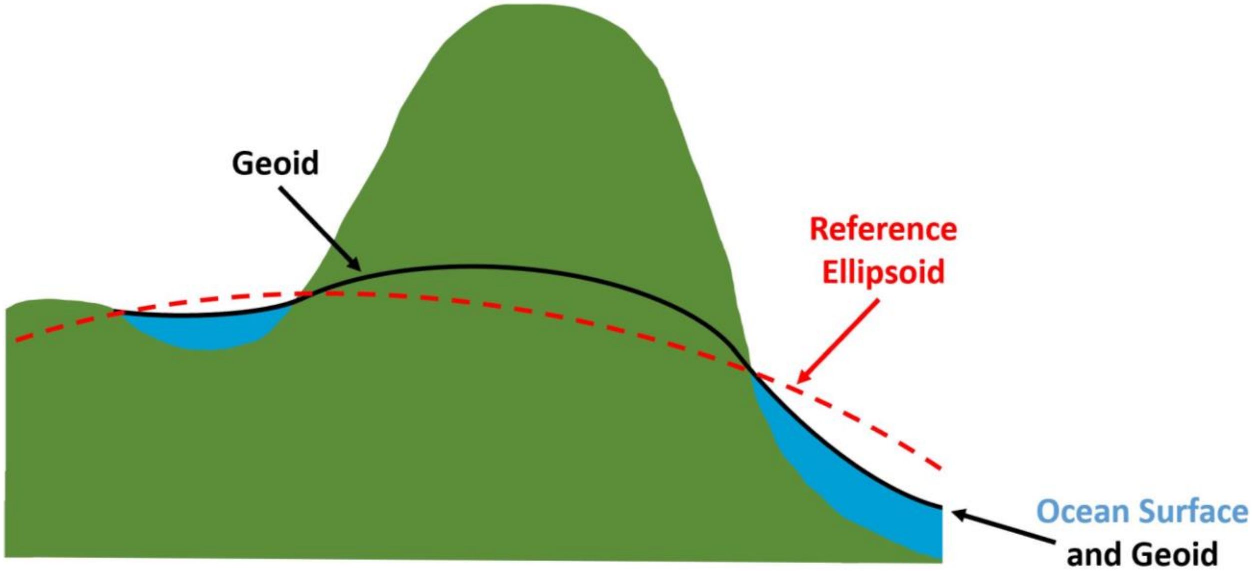

Figure 3.4: Comparison of the geoid and reference ellipsoid. The shape of the geoid is influenced by underlying mass.

The most significant variation, in both magnitude and scale, of the Earth's gravity field is caused by the Earth's approximate ellipsoidal shape and rotation. The *latitude correction* considers the shape of a reference ellipsoid, estimating the shape of the surface of the Earth and the centrifugal acceleration resulting from the Earth's rotation. The variation contributed by the shape of the Earth's surface is due to the changing distance of the surface from the centre of the Earth, meaning on an ellipsoid the radius of the Earth varies with latitude, λ [Eqn. 3.4], as does the gravity. Improved geodetic knowledge acquired from satellites have helped to establish the best-suited ellipsoidal surface used today (Blakely, 1995).

The currently accepted representation for the *theoretical* or *normal gravity*, g_0, redefined by the *International Association of Geodesy* (IAG), is the *World Geodetic System* (WGS) 1984 given by:

$$\boldsymbol{g}_0 = 9.7803267714 \frac{1+0.00193185138639 \sin^2 \lambda}{\sqrt{1-0.00669437999013 \sin^2 \lambda}} \quad \text{mGal} \tag{3.9}$$

Equation 3.9 considers only the broadest scale latitudinal variations in the radius of the Earth and neglects variations with longitude (Telford et al., 1990).

3.3.2 Free-Air Correction and Anomaly

As shown in [Eqn. 3.4], the Earth's gravitational acceleration decreases inversely with the square of the distance from its centre (*i.e.*, $\frac{1}{r^2}$). Consequently, any increase in distance above or below the reference ellipsoid will affect any field measurements taken (Blakely, 1995). To account for the vertical difference in elevation between the gravimeter location and the reference ellipsoid, a *free-air correction* is applied. The free-air correction considers only the effect of elevation and not any material that may exist between the measurement height and the ellipsoid and is given by:

$$\boldsymbol{g}_{fa} = -0.3086 \times 10^{-5} h \tag{3.10}$$

where, h is the height in metres, above or below sea level and $\boldsymbol{g}_{fa}$ is measured in mGal. Equation 3.10 is derived from differentiating [Eqn. 3.4] with respect to r, whereby the value of 0.3086 assumes an average value of r_e. Therefore, since the radius of the Earth varies with latitude (Section 3.3.1), the above-mentioned value varies also, from 0.3072 at the equator to 0.3102 at the poles. If the gravimeter is located above sea level, $\boldsymbol{g}_{fa}$ is added to the observed gravity and if it is located below sea level, $\boldsymbol{g}_{fa}$ is subtracted from the measured gravity [Fig. 3.5].

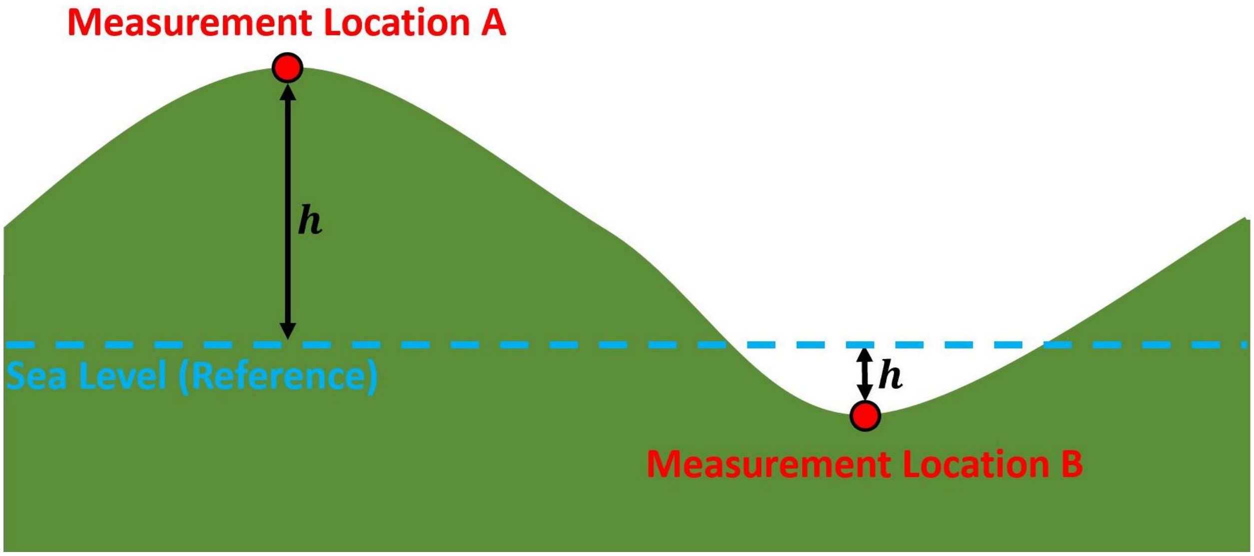

Figure 3.5: Schematic representation of the free-air correction. Vertical differences in elevation between the measurement locations and the reference ellipsoid (sea level) are accounted for.

Applying the free-air correction yields the *free-air anomaly* expressed as:

$$\Delta \boldsymbol{g}_{fa} = \boldsymbol{g}_{obs} - \boldsymbol{g}_0 - \boldsymbol{g}_{fa} \tag{3.11}$$

where $\boldsymbol{g}_{obs}$ is the observed gravity at a given observation location (Blakely, 1995). Some of the main uses of free-air gravity include gravity studies of the Moon and other planets and surveys over the Earth's oceans, where the free-air gravity anomaly is a proxy for sea floor topography.

3.3.3 Simple Bouguer Correction and Anomaly

As previously discussed in Section 3.3.2, the free-air correction allows solely for the effect of elevation and does not consider the attraction of additional mass between sea level and the observation location. On land, this leads to an undesirable correlation between the free-air anomaly and topography. The *simple Bouguer correction* is a first-order correction that accounts for the mass that was ignored by the free-air anomaly and mostly eliminates the unwanted correlation with topography (Blakely, 1995). The simple Bouguer correction approximates the mass above sea level using an infinite, uniform density slab of thickness equal to the measurement point height, h, as shown in [Fig. 3.6].

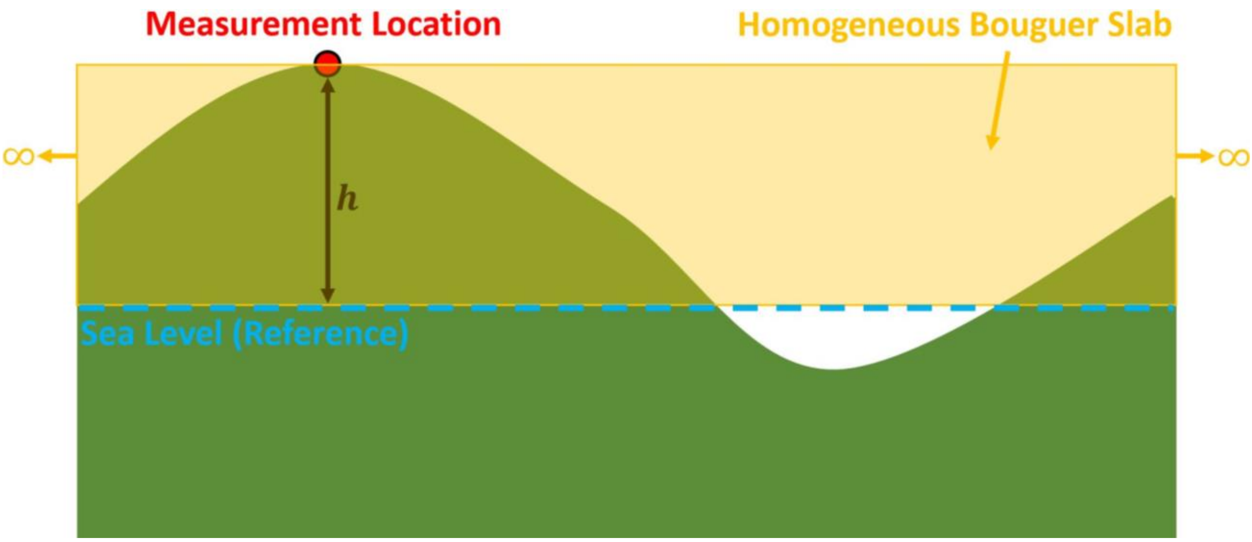

Figure 3.6: The Bouguer slab approximation for the simple Bouguer correction.

The gravity of such slab is given by:

$$\boldsymbol{g}_{sb} = 2\pi\gamma\rho h \tag{3.12}$$

Assuming a typical crustal density of *2670 kg/m³*, which agrees within the uncertainty of most of the densities of the study area provided in Table 2.1, the simple Bouguer correction becomes:

$$\boldsymbol{g}_{sb} = 0.1119 \times 10^{-5} h \tag{3.13}$$

If the gravimeter is located above the datum, $\boldsymbol{g}_{sb}$ is subtracted from the measured gravity and if it is located below the datum, $\boldsymbol{g}_{sb}$ is added to the observed gravity (Gibson et al., 2003).

The resultant *simple Bouguer anomaly* reflects "*anomalous*" mass, thus providing information about subsurface features with density values above or below the value used in the Bouguer correction (*2670 kg/m³*). It is expressed as:

$$\Delta\boldsymbol{g}_{sb} = \boldsymbol{g}_{obs} - \boldsymbol{g}_0 - \boldsymbol{g}_{fa} - \boldsymbol{g}_{sb} \tag{3.14}$$

3.3.4 Terrain Correction and Complete Bouguer Anomaly

As the simple Bouguer correction exploits a homogeneous infinite slab to estimate the mass, the resulting simple Bouguer anomaly overlooks the shape of topography surrounding the measurement location. The slab approximation does not consider that highlands above the observation location exert an upward "*pull*" on the gravimeter, while lowlands beneath the measurement site generate voids within the slab [Fig. 3.7]. The simple Bouguer correction does not compensate for these effects and requires a *terrain correction* to rectify this (Blakely, 1995).

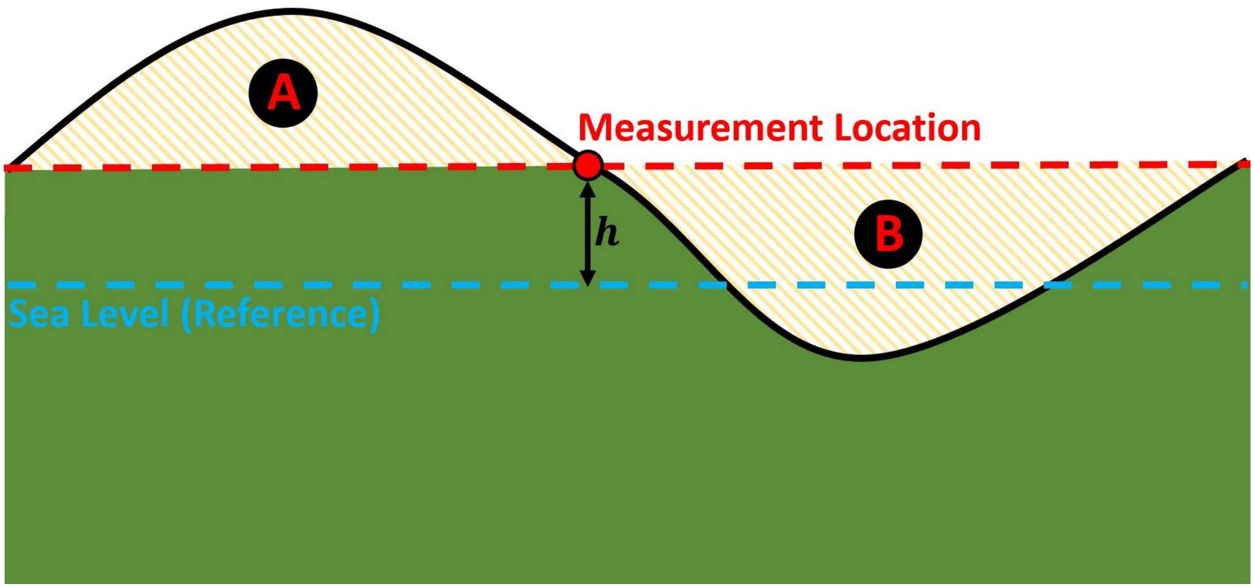

*Figure 3.7: The slab approximation does not take into account **A**: The upward pull of the mass of this hill above the measurement point or **B**: The lack of downward pull because of the mass deficit in this topographic low beneath the observation location.*

In areas of moderate to severe topographic relief, the terrain correction, $\boldsymbol{g}_t$, is a critical step in the data reduction process as there is a significant effect of topographic features surrounding the measurement site. The terrain correction adjusts for these topographic irregularities around the observation location by approximating the topography using a *Digital Elevation Model* (DEM) and forward modelling techniques to evaluate the gravitational attraction of the model (Blakely, 1995). It is the most sophisticated and computational correction required for any gravity survey.

Executing the terrain correction results in the *complete Bouguer anomaly*:

$$\Delta \boldsymbol{g}_{cb} = \boldsymbol{g}_{obs} - \boldsymbol{g}_0 - \boldsymbol{g}_{fa} - \boldsymbol{g}_{sb} - \boldsymbol{g}_t \tag{3.15}$$

which describes the gravity response due entirely to the target source: density variations in the crust and upper mantle. For observations above sea level, $\boldsymbol{g}_t$, is always negative, therefore the complete bouguer anomaly is always more positive than the simple bouguer anomaly.

3.3.5 Earth Tide Correction

Earth-tides provoked by movement of the Sun and the Moon can have small, but measurable effects on the observed gravity. These effects are due to a combination of the gravitational attraction between the Sun and the Moon and the weight on the spring (directly), and the deformation of the Earth in response to these gravitational forces. They are sinusoidal in nature [Fig. 3.8] and can range up to nearly 0.3 mGal.

The *Earth tide correction* can be computed if the positions of the Sun and Moon are known, but because the fluctuation is smooth and fairly slow, it is sometimes included in the drift correction (Telford et al., 1990). The tidal effect depends on time and latitude, such that the latitudinal location must be known within approximately 2 kilometres. To achieve this, a GPS is attached to the CG-5 and subsequently the tidal effects can be approximated and removed using Longman's formulas (Longman, 1959), which are incorporated into the gravimeter [Fig. 4.2].

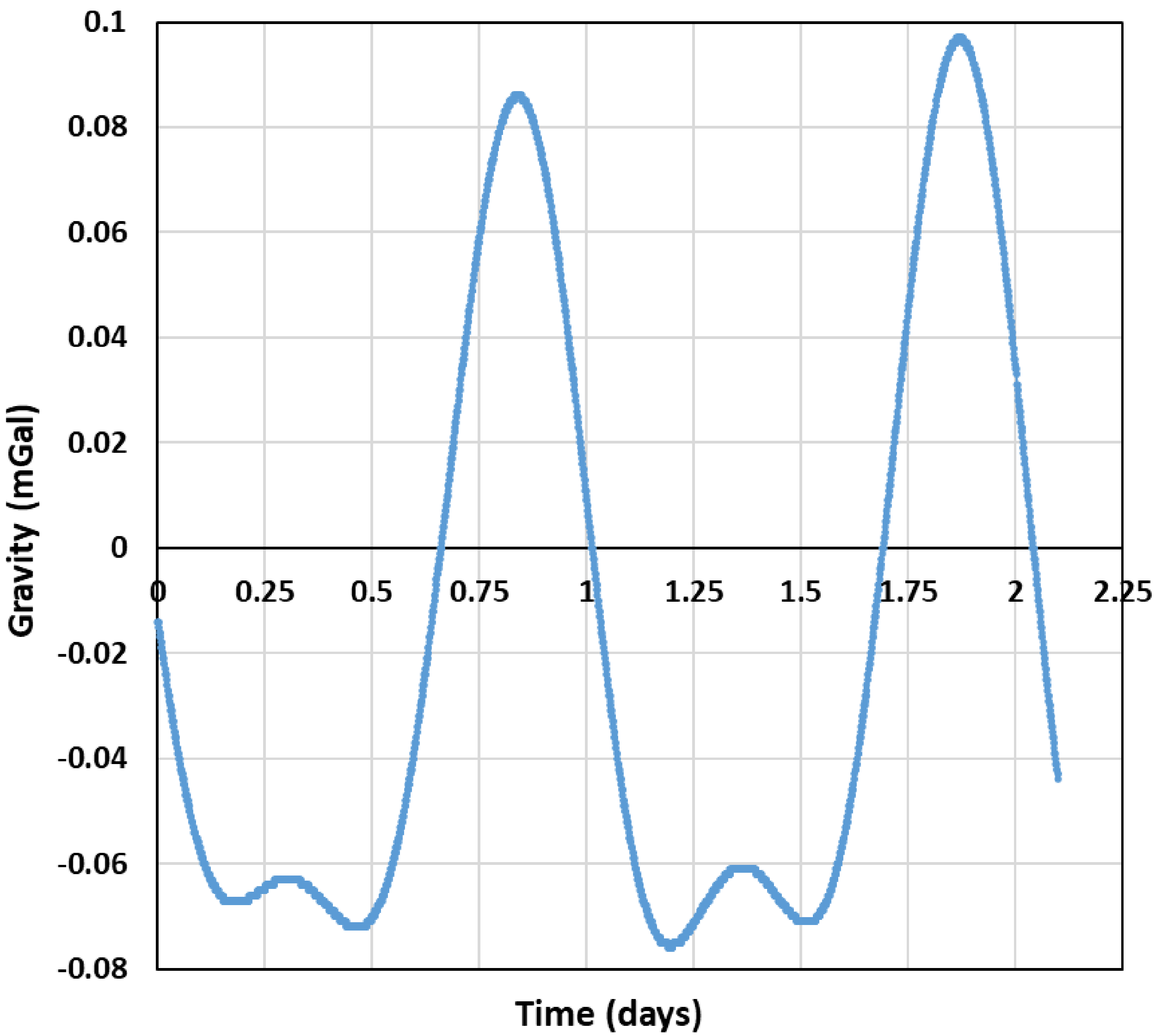

Figure 3.8: The sinusoidal Earth tide effects on the observed gravity measured during a drift calibration in August 2019.

3.3.6 Drift and Travel Corrections

As the spring system inside the gravimeter is not perfectly elastic, it is subject to slow and continual creep, resulting in a change in the spring constant. Gravity readings therefore change slowly in a process known as instrument drift. To correct for this, a *drift calibration* is performed internally by the gravimeter and a resulting drift correction [Fig. 3.9] is obtained. During a drift calibration, the instrument continuously measures the relative gravity at the same location for approximately 24 to 26 hours. This time is chosen to allow the sinusoidal effects of the Earth tides [Fig. 3.8] to cancel out, when finding a linear trend through the data [Fig. 3.9]. Therefore, it is important that the chosen environment is stable in order to obtain a meaningful calibration (Scintrex, 2009). While the drift correction is linear, over a longer timescale the drift is not, therefore it is imperative that drift calibrations are carried out at regular intervals. Gravimeter drift can vary from less than 1 mGal per week to 1 mGal per day [Fig. 3.9] thus, when performing gravity surveys, it is common practice to take repeat measurements at a chosen base station during every field day (Alsadi et al., 2014).

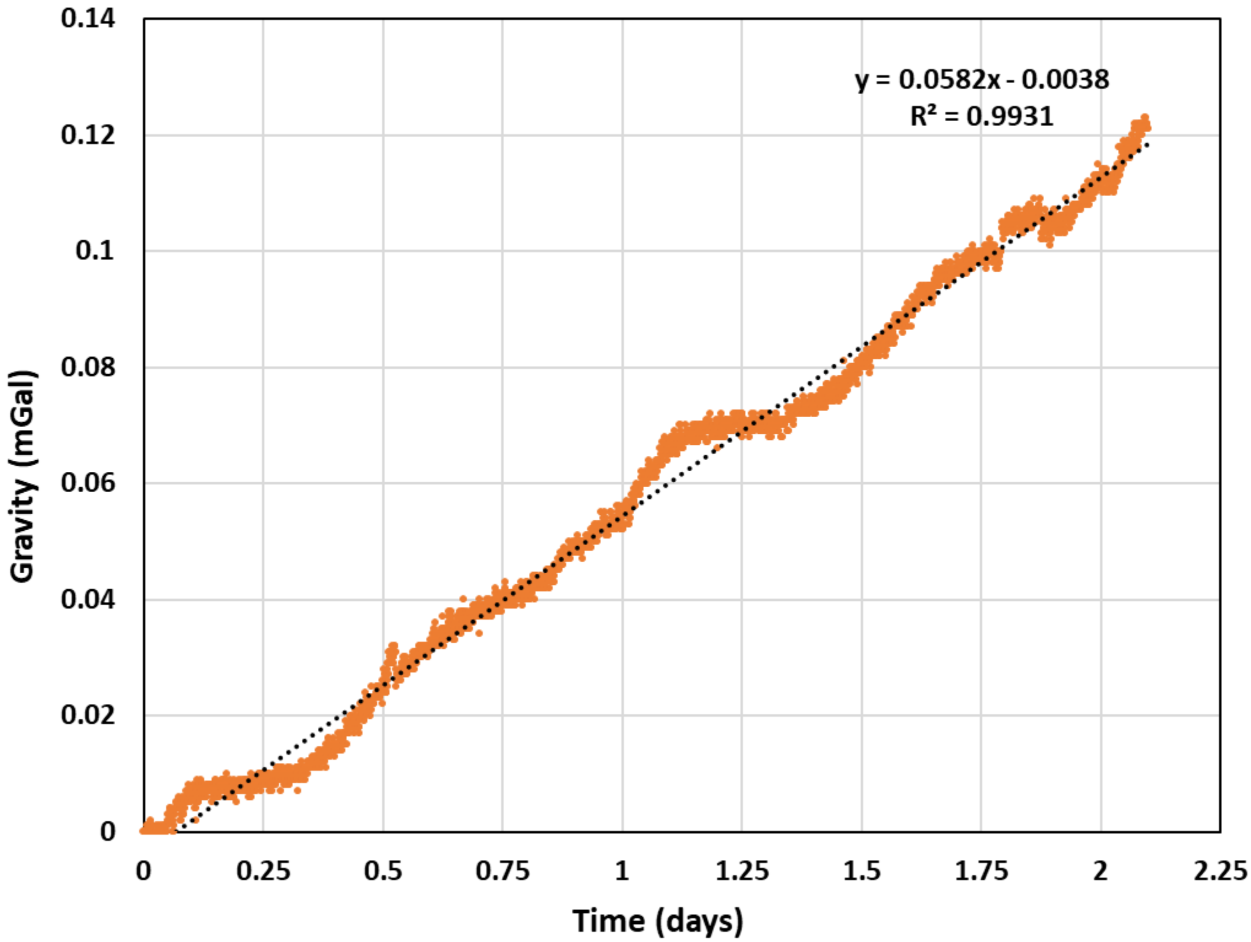

Figure 3.9: August 2019 drift calibration plot including the linear drift correction line (black dotted) and associated values ($y = mx + b$).

In addition to the slow creep and fluctuations in the spring from jostling, gravimeter offsets can arise from small, unsystematic changes associated with instrument transport. These variations can be positive or negative and unlike the drift, they cannot be rectified through calibration. Therefore, to minimize these offsets, extreme care is taken when transporting the instrument, and whenever possible, its robust, padded travel box is used. Moreover, it is important that the interior of the instrument maintains a relatively constant temperature as to further avoid thermal stresses to the spring which could affect its properties. It can take days to stabilize if the instrument warms to room temperature and once settled, a calibration is essential.

3.4 BASIC ELECTROMAGNETIC THEORY

The fundamentals of ground penetrating radar lie in electromagnetic theory. The signals that GPR systems transmit are electromagnetic waves within a subset of the full electromagnetic spectrum. Maxwell's equations (Section 3.4.1) describe the behaviour of electric and magnetic fields, while constitutive relations (Section 3.4.2) characterize their interaction with material properties. Together, these two sets of relations provide the foundations for quantitatively describing GPR signals (Annan, 2003). The following overview provides the basic theoretical understanding required to work with GPR.

3.4.1 Maxwell's Equations

Maxwell's equations are a set of four equations that mathematically define electric and magnetic (electromagnetic) fields and their related properties.

In differential form within magnetic, conductive and polarizable media, Maxwell's equations are expressed follows:

$$\nabla \cdot \mathbf{D} = \rho \qquad \text{(Eqn. 3.16)}$$

$$\nabla \cdot \mathbf{B} = 0 \qquad \text{(Eqn. 3.17)}$$

$$\nabla \times \mathbf{E} = -\frac{\partial \mathbf{B}}{\partial t} \qquad \text{(Eqn. 3.18)}$$

$$\nabla \times \mathbf{H} = \frac{\partial \mathbf{D}}{\partial t} + \mathbf{J} \qquad \text{(Eqn. 3.19)}$$

where,

$\nabla \cdot$ is the *divergence operator*;
$\nabla \times$ is the *curl operator*;
$\mathbf{D}$ is the *electric displacement field* (C/m^2);
$\mathbf{B}$ is the *magnetic flux density* (T);
$\mathbf{E}$ is the *electric field strength* (V/m);
$\mathbf{H}$ is the *magnetic field strength* (A/m);
$\mathbf{J}$ is the *total electric current density* (A/m^2);
$\frac{\partial \mathbf{D}}{\partial t}$ is the *displacement current density* (A/m^2);
ρ is the *total charge density* (C/m^3);

Equation 3.16 is *Gauss's law for electricity*, [Eqn. 3.17] is *Gauss's law for magnetism*, [Eqn. 3.18] is *Faraday's law of induction*, and [Eqn. 3.19] is *Ampère's law* (Lorrain et al., 1987). Collectively, these laws, and the associated media properties, define all electromagnetic phenomena (*i.e.*, radio waves, circuit theory, induction, resistivity, etc.).

3.4.2 Constitutive Relations and Material Properties

Constitutive equations are the mechanisms for describing a material's response to electromagnetic (EM) fields. These equations [Eqn. 3.20 – 3.22] express the behaviour of electrons, atoms, molecules and ions due to an applied EM field and they help to specify the dependence of *polarization*, *magnetization* and *conductivity* on these applied fields. Polarization describes how a material responds to and changes an applied electric field, while magnetization is a measure of the response of a material to a magnetic field (Jol, 2008).

The electric and magnetic properties embodied within the constitutive equations are important for GPR, particularly, *electrical conductivity* (σ), *dielectric permittivity* (ε) and *magnetic permeability* (μ). The way the electromagnetic fields interact with natural materials controls how electromagnetic fields spread into a medium and are attenuated (Annan, 2003).

The constitutive equations that describe the interaction of the EM fields with surrounding linear, homogeneous, and isotropic media are:

$$\mathbf{J} = \sigma\mathbf{E} \qquad \text{(Eqn. 3.20)}$$

$$\mathbf{D} = \varepsilon\mathbf{E} \qquad \text{(Eqn. 3.21)}$$

$$\mathbf{B} = \mu\mathbf{H} \qquad \text{(Eqn. 3.22)}$$

Here, linear media implies that over the range of field strengths of interest, the conductivity, permittivity, and permeability are constant to a good approximation (i.e., they do not depend on **E** and **B**: they may change as the material changes). Electrical conductivity (σ), expressed in Siemens per metre, quantifies how easily electrical charges move through a given material when an external electric field is applied. In Equation 3.22, σ represents the ratio between the *electric current density* (**J**) within a material and the *electric field* (**E**). This relationship [Eqn. 3.20] is known as *Ohm's law* (Annan, 2005). Dielectric permittivity (ε) characterizes the degree of electrical polarization a material experiences under the influence of an applied electric field and has units of Farads per metre. With respect to [Eqn. 3.21], ε is the relation between the *electric field* (**E**) within a material, and the corresponding *electric displacement* (**D**) (Jol, 2008). Magnetic permeability (μ) defined in

Henries per metre, describes the degree of magnetization of a material in response to an applied magnetic field. Examining Equation 3.22, μ defines the ratio between the *magnetic flux density* (**B**) within a material, and the intensity of an applied *magnetic field* (**H**) (Annan, 2003).

In the above equations [3.20 – 3.22], the properties are defined as simple constants, valid for uniform, homogenous material with no losses or anisotropy. In general, these material properties (σ, ε and μ) are tensors and can be non-linear. However, for essentially all practical GPR issues, these quantities are treated as field-independent scalar quantities, meaning that the response is in the same direction as the exciting field and independent of the field strength (Annan, 2003).

Ground penetrating radar is most effective in low-electrical-loss materials. The one-dimensional electromagnetic wave equations in a linear, conductive medium (Griffiths, 1999) are:

$$\frac{\partial^2 \boldsymbol{E}}{\partial z^2} = \mu\varepsilon \frac{\partial^2 \boldsymbol{E}}{\partial t^2} + \mu\sigma \frac{\partial \boldsymbol{E}}{\partial t} \qquad \text{(Eqn. 3.23)}$$

$$\frac{\partial^2 \boldsymbol{B}}{\partial z^2} = \mu\varepsilon \frac{\partial^2 \boldsymbol{B}}{\partial t^2} + \mu\sigma \frac{\partial \boldsymbol{B}}{\partial t} \qquad \text{(Eqn. 3.24)}$$

where $\boldsymbol{E}$ and $\boldsymbol{B}$ are the electric and magnetic vector field components of the electromagnetic wave, z is distance and t is time. Equations 3.23 and 3.24 illustrate the importance of attenuation due to the electrical properties of the ground.

Therefore, in most GPR applications, particularly geophysical/geological situations, variations in dielectric permittivity and electrical conductivity are the most significant, while changes in magnetic permeability are seldom of concern. The dielectric permittivity is often expressed in terms of relative permittivity or *dielectric constant* (κ) which is defined as:

$$\kappa = \frac{\varepsilon}{\varepsilon_0} \qquad \text{(Eqn. 3.25)}$$

where ε_0 is the *permittivity of free space* equal to 8.89×10^{-12} F/m. It is the variation in these physical properties, specifically the electrical properties [Tbl. 3.1], that gives rise to the observed subsurface reflections obtained with a GPR system (Jol, 2008). This can be demonstrated through the one-dimensional solutions to the above wave equation [Eqns. 3.23, 3.24], which describe an EM wave with an amplitude which decays as it propagates:

$$\vec{\mathbf{E}}(\mathrm{z,t}) = \overrightarrow{\mathbf{E}_0}\mathrm{e}^{-\mathrm{kz}}\cos(\mathrm{kz}-\omega\mathrm{t}+\delta_{\mathbf{E}})\,\hat{x} \qquad \text{(Eqn. 3.26)}$$

$$\vec{\mathbf{B}}(\mathrm{z,t}) = \overrightarrow{\mathbf{B}_0}\mathrm{e}^{-\mathrm{kz}}\cos(\mathrm{kz}-\omega\mathrm{t}+\delta_{\mathbf{E}}+\varphi)\,\hat{y} \qquad \text{(Eqn. 3.27)}$$

$$\varphi = \tan^{-1}(\kappa/k) \qquad \text{(Eqn. 3.28)}$$

where $\overrightarrow{\mathbf{E}_0}$ and $\overrightarrow{\mathbf{B}_0}$ are the wave component amplitudes at z = 0, κ is the decay rate, k is the wave number, $\delta_{\mathbf{E}}$ is the initial phase angle of the electric field, φ is the phase delay of the magnetic field and ω is the angular frequency.

Table 3.1: Typical dielectric constant (κ), conductivity (σ), velocity (v), and attenuation values (α) for common geological materials (from Annan, 2005).

Material	K	σ (mS/m)	v (m/ns)	α (dB/m)
Air	1	0	0.30	0
Distilled water	80	0.01	0.033	2 × 10–3
Fresh water	80	0.5	0.033	0.1
Sea water	80	3000	.01	103
Dry sand	3–5	0.01	0.15	0.01
Saturated sand	20–30	1–10	0.06	0.03–0.3
Limestone	4–8	0.5–2	0.12	0.4–1
Shales	5–15	1–100	0.09	1–100
Silts	5–30	1–100	0.07	1–100
Clays	5–40	2–1000	0.06	1–300
Granite	4–6	0.01–1	0.13	0.01–1
Dry salt	5–6	0.01–1	0.13	0.01–1
Ice	3–4	0.01	0.16	0.01

3.5 GPR SYSTEM OPERATION: BASIC PRINCIPLES

Ground penetrating radar is a non-destructive electromagnetic geophysical survey device that uses high-frequency (usually between 10 and 1000 MHz) electromagnetic wave propagation and scattering to image the subsurface. This subsurface imaging is achieved by locating and identifying changes in electrical properties within the ground (Annan, 2003). Unlike lower frequency EM methods, GPR exploits electromagnetic radiation in the radio-frequency and microwave band of the radio spectrum and detects the reflected signals from subsurface structures. These identified responses are due to a wide range of features including soil anomalies and material changes such as layers, voids and cracks. As a result, this technique is optimal in a variety of media, including rock, soil, ice, freshwater, various pavements and infrastructures (Melvin, 2014).

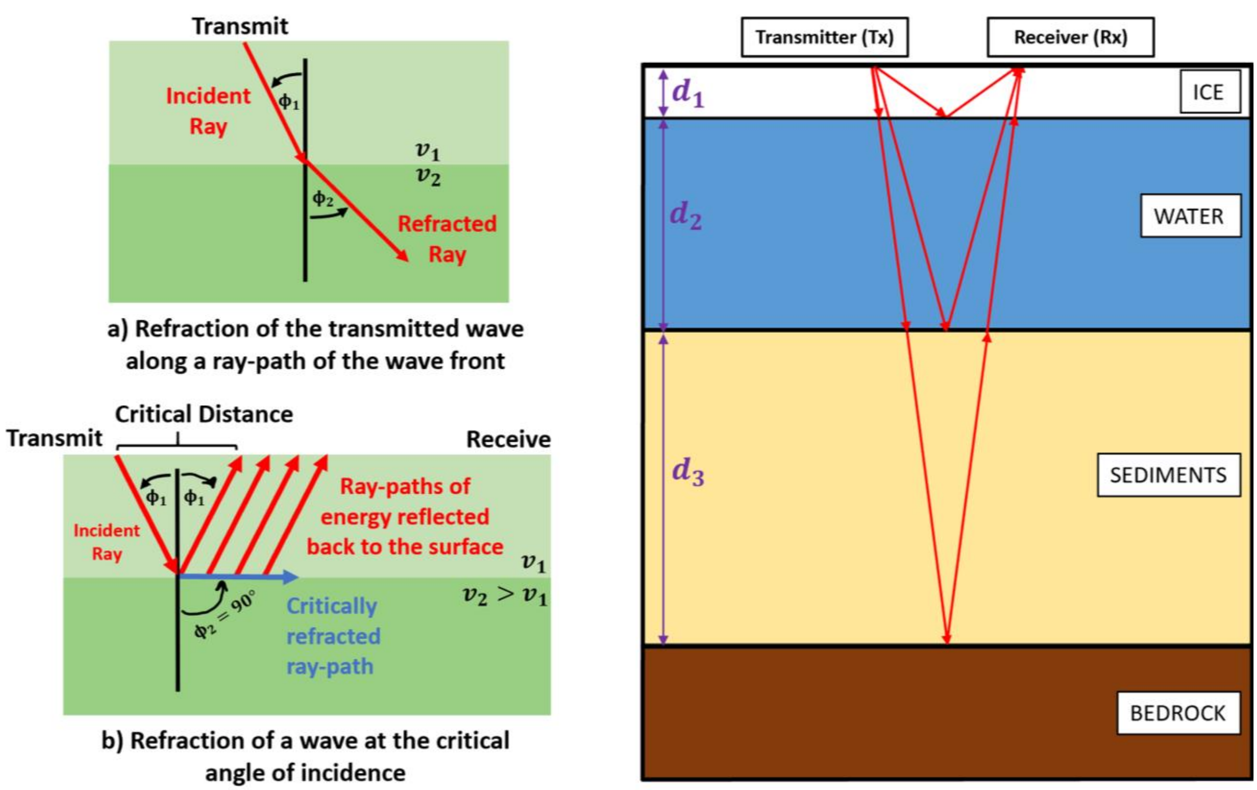

Figure 3.10: Left: Scattering of transmitted EM wavefront at interface between contrasting permittivity (modified from Daniels, 2000). Right: Schematic diagram illustrating the transmitted and reflected waves generated by the transmitter and recorded by the receiver of a GPR device.

As illustrated in Figure 3.10, the electromagnetic pulse is emitted from a transmitting antenna (Tx) and travels through the medium at a velocity governed by its electrical properties. The wave radiates downwards and outwards until it encounters an object or boundary with different electrical properties than the surrounding material (*e.g.*, buried pipeline or ice - water contact). The pulse is then dispersed, and a fraction of the wave's energy continues to travel downward, while a portion of the energy reflects back to the surface. The reflected waves are captured by a receiving antenna (Rx) at the surface and are recorded on a digital storage device. The data is most commonly displayed as signal amplitude versus time and is referred to as a trace (Daniels, 2000). Interface depths (d_i) can be obtained from the travel times of the reflected waves if the velocity of the pulse within the material, which for materials of low conductivity depends largely on the electrical permittivity, is known. For certain media such as air, water and ice, wave velocities are well known and relatively constant. For other materials with variable composition, like soils, the velocity can vary extensively and is often contingent upon the water content. Typical wave velocities for common materials are shown below in Table 3.2.

Table 3.2: Typical wave velocity values for common materials (from Annan, 2003).

Material	Velocity (m/ns)
Air	0.30
Ice	0.16 - 0.17
Water	0.033
Wet Soil	0.06
Rock	0.12

3.5.1 Stacking

To reduce noise and improve interpretation, the GPR receiver "stacks" the data during acquisition (further discussed in Section 5.1.1). Stacking involves averaging a set of repeated GPR shots, effectively improving the signal to noise ratio for GPR data collected at a particular location. Here, it is assumed that the noise is random. As illustrated in Figure 3.11 below, an increased number of stacks produces more coherent return signals. However, increasing the number of stacks raises the acquisition time, so it is important to determine the optimal number of stacks required for your survey area to maintain performance.

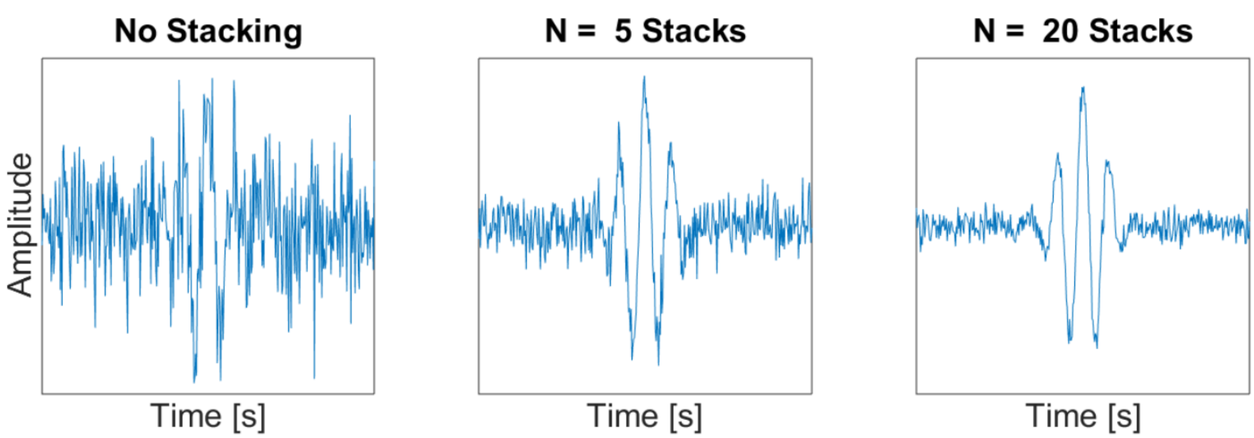

Figure 3.11: Illustrative plots showing how averaging multiple traces from the same transmitter (Tx) – receiver (Rx) pair (i.e., stacking) can enhance the signal to noise ratio, resulting in an improved image of the receiving signal (from GeoSci, 2018).

3.6 REAL-TIME KINEMATIC POSITIONING

Satellite positioning and navigation techniques have been long-established, with major advances occurring during the last two decades. They are classified as code-based or carrier-based, depending on the type of signal that is used to measure time. Code-based methods, like the common stand-alone hand-held GPS receiver, establish position and time through Pseudorandom Noise (PRN) codes transmitted by four or more satellites (NovAtel, 2015). Receivers of this style can determine their position with an accuracy of a few metres, which is likely sufficient for most navigational needs. However, when conducting gravity surveys, centimetre-scale accuracy is required, as gravity varies significantly with elevation. From Equation. 3.10, this change is approximately 0.3086 mGal per metre, requiring the advanced positioning accuracies of a Real-Time Kinematic (RTK) system.

RTK positioning is a complex, carrier-based satellite navigation technique employed to enhance the precision of position data obtained from global navigation satellite systems (GNSS) including *GPS* (NAVSTAR), *GLONASS*, BeiDou (BDS), *Galileo* and *IRNSS* (NovAtel, 2015). This system can deliver location information that is orders of magnitude more precise than its code-based counterpart (*i.e.,* the stand-alone receiver). It exploits a base station that acquires satellite data throughout the entirety of the survey, which routinely spans several hours. The GNSS satellites transmit radio signals that are received by the GNSS antennas and send them to the receivers [Fig. 3.12]. The receivers process the obtained satellite signals to determine the exact position and time (Trimble, 2017).

Unlike the stand-alone receiver, which uses the phase modulation of the carrier wave to obtain range measurements, the RTK system calculates the number of carrier cycles between the satellite and the known base station location. The number of cycles together with the wavelength determine the distance between the satellite and the base. Enhanced precision is achieved as the wavelength of the carrier wave is much shorter than the phase modulation of the PRN.

Given that RTK positioning exploits a base-rover pair, errors related to changes in the ionosphere and atmosphere can be resolved since the distance variations will be communal to both units. If the absolute location of the base station is not known, the acquired “static” data (i.e., positional information acquired by a fixed base station over several hours) is subject to post processing through *Natural Resources Canada*, whereby orbit ephemerides are used to rectify the satellite position (further discussed in Section 4.2.3). These corrected coordinates are used to determine the absolute geographical location (Trimble, 2017).

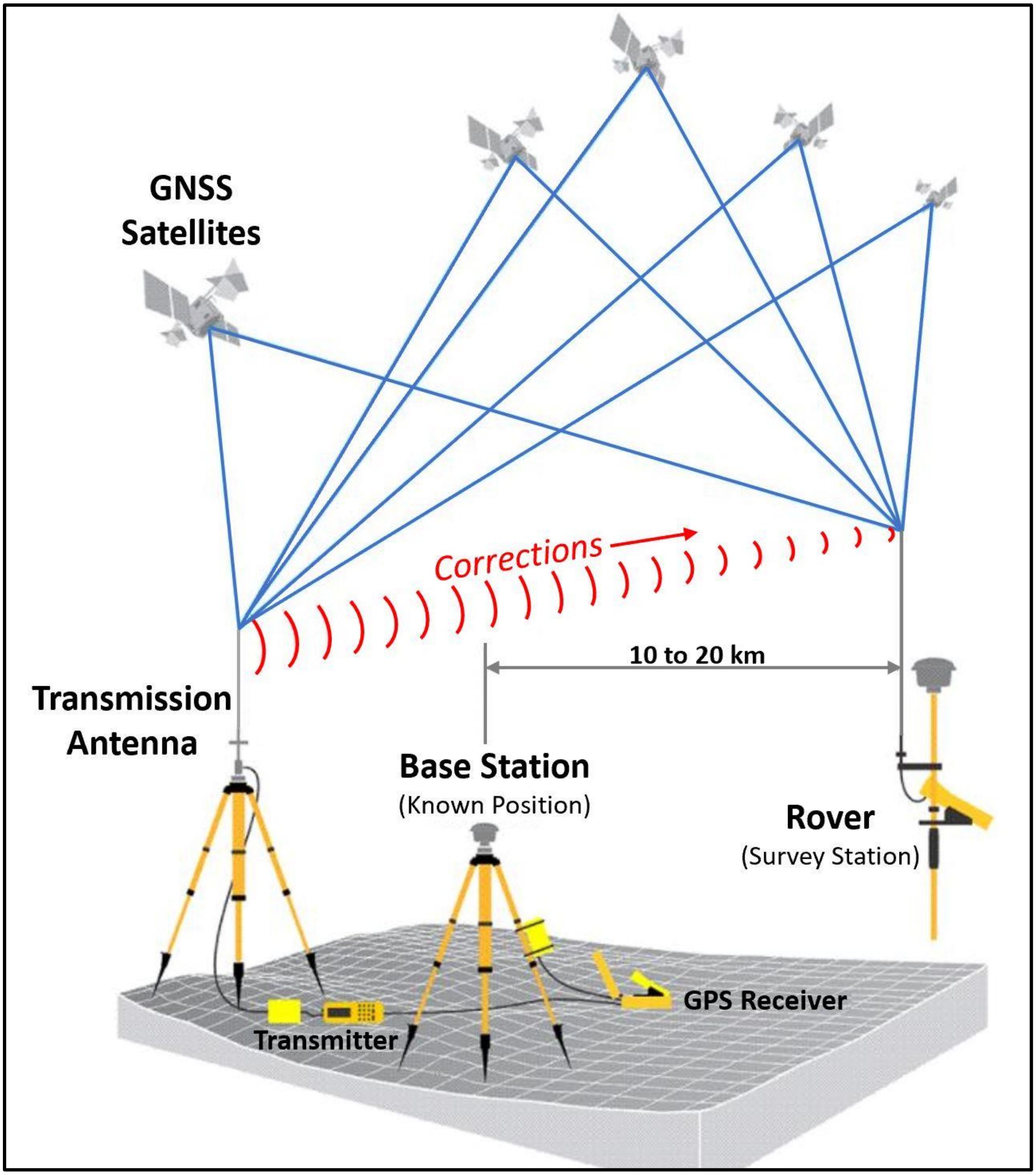

Figure 3.12: Schematic diagram showing the general RTK system components. The setup of this study has a combined transmitter and base station tripod (modified from Van Sickle, 2015).

3.7 SOUND NAVIGATION RANGING

Sound navigation ranging, commonly known as sonar, is a technique that exploits sound wave propagation to navigate and detect features beneath the water's surface. Sonar systems are akin to radar techniques (Section 3.5), in that their functionality is based on the reflection of waves between a target and a receiver. The fundamental difference between these methods is that the energy observed by sonar is transferred by mechanical vibrations propagating in water (or solids or gases), rather than electromagnetic waves (Hodges, 2010).

Sonar technology can be passive or active. In a passive source approach, energy initiates at a target and radiates to a receiver (passive infrared detection). There is no signal emission, rather, the system only detects acoustic waves that are emanating towards it. Unaided, passive sonar methods are unable to quantify the range of an object or interface (NOAA, 2020). Active sonar systems emit acoustic energy into the water, whereby sound waves propagate from a transmitter to a target and back to a receiver (pulse-echo radar). Typically, the active approach consists of one or more transducers that convert electrical pulses into directional sound and back again, functioning as both the transmitter and the receiver (Hodges, 2010). As the energy disperses underwater, any feature that is detected will reflect part of this energy which is then observed by the transducer [Fig. 3.13].

By measuring the time, t, that it takes the sound pulse to travel from the transducer to the target and back again, the range, R, of the target can be determined from the following equation:

$$R = \frac{t}{2v} \tag{3.29}$$

where v is the *speed of sound in water* (Creasey, 1976).

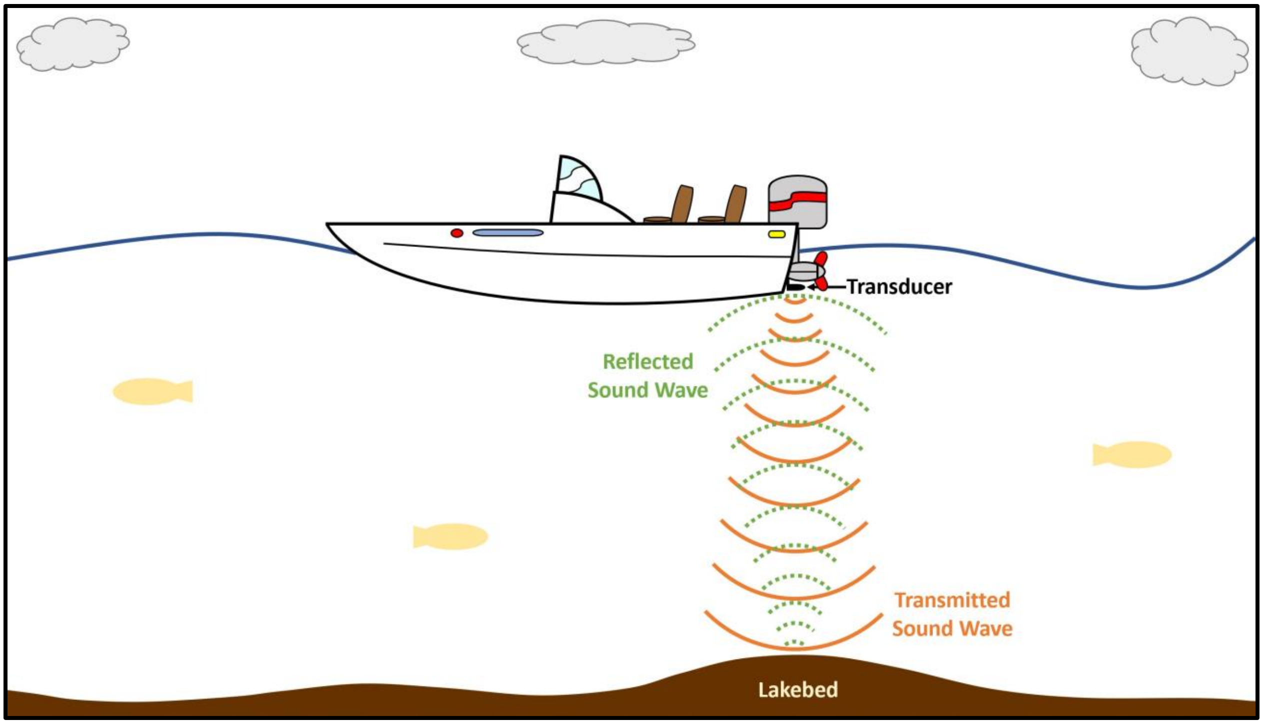

Figure 3.13: Simplified schematic representation of the active sonar system operation.

In geophysical exploration, active sonar methods are employed for both large- and small-scale applications. Seismic vessels employ arrays of sonar hydrophones to determine seafloor topography and stratigraphy for geological features that may indicate oil and gas presence, as well as geohazards including debris and cables. In this study, a fish finder is employed in freshwater lakes to obtain depth information and subsequently generate high-resolution bathymetry maps that assist with gravity corrections (further discussed in Section 5.1.2).

4 GRAVITY SURVEYS

4.1 SURVEY SETUP AND PROCEDURE

To determine the subsurface extent of the gold-bearing alteration zone at the Valentine Gold Project and increase resources by delineating areas suitable for exploratory drilling, a 22 line-kilometre property-wide gravity survey was carried out over four field seasons to produce a residual Bouguer gravity map [Fig. 4.11] from the collective 252 gravity stations [Fig. 4.1].

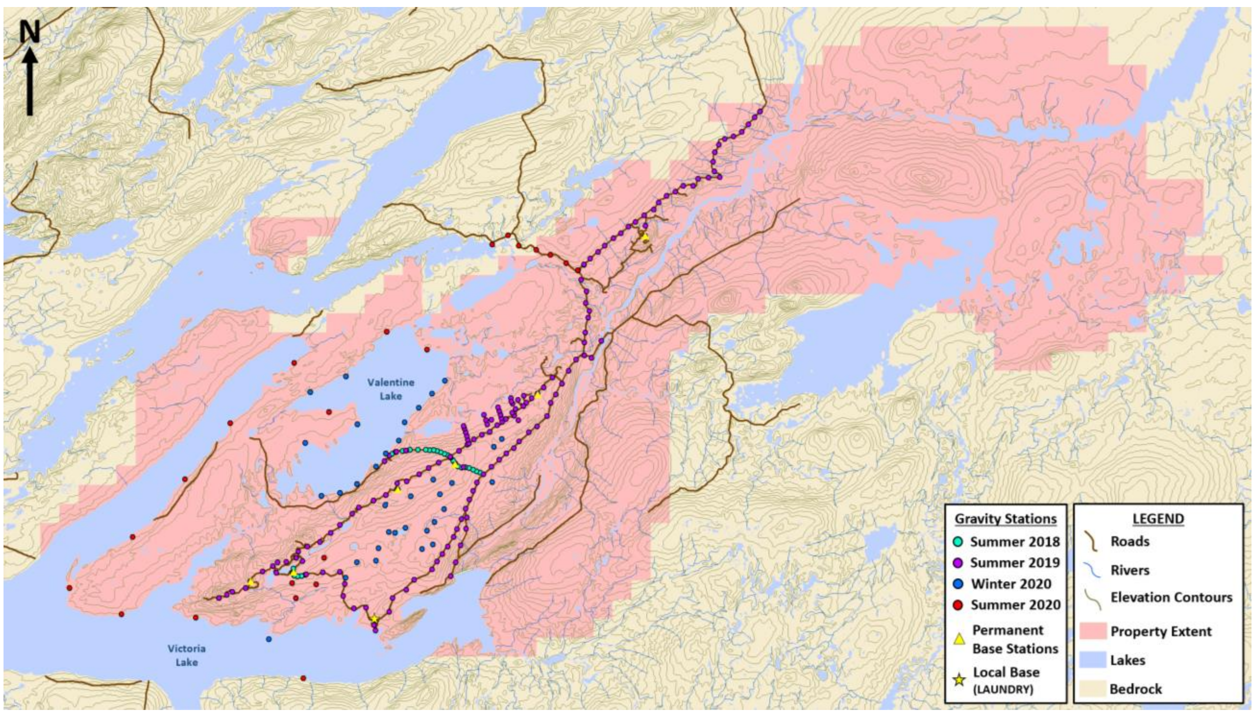

Figure 4.1: ArcGIS location map of the 252 gravity stations that formulate the 22 line-km broad-scale gravity map extending from the southwest to the northern property boundary. The summer 2018 stations (turquoise) were proof-of-concept, while the 2019 data (purple) covered all main roads and tracks. 2020 winter acquisition (dark blue) focused on lakes and bogs and the summer (red) shorelines, old access roads and drill roads. The locations of permanent base stations established by Marathon are represented by yellow triangles and the local base station LAUNDRY is denoted by the yellow star.

4.1.1 Pre-Field Preparation, Travel and Camp Setup

Prior to conducting gravity surveys at the Valentine Lake Property, it was necessary to carry out a drift calibration (see Sections 3.3.6 and 4.2.4). When not in use, the gravimeter is stored in a stable resting position in the basement of *Memorial University's* Alexander Murray Building, defined as *MURRAY*. This reference station was used to measure the drift constant prior to entering the field and generally remained the drift value utilized for the entirety of the field stint.

With an appropriate drift assigned, packing list verified and fully charged batteries, the gravimeter and all other equipment were loaded into the back of a pickup truck provided by *Marathon Gold Corporation*. Throughout the average 8-hour commute from St. John's to the Valentine Lake Property, stops were made in Clarenville, Grand-Falls Windsor and Millertown to collect gravity readings, which were used as reference stations to obtain absolute gravity and monitor long-term drift (see Section 4.2.7 and Appendix B). Once at camp, all equipment was unloaded into a storage shed, where it was stored and recharged, when not use, for the duration of the fieldwork.

Before commencing any surveys, a local base station, dubbed *LAUNDRY*, was established as the beginning and end of day reference for each gravity survey (see Sections 3.3.6, 4.2.4 and 4.2.7). It was set up at the Valentine Gold camp in the gravel parking lot between the laundry facility and the female living quarters. Defined by spray paint and small stones, the exact location was 5.5 metres from the women's bunkhouse veranda toward the laundry room, on a line defined by the outer corner of the wall between the bunkhouse and the veranda (Appendix B).

4.1.2 Daily Operations

Each gravity survey began and ended with repeat readings at the local base station. The typical procedure involved one field member taking the beginning of day *LAUNDRY* measurement, while the rest of the crew ensured all gear was loaded into the truck, utility task vehicle (UTV), or snowmobile, depending on season and logistical availability. In an effort to minimize offsets related to instrument travel (Section 3.3.6), the gravimeter was primarily transported to and from the field in a large, well-padded, rigid blue plastic box [Fig. 4.2], in either the pan of the UTV, or truck during the summer, or the towed sled, during the winter. Depending on the terrain, it was sometimes safer to place it on a thick piece of foam on the floor of the front seat of the UTV where it was held upright by the passenger. In the case when travel by foot was required, the gravimeter was placed in a less robust, portable backpack [Fig. 4.2] and transported into the field site.

Figure 4.2: The UTV method of transporting the gravimeter and associated equipment into the field. The rigid blue box as well as the lighter backpack can be seen in the back of the pan (left).

The gravity surveys were conducted using a CG-5 Autograv relative gravimeter by *Scintrex Ltd.* This system is equipped with a levelling tripod, to ensure that the internal fused quartz spring is level to within 10 arcseconds, and a removable *Garmin* GPS. On the top of the instrument is a screen that displays a graph of the data in real-time [Fig. 4.3]. During the winter surveys it was common practice to place wooden blocks underneath the tripod to keep it from sinking into the ice or snow [Fig. 4.3], which can result in large tilt values (*i.e.*, greater than 30 arcseconds). As the device is extremely sensitive to touch or nearby movement during acquisition (e.g., rain droplets, snowflakes, and footsteps), which can yield an undesirable amount of rejected data, a remote was used to initiate readings. To further ensure accurate results, a minimum of two 60 second readings were obtained at each station and examined for measurement repeatability of less than 0.01 mGal and standard deviations under 0.1 mGal and any values exceeding these standards were retaken.

Figure 4.3: CG-5 gravimeter setup during a station measurement (left) and associated components including a data recorder (centre) and portable RTK roving receiver (right).

Precautionary measures were taken to ensure no data was lost by hand-recording all gravity measurements in a field book [Figs. 4.3, 4.4], in addition to the gravimeter storing the data internally [Fig. 4.4]. Each gravity station was assigned an appropriate name (see Tbl. 4.1 below) and the corresponding gravity measurements were read off the instrument and transcribed below the station name, skipping a line on the page between readings for clarity. While the attached GPS is sufficient for one of the important corrections, the *Earth tide correction* (Section 3.3.5), because precise elevation data is imperative for the other gravity corrections, each station was subsequently surveyed with a *Topcon* HiperV Real Time Kinematics GPS system [Fig. 4.3] which achieves centimetre precision (see Section 4.2.3). To ensure proper correlation of each RTK point to gravity station, each RTK station number was also recorded in the field book alongside the station name and gravimeter values [Fig. 4.4].

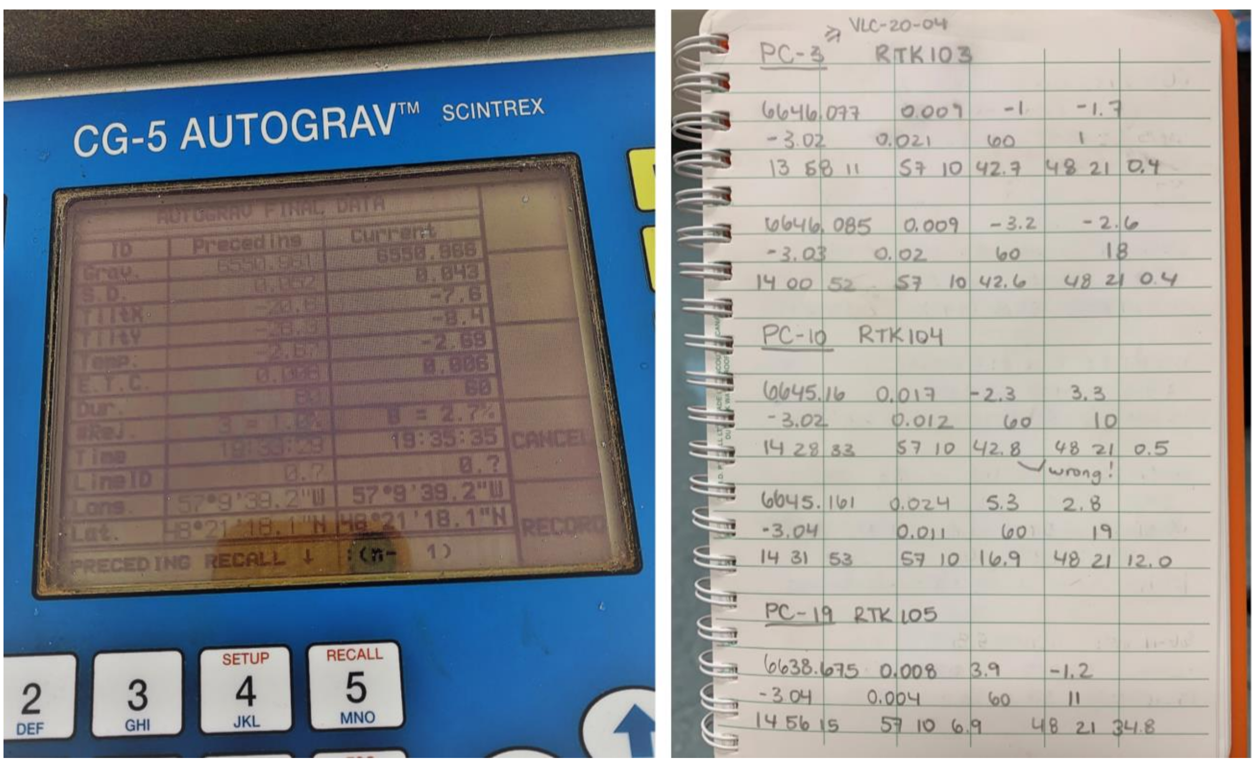

Figure 4.4: Gravity survey data recording procedure. Left: Output parameters of the gravimeter, which are stored internally and transcribed. Preceding and current measurements are shown. Right: Field notes showing the method for recording gravity readings, including station name and corresponding RTK point as well as additional comments such as incorrect GPS readings.

Throughout the daily recordings, it was observed that in some cases, the first measurement at a new station retained the location information of the previous station. To prevent this from reoccurring and ensure a fresh location reading, the attached GPS was given time to settle at the next station before a measurement was made. Whenever a poor location reading was recorded, it was noted in the field book [Fig. 4.4] so that it could be omitted later in processing (Section 4.2.2).

Transport offsets were monitored throughout the day, by taking repeat measurements periodically at several secondary reference stations, which were permanent base stations established by *Marathon* [Tbl. 4.2]. These base stations were used primarily to set up the RTK base receiver for the accompanying RTK surveys. However, occasionally, thick tree coverage prohibited signal transmission, requiring the need to set up a temporary base station in a clear, accessible area (see further details in Section 4.2.3).

The predetermined drift was also evaluated throughout the daily gravity surveys and was sometimes subject to a secondary drift correction while in the field. When this was necessary (i.e., daily *LAUNDRY* readings did not agree beyond the effects of daily drift), the drift calibration was carried out on a solid concrete slab in the crawl space beneath the male bunkhouse at the Valentine Gold camp. The acquired drift constants were compared through drift plots in Excel, and the most reasonable value was assigned to the instrument for future surveys.

Upon return back to camp at the end of each day, the repeat *LAUNDRY* reading was recorded before the gravimeter was placed in its resting place beneath the men's bunkhouse, where it was plugged into an external power source to recharge the internal batteries. The data was then downloaded onto a USB stick for preliminary processing in the evening and the remaining equipment was returned to the storage shed.

4.1.3 Surveys

The 2018 gravity survey (Section 2.3.4) was a proof-of-concept, designed to cross the contact between the non-mineralized Rogerson Lake Conglomerate and the gold-hosting quartz porphyry subset of the VLIC [Fig. 2.2]. The encouraging low gravity response [Fig. 2.6] over this hydrothermal alteration zone motivated the ensuing broad-scale gravity collection. The preliminary 33-station summer acquisition revealed that surveying over soft, spongy surfaces of bogs and within forests is cumbersome, and although doable, far more time-consuming than along hardened roadways and tracks. The mossy, boggy terrain beneath the trees posed a challenge for finding suitable sites to place the gravimeter and often involved digging up some ground cover to access a firm surface for leveling the instrument. Additionally, obtaining a consistent fixed signal from the RTK GPS system was problematic under shaded areas. Therefore, given the multitude of roads and pathways throughout the Valentine Lake Property [Fig 4.1] which span the alteration zone, the intention was to concentrate on these accessible routes moving forward to compile property-wide gravity data.

The summer of 2019 data collection comprised a 14.2 line-kilometre broad-scale gravity survey that encompassed all workable terrain from the southwest to the north-northeast extent of the property boundary [Fig. 4.1]. The survey area covered all main roads within the Valentine Lake Property, as well as, several drill roads, water pump tracks, quad trails and two mulch lines (see Section 2.3.3), all of which were accessible using all-terrain vehicles (ATVs), a UTV, and trucks. Roads were composed of well-compacted dirt and mud with some stones and twigs, and pathways were often lightly grass-covered, enabling rapid measurements at each station. The mulch lines had a thick mossy surface covered with broken branches and rocks, which required longer acquisition time, due to the need to clear and dig up ground cover before taking a reading. The station spacing was determined using the odometer of the vehicle. It was approximately 200 to 300 metres, depending on the local terrain and feasibility of measurement locations: a total of 159 stations were collected. All acquisition sites were chosen on flat terrain, away from ditches and hills, and marked using high visibility spray paint. Since this survey spanned the main routes throughout the Valentine Lake Property, the chosen station naming system was designed using a sequence of letters and numbers such that it could be easily understood where it was located and the direction of acquisition. For example, as shown in Table 4.1 below, stations along the main road (M) from Frozen Ear Road (F) to camp (C) were labelled *MFC1*, *MFC2*, etc., while stations recorded in the opposite direction, along the main road (M) from camp (C) to Frozen Ear Road (F) were assigned *MCF1*, *MCF2*, etc.

Table 4.1: Examples of the naming convention used for the collected gravity stations at the VGP.

Property-wide Gravity Survey - Station Naming
MFC = Main Road (M) from Frozen Ear (F) to Camp (C)
MCF = Main Road (M) from Camp (C) to Frozen Ear (F)
MVF = Main Road (M) between Victory (V) and Frozen Ear (F)
OMB = Old Marathon (OM) near Base (B) Station
OM = Old Marathon (heading towards gate to Main Road)
MOV = Main Road (M) from Old Marathon (O) to Victory (V)
LC = Road from Leprechaun (L) to Camp (C)
OMm = Old Marathon Road (OM) to Marathon Zone (m)
MDR = Marathon Zone Drill Road
VR = Victory Road (through gate)
MVB = Main Road (M) between Victory (V) and property Boundary (B)
MVF = Main Road (M) between Victory (V) and Frozen Ear (F)
FSZ = Road from Frozen Ear (F) to Sprite Zone (SZ)
SZL = Road from Sprite Zone (SZ) to Leprechaun (L)
JFRH = Road from J. Frank Zone (JF) to Repeater Hill (RH)
MFOM = Main Road (M) from Frozen Ear (F) to Old Marathon (OM)
MOF = Main Road (M) from Old Marathon (O) to Frozen Ear (F)
MAF = Marathon Zone Road (MA) to Frozen Ear (F)
MAF#R = Marathon Zone Road FROM Frozen Ear (R means reverse direction - i.e., Frozen Ear to Marathon)

As measurement viability over problematic summer terrain is enhanced during the winter, when a stable frozen platform is provided for the gravimeter, the winter of 2020 gravity surveys targeted areas that were not at all, or less attainable in the summer, such as ponds and bogs [Fig. 4.1]. Shoreline stations were acquired on Valentine Lake, as well as one reading on Victoria Lake and infill data was obtained on the priority bogs [Fig. 5.7]. The station spacing varied between 500 metres and 2 kilometres on the lakes, and 300 to 400 metres on the bogs, resulting in an additional 36 measurements. Snowmobiles enabled travel between sites, and most locations required excavating nearly a metre of snow to access a solid surface for the gravimeter. The winter results yielded higher standard deviations and transport offsets due to ground instability, provoking reduced precision and the necessity to take additional readings (three or four) per station. This increased shaking of the ground was believed to be a result of winter storms and waves pounding the coast.

The 24 measurements collected in the summer 2020 involved further infill stations along the shorelines of Valentine and Victoria Lakes, a former access road and some newly cut drill roads [Fig. 4.1; red dots]. The lake readings were acquired in conjunction with the sonar surveys [Fig. 5.3] using an aluminum boat and a *Garmin* handheld GPS. The proposed 2-kilometre spaced shoreline points were uploaded into the portable GPS and used to navigate the boat operator to the designated locations along the beach. As the old access trail (marked by northern-most red dots in Fig 4.1) was heavily overgrown with thick bushes and fallen trees, navigating in a UTV (*i.e.*, side-by-side) was unwieldy, but doable. The desired 500 metre station spacing varied somewhat due to the inability of the RTK roving receiver to obtain accurate location and elevation measurements beneath sheltering trees. Recent development related to *Marathon Gold's* ongoing drilling programs included several freshly cleared tracks leading to drill pads, which were comprised of thick mud intermixed with sticks and rocks and could be accessed using ATVs, enabling data collection in these areas.

4.2 DATA PROCESSING

Processing of gravity data to produce accurate maps of subsurface density anomalies involves essential corrections (Section 3.3) for surficial density and topography. The Valentine Lake Property gravity survey followed the conventional correction procedure, as outlined by Blakely (1995). Primary processing was completed in Microsoft Excel (Sections 4.2.1 – 4.2.5, 4.2.7), while the terrain correction (Section 4.2.6 and Appendix D), regional trend removal (Section 4.2.8) and subsequent maps were generated in Oasis Montaj.

The entirety of processing steps carried out on the Valentine Lake Property gravity data are summarized in the following flowchart [Fig. 4.5]. The following Sections 4.2.1 – 4.2.8 describe them in detail.

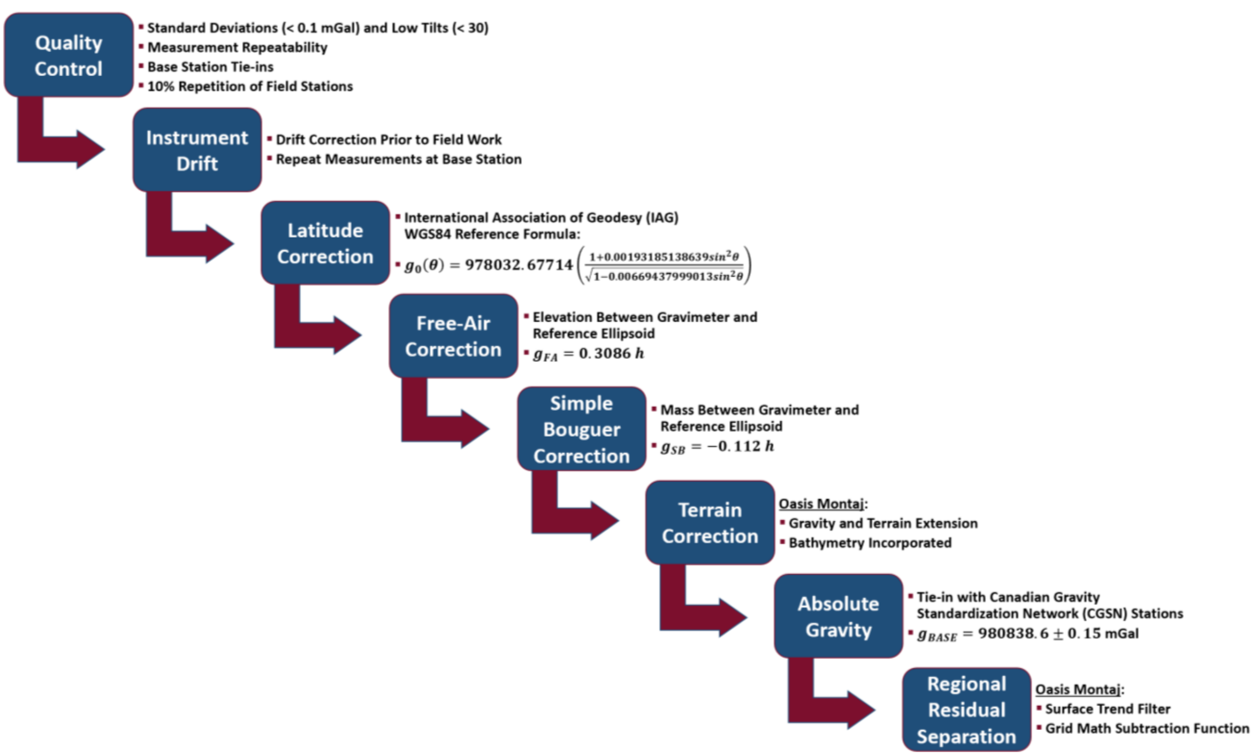

Figure 4.5: Flowchart summarizing the data processing techniques that were applied to the Valentine Lake Property gravity data to produce the complete Bouguer anomaly. Brief explanations and corresponding formulas are included with each correction.

4.2.1 Preliminary Analysis

Preliminary analysis focused on organization and quality control, which began by aligning station names and gravity readings with their associated location and elevation information. Once sorted, the latitudes and longitudes were verified (to within a kilometre) to ensure a correct Earth Tide Correction was achieved (see Section 4.2.2 below). Next, the dataset was examined for standard deviation values less than 0.1 mGal (nearly 1 part in 10 million of the Earth's field) and X and Y tilts under 30 arcseconds. The repeatability of consecutive readings at the same station was also evaluated (Section 4.2.4). Any measurements that exceeded these criteria were rejected.

4.2.2 Earth Tides

The CG-5 gravimeter is designed to automatically adjust for the gravitational attraction and deformation of the Earth due to the Sun and the Moon (Section 3.3.5), provided that the location information obtained from the GPS is approximately correct, along with the time zone. The *Longman*-based internal correction requires the time difference from Greenwich Mean Time (GMT), therefore, the instrument was set to GMT time prior to completing any field work. In doing so, potential errors associated with an incorrect time zone, resulting in an incorrect tidal correction, were avoided. Next, to ensure that the latitudes and longitudes were correct, the location values between consecutive gravity readings were compared and cross-referenced with the field notes [Fig. 4.4]. If the first measurement at a new station was flagged as incorrect, it was omitted and a subsequent station with the proper locations was used (as discussed previously in Section 4.1.2). Thorough examination of the dataset determined that no post-adjustments to the internally computed *Earth tide correction* were required.

4.2.3 Precise Point Positioning

For optimal satellite reception, *Marathon Gold* have established several permanent base stations throughout the Valentine Lake Property [Fig. 4.1]. These base stations [Tbl. 4.2] are situated in well-exposed, unobstructed areas, often at a higher elevation than the surrounding topography. With the absolute base station locations known, the locations of each survey measurement are acquired using a portable roving receiver [Fig. 4.3], which determines its position relative to the base station. The base-receiver pair communicate through ultra-high frequency (UHF) waves, and by adding a range amplifier to the base setup, the signal coverage of UHF waves is extended from a few kilometres to a few tens of kilometres.

Table 4.2: Names and precise locations of the permanent base stations established at the VGP.

Base Station	Easting (m)	Northing (m)	Elevation (m)
Victory	495936.668	5364728.791	331.12
Old Marathon Road	493115.109	5360570.124	356.34
Frozen Ear Road	490949.741	5358738.649	417.672
SZB (Berry Zone)	489444.761	5358071.543	436.857
Leprechaun	486713.069	5355902.955	398.704
Repeater Hill	485592.704	5355663.497	426.459

For most of the gravity surveys, the RTK base receiver was set up on these predetermined base stations [Fig. 4.6; left], however, some of the gravity measurements were in regions beyond the range of any of the defined base stations, in which case, it was necessary to establish a temporary base station [Fig. 4.6; right]. To obtain the exact location of the alternate base with an accuracy of ± 4 millimetres (Topcon Corporation, 2014), the stationary base receiver is set to collect static readings for a minimum of four hours. The static data is later downloaded from the receiver, translated from a proprietary *Topcon* format to the more standardized Receiver

Independent Exchange Format (RINEX), and entered into a Precise Point Positioning (PPP) application available through the *Natural Resources Canada* website (Government of Canada, 2015), where the data is automatically processed using GNSS satellite orbit ephemerides (Section 3.6). With the base station position rectified to its "absolute" location, each gravity station location point collected from the rover can be adjusted using the offsets between the initial and corrected base station values. Finally, the newly generated "absolute" positions of each gravity station are subsequently added alongside their corresponding gravity measurement in the Excel spreadsheet.

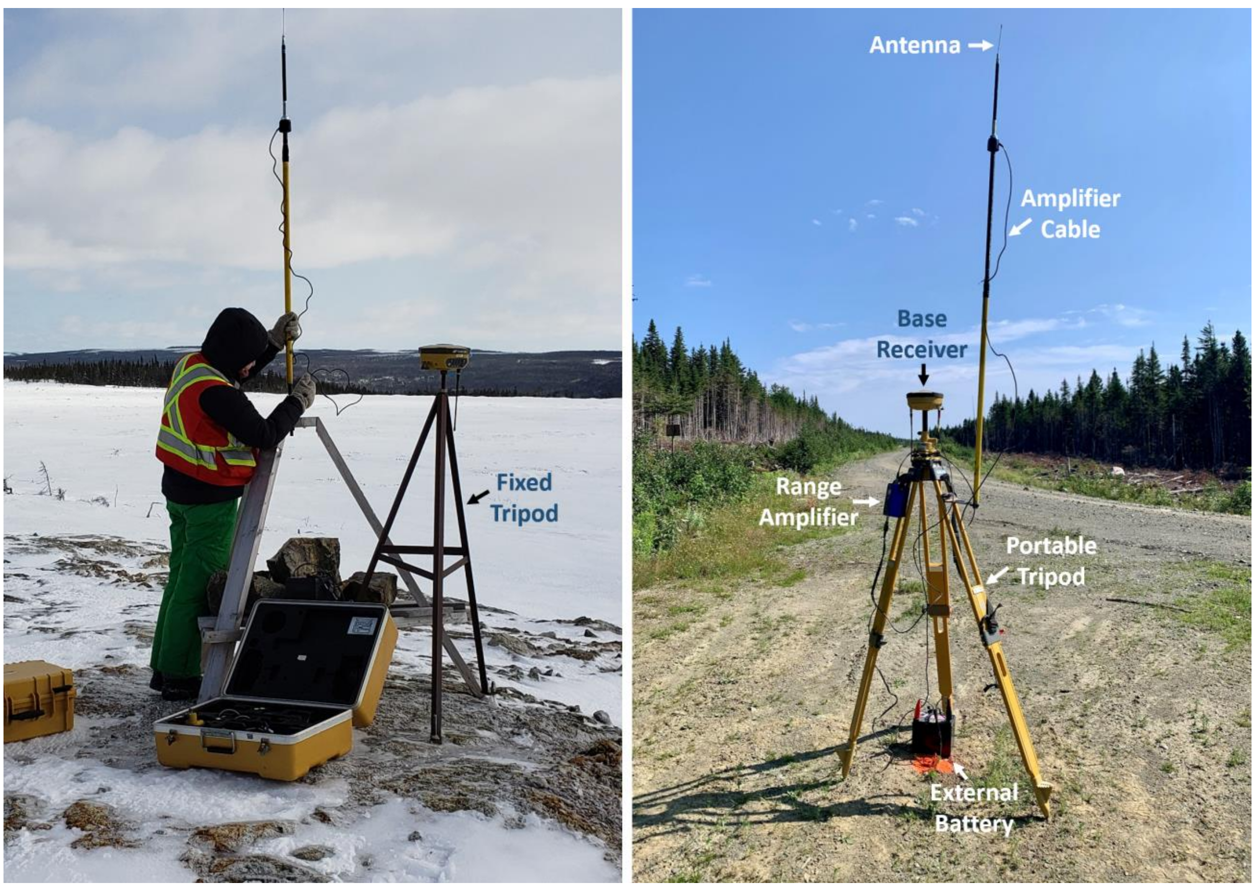

Figure 4.6: The two RTK base station configurations used at the VGP. Left: Permanent base station "SZB" established by Marathon Gold overlooking the newly defined Berry Deposit. Right: Temporary base set up using a portable tripod. All associated components are labelled.

On rare occasions, a stable connection between the base and receiver was unachievable due to thick forest between the pair, prohibiting signal transmission. When this occurred, the rover was employed as a stand-alone device and static data was collected at the measurement location by keeping the instrument in a steady, upright position for 15 to 45 minutes. Exploiting the PPP function, this method was able to achieve an accuracy of $\pm$ 10 centimetres.

4.2.4 Long-Term Instrument Drift and Transport Offsets

Instrument drift occurs as the elastic spring inside the gravimeter ages (*i.e.*, change in the spring constant, κ, with time). These long-term fluctuations were predicted and eliminated by performing a *drift correction* in a stable environment prior to commencing fieldwork. The CG-5 automatically took care of the drift using the appropriate calibration from *MURRAY* or the basement of the male bunkhouse (recall Sections 4.1.1 and 4.1.2)

This drift correction accounts for the natural drift of the instrument but does not consider any offsets due to travel or handling of the device. If the observed gravity variations are small, then even minimal transport offsets (less than 0.1 mGal) can be significant. The associated offsets were evaluated in Excel by comparing the daily repeat readings (Section 4.1.2) and the data was adjusted accordingly.

4.2.5 Latitude, Free-Air and Simple Bouguer Correction

To eliminate any gravity contributions provoked by the oblate spheroidal shape of the Earth, a latitude correction (Section 3.3.1) was carried out using the common *IAG WGS84* reference gravity formula [Eqn. 3.9]. Next, a free-air correction (Section 3.3.2; Equation. 3.10) was applied to correct for the vertical difference in elevation between the gravimeter and the reference ellipsoid. However, when applying the free-air correction, the mass of the underlying topography is ignored. To account for this, a simple Bouguer slab correction (Section 3.3.3; Equation 3.1.3) was performed on the dataset, assuming a typical crustal density of $2.67\ g/cm^3$.

For both the free-air and simple Bouguer corrections, the elevation of each station, measured using the RTK system, was used for the height, *h*. At this stage, the data has been reduced to its full extent in Excel and was ready to be introduced into Oasis Montaj as the “master” database required to conduct the terrain correction.

4.2.6 Terrain Correction

Given the topographic variations at the Valentine Lake Property, a terrain correction was required as one of the final steps in the gravity data reduction process. This is the most sophisticated and computationally involved correction, which allows for changes in topography by calculating the gravitational attraction of surrounding hills and valleys (Section 3.3.4). It can be performed in Oasis Montaj, or through different techniques, such as forward modelling. In this study, the *Gravity and Terrain Correction* extension of Oasis Montaj (and a linear trend filter discussed in Section 4.2.8 below) were used to generate the broad-scale complete Bouguer residual gravity map shown in Figure 4.11. In addition, a secondary complete Bouguer residual anomaly map [Fig. 4.12; panel B] was produced using a forward modelling approach, by Ph.D candidate Michael King, the details of which are provided in Appendix E. Comparative analysis of the two maps is presented in Section 4.4 below.

Simply explained, the terrain correction is computed by exploiting a crude regional Digital Elevation Model (DEM) overlaying a refined, local scale DEM that encompasses the survey area. Here, the local DEM comprised a combination grid of the acquired bathymetry data (Section 5.3.2) and high-resolution LiDAR data [Appendix C] provided by *Marathon Gold Corporation*, over the gravity survey area. For ease of processing, Jason Sylvester used *Python* to reduce the 1 metre by 1 metre resolution LiDAR data by a factor of 10 in both directions [Appendix C]. The regional

DEM [Appendix D; Fig. D.3] was obtained through *Natural Resources Canada*'s Geospatial Data Extraction tool and extended 15 kilometres outside the surveyed region, in all directions. In Oasis Montaj, the terrain correction is executed using a combination of methods derived from Nagy (1966) and Kane (1962). The reduction process is defined by contributions from three zones: the near zone, intermediate zone, and far zone [Appendix D; Fig. D.1], whereby influences from the near zone have the greatest effect on the measurement (Geosoft Inc., 2015). Details on the LiDAR data acquisition, analysis, and map creation, as well as an in-depth explanation of the Oasis Montaj terrain correction technique and executed workflow are given in Appendix C and D, respectively.

4.2.7 Absolute Gravity

As the gravimeter measures relative, not absolute gravity, and instrument drift must be monitored (Section 4.2.4), it is necessary to establish a local base station where start and end of day repeat readings (*i.e.*, loops) are taken and the absolute gravity can be determined. To obtain absolute gravity, the local base station measurements are "*tied-in*" to known stations in the *Canadian Gravity Standardization Network* (CGSN), which include stations in St. John's and Clarenville. By defining the absolute gravity, all relative gravity measurements can be determined with respect to the known value at the base station. The base station, *MURRAY* (Section 4.1.1), is tied into a registered station located within the seismic vault in room SN1108 of *Memorial University*'s Science Building [Appendix B; Fig. B.1] in the city of St. John's. During their most recent visit to *Memorial* in 2017, the Canadian Geodetic Survey of *Natural Resources Canada* measured the absolute gravity at *Station 991399* in the seismic vault to be 980819.5878 ± 0.002 mGal (Leitch, 2017). A second base station, *CLARENVILLE*, established at the former Canada Manpower Centre in the town of Clarenville, is located less than half a metre (thus fundamentally analogous to) another station registered in the CGSN [Appendix B; Fig. B.2].

From tie-ins with measurements obtained at stations *MURRAY* and *CLARENVILLE* during semi-annual fieldwork commutes to and from the Valentine Gold camp (see Section 4.1.1), the absolute gravity at *LAUNDRY* was determined to be:

$$gLAUNDRY = 980838.68 \pm 0.04 \text{ mGal} \tag{4.1}$$

To find the absolute gravity for each station of the survey, the difference between the absolute and relative gravity measurements at *LAUNDRY* were added to the relative value at each station. Detailed descriptions and photos of the above-mentioned gravity reference station locations, as well as two subsidiary stations defined during travel through Grand-Falls Windsor (*CNA-GFW*) and Millertown (*MILLERTOWN*) are available in Appendix B.

4.2.8 Regional – Residual Separation

When the Oasis Montaj terrain correction values are added to the simple Bouguer gravity data, the resulting "complete" Bouguer anomaly [Fig. 4.10] still exhibits regional gravity contributions. Therefore, to better understand the gravity signature due to the alteration zone, it was necessary to remove the regional trend. This was accomplished using a *linear trend filter* (which can apply higher order polynomials) in Oasis Montaj. The parameters were set to establish the trend using all data points and then remove it from the complete Bouguer dataset to yield the final product, the residual Bouguer gravity map [Fig. 4.11]. To quantify the linear trend, a simple grid subtraction was defined using the *Grid Math* function of Oasis Montaj, whereby the linear trend, shown below in Figure 4.7, is the difference between the regional [Fig. 4.10] and residual [Fig. 4.11] maps.

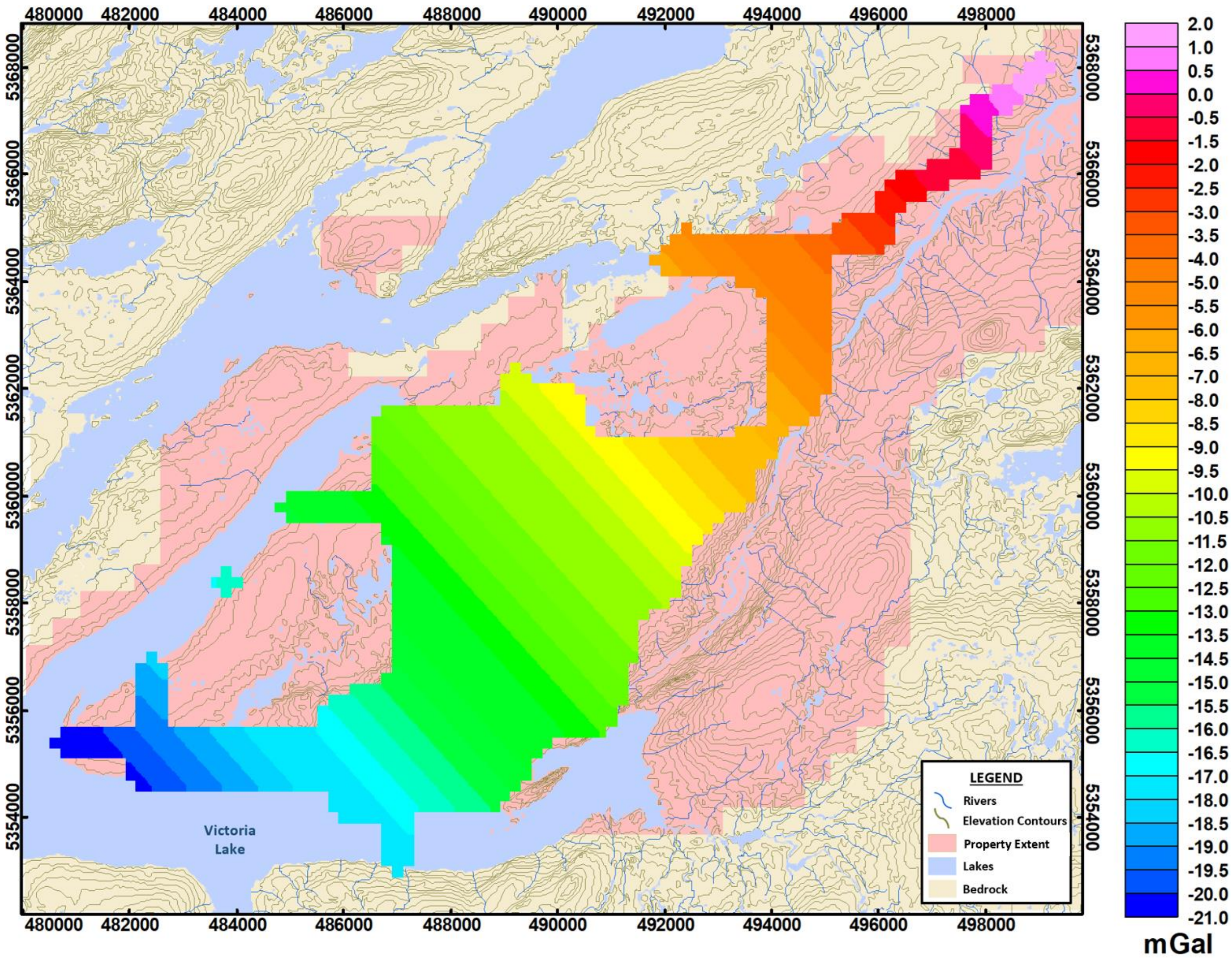

Figure 4.7: The linear trend of increasing gravity to the northeast, that was removed from the complete Bouguer gravity data using a polynomial fit-based linear trend filter in Oasis Montaj.

To quantify how the above observed linear trend [Fig. 4.7] in the Valentine Gold Project gravity data compares with a broader scale gravity field, regional gravity data for the island of Newfoundland was acquired from the *International Gravimetric Bureau* (BGI). The extracted data exploited the World Gravity Map (WGM) 2012 global model and comprised complete Bouguer [Fig. 4.8], free-air and topographic information, as well as an associated report.

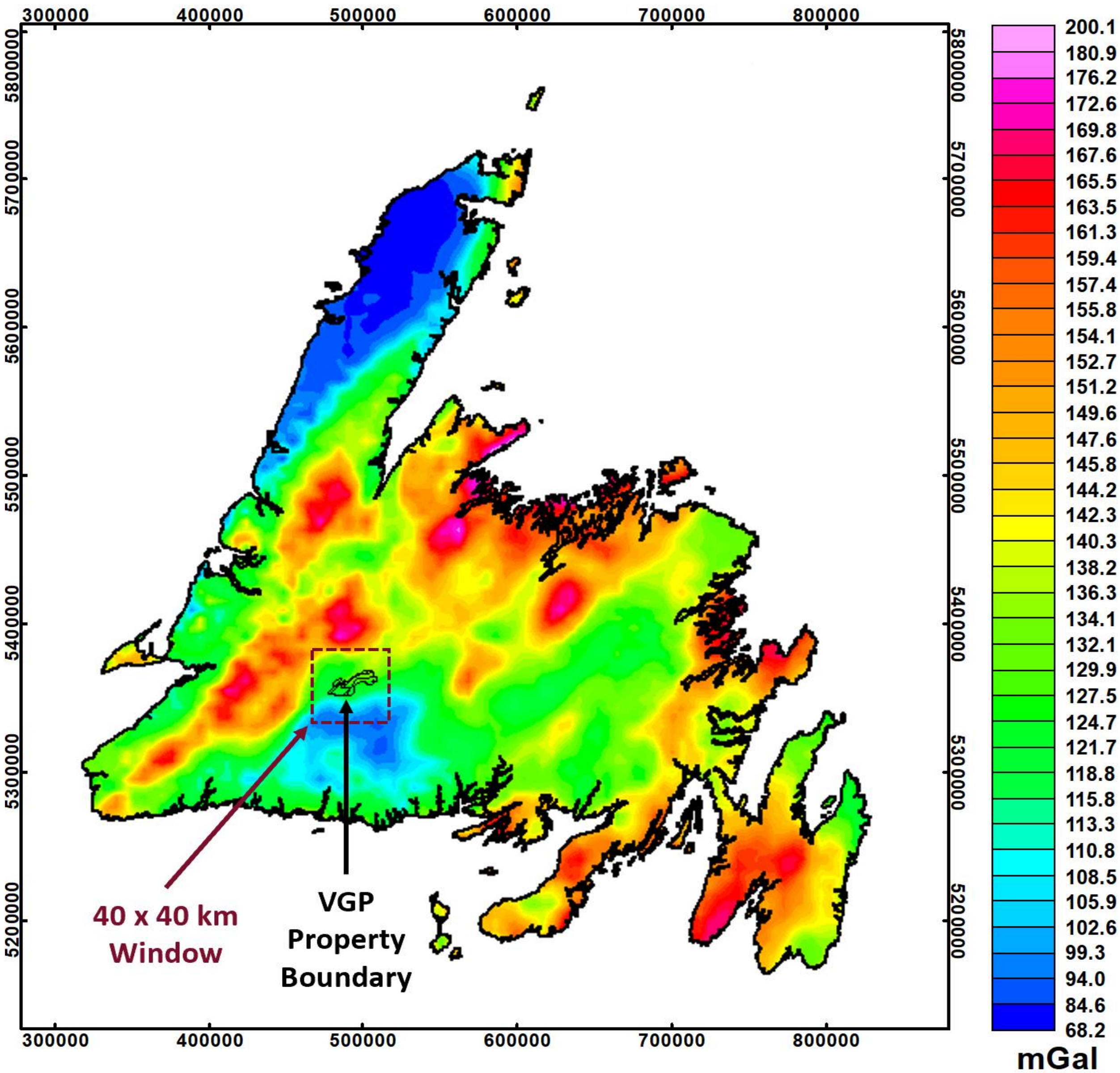

Figure 4.8: WGM 2012 complete Bouguer gravity map of Newfoundland gridded using minimum curvature, a cell size of 6000 metres and histogram equalization colour method. Included are the Valentine Lake Property boundary (black lines) and the 40x40km region fencing the property, chosen for comparison with the local complete Bouguer gravity data (described below).

The complete Bouguer anomaly map of Newfoundland showcases a generalized trend of alternating nonuniform northeast-southwest oriented bands of high and low gravity, with the Valentine Lake Property boundary occupying a nondescript region of green (*i.e.*, semi-low gravity) [Fig. 4.8]. While it can be assumed that there is gradient to the north of the property boundary, to properly characterize the regional trend in the vicinity of the Valentine Lake Property, it was necessary to reduce the scale of the regional dataset to a 40 x 40-kilometre area surrounding the property. The enhanced resolution of the windowed region revealed a distinct trend of increasing gravity from south to north, with the property boundary situated within a slight regional high [Fig. 4.9; panel A] that was previously seen as a moderate gravity low [Fig. 4.8].

Having established an appropriate scale to observe where the Valentine Lake Property fits into the regional field, the linear regional trend in locally acquired gravity survey could be compared by introducing an offset of + 135 mGal into the dataset [Fig. 4.9; panel B] so that the colour scales of the two maps [Fig. 4.9; panels A and B] were aligned. Superimposing the adjusted local gravity (with associated regional trend) onto the regional gravity map [Fig. 4.9; panel C] showed a reasonable correlation in the linear trends of the two maps, apart from the observed circular high toward the northeast of the VGP gravity anomaly, which has been deemed not part of the regional trend, but rather a contribution from a neighbouring gabbro unit.

As mafic magmatism can initiate fluid movement by providing heat and pathways, it is speculated that the semi-regional high in which the property is sitting on [Fig. 4.9; panel A] is indicative of excess mafic rocks, which may have some relationship to the property mineralization.

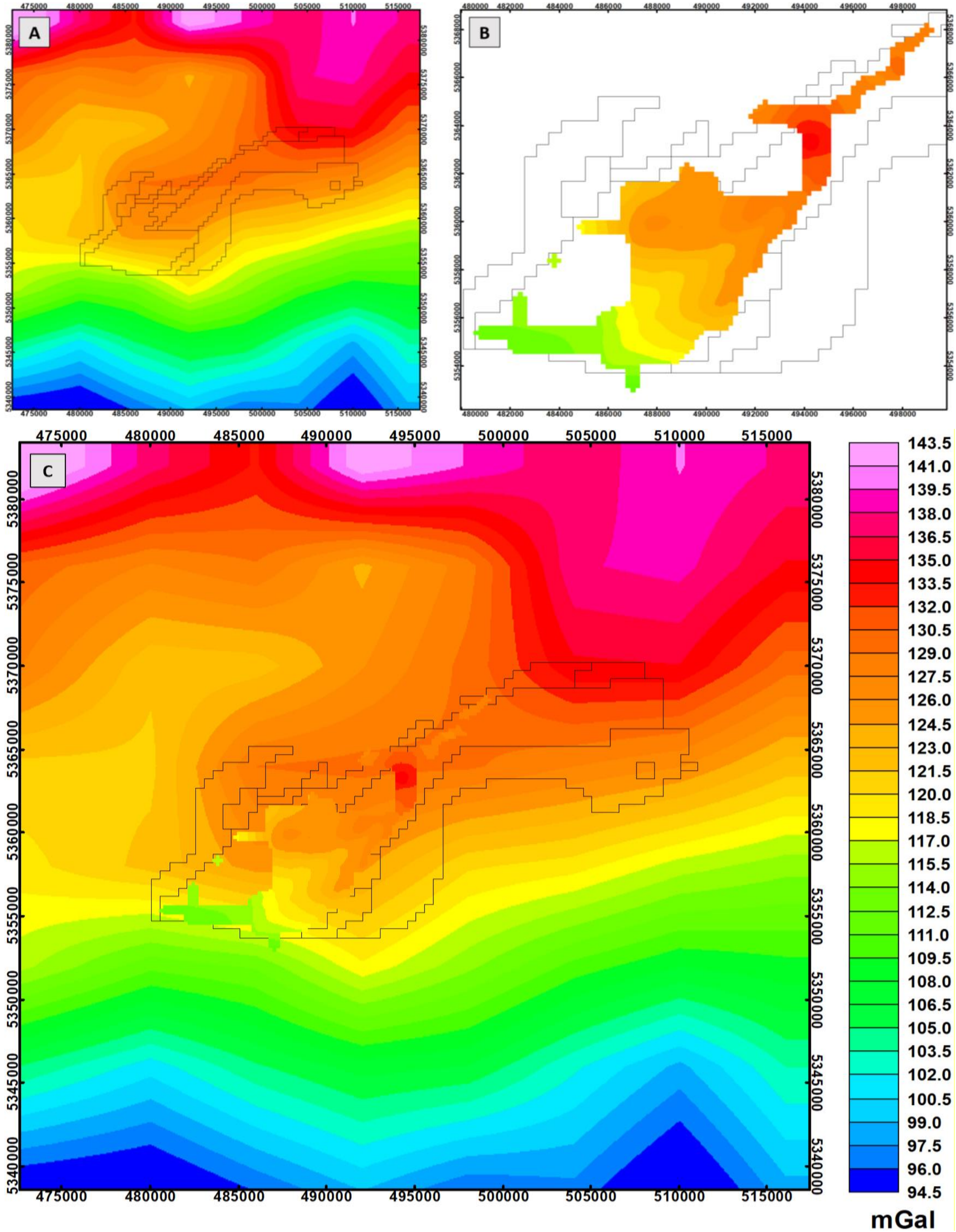

Figure 4.9: A) WGM 2012 regional gravity data refined to a 40x40km region around the VGP. B) Local complete Bouguer gravity data offset by 135 mGal to match regional scale. C) Adjusted local complete Bouguer (B) anomaly superimposed onto the windowed regional gravity (A).

4.3 RESULTS

4.3.1 Maps

The results of the property-wide gravity survey aimed at delineating the ore-hosting alteration zone at the Valentine Gold Project are displayed in Figures 4.10 and 4.11 as complete Bouguer anomaly maps, with and without the linear regional trend contributions, respectively. That is, Figure 4.10 encompasses all corrections outlined in Sections [4.2.1 – 4.2.7], while Figure 4.11 comprises these same corrections, plus the regional correction described in Section 4.2.8.

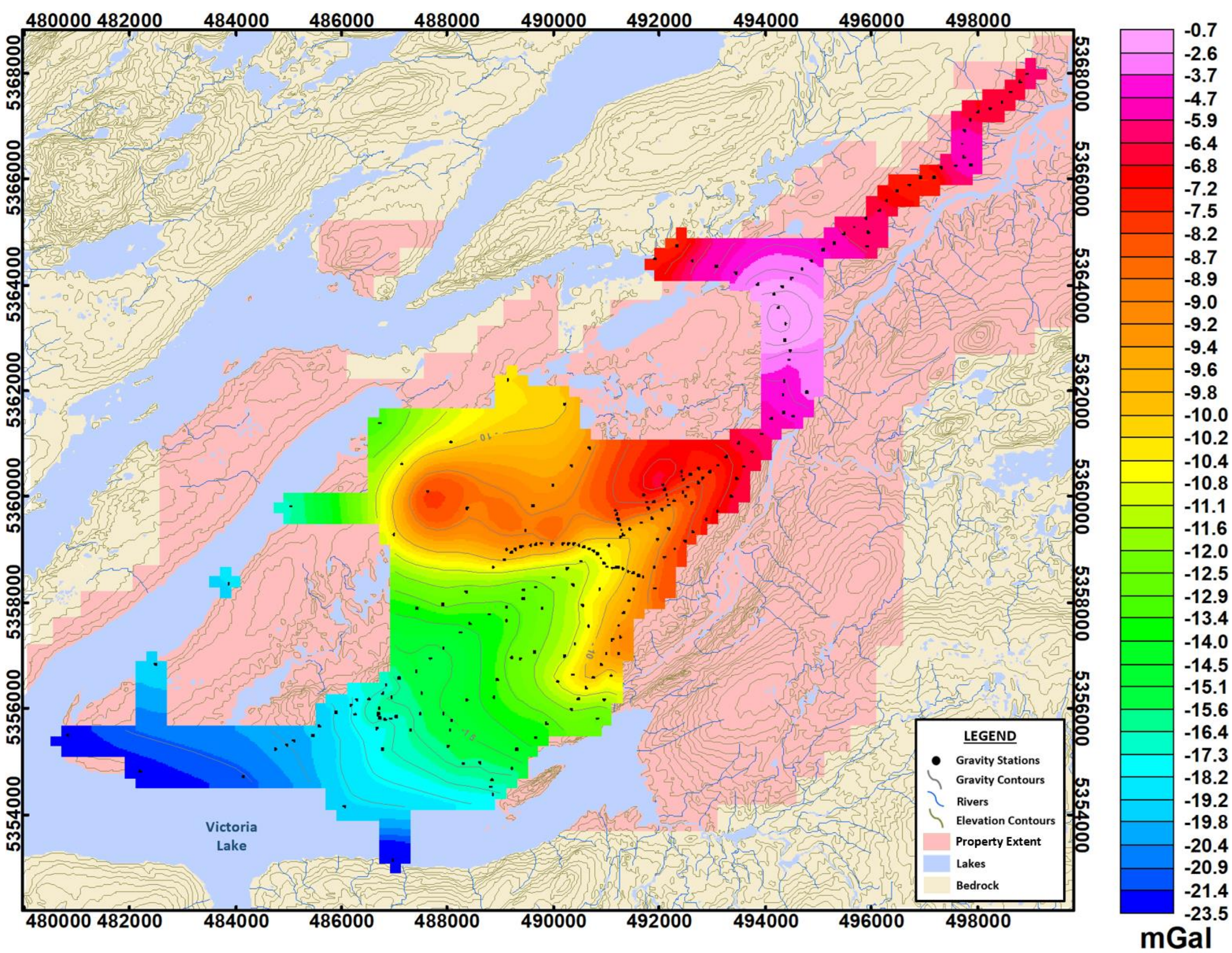

Figure 4.10: Complete Bouguer anomaly map of the Valentine Lake Property containing influences from the linear regional trend. The gridding method was minimum curvature with a cell size of 200 metres. The cells to extend data beyond was set to 1 and the colour method was linear.

The magnitudes of the aforementioned corrections (Sections 4.2.5 and 4.2.6) that were applied to produce the complete Bouguer anomaly maps [Figs. 4.10, 4.11] were on the order of several mGal for the elevation (free-air) corrections and the terrain corrections were primarily fractions of mGal, but up to a few mGal in some areas. The latitude correction was significant at nearly 1.6 mGal, the same magnitude as the preliminary negative gravity anomaly associated with the alteration zone [Fig. 2.8].

Upon initial review of the broad-scale complete Bouguer gravity map [Fig. 4.10], it is evident that it shows a distinct regional trend of increasing gravity from the southwest to the northeast of the property. Specifically, the negative gravity values down to -23.5 mGal in the southwestern extent increase to between -6.4 mGal and -0.7 mGal in the northeast, for a range of 22.8 mGal. However, despite the dominant regional trend contributions, it can be seen that there is a measurable response from the alteration zone, based on the distortion of the northwest-southeast gravity contours from the approximately -8.9 mGal region (orange to yellow) at the centre of the map (~ 492000 m E, 5360000 m N) towards the roughly -16 mGal section (green to turquoise) of lower gravity to the southwest (~ 487000 m E, 5356000 m N). Another principal feature is the -3.6 to -0.7 mGal gravity high (light pink) to the northeast (~ 494000 m E, 5363500 n N), which is clearly not a component of the regional trend. To better resolve the full extent of the alteration zone, it was necessary to remove the regional trend as discussed in Section 4.2.8.

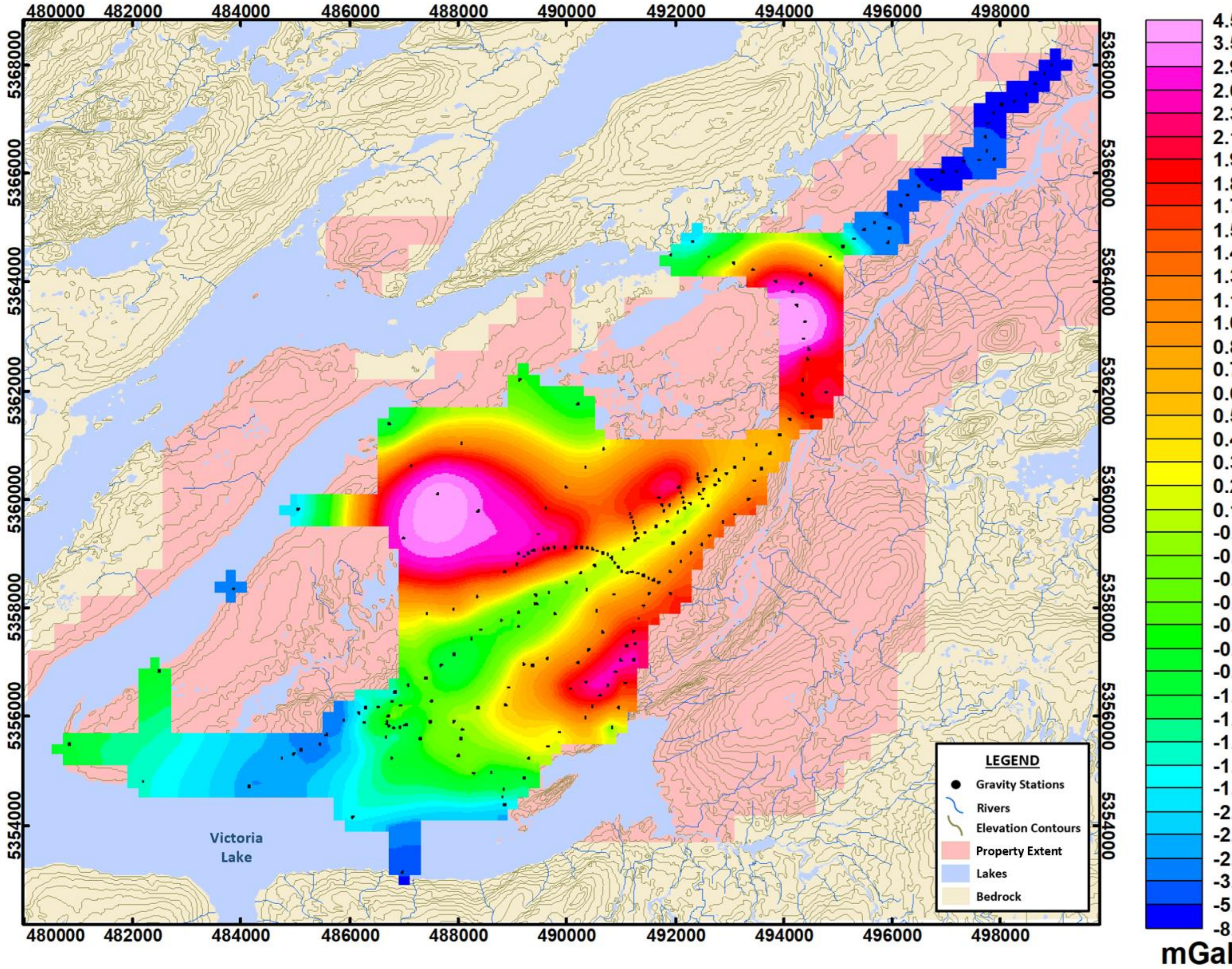

Figure 4.11: Complete Bouguer anomaly map of the Valentine Lake Property with the regional linear trend contributions removed (i.e., residual). The gridding method was minimum curvature with a cell size of 200 metres. The cells to extend data beyond was set to 1 and the colour was histogram equalization.

The outcome of the trend removal is a well-defined residual Bouguer gravity map of the Valentine Lake Property [Fig. 4.11], comprising a combination of negative and positive gravity anomalies that were previously partially masked by the regional trend in Figure 4.10. The central to southwest region of distorted gravity contours, understood to reflect the alteration zone associated with gold-bearing veins, has been refined into a well-constrained northeast-southwest thin linear negative gravity anomaly (green) of up to -1.7 mGal. This ore-hosting low gravity corridor is bounded to the north-northwest and south-southeast by two juxtaposing high gravity anomalies [Fig. 4.11]. The northeast-southwest elongated positive gravity feature to the south-

southeast of the interpreted alteration zone (~ 493000 m E, 5360000 m N to ~ 489000 m E, 5356000 m N) intensifies from 0.4 mGal to 2.3 mGal (yellow-orange to pink-red) as it spans toward the southeast and is speculated to represent the non-mineralized Rogerson Lake Conglomerate [Fig. 6.1; pale orange unit; Tbl. 2.1; ρ_{avg} = *2.76 g/cm*^{3}]. Similarly, the oval high gravity response to the northwest (~ 488000 m E, 5358500 m N) ranges from 0.4 mGal to the observed maximum of 4.5 mGal (yellow-orange to light pink) at its centre and is presumably associated with the non-mineralized granitoid suites [Fig. 6.1; light purple unit; Tbl. 2.1; ρ_{avg} = *2.69 g/cm*^{3}]. This oval high blends into an elongated gravity high adjacent to the northeast extent of the identified hydrothermal zone (~ 492000 m E, 5361000 m N to ~ 490000 m E, 5359500 m N), which varies from 0.6 mGal to 2.1 mGal (orange to red) and is interpreted as a denser gabbro unit of the VLIC [Fig. 6.1; dark purple unit] having an average density *3.03 g/cm*^{3} (Telford et al., 1990). Likewise, the positive gravity anomaly to the northeast (~ 494000 m E, 5363500 n N), previously noted in Figure 4.10 as inconsistent with the linear regional trend, has been sharpened into a gravity high of up to 4.5 mGal (pink) at its centre [Fig. 4.11]. This refinement aids in the comprehension of the source of this high gravity anomaly, which is also considered to be the denser gabbro unit of the VLIC [Fig 6.1; dark purple unit].

To validate the proposed lithological interpretations of the identified anomalies, the residual Bouguer gravity data was superimposed onto the property geology map [Fig. 2.2] for comparative analysis. These results and the associated discussion and final interpretations are presented in Section 6.2.

4.4 TERRAIN CORRECTION: METHOD COMPARISON

In geophysical exploration, it is good practice to compare results of different methods or procedures to ensure confidence, particularly when the outcome is based on newly acquired data, as presented in this research. Therefore, to corroborate the property-wide gravity survey results, a comparative analysis of two different procedures for completing the associated terrain correction is discussed below.

While the terrain corrections reflected within the complete Bouguer results of this study [Fig. 4.12; panel A] were completed using Oasis Montaj processing tools, as a comparative exercise, a secondary terrain correction was computed using forward-modelling methods. The details of the forward modelling approach are provided in Appendix E, however, the following is a brief summary of how the method worked to aid with the comparison. The alternate approach involved generating several 3-dimentional topographic models of the VGP using combinations of LiDAR, regional topography, and bathymetry data. Forward modelling was then conducted on each model based on the free-air gravity data and the subsequent terrain correction (and linear trend removal) was computed. The model-based complete Bouguer anomaly map created by *Memorial University* Ph.D. candidate, Michael King is displayed in panel B of Figure 4.13 for direct comparison with the primary map in panel A.

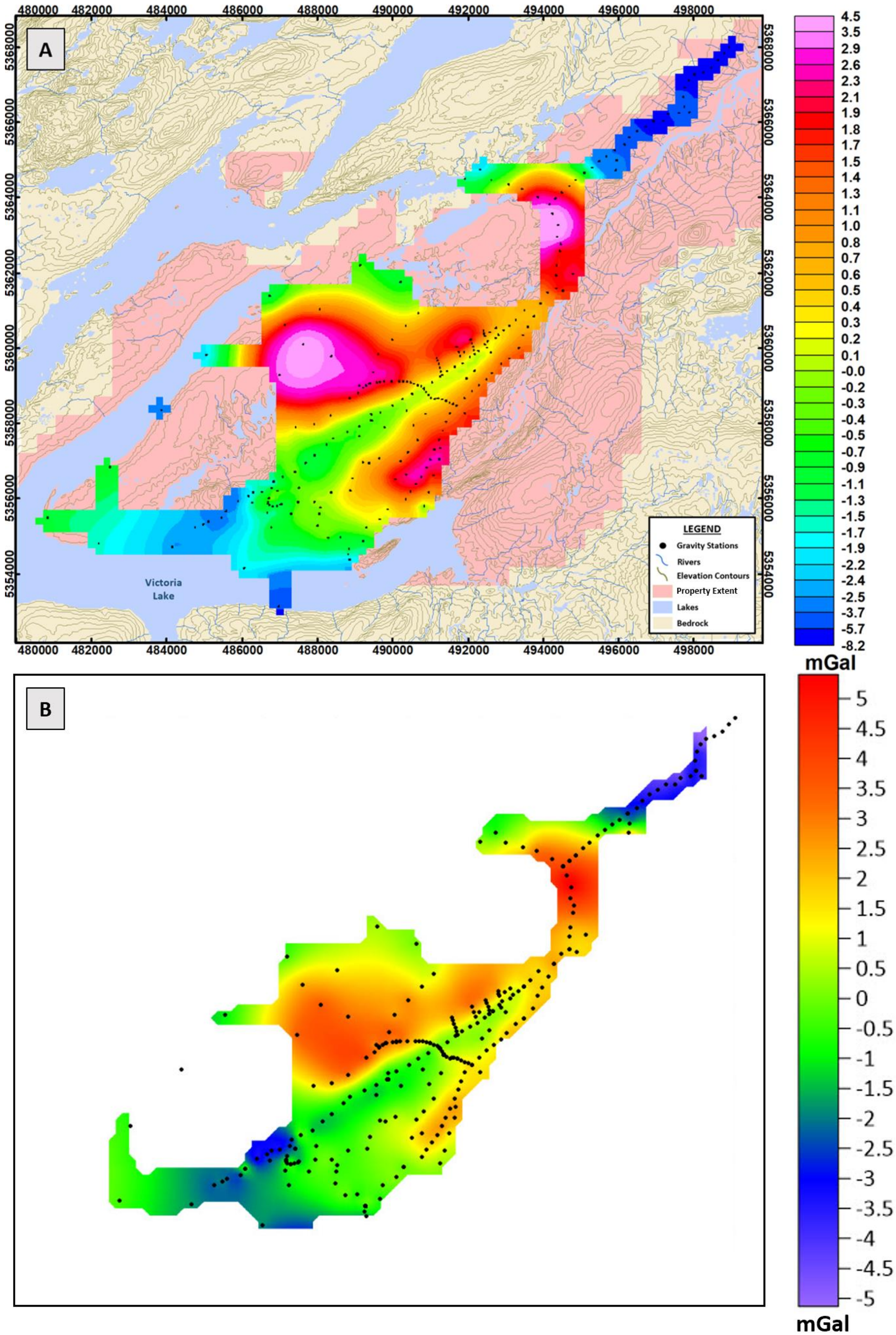

Figure 4.12: Terrain correction comparative analysis. A) Residual Bouguer anomaly map resulting from the Oasis Montaj terrain correction method. B) Residual Bouguer anomaly map produced using the forward-modelling terrain correction technique.

Initial inspection of the two maps is encouraging, as they undoubtedly reveal the same general pattern of positive and negative gravity anomalies. Most notably, the northeast-southwest thin linear corridor of low gravity conjectured as the alteration zone, is observed along the centre of both maps [Fig. 4.13]. Likewise, the juxtaposing positive gravity anomalies to the north-northeast of the alteration zone exhibit the same shape and high amplitude gravity values between maps [Fig. 4.12] along with the observed gravity high to the northeast, which display the maximum gravity values of 4.5 mGal and 5.5 mGal for panels A and B, respectively.

Upon thorough inspection of each map scale, it is recognized that the slight visual differences observed between anomalies are simply an effect of the different colour scales between methods and that the resulting anomalous gravity values do agree. Similarly, the range of the two gravity scales vary, particularly at the minimum extent, as panel A gravity values decrease to -8.2 mGal, while panel B reduce to -5 mGal. This discrepancy is justified as the forward-modelling map [Fig. 4.12; panel B] omits the four gravity stations furthest to the northeast, which correspond to the lowest gravity values observed on the Oasis Montaj generated complete Bouguer anomaly map [Fig. 4.12; panel A]. The slight offset in the maximum observed gravity is considered a reasonable discrepancy related to slight differences between how the modelling based program (Appendix E) specifies the zones and correction distances compared to the Nagy (1966) and Kane (1962) methods exploited by Oasis Montaj (Appendix D).

Overall, the two different terrain correction techniques produce essentially the same result, which instils confidence that the complete Bouguer gravity map computed in this study [Fig 4.12; panel A] provides an accurate representation of the subsurface anomalies.

5 GROUND-PENETRATING RADAR AND SONAR

5.1 SURVEY SETUP AND ACQUISITION

5.1.1 GPR

GPR data was obtained throughout the Valentine Lake Property [Fig. 5.1] for three reasons: to provide insight on infrastructure placements, allow for the effects of the low-density overburden regions within the property (*i.e.*, bogs, lakes and soils) during the gravity corrections (Section 4.2.6) and deliver high-resolution bathymetry information for four specific locations [Fig. 5.1], defined by *Marathon Gold*, to aid with their ongoing environmental and feasibility studies.

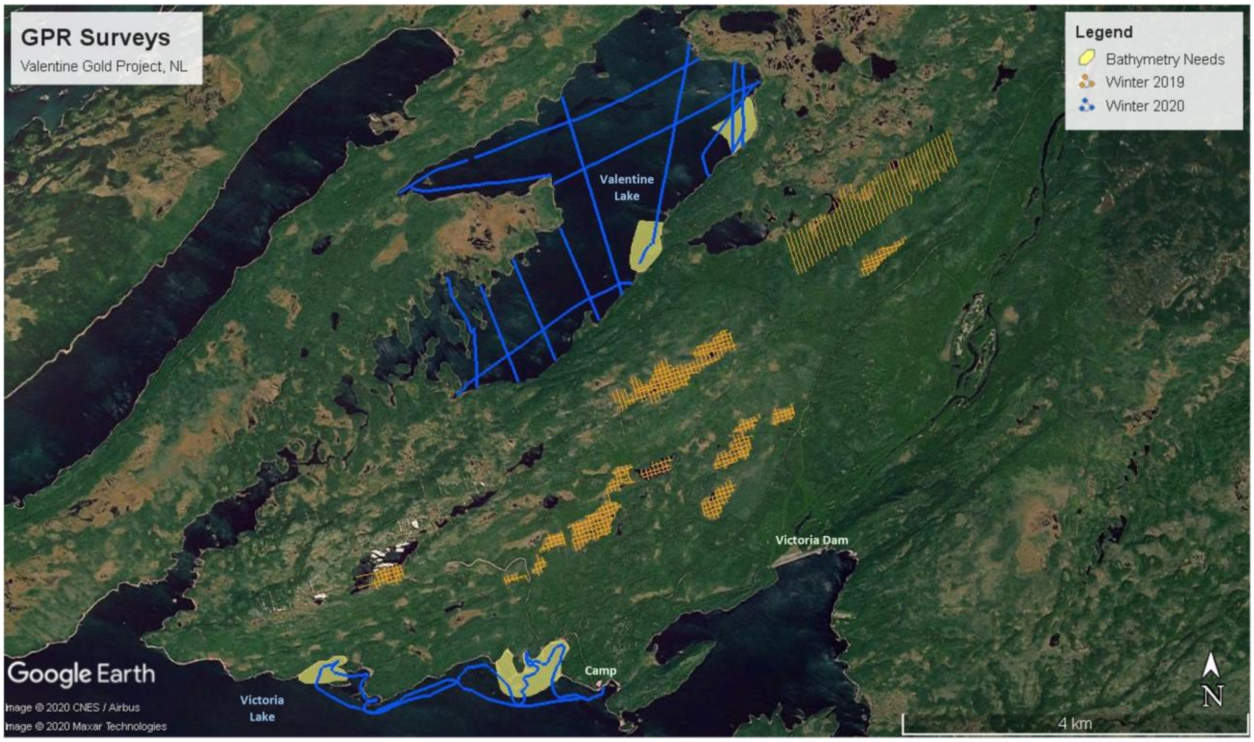

Figure 5.1: Google Earth map displaying the GPR surveys completed at the Valentine Lake Property. The 2019 data (orange) comprised bogs and ponds, while the 2020 surveys (blue) covered freshwater lakes. The bathymetry needs of Marathon Gold are defined in yellow.

To enable surveying over lakes and ponds, ground penetrating radar surveys were conducted during the winters of 2019 and 2020, using a pulseEKKO Pro system by *Sensors and Software* and additional equipment (skis and receiver mounts) designed and fabricated exclusively for winter acquisition by *Memorial's* Technical Services. The system configuration involved a transmitter and receiver which were fastened onto a set of antennas that were secured within a pair of wood and fibreglass skis. The skis were towed behind a 2-metre-long black sled which carried the operator and the control unit, all of which was pulled by a snowmobile [Fig. 5.2]. A *Topcon Hiper V* Real-Time Kinematics (RTK) roving receiver (Section 3.6) was mounted in a fixed position in the black sled and connected to the GPR control unit, to obtain and record accurate GPS measurements during data acquisition. The GPR system was operated in "free-run" mode (*i.e.*, continuous acquisition), travelling at approximately 7-8 kilometres/hour, and was equipped primarily with 50 MHz antennas which are capable of imaging the subsurface to a depth of 20 metres. Less data were collected using 100 MHz antennas, which obtained subsurface information to a depth of approximately 5 metres.

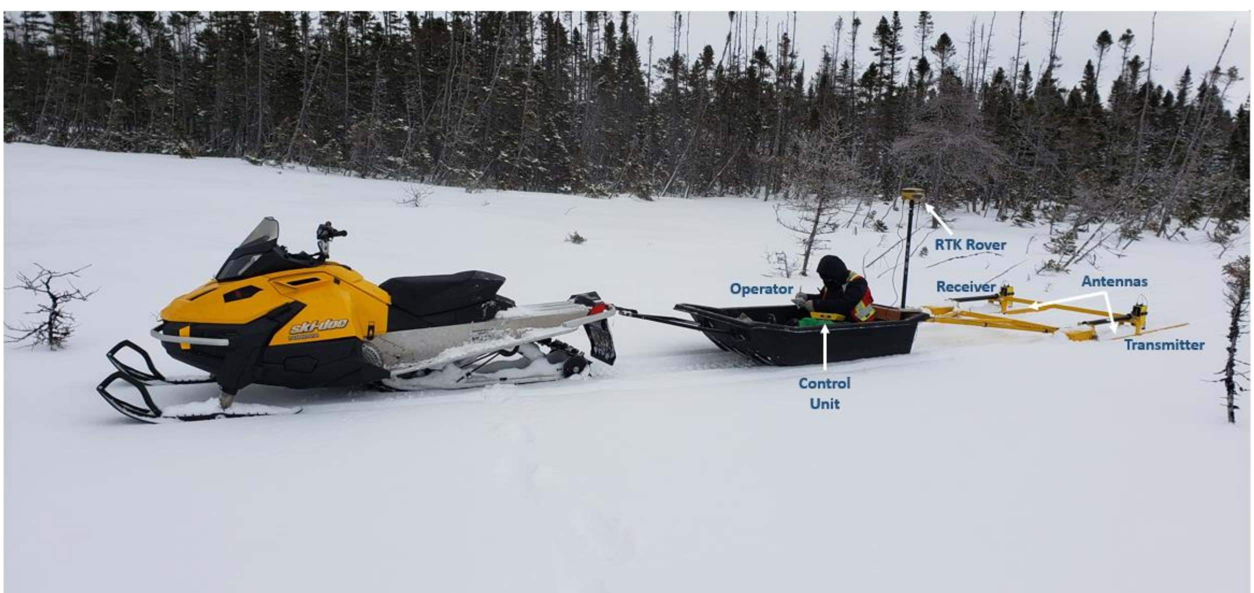

Figure 5.2: GPR system configuration and components including a snowmobile, black sled for the operator and RTK rover and yellow skis for housing the transmitter, receiver and antennas.

The 2019 fieldwork [Fig. 5.1] comprised of ground penetrating radar surveys over 8 bogs, designated as priorities by the *Marathon Gold* engineering team [Appendix F; Fig. F.1]. Some of the bogs contained small ponds. The surveys were designed as grids with the transect lines (Y) following the 343°/163° drilling orientation, perpendicular to the VLIC – conglomerate contact along the NE-SW thrust fault [Fig. 2.2]. The tie lines (X) were parallel to the thrust fault and the grid edges were defined by the existence of trees. The priority areas comprised 184 survey lines, spaced at 50 metres, with line lengths varying between 40 and 820 metres. Given the sizes of the field areas, grid setup and access were challenging and required assistance from *Marathon* personnel. Field crew defined the start and end points of each grid line. Using a handheld GPS, field assistants snowshoed to defined points on either edge of the line and communicated their arrival through a two-way radio. Once both positions were confirmed, the snowmobile operator aligned with the "markers" and began acquisition, repeating this process for every line. To help define surface conditions under tree-covered regions of the property, additional transect-only (Y) data were collected along the 44 mulch lines, which were the focus of the previous seismic surveys (Section 2.3.3). The unusually broad cut lines followed the same orientation and spacing as the priority area transects and were approximately 400 to 600 metres in length, contributing to a collective total of 228 survey lines.

To optimize data collection, a new Ultra receiver (Sensors and Software, 2020) compatible with the existing pulseEKKO pro system was rented from *Sensors and Software* and used for the winter 2020 surveys. This receiver was capable of stacking many more pulses than the standard receiver, resulting in higher signal to noise (Section 3.5.1), and hence theoretically it could resolve features at twice the depth. It was anticipated that this system enhancement would identify bedrock and other features within the previously surveyed bogs, ponds and mulch lines that were poorly resolved in the 2019 data. Initial acquisition involved resurveying 21 transect lines from Area 6 [Appendix F; Fig. F.7] to compare the resolution and data quality of the two receivers. Based on the 2019 analysis, which revealed possible evidence of patchy, irregular bedrock in some areas, an additional 6 transects from Area 7 [Appendix F; Fig. F.8] were resurveyed. Reflections from air pockets, tree roots and cobbles rendered the 2019 mulch line data uninterpretable, therefore, in 2020, 4 cut lines were resurveyed and evaluated for reduced signal scattering. Unfortunately, while the Ultra receiver data contained less noise [Fig. 5.5], it did not provide any new information. It had no greater success along the mulch lines nor was it able to resolve the till/bedrock interface.

In addition to the 31 lines resurveyed with the Ultra receiver, bathymetry data was obtained from Valentine Lake and Victoria Lake [Fig. 5.1]. A 7.07 km^2 ground penetrating radar survey of Valentine Lake was conducted (Section 4.2). The survey was intended to maintain the same grid orientation as the 2019 surveys (Y perpendicular and X parallel to the shear zone) and the target line spacing was 500 metres. However, line bearings and positions varied [Fig. 5.1] due to safety risks associated with nearby brooks and poor ice and weather conditions. Blowing snow caused reduced visibility and hampered precise navigation. A secondary 10.3 line-kilometre GPR survey of Victoria Lake was carried out to cover additional bathymetry requests of the industry partner [Appendix F; Fig. F.10]. These data were collected continuously with no specific line spacing or direction [Fig. 5.1].

To assist with the analysis, ice and snow thickness measurements were obtained from several small ponds within the priority areas in the winter of 2019 [Appendix G; Tbl. G.1, G.2]. During the summer of 2019, a common-midpoint (CMP) survey was completed, various depth measurements were taken, and 13 bog and 5 soil samples were collected and analyzed for water content (further discussed in Section 5.2.1). In addition, water depth and snow and ice thickness measurements from different gravity station locations were acquired during the winter of 2020.

5.1.2 Sonar

To facilitate the gravity corrections (Section 4.2) using detailed bathymetry maps (Section 5.3.1) and fulfill the bathymetry requests from the company [Appendix F; Fig. F.10], several sonar surveys were carried out on Valentine Lake and Victoria Lake during the summers of 2019 and 2020 [Fig. 5.3].

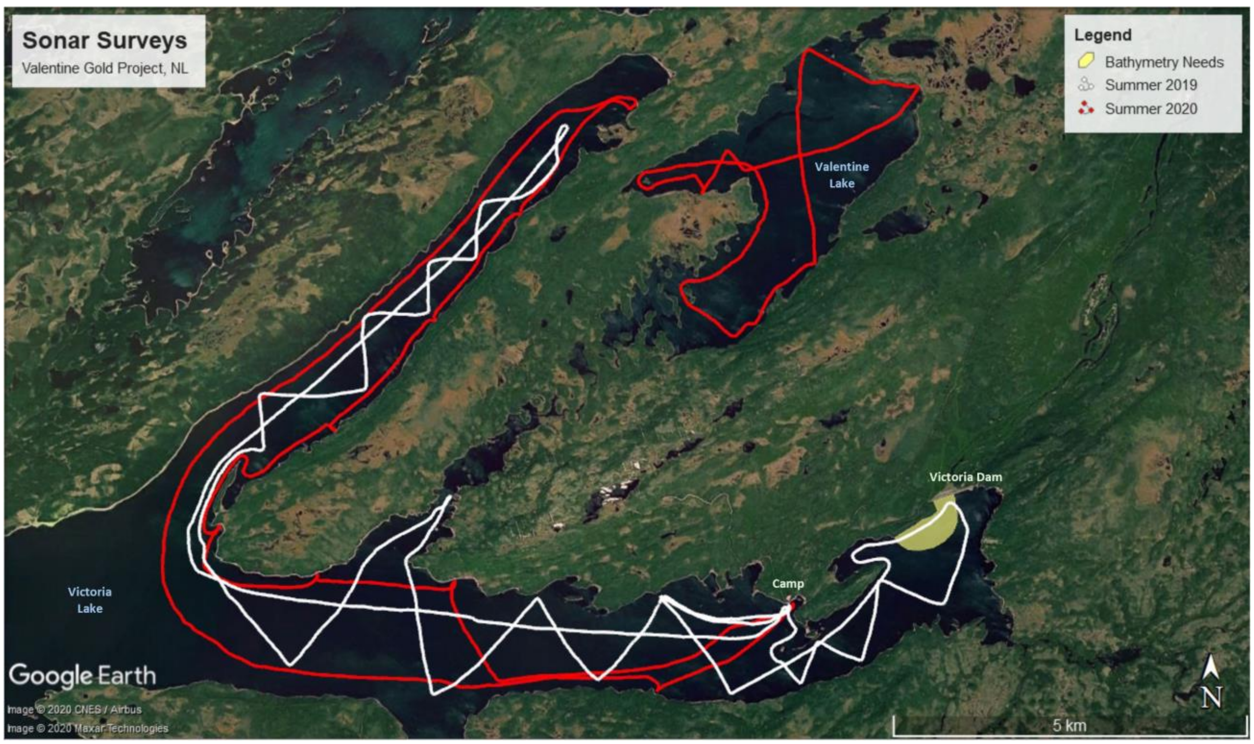

Figure 5.3: Google Earth map showing the 2019 (white) and 2020 (red) summer sonar surveys carried out on Valentine Lake and Victoria Lake. The shaded yellow region highlights the bathymetry needs of Marathon Gold.

The surveys were conducted using a *Garmin* GPSMAP 527xs system, which emits an acoustic signal at 200 kHz, and a *Crestliner* aluminum boat. A 10-centimetre-long transducer was mounted on a wooden board and fastened to the stern of the boat so that it was submerged in the water. The boat was driven at a close to constant speed of 10 kilometres/hour and the data was recorded and viewed in real-time on the *Garmin* display screen [Fig. 5.4].

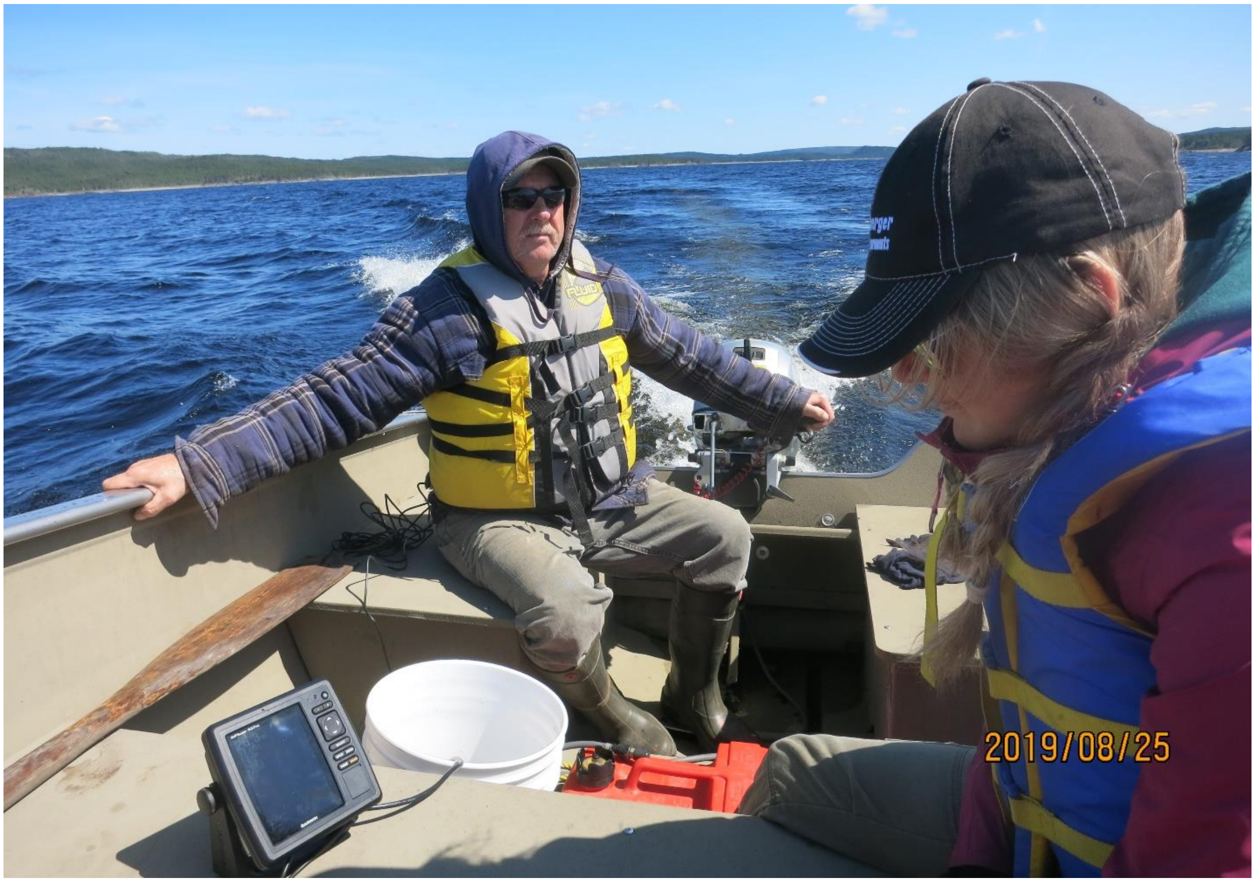

Figure 5.4: Sonar survey setup and acquisition. Shown are the boat operator and the author observing the data in real-time on the Garmin device.

During the summer of 2019, a 17.35 km^2 survey of Victoria Lake reservoir was completed. It was designed as a "zig-zag" pattern with a central "tie-line" to obtain optimal coverage [Fig. 5.3] and was conducted in two parts. The small-scale morning survey extended east of the Valentine Gold camp, alongside the Victoria dam and circling the cove for a total of 2.94 km^2. The extensive 14.41 km^2 afternoon survey spanned west and northwest of camp, continuing into the northern arm towards Valentine Lake.

In-fill surveys were carried out on Valentine Lake and Victoria Lake in the summer of 2020. The 16.3 line-kilometre Valentine Lake survey [Fig. 5.3] was supplementary to the winter 2020 GPR survey (Section 5.1.1). The aim was to fill data gaps along the shorelines and in areas near streams and brooks that had risky unstable ice cover in the winter, as well as to survey regions that were unnoticed due to previous whiteout weather conditions. The 39.3 line-kilometre Victoria Lake survey [Fig. 5.3] focused primarily on shoreline data which served as additional “tie-lines” for the 2019 survey. These auxiliary datasets enabled the creation of well-defined bathymetry maps [Fig. 5.8, Fig. 5.9] by reducing undesired interpolations between widely spaced survey lines.

5.2 DATA PROCESSING

5.2.1 Ground-Penetrating Radar

Processing of GPR data enables accurate interpretations of a GPR section that is a close approximation of the subsurface and allows the production of detailed bathymetry and hypsometry maps. In this study, the ground-penetrating radar data acquired (Section 5.1.1) was analyzed and interpreted using EKKO_Project, an all-inclusive software designed by *Sensors and Software Inc*. Quality control and additional corrections (described below) were performed in Microsoft Excel and subsequent bathymetry and hypsometry maps were generated using Oasis Montaj, a visualization software provided by *Seequent Ltd*.

Primary processing was carried out using the *LineView* module of EKKO_Project which displays the individual line data so that prominent reflectors can be identified and subsequently defined using the *Interpretation* menu (further discussed below). It allows for multiple line data to be displayed in a single window, so that features between neighbouring lines can be compared to help validate interpretations. For these data (Section 5.1.1), the interpretations are primarily a sequence of hand-chosen points that define the interfaces between materials with differing electrical properties [Fig. 5.5], for example a water-sediment or overburden-till boundary. Secondary interpretations include hyperbolic reflections associated with point diffractors, such as boulders. Figure 5.5 below was acquired using the Ultra receiver, resulting in sections with lower noise than the standard pulse EKKO "model" receiver, though resolving the same interfaces.

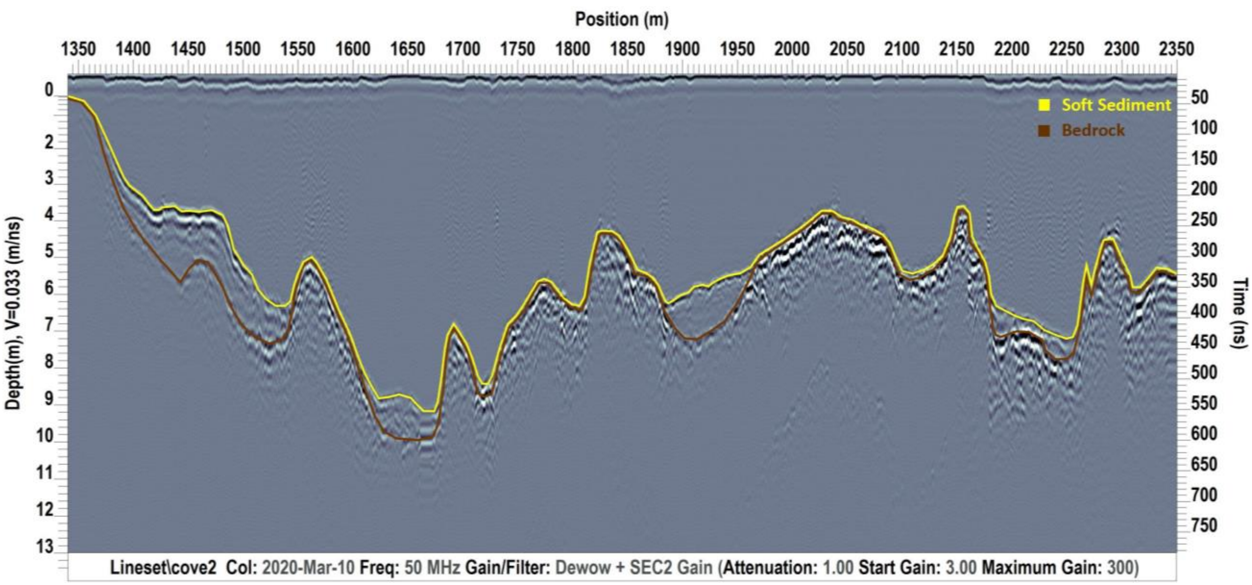

Figure 5.5: A Victoria Lake GPR section displayed in LineView where gain adjustments and filters have been applied to improve resolution so that correct interpretations can be made.

5.2.1.1 Wave Velocity

To ensure that accurate depth information is obtained, it is paramount that an appropriate wave velocity is chosen for the desired subsurface analysis (*e.g.*, lake or bog) prior to making any interpretations. EKKO_Project applies apparent wave velocity, which is the average velocity of a wave travelling within the entire subsurface, not an individual layer. Although individual layer velocities are ideal for determining the depth of each interface, establishing them is laborious and requires additional sophisticated software and common midpoint gather (CMP) data. While every reflection implies a change in velocity, this study deals with very homogeneous layers (i.e., bogs and lakes) with only one reflection of interest, the bottom. Therefore, it is reasonable to assume a constant (well known) velocity in the bottom layer. The only complication is the top snow and ice layer (see two-layer system analysis in Appendix H). To determine the wave velocity of the bogs [Fig. 5.1], several samples were collected using a bog corer and transported to a laboratory at *Memorial University* where they were measured for water content. The details of this analysis are shown in Appendix G; Table G.3. Results revealed that the bogs were comprised, on average, of 90% water, so an apparent velocity of *0.035 m/ns* was chosen (see Appendix G; *calculating dielectric constant in wet bogs*). For the freshwater lakes, the standard wave velocity of water, *0.033 m/ns*, [Tbl 3.2] was applied.

5.2.1.2 GPS Offset

Once the appropriate velocities were incorporated and the depth axis adjusted accordingly, reliable interpretations of the various interfaces were created using the *Polyline* tool within the EKKO_Project *Interpretation* menu. The hand-selected points that define the polylines have associated location (UTM) and elevation information obtained from the attached RTK rover during acquisition. However, in the GPR system configuration [Fig. 5.2] there is an offset between the RTK receiver and the GPR antennas. To adjust the UTM coordinates to the GPR measurement locations, the difference in position (x, y and z) between the GPR antennas and the RTK rover is measured in the field and then corrected for using the *GPS Offset* function in EKKO_Project. The measured offsets and correction setup are defined in Figure 5.6 below.

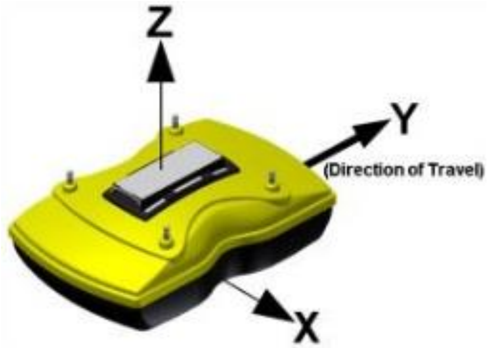

- **Lateral Offset (X):** 0.25 m
- **Survey Line (Y):** 3.15 m
- **Height (Z):** 1.34 m

Figure 5.6: Schematic of the GPS offset correction defined by the lateral (X), survey line (Y) and height (Z) offsets between the GPR antennas and RTK receiver (from EKKO_Project software). The offset is measured from the center of the GPR at (0,0,0) to the center of the RTK antenna.

With the locations rectified, the interpreted GPR data was imported into Excel for quality control and additional correcting. Akin to the gravity surveys, for the majority of GPR acquisition the RTK base receiver was fixed on a permanent base station, however, on a few occasions a temporary base was set up, and further refinement of the absolute locations of measurements using static data and Precise Point Positioning (Section 4.2.3) was required and adjusted for in Excel. At this stage, the hypsometry data (*i.e.*, bogs) was imported into Oasis Montaj where maps of these priority areas were created using the appropriate depth information (Section 5.3.1).

5.2.1.3 Assumptions

In processing the winter bathymetry data, the following assumptions were made:

1. The ice surface elevation was **not constant** over the lakes.
2. The ice was approximately **70 cm thick** based on an ice thickness measurement from Valentine Lake, and previous experience with lakes and bogs in Newfoundland winters.
3. The GPR signal was travelling at the velocity of water **0.033 m/ns**.
4. The RTK elevation was the **water surface elevation**.

Under these assumptions, subtracting the bathymetry from the lake surface level gave the **elevation of the lakebed relative to sea level** [Eqn. 5.1].

Given that the freshwater lakes (*i.e.*, Valentine and Victoria Lakes) were partially frozen during acquisition, *0.5 m*, was added to the depth to sediment values to allow for the wave travelling much faster in ice ($v = 0.16$ *m/ns*) than in water ($v = 0.033$ *m/ns*). Further details on this analysis are provided in Appendix H. Subsequently, to obtain the corrected elevation of the lakebed relative to sea level (for the gravity corrections; Section 4.2), the corrected depth information was subtracted from the lake surface level using the following equation:

$$Elevation = Lake\ Surface\ Level - Depth \qquad \text{(Eqn. 5.1)}$$

where,

1. *Lake Surface Level* = RTK elevation (corrected where necessary)
2. *Depth* = Depth corrected for ice layer

5.2.1.4 Zero Offset

As observed in the EKKO_Project GPR profile presented in Figure 5.5, the vertical axes present the calculated depth (left) and two-way travel time (TWT; right) of the wave reflection traces. Examination reveals that while the time axis is linear, beginning from zero at the top of the profile, the depth axis is not perfectly linear at shallow depths and an offset exists between zero-time and zero-depth [Appendix H; Fig. H.1]. Unlike the time axis, the depth axis is determined from the antenna separation and the subsurface velocity (assumed constant), which are specified by the user. The nonlinearity and offsets are a consequence of the antenna separation and inaccuracies arise particularly in the zero depth, if the GPR system is travelling over snow or ice. Since the lakes and bogs in this study were under such cover at the time of the GPR surveys, the resulting maps (Section 5.3) contain these errors. An in-depth analysis on how to account for these effects, to provide increased accuracy in the depth estimates is provided in Appendix H, however, the bottom-line corrections, which were applied to the results of this study, are described below.

The objectives of the lake bathymetry surveys were to carry out gravity terrain corrections and evaluate unfrozen water levels during the winter for environmental purposes (i.e., maintaining aquatic life). In both cases, water depth measurements in shallow regions (< 1 m) are insignificant, therefore, a general correction of adding 0.5 metres to all bathymetry data (as discussed in Section 5.2.1.3) is sufficient. A similar case is made for the bogs, stating that the existing hypsometry maps [Figs. 5.7, F.2 – F.9] reveal the qualitative variation with depth. For apparent depths greater than 1 metre, the true depth is shallower by only 10 or 20 centimetres, which is comparable to the resolution of the GPR. For apparent depths less than 1 metre, the true bog depths are greater by a few decimeters, to a maximum of 50 centimetres.

5.2.2 Sonar

Unlike gravity and GPR, the collected sonar data (Section 5.1.2) did not require any significant processing, allowing any necessary corrections to be completed in Microsoft Excel. The *Garmin* sonar system collected depth information in the form of "depth logs" which were exported from the GPSMAP 527xs into HomePort, *Garmin's* marine navigation software. The data tracks were reviewed, and depth logs combined prior to being imported into Excel.

5.2.2.1 Assumptions

The data underwent quality control, and the following assumptions were generated to obtain additional information from the dataset:

1. The water levels of the lakes were **constant**.
2. The lake levels at the time of the surveys were determined, using the RTK system, to be:

- Victoria Lake = **323.20 m** (Summer 2019)
- Victoria Lake = **323.73 m** (Winter 2020 – below the ice)
- Victoria Lake = **323.58 m** (Summer 2020)
- Valentine Lake = **324.59 m** (Summer 2020)

The computed elevation column was the **lake level <u>at the time</u> minus the depth** [Eqn. 5.1]. Since the sonar data provided only information on depth and not the elevation of the lakebed relative to sea level, this "elevation" column had to be manually generated using Equation. 5.1, where the lake surface level was a constant value, defined in the above assumptions based on the acquisition date.

5.2.2.2 Supplementary data

To enhance the bathymetry maps (Section 5.3.2), additional sonar data collected by *Stantec Inc.* in 2018 was obtained [Appendix I; Tbl. I.1, Fig. I.2] and incorporated into the datasets. As with the sonar collected in this study, the *Stantec* data was presented in terms of depth, so the elevation of the lakebed relative to sea level was also obtained using Equation 5.1. The lake water levels were not known at the time of acquisition, but a comparative depth analysis between the collected data and the provided *Stantec* data (see Appendix I) revealed that the depth differences between the two datasets at cross-over locations were within standard error, suggesting that the 2019 and 2020 measured lake surface levels were suitable for the *Stantec* data analysis. Thus, a water level of *324.6 m* was used for *Stantec's* Valentine Lake data and an assumed average water level of *323.5 m* for Victoria Lake.

The collective sonar depths were combined with the corrected bathymetry depths to produce detailed bathymetry maps in Oasis Montaj (Section 5.3.2), which were incorporated into the gravity terrain corrections using the computed elevations (Section 4.3.2).

5.3 RESULTS

5.3.1 Hypsometry Map

When planning the locations of future mine infrastructure, such as a processing plant or a heap leach pad, there are numerous factors to consider, one of which is overburden thickness. The amount of overburden controls the type and size of equipment necessary to remove it, so an understanding of the depth of bog material is critical for establishing suitable sites for the superstructures. The results of the GPR surveys over the 8 priority areas [Appendix F; Fig. F.1] are presented in Figure 5.7 as a combined hypsometry map revealing the depth to the bottom of each bog and any associated small ponds. Unfortunately, because the GPR surveys were not able to resolve the till/bedrock interface (Section 5.1.1), these “overburden” results represent bog thicknesses only, while there is likely till beneath the bogs, as clearly suggested by Figure 2.8. Individual maps of each area, which provide additional details, including the data measurement locations, are included in Appendix F. Given the zero-depth offset produced by the GPR system when travelling over snow or ice (i.e., winter bogs), these hypsometry maps showcase the qualitative variation with depth (see Section 5.2.1.4 and Appendix H).

In general, all areas shallow to the edges and the following observations refer mainly to the deeper, central sections of each bog. Overall, the areas vary in depth up to 4.8 metres, with the thickest overburden present in Area 4 and the least existing in Area 8 [Fig. 5.7]. The average thickness is estimated to be between 1.2 and 2.4 metres. Area 1 exhibits a general increase in overburden thickness from the northwest to the southeast, with a maximum depth of 3.2 metres seen to the southwest of the bog’s centre [Appendix F; Fig. F. 2]. Area 2 is deepest to the north, with a top depth of 2.7 metres, but overall maintains a relatively uniform thickness throughout

[Appendix F; Fig. F. 3]. Area 3 overburden is thickest in the south at 3.2 metres, with thinning occurring at the bog's centre and a regain in depth to the north [Appendix F; Fig. F.4]. In Area 4, the bog increases in thickness from east to west, with the greatest depth of 4.8 metres existing in the southwest [Appendix F; Fig. F.5]. Area 5 varies in depth between the bog (west) and the small pond (more easterly). The thickest, 2.9 metre, section of the bog exists to the south and lies between two regions of lower depth to the west and east. The associated pond is shallower than the bog and maintains a fairly consistent depth throughout, averaging between 1.0 and 1.6 metres from the west to the east-northeast [Appendix F; Fig. F.6]. Area 6 maintains an average overburden thickness of 2.1 metres throughout its central regions, with the deepest region of 3.6 metres observed at the northeast extent of the bog along with two sections of 3.0-metre-thick overburden exhibited south of the bog's centre and at the southwestern edge [Appendix F; Fig. F.7]. Area 7 showcases a general linear trend of maximum depth spanning southwest to northeast along the centre of the bog, with an area of reduced thickness observed directly east of the bog's centre. This 1.4-metre-thick area separates two 3.7-metre-deep lenses to the west and east, with the thickest overburden exhibited as a 4.2-metre lens to the southwest [Appendix F; Fig F.8]. Finally, Area 8 contains the least amount of overburden, having a maximum thickness of 1.8 metres to the northwest, with the remaining bog margins (west, east and south) being less than 0.5 metres deep [Appendix F; Fig. F.9].

Based on the results described above, which for the most part, exhibit moderate overburden thicknesses, this material can likely be removed using equipment such as an excavator or a bulldozer and does not require the use of larger machinery or other more costly methods.

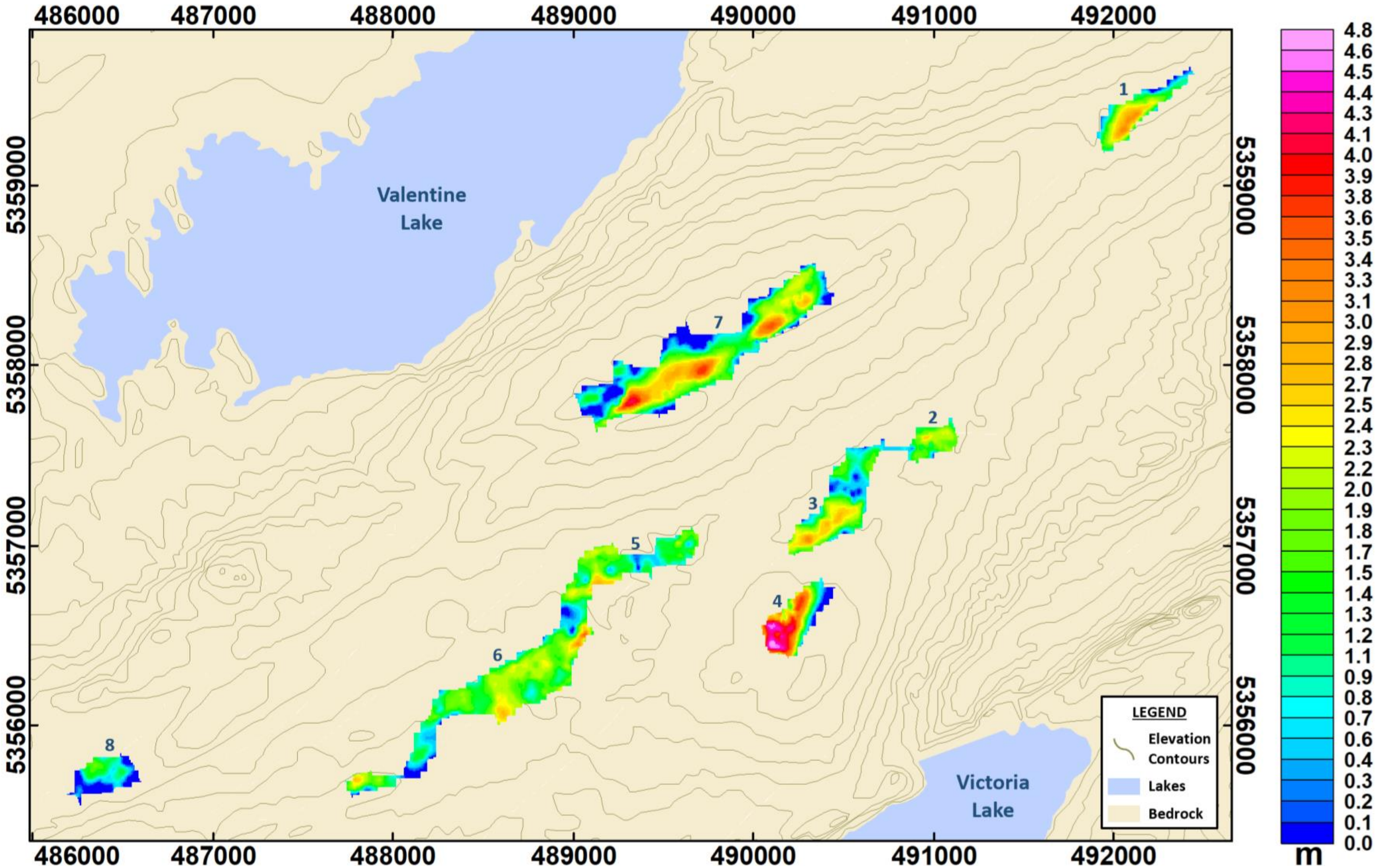

Figure 5.7: Map of the 8 priority areas showing qualitative variation with depth. It was gridded using minimum curvature with a cell size of 8 metres, cells to extend data beyond set to 0 and linear colour method.

5.3.2 Bathymetry Maps

As gravity surveys are greatly influenced by near surface features of varying density and topography, it is important that the bathymetry of two major lakes within the study area, Valentine Lake and Victoria Lake, be incorporated into the gravity terrain correction. To accomplish this, a combination of summer sonar and winter GPR surveys were completed, and the necessary depth information obtained, to generate detailed bathymetry maps of these water bodies, as shown below. Figure 5.8 is Valentine Lake and Figure 5.9 is Victoria Lake. While the zero-depth offset exists when the GPR is travelling over frozen lakes (i.e., ice and snow), their effects on shallow depths have been considered in both bathymetry maps, as explained in Section 5.2.1.4 and Appendix H.

The maps reveal that at the time of the surveys, Valentine Lake [Fig. 5.8] is half as deep as the surveyed section of Victoria Lake [Fig. 5.9]. It is noted that Victoria Lake is a hydroelectric reservoir which results in frequent fluctuations in its water level, however, throughout the duration of this study, they remained adequately consistent (Section 5.2.2.1) to use an average value for the terrain correction. Valentine Lake varies in depth up to 24 metres and exhibits a general trend of increasing depth towards the centre and shallowing from approximately 10 metres to zero in approach of the shorelines. The southwest-northeast shores shelve quickly (within 100 metres) to nearly 10 metres depth and two deeper troughs are observed, within the centre of the two main trends of the lake shores. The deepest section is observed to the south of the lake’s centre, which extends linearly to the southwest and northeast, maintaining depths above 11 metres. To the north-northwest is an additional 11-to-16-metre-deep section that approaches the northern coastline. Victoria Lake presents a similar pattern, deeper throughout the centre of the lake and shallower towards the shores, which is a common expectation of lakes, particularly relatively young ones, like those in this study. Maximum depths of 50 metres are seen to the south and southwest of the map and again, appear to extend linearly to the east, west and along the northwestern arm, sustaining depths above 24 metres. The most consistent regions of shallow water levels are seen in the vicinity of the current Valentine Gold camp, near UTM (488000 m, 5354000 m) and at the northwestern most tip of the northern arm, where for the last roughly 2.5 kilometres, central depths are 16 metres or less.

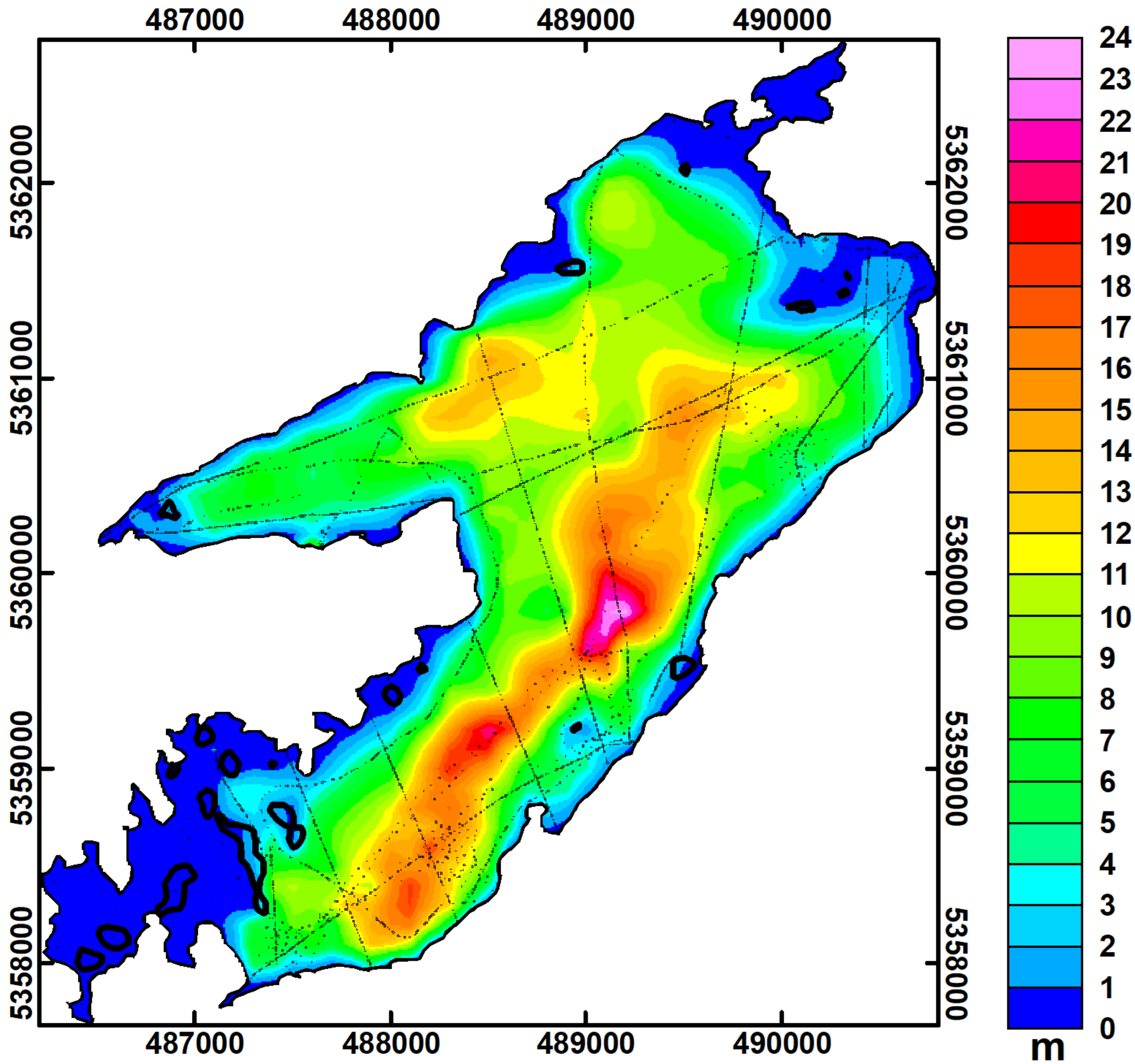

Figure 5.8: Bathymetry map of Valentine Lake with the data measurement locations shown as dotted black lines. The gridding method was minimum curvature with a cell size of 100 metres, cells to extend data beyond set to 2. The colour method was linear and any interpolated data extending outside of the lake boundary (coastline) was masked.

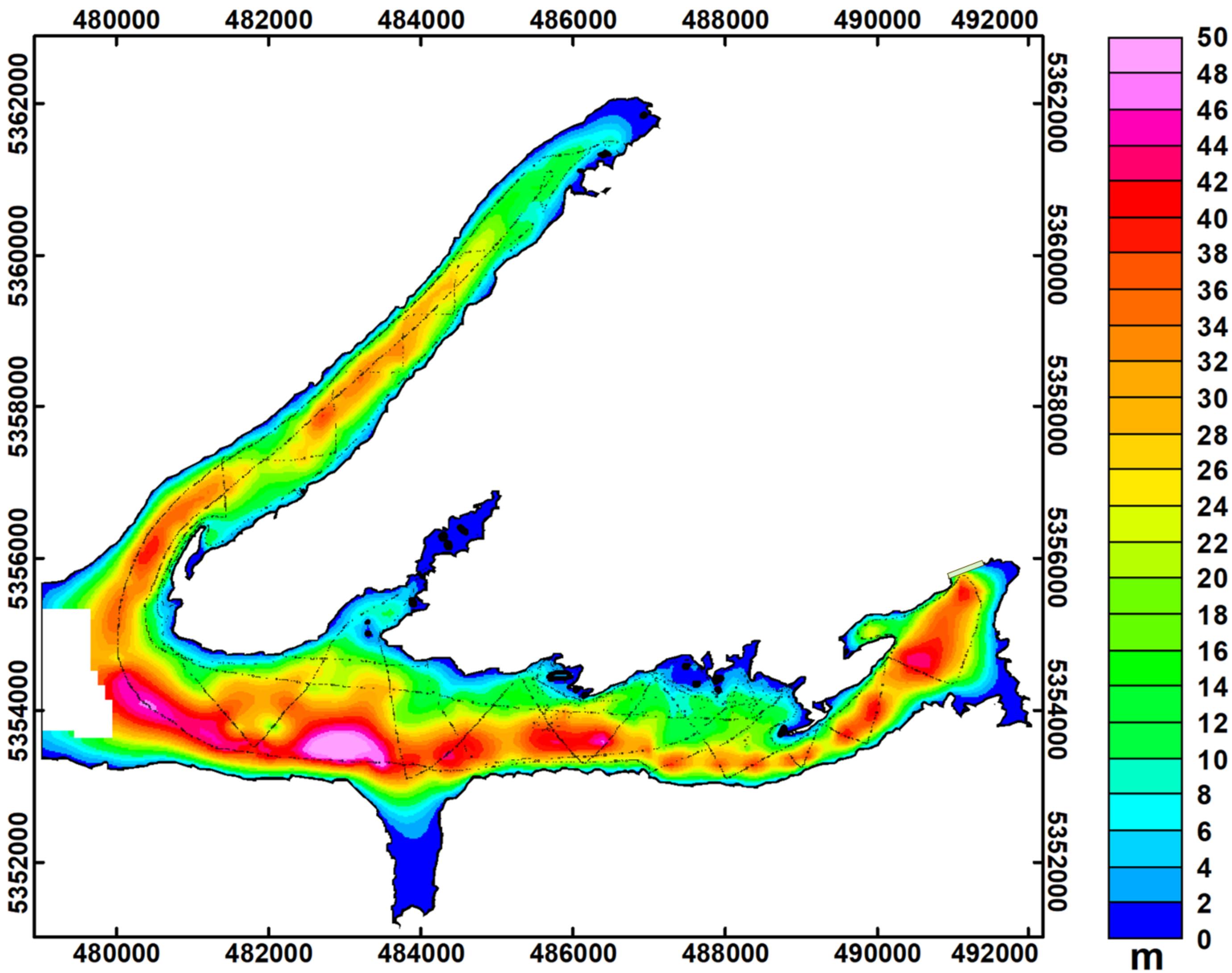

Figure 5.9: Bathymetry map of Victoria Lake with the data measurement locations shown as dotted black lines. The dam location is marked by a light green rectangle on the eastern tip of the lake (near 491000 m E, 535600 m N). The gridding method was minimum curvature with a cell size of 100 metres, cells to extend data beyond set to 2. The colour method was linear and any interpolated data extending outside of the lake boundary (coastline) was masked.

6 DISCUSSION AND CONCLUSIONS

In mineral exploration, the objective is to locate and develop significant mineral resources to advance prospective deposits through to production. Exploration at the Valentine Gold Project has advanced significantly over the past ten years, following acquisition by the growth-oriented gold development company, *Marathon Gold Corporation*. Since 2011, extensive drilling efforts have facilitated the discovery of five major orogenic gold deposits, namely, Leprechaun, Sprite, Berry, Marathon, and Victory [Fig. 2.2]. While drilling has proven effective in expanding the resources at the VGP, it is optimal to combine it with other geological or geophysical techniques that can enhance the pursuit by defining subsurface targets which enables less exploratory drilling and more directed drilling focused on increasing ounces. Directed at pursuing this strategy, several geophysical methods commonly employed in mineral exploration were carried out over in the property, including induced-polarization (IP), ground magnetics and seismic surveys, however, they provided minimal insight on prospective zones of mineralization.

Motivated by the poor outcome of the previous methods, this study conducted gravity surveys targeted at providing practical knowledge into the subsurface extent of the gold-bearing alteration zone. Additionally, GPR surveys (supplemented by sonar) were completed to assist with the ongoing mine development plans by mapping bogs as prospective sites of future infrastructure and gaining insight on water reserves. The results, presented as residual Bouguer [Fig. 4.11], hypsometry [Fig. 5.7] and bathymetry maps [Figs. 5.8, 5.9] were successful in achieving these goals, suggesting that these methods can be successfully applied to similar hydrothermal deposits in Newfoundland and other places in the world.

6.1 GEOLOGICAL INTERPRETATIONS

To corroborate the suggested lithological analysis of the gravity anomalies previously described in Section 4.3.1, the residual Bouguer anomaly was rendered semi-transparent and overlaid onto the local geology map of the Valentine Lake Property presented in Section 2.2 [Fig. 2.2] for direct comparison.

Upon initial comparison with the local geology map [Fig. 6.1] it is evident that the northeast-southwest thin linear negative gravity anomaly spanning the central to southwest region of the map (~ 492000 m E, 5360000 m N to ~ 487000 m E, 5356000 m N) corresponds to the location of the Valentine Lake Thrust Fault (shear zone) and known areas of mineralization (QTP-veining; yellow/green stars), within the porphyry unit of the Valentine Lake Intrusive Complex, which from Table 2.1, have an average density of ρ_{avg} = *2.65 g/cm*^{3}. The elongated gravity high to the south-southeast and parallel with low gravity corridor (~ 493000 m E, 5360000 m N to ~ 489000 m E, 5356000 m N) corresponds to the relatively dense Rogerson Lake Conglomerate (Tbl. 2.1; ρ_{avg} = *2.76 g/cm*^{3}), however it is observed to span further towards the southeast into a generalized unit of siliciclastic sediments (*i.e.*, breccia, conglomerate, sandstone, siltstone, and shale), which is reasonable given the assumption of ρ_{avg} = *2.72 g/cm*^{3} for the metasediment unit. Similarly, the oval-shaped gravity high to the northwest of the alteration zone (~ 488000 m E, 5358500 m N) overlies primarily the Cambrian – Ordovician granitoid suites, and towards the east, the Precambrian VLIC trondhjemite and gabbro units. This is a strong anomaly, similar in magnitude to that associated with the anomaly in the northeast (~ 494000 m E, 5363500 m N), interpreted as due to a large gabbro unit of the VLIC (Section 4.3.1), which from Figure 6.2 and through communication with Project Manager, Adam Wall, is confirmed to extend in that direction. Having a density range of *2.70 – 3.50 g/cm^3* and an average density of ρ_{avg} = *3.03 g/*cm^3 (Telford et al., 1990), gabbro is significantly more dense than quartz porphyry (Tbl 2.1; ρ_{avg} = *2.69 g/cm^3*) and trondhjemite (Tbl 2.1; ρ_{avg} = *2.68 g/cm^3*). This suggests that the western body contains or is underlain by more than "minor" gabbro, as previously understood. Likewise, the elongated high directly to the north of the alteration zone (~ 492000 m E, 5361000 m N to ~ 490000 m E, 5359500 m N) concurs with the location of the more recently defined, large gabbro unit of the VLIC. To better understand the extent of this gabbro unit, a simplified geology map generated by former Project Manager, Tanya Tettelaar, is shown in Figure 6.2.

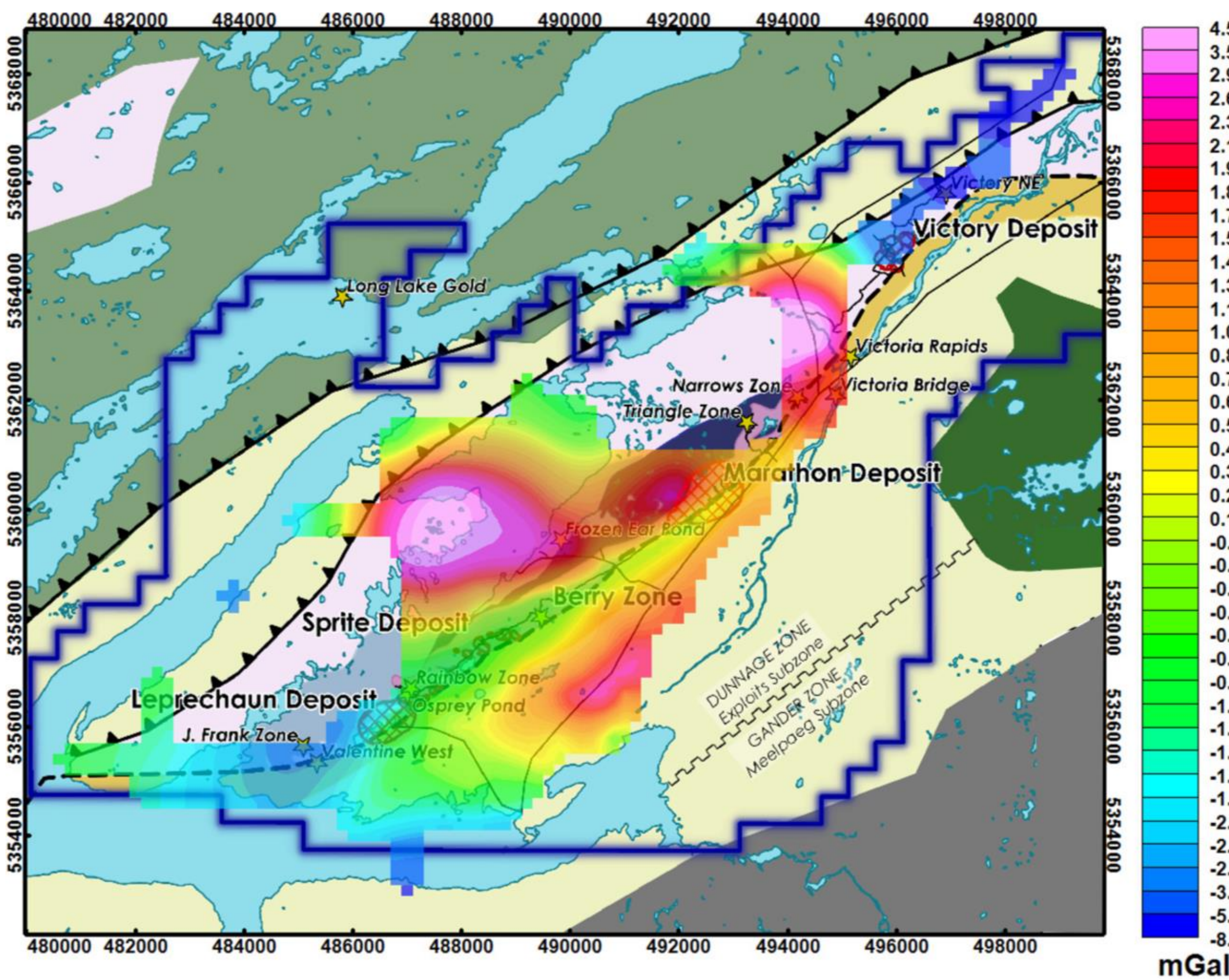

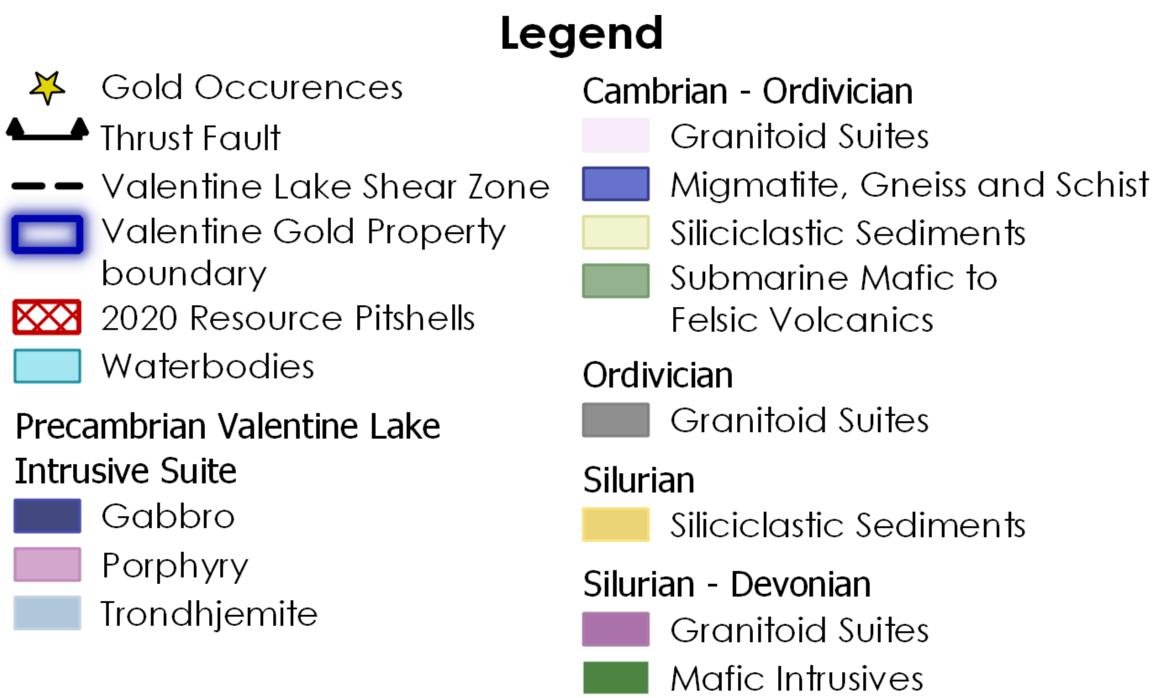

Figure 6.1: Semi-transparent residual Bouguer anomaly superimposed onto the local geology map of the Valentine Gold Project (from Marathon Gold Corporation, 2021) for comparative analysis.

The simplified geology map of the VGP [Fig. 6.2] exposes the full extent of a large gabbro unit, which is observed to extend further towards the west, across Valentine Lake and to the northeast into Victoria southwest. Recent drilling in the Marathon Waste Dump agrees with this regional mapping, confirming that the observed gravity highs to the northwest, north and northeast of the linear low gravity anomaly are associated with this extensive gabbro unit.

Upon further examination of Figure 6.2, it is observed that the thin gravity low is strongly correlated with the quartz eye porphyry (QEP) unit wedged between the gabbro to the north and the conglomerate and metasediments to the south, tapering out toward the northeast as the QEP is pinched out almost entirely. Therefore, it is likely that the low gravity signature is associated with the QEP and trondhjemite units as a whole and not necessarily just the alteration zone. It is thought that at the current scale, it would be difficult to distinguish between the altered and unaltered units.

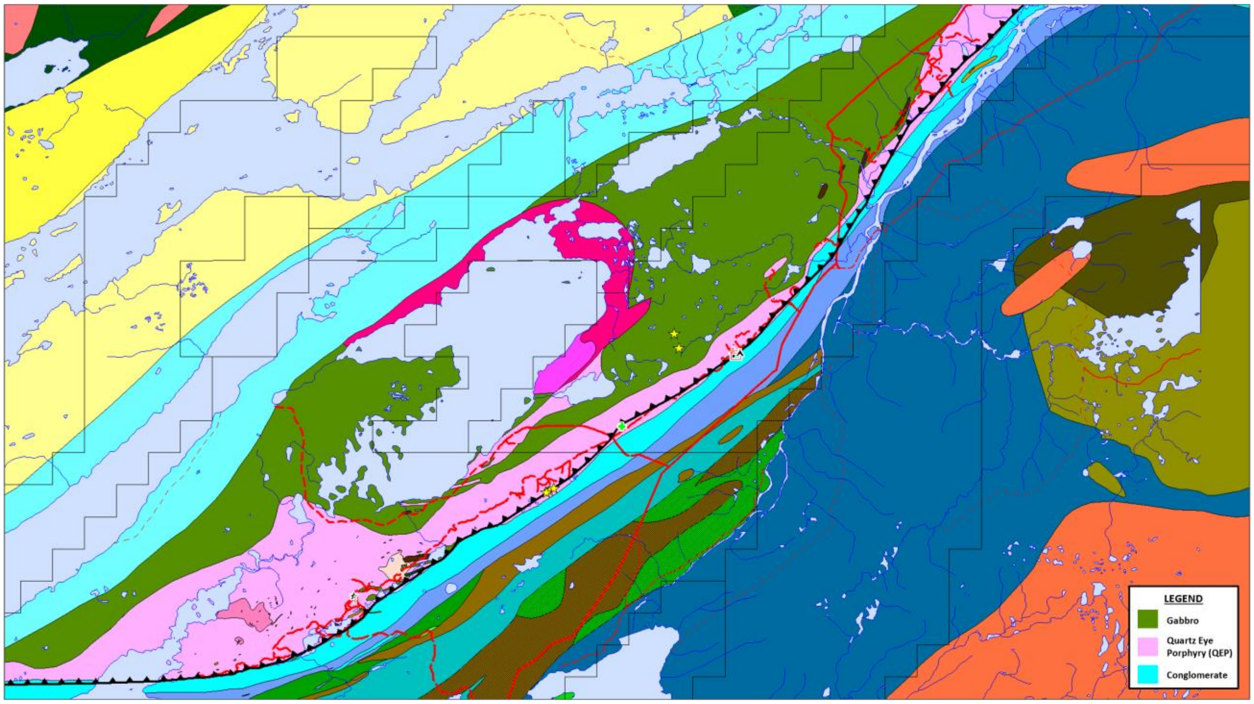

Figure 6.2: Simplified geology map of the Valentine Lake Property generated by former Marathon Project Manager, Tanya Tettelaar, which reveals the full extent of a large gabbro unit (from Marathon Gold Corporation, 2021).

6.2 MINERALIZED ZONE MODELS

To further compare the gravity responses obtained in this study and the 2018 modelling of the alteration zone (Appendix A) with the known areas of mineralization at the Valentine Gold Project, a model of the mineralized zones generated by *Marathon Gold Corporation* is presented in Figure 6.3. Upon examination, it can be considered that the width and locations of the Berry and Leprechaun deposits agree within reason with the suggested 400-metre-wide alteration zone modelled in Appendix A. This suggests that gravity surveys could help discover new zones/deposits which could help extend the future mine life.

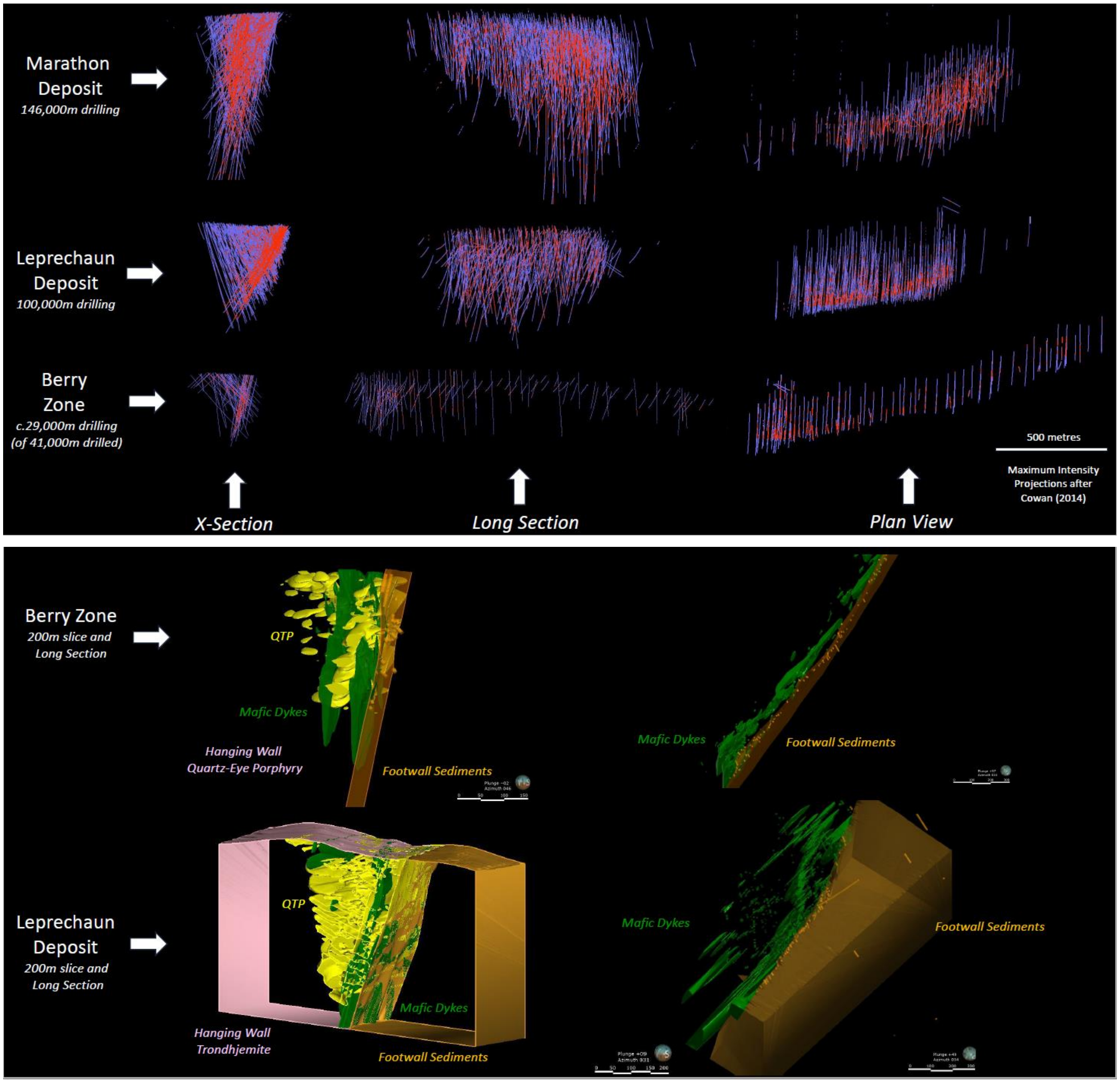

Figure 6.3: Top: Gold mineralization distribution at the Marathon, Leprechaun and Berry deposits. Bottom: 3D modelling of the Berry and Leprechaun deposits (from Marathon Gold Corporation, 2020).

6.3 CONCLUSIONS

Incorporating new geophysical techniques and associated data with pre-existing knowledge of the Valentine Gold Project to potentially discover new prospects and enhance future mine development has been the foundation of this research. Gravity surveys were executed to delineate the alteration zones within the host rocks which contain the gold, and GPR was used for gravity corrections, to map bogs which may be sites for future mine infrastructure and, together with sonar, for surveying water resources.

Results from the 2018 preliminary gravity and GPR surveys at the Valentine Lake Property suggested that both techniques were suitable for their aims in surveying the property. Therefore, this study comprised extensive fieldwork throughout 2019 and 2020 to acquire 184 lines of GPR data over 8 priority bogs, 42 square kilometres of sonar data over Valentine and Victoria Lakes and a 22 line-kilometre property-wide gravity survey. Bog hypsometry maps showcased thin to moderate overburden thicknesses up to 4.8 metres, while the bathymetry map of Victoria Lake included depths up to 50 metres and that of Valentine Lake was observed to vary in depth up to 24 metres. The residual Bouguer gravity map defined a long, narrow (few hundred metres) negative (-1.7 mGal) gravity anomaly interpreted to partially represent the gold-bearing zone of hydrothermal alteration. While the only method to determine the true extent and gain a profound understanding of the deposits is through additional drilling, the results of the gravity survey could aid in discovering new potential zones which may lead to additional ounces through drilling. The results of the GPR surveys will aid in determining the scope of groundworks required for the placement of tailings ponds and other superstructure as *Marathon Gold Corporation* initiates construction in 2022 and further advances the property through to production in 2023.

REFERENCES

Alsadi, H.N., and Baban, E.N. 2014. Introduction to Gravity Exploration Method: First Edition. University of Sulaimani, Sulaimaniyah, Kurdistan Region.

Annan, A.P. 2005. Chapter 11: Ground Penetrating Radar. *In* Near-Surface Geophysics. Society of Exploration Geophysicists, Tulsa, OK. SEG Library [online]. Available from https://library.seg.org/doi/10.1190/1.9781560801719.ch11 [cited 10 April 2019].

Annan, A.P. 2003. Ground Penetrating Radar Principles, Procedures and Applications. Sensors and Software Inc., Mississauga, ON. pp. 286.

Blakely, R.J. 1995. Potential Theory in Gravity and Magnetic Applications. Cambridge University Press, Cambridge, UK.

Barbour, D.M. 1999. Assessment Report on Geological, Geochemical, Trenching and Diamond Drilling Exploration for 1999 Submission for the Anglo-Newfoundland Development Company Limited Charter and Reid Lots 227 and 229 in the Valentine Lake Area, Central Newfoundland. Mountain Lake Resources Inc.

Brown, M. 2012. Gravity. *In* ESS 403 – Global Tectonics Course Webpage, Washington University [online]. Available from http://courses.washington.edu/ess403/ESS_403/Lectures_files/gravityppt.pdf [cited 20 November 2019].

Colman-Sadd, S.P., Hayes, J.P. and Knight, I. 1990. Geology of the Island of Newfoundland. Newfoundland Department of Mines and Energy, Geological Survey Branch, Map 90-01.

Creasey, D.J. 1976. Sonar Methods. *In* Remote Sensing for Environmental Sciences. Ecological Studies. *Edited by* E. Schanda. Springer-Verlag Berlin, Heidelberg, BW. pp. 277–303.

Daniels, D.J. 2004. Ground Penetrating Radar: Second Edition. The Institution of Electrical Engineers, London, UK.

Daniels, J.J. 2000. Ground Penetrating Radar Fundamentals. Department of Geological Sciences, The Ohio State University, Columbus, OH.

Dentith, M., and Mudge, S.T. 2014. Geophysics for the Mineral Exploration Geoscientist, Cambridge University Press, Cambridge, ENG. pp. 438.

Dunsworth, S., Capps, N., and Tettelaar, T. 2017. Assessment Report of Diamond Core Drilling, Seismic Surveying, Environmental Studies and Road Repair and Maintenance, Valentine Lake Property, Central Newfoundland. Marathon Gold Corporation, Toronto, ON.

European Space Agency (ESA). 2021. Earth Online: Gravity in detail [online]. Available from https://earth.esa.int/web/guest/missions/esa-operational-eo-missions/goce/content/-/asset_publisher/TA2e/content/gravity-in-detail-5728#_101_INSTANCE_TA2e_matmp [cited 28 January 2021].

Evans, D.T.W., and Wilson M. 1994. Epigenetic Gold Occurrences in the Eastern Dunnage Zone, Newfoundland: Preliminary Stable-Isotope Results. Report 94-1, Newfoundland Department of Mines and Energy, Geological Survey Branch, St. John's, NL.

Evans, D.T.W., Kean, B.F., and Dunning, G.R. 1990. Geological Studies, Victoria Lake Group, Central Newfoundland. *In* Current Research (1990), Report 02-1, Newfoundland Department of Mines and Energy, Geological Survey Branch, St. John's, NL.

GeoSci. 2018. Geophysical Surveys – Ground Penetrating Radar: Data [online]. Available from https://em.geosci.xyz/content/geophysical_surveys/gpr/data.html [cited 31 May 2021].

Geosoft Incorporated. 2015. Montaj Gravity and Terrain Correction How-To-Guide. Geosoft Inc., Toronto, ON.

Gibson, P.J., and George, D.M. 2003. Environmental Applications of Geophysical Surveying Techniques. Nova Science Publishers Inc., New York, NY.

Government of Canada. 2020. Natural Resources Canada [online]. Available from Data – Stations – Gravity (CGSN): https://webapp.geod.nrcan.gc.ca/geod/data-donnees/station/cgsn.php?id=99131999 [cited 12 February 2021].

Government of Canada. 2015. Natural Resources Canada [online]. Available from Tools and Applications: https://webapp.geod.nrcan.gc.ca/geod/tools-outils/ppp/php?locale=en [cited 2 February 2021].

Gowans, R.M., Murawhi C., and Stubens, T.C. 2012. Technical Report on the Updated Mineral Resource Estimate for the Leprechaun Gold Deposit, Valentine Lake Gold Project, Central Newfoundland, Canada. Micon International Limited, Toronto, ON.

Griffiths, D.J. 1999. Introduction to Electrodynamics. Prentice Hall, Hoboken, NJ.

Hickin, A. 2003. Ground penetrating radar (GPR) and fluvial placers in tropical setting, Maple Creek, Guyana. M.Sc. thesis, School of Earth and Ocean Sciences, University of Victoria, Victoria, BC.

Hodges, R.P. 2010. Underwater Acoustics: Analysis, Design and Performance of Sonar. Wiley, Hoboken, NJ.

Hrabi, B. 2014. Structural Geology Investigation of the Valentine Lake Gold Project, Newfoundland. SRK Consulting (Canada) Inc. Toronto. ON.

Jol, H.M. 2008. Ground Penetrating Radar: Theory and Applications. Elsevier Science, Amsterdam, NL.

Kane, M.F. 1962. A comprehensive system of terrain corrections using a digital computer. Geophysics, **27** (4): 455-462.

Kruse, S. 2020. Structural Analysis of the Valentine Gold Project. Terrane Geoscience Inc. Fredericton, NB.

Leitch, A.M. 2017. Degrees of accuracy: Visiting experts test Memorial's absolute gravity reference station. Available from the Gazette: Campus and Community, Memorial University of Newfoundland, St. John's, NL.

Lincoln, N., Farmer, R., Eccles, R., and Deering, D.D. 2018. Preliminary Economic Assessment of the Valentine Lake Gold Project, Newfoundland NL, Canada. Technical Report, Lycopodium Minerals Canada Ltd, Mississauga, ON.

Longman, I.M. 1959. Formulas for Computing the Tidal Accelerations Due to the Moon and Sun. Journal of Geophysical Research, **65**: 540-552.

Lorrain, P., Dale, R.C., and Lorrain, F. 1987. Electromagnetic Fields and Waves: Including Electric Circuits. W.H. Freeman and Company, New York, NY.

Marathon Gold Corporation. 2021. Updated figures provided by Project Manager, Adam Wall.

Marathon Gold Corporation. 2020. Valentine Gold Project: Geology [online]. Available from https://www.marathon-gold.com/ [cited 10 November 2020].

Marathon Gold Corporation. 2020. PowerPoint Presentation: Developing the Valentine Gold Project in Newfoundland and Labrador [online]. Available from https://www.marathon-gold.com/ [cited 08 September 2020].

Melvin, W.L., and Scheer, J.A. 2014. Principles of Modern Radar: Radar Applications, Volume 3. Institution of Engineering and Technology, Stevenage, ENG.

Melanson, D., and Parks, C. 2019. Marathon Gold: Valentine Mine. Final Report on LiDAR Survey. Aethon Aerial Solutions, Burlington, ON.

Murahwi, C. 2017. Technical Report on the Mineral Resource Estimate of the Valentine Lake Gold Project, Newfoundland, Canada. Micon International Limited, Toronto, ON.

Nagy, D. 1962. The prism method for terrain corrections using digital computers. Pure and Applied Geophysics (*PAGEOPH*), Dominion Observatory, Ottawa, ON. **63**: 31-39.

National Oceanic and Atmospheric Administration (NOAA). 2020. What is Sonar? [online]. Available from https://oceanservice.noaa.gov/facts/sonar.html [cited 15 September 2020].

NovAtel Inc. 2015. An Introduction to GNSS: GPS, GLONASS, BeiDou, Galileo and other Global Navigation Satellite Systems: Second Edition. NovAtel Inc. Calgary, AB.

Pawluk, C. 2010. Geophysical Survey Logistics Report, Valentine Lake Project. C-99. Insight Geophysics Inc., Oakville, ON.

Piercey, S.J., Squires, G.C., and Brace, T.D., 2014. Lithostratigraphic, Hydrothermal, and Tectonic Setting of the Boundary Volcanogenic Massive Sulfide Deposit, Newfoundland Appalachians, Canada: Formation by Subseafloor Replacement in a Cambrian Rifted Arc. Economic Geology. **109** (3): 661-687.

Scintrex Limited. 2009. CG-5 Scintrex Autograv System Operation Manual. Scintrex Limited, Concord, ON.

Sensors and Software Inc. 2020. pulseEKKO Ultra Receiver: For the GPR Professional [online]. Available from https://www.sensoft.ca/wp-content/uploads/2020/02/pulseEKKO-Ultra-receiver.pdf [cited 10 May 2021].

Sensors and Software Inc. 2019. Ground Penetrating Radar [online]. Available from https://www.sensoft.ca/ [cited 5 April 2019].

Speight, J.G. 2015. Exploration: Gravity Methods. *In* Subsea and Deepwater Oil and Gas Science and Technology. CD & W Inc., Laramie, Wyoming, US. pp. 107-126.

Telford, W.M., Geldart, L.P., and Sheriff, R.E. 1990. Applied Geophysics: Second Edition. Cambridge University Press, Cambridge, UK.

Tettelaar, T., and Dunsworth, S. 2015. Supplementary Assessment Report of Diamond Core Drilling, Prospecting, Trenching, Channel Sampling, Trench Rehabilitation, Geological Trench Mapping, Line Cutting, Ground Magnetometer Survey, Environmental Studies, and Road Repair and Maintenance. Marathon Gold Corporation, Toronto, ON.

Topcon Corporation. 2014. Topcon Dual Frequency GNSS Receiver [online]. Available from https://topconpositioning.com/products/gnss/receivers/hiper-v [cited 27 January 2021].

Trimble Incorporated. 2017. All About GPS Tutorial: Code-Phase GPS vs. Carrier-Phase GPS [online]. Available from https://www.trimble.com/gps_tutorial/sub_phases.aspx [cited 14 September 2020].

Van Sickle, J. 2015. GPS for Land Surveyors: Fourth Edition. CRC Press, Boca Raton, FL.

Wall, A. 2017. Delineating the Alteration Zone at the Big Easy Prospect using Geophysical Methods. M.Sc. thesis, Department of Earth Sciences, Memorial University of Newfoundland, St. John's, NL.

Webster, B., and Jelemic, A., 2012. Geophysical Report on Clarity3D DSIP Surveys Over the Valentine Lake Gold Project, Leprechaun Deposit. JVX Ltd., Richmond Hill, ON.

Woods, G. 2009. 2005-2008 Exploration Programs, Valentine Lake Gold District, A Joint Venture with Richmont Mines Inc., central Newfoundland, NTS 12A/06 and 12A/07.

Valverde-Vaquero, P., and Van Staal C.R. 2001. Relationships Between the Dunnage-Gander Zones in the Victoria Lake-Peter Strides Pond Area. *In* Current Research, Report 02-1, Newfoundland Department of Mines and Energy, Geological Survey Branch, St. John's, NL.

Van Staal C.R., Valverde-Vaquero, P., Zagorevski, A., Rogers, N., Lissenberg, C.J., and McNicoll, V.J. 2005. Geology, Victoria Lake, Newfoundland and Labrador. Geological Survey of Canada, Open File 1667, scale 1:50000.

APPENDIX A

2018 PRELIMINARY REPORT:

PROOF-OF-CONCEPT GEOPHYSICAL SURVEYS AT THE VALENTINE GOLD PROJECT

Valentine Lake Report on Preliminary Geophysical Surveys

Alison Leitch August 2018

Preamble

Dr. Alison Leitch and undergraduate geophysics student Stephanie Abbott visited the Valentine Gold Marathon property on June 1 to 3, 2018, to carry out preliminary geophysical surveys. The purposes of the surveys were to:

1) Find out where and whether geophysical surveys such as magnetics, gravity, GPR, sonar, DCR, EM31, RTK and drone mapping would be feasible over the property.

2) Ascertain whether drilling noise would interfere with gravity surveys.

3) Carry out a preliminary gravity survey over the alteration zone to see whether it had a measurable signature; carry out necessary companion RTK survey.

4) Carry out a preliminary GPR survey over a bog to see whether it could map bog thickness.

5) Test new design of bog corer and obtain bog core samples for lab measurements, particularly water content.

6) Carry out a preliminary EM31 survey over a bog to see how well it measured bog properties.

Surveys

June 1: Establish gravity reference station LAUNDRY at base camp
Tour property to view terrain and rocks
Gravity survey over cut line L17200
Carry out gravity drift calibration under cabin

June 2: One line of GPR and EM31 over Berry Zone
Collected bog core samples with bog corer
Start gravity survey on road to Frozen Ear
RTK survey of gravity stations

June 3: Complete gravity survey over Frozen Ear road
Carry out gravity survey over Leprechaun Pond road
RTK survey

Results

1. Geophysical Surveys and Terrain

The terrain is varied with in places thick trees with mossy, spongy undergrowth, rocky outcrops, bogs, ponds, and dirt roads, some only traversable with ATVs. The cut lines are somewhat overgrown and difficult to traverse. The mulch lines are difficult to walk through. The rocks, both sheared sediments and altered igneous, appear highly silicic. This influences feasibility of geophysical surveys as follows.

***Magnetics*: ** Our magnetometer can be carried easily wherever anyone can walk, so fill-in or extra magnetic surveys could be carried out. We have gradiometry capabilities – to measure vertical magnetic gradient – but that is awkward under trees because of the extra height of the sensor stack. The only caveat is that the GPS on the magnetometer might not receive good signals under trees, so there would have to be quality control on positioning and, for example, fiduciary flags at known points. The mulch lines would be best surveyed over packed snow, with snowshoes. We could possibly also tow the magnetometer behind a snowmobile, over bogs, for example, but it would have to be a long tow line to reduce the effect of the magnetic noise of the engine.

***Gravity*:** The gravity meter performed very well in all environments. All measurements were repeatable and precise. In the mossy, boggy ground under the trees it was necessary to dig up some ground cover in order to place the instrument tripod on a firm surface. On the gravel roads, readings could be taken very quickly (~2 minutes). On the cut lines it was much slower (~12 minutes) because of the need to prepare the site (and sometimes to find the line). Also, Marathon's old RTK performed poorly under the trees, and it is essential in gravity surveys to know the elevation within less than 3 cm. This requires a solid 'fix' from the RTK. Another problem with gravity along the cut lines was not knowing the depth of the soil layer above bedrock, given that this layer appears highly organic so significantly less dense than bedrock.

Given this, and the silicic nature of the rocks, the recommendation is to carry out gravity surveys at, say, 50 to 100 m spacing on all the roads and tracks throughout the property to obtain a broad scale gravity map. If there was sufficient ice cover in the winter, gravity surveys could be carried out over the ponds. It would be good to extend the survey beyond the property boundaries for several km at coarser resolution. The aim would be to map the subsurface extent of the alteration zone. If the results looked promising, targeted surveys through less hospitable environments could be carried out.

***GPR*:** GPR works very well on bogs and ponds. The surveys are easier in the winter: we have sleds and skis for fast acquisition of GPR information over frozen bogs and ponds. Our RTK can be attached to the GPR for precise positioning. Summer surveys over bogs, using a SmartCart, are possible but much more strenuous and time-consuming because of the bushy growth and puddles. Our system can see down about 35 m in fresh water and can distinguish soft mud from bedrock.

It would not be practical to do GPR on the cut lines: they are too rough. Therefore, some other method of finding depth to bedrock (e.g., bog corer) would have to be used if wanting to do gravity. GPR *might* work on the mulch lines if they were covered with packed snow in the winter.

***Sonar*:** For deeper water or (even slightly) salty water, we could use a sonar system on a boat in the summer to measure the bathymetry of ponds. We might need to get a dual frequency sonar, however, to distinguish mud from bedrock.

***DCR*:** The scales are generally too large for our system. It can only see down about 25 m. It might be useful as a supplement to GPR to look at subsurface of bogs if that was a particular target.

EM31**:** Sees down about 6 m. Might be useful to supplement GPR if bog properties were of interest. For shallow bogs (< 2 m) differences in the conductivity and isotropy of underlying rock could be indicated.

RTK**:** Required for gravity survey.

Drone**:** Could be useful in mapping trenches, making topo maps, mapping bog vegetation (as clues to underground properties). We don't have one, but are interested in acquiring one, and have some local experts to consult.

2. Drilling Noise

Drilling noise is not a problem. We were concerned that the vibrations due to drilling might interfere with gravity surveys by introducing noise. This was not the case. We took readings on the road 75-100 m away from operating drill VL18-675, and the noise level was just as low as other readings elsewhere on the property.

3. Gravity Surveys

Variations in the density of the subsurface lead to small changes in the gravity measured on the surface. In order to detect these small changes, it is essential to allow for gravity variations due to other factors, including: elevation, instrument drift, latitude, 'Earth' tides (due to the Sun and Moon), terrain (nearby variations in elevation), and (sometimes) overburden and ocean tides. Once these are accounted for, the residual signal, called the '*Complete Bouguer anomaly*', indicates the density variations in the subsurface.

Three lines of gravity data were obtained: one along cut line L17200, one along Frozen Ear road and its extension, and one along Leprechaun road. All readings were repeatable and had low noise. In all cases there were considerable changes in elevation, so elevation and terrain corrections were required.

3.1 <u>*Gravity Base Station LAUNDRY*</u>

Since the CG-5 gravimeter measures relative, not absolute, gravity, and instrument drift is significant, it is necessary to set up a base station where repeat measurements can be taken at the beginning and end of every survey to check for any small changes (due to changes in the gravimeter spring) with time. To obtain absolute gravity, the base station can be 'tied in' to known stations in the *Canadian Gravity Standardized Network* (CGSN). There are CGSN stations in St. John's, Clarenville and Springdale.

We set up a local base station called *LAUNDRY* at the Marathon base camp between the laundry and the women's bunk house. The exact location is 5.5 m from the woman's bunk house veranda toward the laundry, on a line defined by the wall between the bunkhouse and the veranda.

From tie-ins with stations *CLARENVILLE* and *MURRAY* (in the basement of the Alexander Murray Building at MUN), taken coming and going to the base camp, the absolute gravity at *LAUNDRY* is:

$$g_{LAUNDRY} = 980838.6 \pm 0.15 \text{ mGal}$$

3.2 *Survey along cut line L17200 (1 June 2018)*

Figure A.1 shows a measurement being taken south of the dirt road on Line 17200. Unfortunately, the RTK used to get locations on the cut line could not get a good fix of location (in particular elevation) under the trees, so it was impossible to make essential corrections and these data are of limited use.

Figure A.1: Gravity measurement on cut line L17200. The gravimeter tripod is sitting on plastic pucks in a dug hole.

As shown in Figure A.2, the readings along L17200 are smooth and repeatable. Standard deviations for the measurements are typically 0.02 to 0.10 mGal. Two or three readings were taken at each station, and these were repeatable to within 0.004 mGal. Readings were taken at distance 0 (in the middle of the gravel road) at three separate times at the beginning, middle and end of the 5-hour survey: the data points are indistinguishable on the graph. Since elevation has the greatest effect on gravity, an approximate elevation scale is supplied on the right side of the graph.

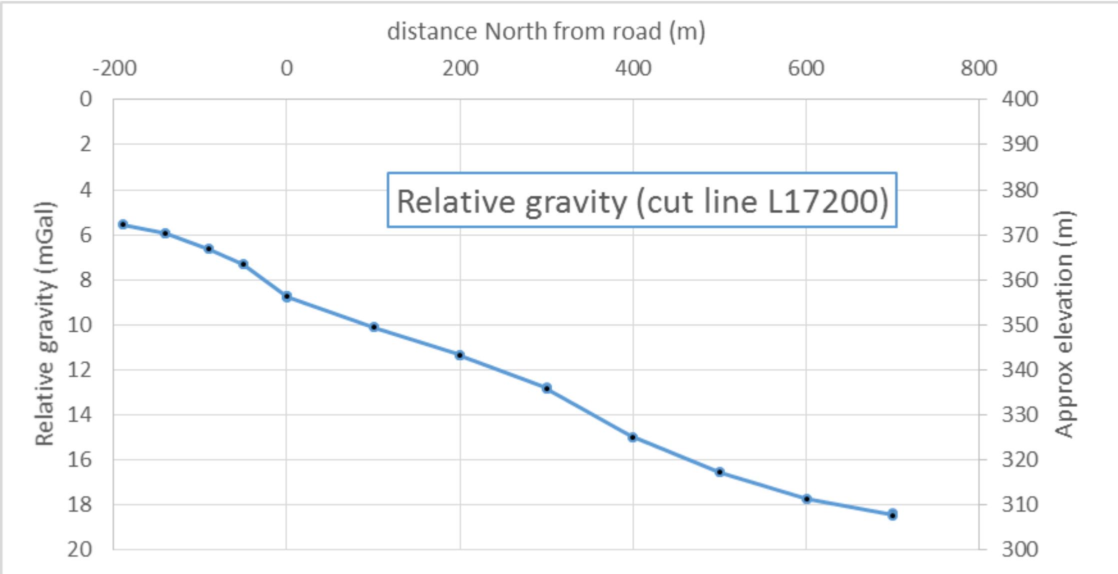

Figure A.2: Gravity relative to base station LAUNDRY. Data has been corrected for drift.

3.3 *Survey along Frozen Ear Road (2 & 3 June 2018)*

A survey was taken, mostly by Stephanie and Dylan Abbott, along Frozen Ear Road and its extension, for a distance of about 3 km at 100 m spacings. Figure A.3 shows the operators taking a reading on the extension road. This survey was much easier and faster than the survey on the cut line, and there were few problems obtaining good locations with the RTK.

Figure A.3: Stephanie and Dylan taking a gravity measurement on the extension of Frozen Ear Road. This used to be a gravel road, now covered in grass.

The data were processed using the Gravity Extension Package on Oasis Montaj. Figure A.4 shows the path of the road (UTM's) and the elevation as a function of Easting. The complete Bouguer anomaly is shown in Figure A.5. The shape of the curve is more significant than the absolute values. The variation along the line is 1.6 mGal. This is a small number, emphasizing that terrain corrections (which are between 0.6 and 0.9 mGal) must be calculated in this environment. However, this difference is well above the measurement uncertainty (about 0.1 to 0.2 mGal), indicating that gravity measurements can detect variations in subsurface density, and so potentially could be used to map the alteration zone.

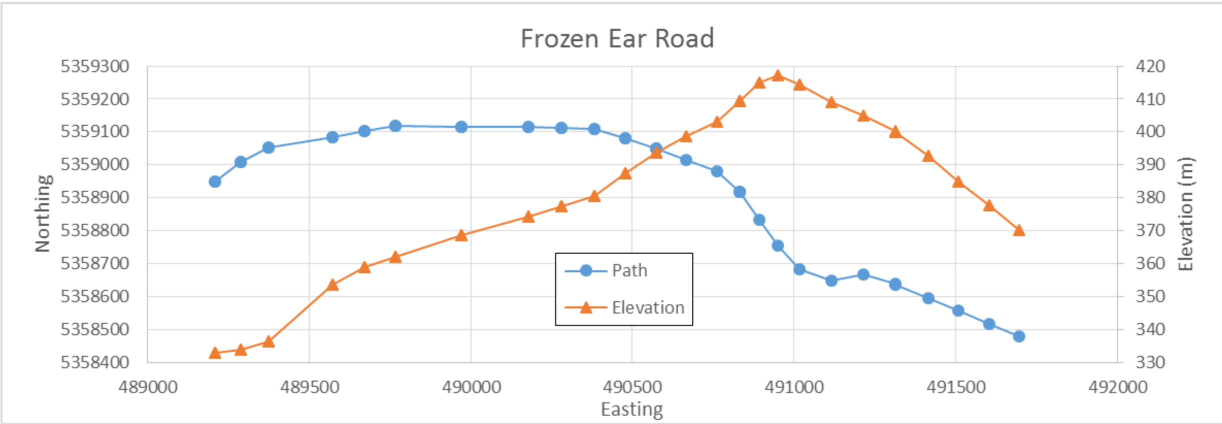

Figure A.4: Location of the gravity stations along Frozen Ear Road, and the station elevations.

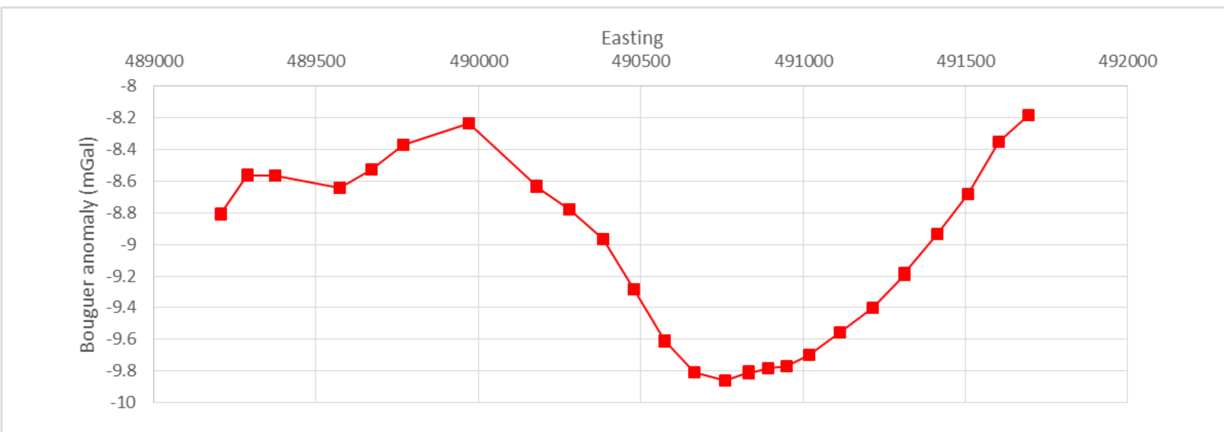

Figure A.5: Complete Bouguer anomaly along Frozen Ear Road.

3.4 *Forward modeling*

To further ascertain whether this gravity anomaly is consistent with the rock densities and general structure of the mineralized region, simple forward modeling of the gravity anomaly was carried out using the program *Potent*. The alteration zone was modeled as a steeply dipping slab with a uniform thickness and density anomaly. The thickness of the model slab was estimated from the width of the gravity anomaly, and the density deficit was informed by the densities of the main rock units on the Marathon property.

Densities of samples of the major rock units are shown in Figure A.6, and averages in Table A.1.

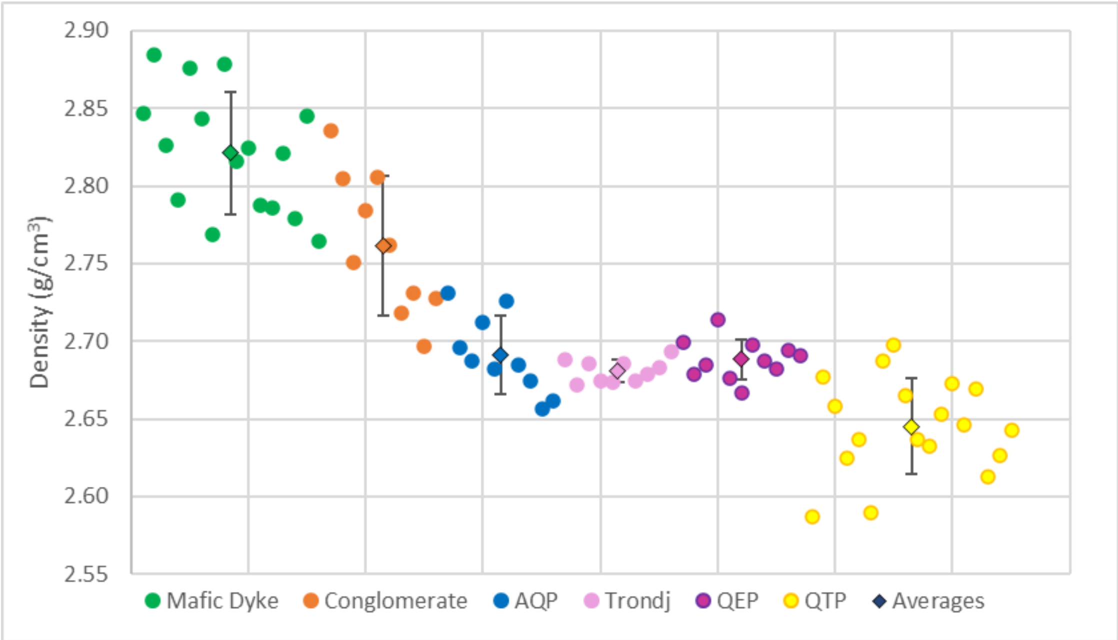

Figure A.6: Sample densities of key rock units on the Marathon Gold property provided by Project Manager, Adam Wall. Error bars show standard deviations. The QTP unit comprises samples of trondhjemite or QEP.

Table A.1: Averages and standard deviations for densities of unit samples shown in Figure A.6.

Lithological Unit	**Symbol Colour**	**Number of Samples**	**Density (g/cm^3)**	**Standard Deviation**
Mafic Dyke	Green	16	2.82	0.04
Conglomerate	Orange	10	2.76	0.05
Aphanitic Quartz Porphyry	Blue	10	2.69	0.03
Trondhjemite	Pink	10	2.68	0.01
Quartz Eye Porphyry	Purple	11	2.69	0.01
Quartz-Tourmaline-Pyrite	Yellow	18	2.65	0.03

As Figure A.6 indicates, there is a significant difference in the average densities of the different rock units, however also significant scatter. It must also be noted that in the drill cores the units are often interspersed: the alteration zone includes mafic dykes and unmineralized quartz porphyrys. Therefore, the average density of rocks within the alteration zone will not be as low as the QTP average, and the density contrast with surrounding units not as great. Nevertheless, the density differences in Figure A.6 and Table A.1 provide some constraints for forward modeling aimed at matching the anomaly profile in Figure A.5.

The density difference between the densest mafic dyke sample and the least dense QTP sample is 0.29 g/cm^3; between the average of the conglomerates and the QEP it is 0.07 g/cm^3; and between the average QTP (altered and mineralized unit) and the quartz porphyry units (QEP and AQP) it is 0.04 g/cm^3.

The width of the anomaly in Figure A.5 is about 1000 m. Since altered rocks are seen close to the surface, this suggests an alteration zone width of a few 100 m. Drilling indicates that mineralization extends several hundred meters in depth, and the interface between the mineralized region and the largely unmineralized conglomerate dips at about 70 degrees to the north west.

Figure A.7 illustrates two models with different widths, depths, and density deficits. The anomalies in both cases are narrower and stronger than observed.

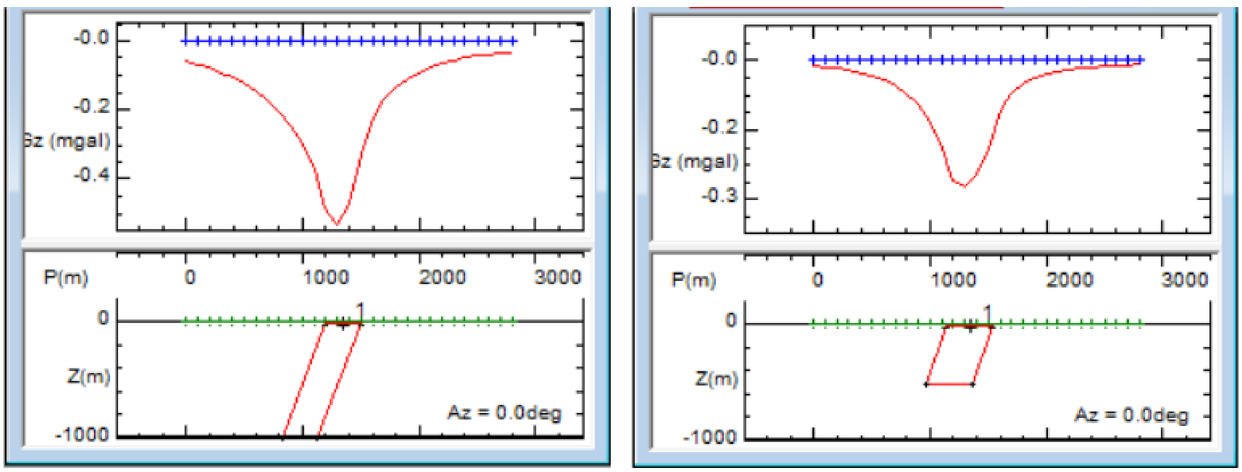

Figure A.7: Left: Top panel, gravitational anomaly due to slab shown in bottom panel, width 300 m, depth below surface 20 m, height 1000 m, density deficit 0.05 g/cm^3. Right: As for left for slab width 400 m, depth below surface 20 m, height 500 m, density deficit 0.03 g/cm^3. Distance on the x-axis is measured in metres from west to east.

The approximate width (~1000 m), magnitude (~0.16 mGal) and shape (steeper to the west) of the gravitational anomaly is matched in the model illustrated in Figure A.8, by a slab of width 400 m, depth 2000 m and density deficit 0.01 g/cm^3. It is noteworthy that a slab with a plausible geometry and this very modest density deficit can reproduce our results. This bodes well for the success of the method.

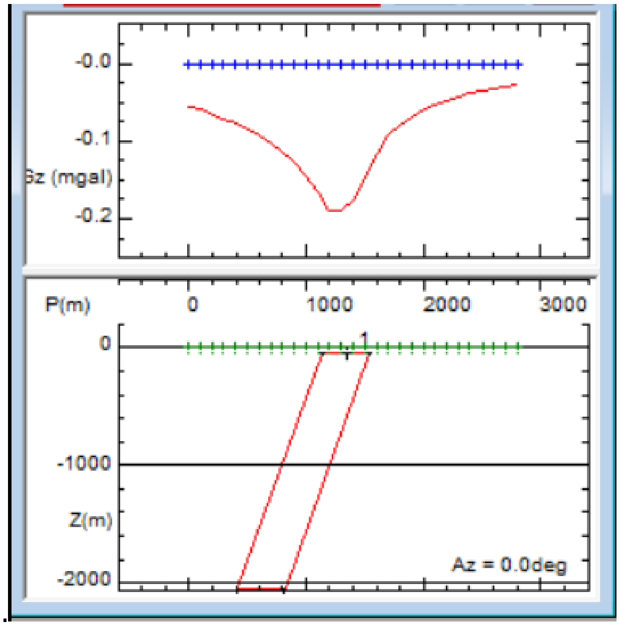

Figure A.8: Upper panel, calculated gravity anomaly of the slab outlined in the lower panel, with width 400m, depth below surface of 50 m, depth 2000 m and a density deficit of 0.01 g/cm^3.

3.5 *Survey along Leprechaun Road (3 June 2018)*

In the afternoon of 3 June, a short 500 m survey was taken along Leprechaun Road. Location, elevation and complete Bouguer anomaly are shown in Figure A.9. Along this short transect, the Bouguer anomaly varied systematically by 1.0 mGal. It is noteworthy that the absolute values of the anomaly are significantly different (by 8 mGal) from those of Frozen Ear Road. This indicates there are significant along-strike variations over the prospect that could be mapped with a gravity survey.

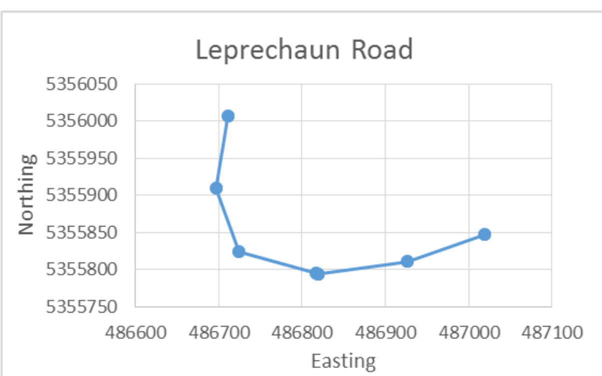

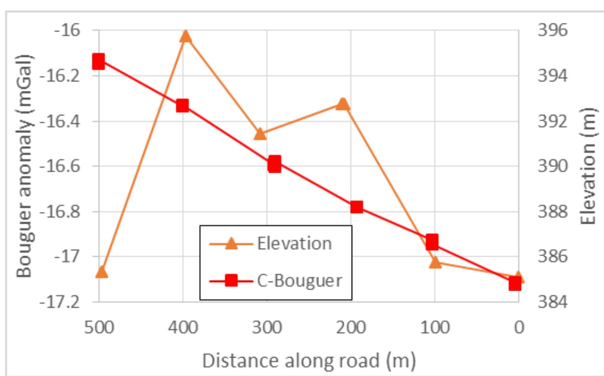

Figure A.9: Left: UTM locations of gravity measurements along Leprechaun Road. Right: Elevation and complete Bouguer anomaly as a function of distance along Leprechaun Road.

4. GPR Survey

We have a *Sensors & Software* EKKO-Pro system with three antennas: 250 MHz, 100 MHz, and 50 MHz, which 'see' down into the ground about 4 m, 10 m and 20 m respectively. Penetration depths in very fresh water are greater (~40 m for 50 MHz antennas) because of lack of scattering in a homogeneous medium like water. Bogs tend to be fairly homogeneous as well. Any salt (e.g., washed in road salt) severely restricts penetration of radar: GPR cannot see through conductors. Conductors within or below non-conducting material will produce a strong reflection.

We carried out a line of GPR across Berry Zone using 100 MHz antennas on the Smart Cart. A route was first scouted out because there were puddles of water on the bog. A 300 m line was measured out (Fig. A.10, left) and staked at 50 m intervals. Using a handheld device, GPS readings were taken at each stake position (Fig. A.10, right).

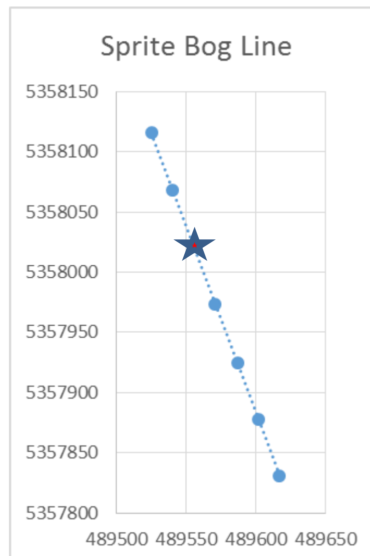

Figure A.10: Left: Dylan, Sarah and Stephanie setting up a N-S line across Berry Zone for GPR and EM31 profiles. Right: GPS points defining the GPR/EM31 profile line across Berry Zone. The star indicates the location of the bog sampling (Section 5 below).

The GPR was hauled and pushed across the bog (Fig. A.11) with some difficulty due to the vegetation. The antennas stick out past the wheels and catch: they are supposed to skim just above the surface. It is much easier to survey over snow or ice (or grass).

Figure A.11: Dylan Abbott pulled the GPR SmartCart holding 100 MHz antennas, with a rope arrangement around his hips, while Sarah or Adam pushed.

The GPR profile obtained (Fig. A.12) shows that the bottom of the bog is well resolved. The maximum depth, in the centre of the line, is 3 m, and the depth decreases to about 0.5 m at each end. The depth obtained using the Geography Department's bog probe (white line) agrees well with the calibrated depth from the GPR profile. The bottom interface features many hyperbolic features, and there are some such features a few dm above the interface. These hyperbolic features are caused by cobbles and boulders, suggesting the bottom of the bog is covered with glacial material. In the bog itself there is some subtle internal structure, particularly beneath about 1.5 m in the northern half of the profile. The deeper parts of the bog are slightly less water rich than the top (see also Fig. A.13). Small features above "0.0 m" depth are related to signals going between the antennas through the air or vegetation on top of the bog, and are not particularly significant.

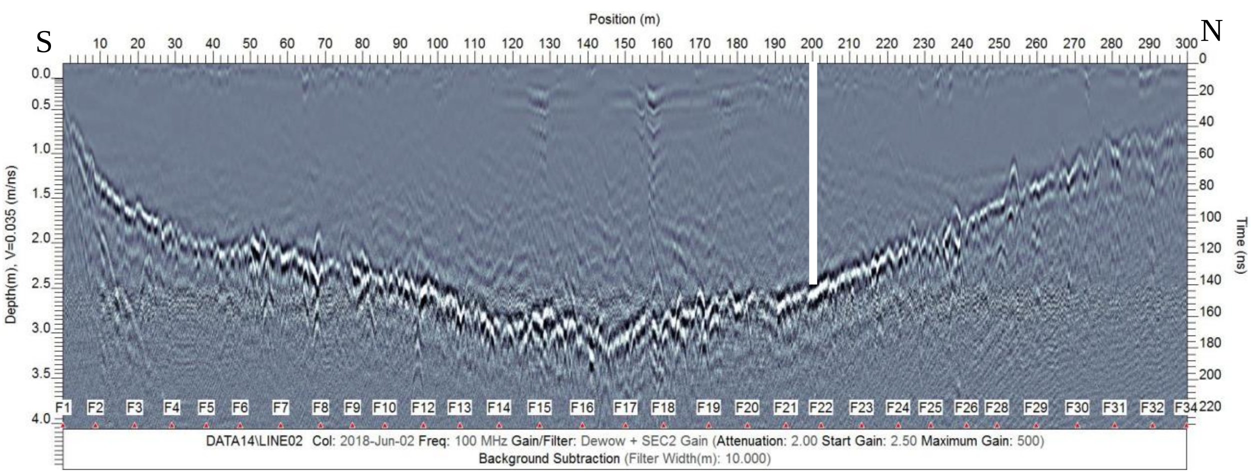

Figure A.12: GPR profile over the profile line. Depth scale based on a wave velocity of 0.035 m/ns, obtained from measuring the water content in the bog (Section 5).

5. Bog Sampling

GPR, like seismic, produces results in terms of the two-way travel time of the reflected signal pulse. To convert this to depth, the velocity of the pulse in the medium must be known. In overburden, the velocity depends strongly on the water content (Topp et al., 1980), so samples of the Berry Zone were obtained 100 m from the north end of the profile line.

We first tried out a wide-bore coring system developed by Joseph Pittman (B.Sc. Hons. student) and myself. Joey built the ‘bog cutter’ (Fig. A.13; top), which was used to cut through the roots at the top of the bog, creating a cylinder of cut bog: the core-catcher system (Fig. A.13; bottom) was then pushed down over the cut is to collect the bog cylinder. The advantage of the wide, plastic-encased core is that it can be run through our Multi-Scanner Core logger to obtain high resolution profile of density, and hence water content. As it happened, the bog cutter captured bog samples from the top of the bog. So, our system needs some modifications. We bagged bog cutter samples from the top half meter of the bog for water analysis.

We had also brought a ‘regular’ bog sampler, borrowed from the Geography Department (Fig. A.14). We were able to push this down until it hit the bottom of the bog (2.48 m) and obtained samples from the bottom 2 m of the bog.

Figure A.13: Top: Bog-cutter designed and built by Joey Pittman, containing material from the uppermost half meter of Berry Zone. Bottom: Plastic core liner with core-catcher, containing material from about 0.5 to 1 m depth in the bog.

Figure A.14: Bog corer (on loan from Geography Department), containing bog material from 1.0 m to 2.28 m depth.

To find the water content of the bog samples, the samples were weighed, placed in glass jars in an oven at 100 C overnight to dry out, and then weighed again. The results are shown in Figure A.15.

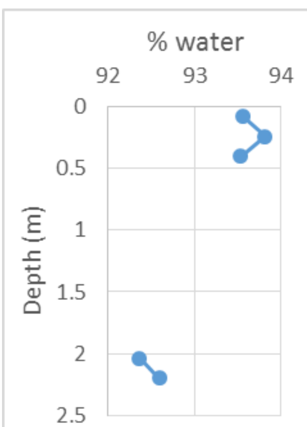

Figure A.15: Weight % fraction of water in bog samples taken from various depths of the Berry Zone at the location indicated by the star in Figure A.10 and the white line in the GPR profile, Figure A.12.

Using the formula from Topp et al. (1980) for dielectric constant vs water content for organic soils, the predicted EM wave velocity in the bog is 0.035 m/ns (that is, between 0.0350 and 0.0347). The GPR profile (Fig. A.12) uses this velocity for the depth scale.

6. EM31 Survey

The *Geonics* EM31 is a 'ground conductivity meter'. It consists of a long (3.66m = 12 foot) boom with a transmitter coil at one end, a receiver coil at the other end, and a control unit in the middle. It is disassembled into 3 sections for storage and transport (Fig. A.16) and assembled in the field. It can be carried by one person using a shoulder strap. It is calibrated to measure the electrical conductivity of a uniform subsurface when held about 1 meter above the surface ('hip height') and orientated in the usual, VMD (vertical magnetic dipole) orientation. In this orientation, the axes of the coils (and hence the magnetic dipole field the transmitter generates) are vertical, and it 'sees' about 6 m into the ground (Fig. A.17; left). It can be rotated along the boom axis to the HMD (horizontal magnetic dipole) orientation (Fig. A.17; right): in this orientation it 'sees' about 3 m into the ground, so comparing the two readings can indicate whether conductivity increases or decreases with depth. By taking multiple readings at different orientations and distance from the surface (hip and ground – laying the instrument on the ground – are the common ones) it is possible to determine the layer depth and conductivities of the ground, provided it is simple (i.e., layers are relatively flat and have constant conductivities).

Figure A.16: Stephanie carrying the disassembled EM31 in from the field survey.

Figure A.17: Students taking ground conductivity measurements with the EM31. Left: in the VMD orientation. Right: in the HMD orientation.

Isolated conductors, such as metal pipes, generate isolated peaks in the readings. These may be positive or negative, single or multiple, depending on the positions and geometries of the coils and the conductor. The magnitude of the reading is not meaningful however, the pattern of peaks can be used to find the location and perhaps the burial depth of the conductor.

The EM31 was carried along the same profile line as the GPR was, in Berry Zone, with readings taken every 10 m. First, the EM31 boom was held parallel to the line, and VMD and HMD readings were taken. Then, the EM31 boom was swung 90 degrees in the horizontal and held perpendicular to the line and VMD and HMD readings were taken. Comparing readings with the boom direction changed allows the user to check for anisotropy in the ground. Bogs are generally isotropic. Results are shown in Figure A.18.

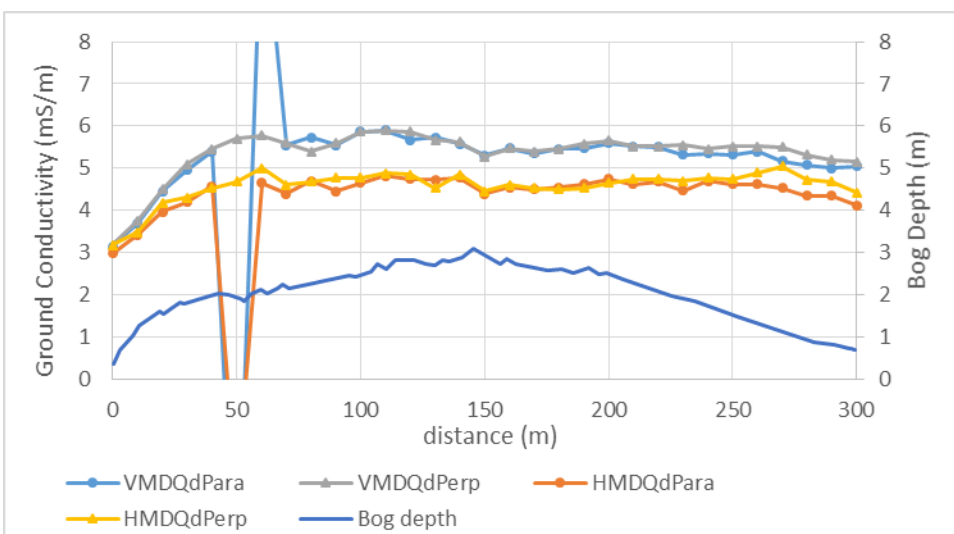

Figure A.18: EM31 ground conductivity measurements along S-N profile (Fig. A.10; right) over Berry Zone. Bog depth, extracted from the GPR data (Fig. A.12) is shown as the solid blue line.

The readings, between 3 and 6 mS/m are typical for a wet, clean, organic bog. The VMD ‘Para’ and ‘Perp’ are mostly very similar to each other, as are the HMD ‘Para’ and ‘Perp’ readings, indicating that, as expected, the bog is isotropic. There is a suggestion of difference in the north end of the line. Since the bog is less than 1.5 m deep here, this may be related to underlying rocks. The VMD readings are higher than the HMD readings, indicating that conductivity increases with depth. The shape of the profile appears to be influenced by bog depth. In the southern part of the profile, conductivity increases as bog depth increases suggesting the bog is more conductive than the underlying rock. The depth and conductivity profiles do not have identical shapes, however. The conductivity is highest at 110 m while the depth is highest at 145 m, and the conductivity in the north is higher than it is in the south for the same bog depth. This may be related to differences in the underlying rocks.

In the ‘Para’ readings for both VMD and HMD, there is an anomaly at 50 m distance. This looks like the signal of an isolated conductor. It would have to be orientated along the line, since it is not seen in the ‘Perp’ readings. Nothing very obvious is seen in the GPR, though there is a slight change in the bedrock depth and reflectivity. If of interest, this feature would have to be investigated further before conclusions could be drawn.

Summary

All geophysical techniques (gravity, GPR, EM31 and bog probe) performed well over the Valentine Lake prospect. *Memorial*’s CG-5 gravimeter could map gravity anomalies associated with subsurface density variations, as part of an MSc project. This would be best performed over roads and tracks, for logistical reasons. Across strike profiles showed moderate gravity signals: it is important to carry out corrections for terrain variations. Part of this would involve mapping the depth of nearby bodies of water and bogs. This mapping could be carried out using GPR.

Forward modeling indicated that an alteration zone with a modest density deficit, well within the density variations seen in the property’s lithological units, could be responsible for the gravity anomaly observed in this proof-of-concept survey.

GPR surveys over bogs and ponds may be useful for other purposes, such as determining the depth of soft overburden for drill rigs or water resource estimates.

Drone surveys (not undertaken in this visit) could also be useful, for obtaining detailed images for mapping trenches as well as obtaining topographic information in general.

Reference

Topp, G.C., Davis, J.L. and Annan, A.P. 1980. Electromagnetic Determination of Soil Water Content: Measurements in Coaxial Transmission Lines, Water Resources Research. **16** (3): 574 – 582.

APPENDIX B

GRAVITY REFERENCE STATIONS: EXACT LOCATION DESCRIPTIONS

1. <u>MURRAY</u> (Tied-In)

- **ER-1008** - Basement of the Alexander Murray Building at *Memorial University*
  - Located in the corner, on the concrete floor, to the right of a shelving unit, behind the left-swinging door leading into the neighbouring loading bay.

Gravity (CGSN) - 9913-1999

Station 1 of 1

Site Identification					
Name	Province	Unique Number	Classification	Status	Last Inspection
ST. JOHN'S	NL	9913-1999	Absolute Primary	Active	05/2017

Station Coordinates (Scaled)			
Latitude	Longitude	Elevation	Description
N47° 34' 21" ± 50.0 m	W52° 43' 56" ± 50.0 m	60.10 ± 1.00 m	MEMORIAL UNIVERSITY, SEISMIC VAULT

Gravimetric Information					
Adjustment Number	Gravity	Instrument Height	Gradient	Velocity	Epoch
0	980819.8311 ± 1.0000 mGal	0.91 m	0.266 mGal/m		

Station Description
The station is located in room SN1108 - Seismic Station, Physics, Science Building, Memorial University, St. John's, Newfoundland. Access is from the SW corner of the Science courtyard parking lot. Follow the Yellow Pedestrian Line, access tunnel Y4. The station is indicated by a small screw in the centre of the front left pier.

Government of Canada Gouvernement du Canada

Sketch

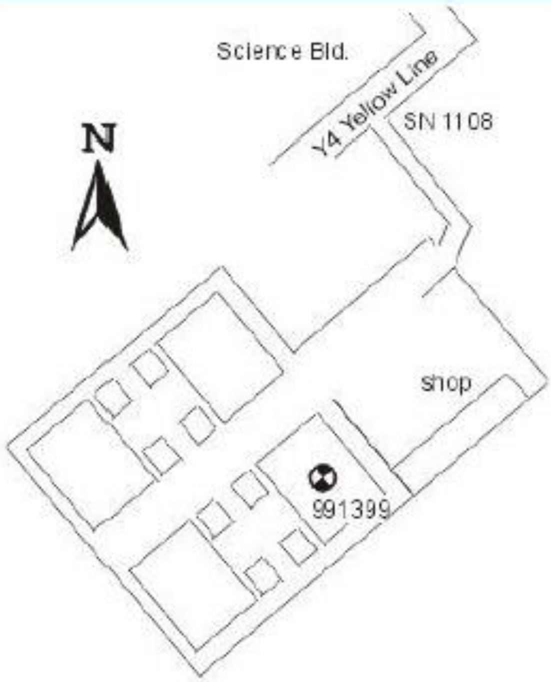

Distant View

Figure B.1: Detailed description of the registered CGSN reference gravity station at Memorial University used for absolute tie-in at MURRAY (retrieved from Government of Canada, 2020).

2. CLARENVILLE (CGSN)

- On the front step (concrete slab) of a commercial building (former Manpower Centre) adjacent to the Clarenville Court
  - The exact location is **30cm** from the glass window and **30cm** from the brick wall (right).

Gravity (CGSN) - 9210-1977

Station 1 of 1

Site Identification					
Name	Province	Unique Number	Classification	Status	Last Inspection
CLARENVILLE	NL	9210-1977	Secondary	Active	07/1977

Station Coordinates (Scaled)			
Latitude	Longitude	Elevation	Description
N48° 10' 15" ± 20.0 m	W53° 57' 43" ± 20.0 m	9.00 ± 1.00 m	MANPOWER CENTRE

Gravimetric Information					
Adjustment Number	Gravity	Instrument Height	Gradient	Velocity	Epoch
1978008	980900.3200 ± .0250 mGal	0.15 m	0.308 mGal/m		

Station Description
The station is located in Clarenville at the Canada Manpower Centre on the concrete floor of the entranceway, 38cm N of the edge of the brick wall of the entranceway. The station is monumented by an aluminum disc mounted horizontally.

Sketch

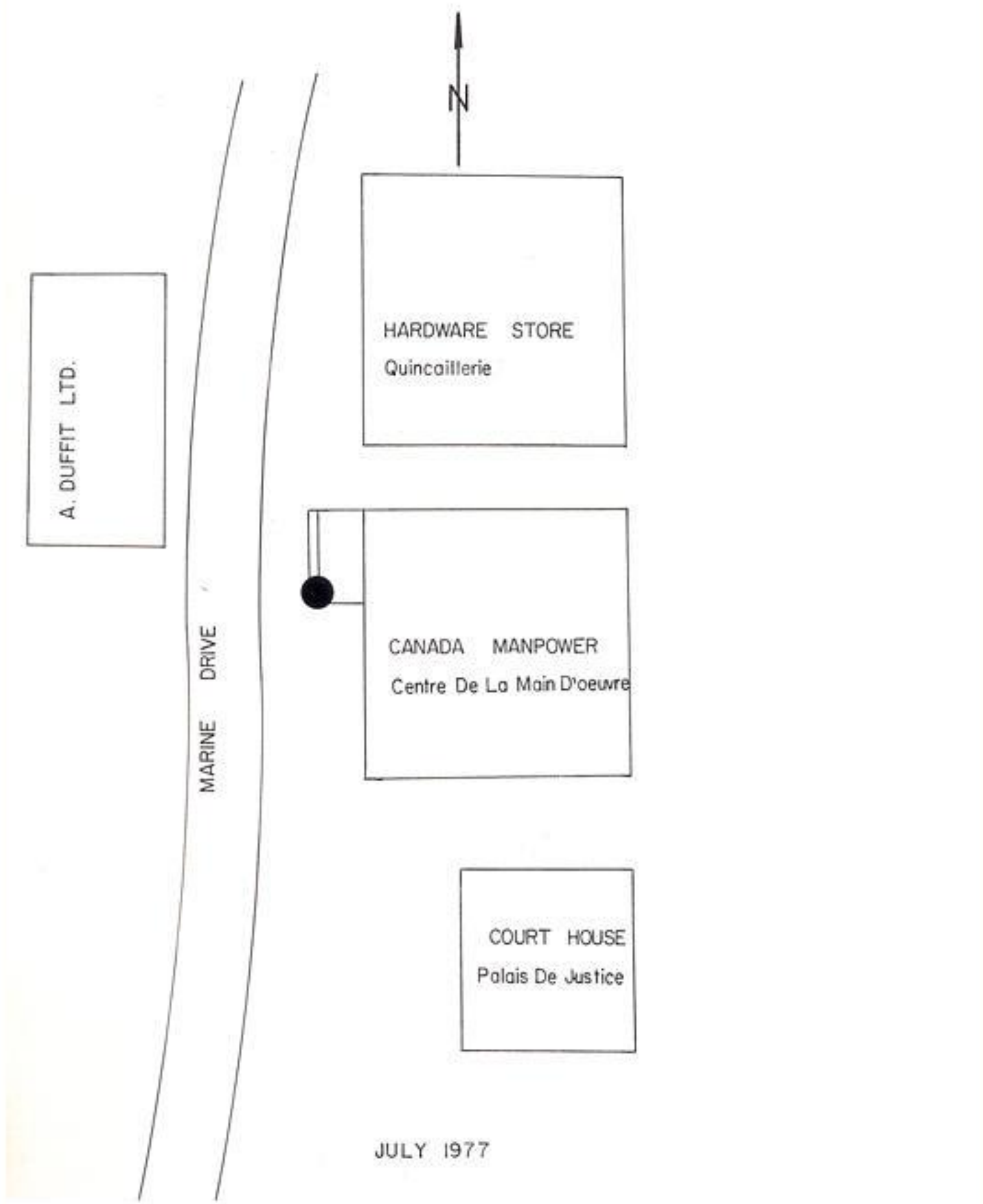
N
HARDWARE STORE
Quincaillerie
A. DUFFIT LTD.
MARINE DRIVE
CANADA MANPOWER
Centre De La Main D'oeuvre
COURT HOUSE
Palais De Justice
JULY 1977

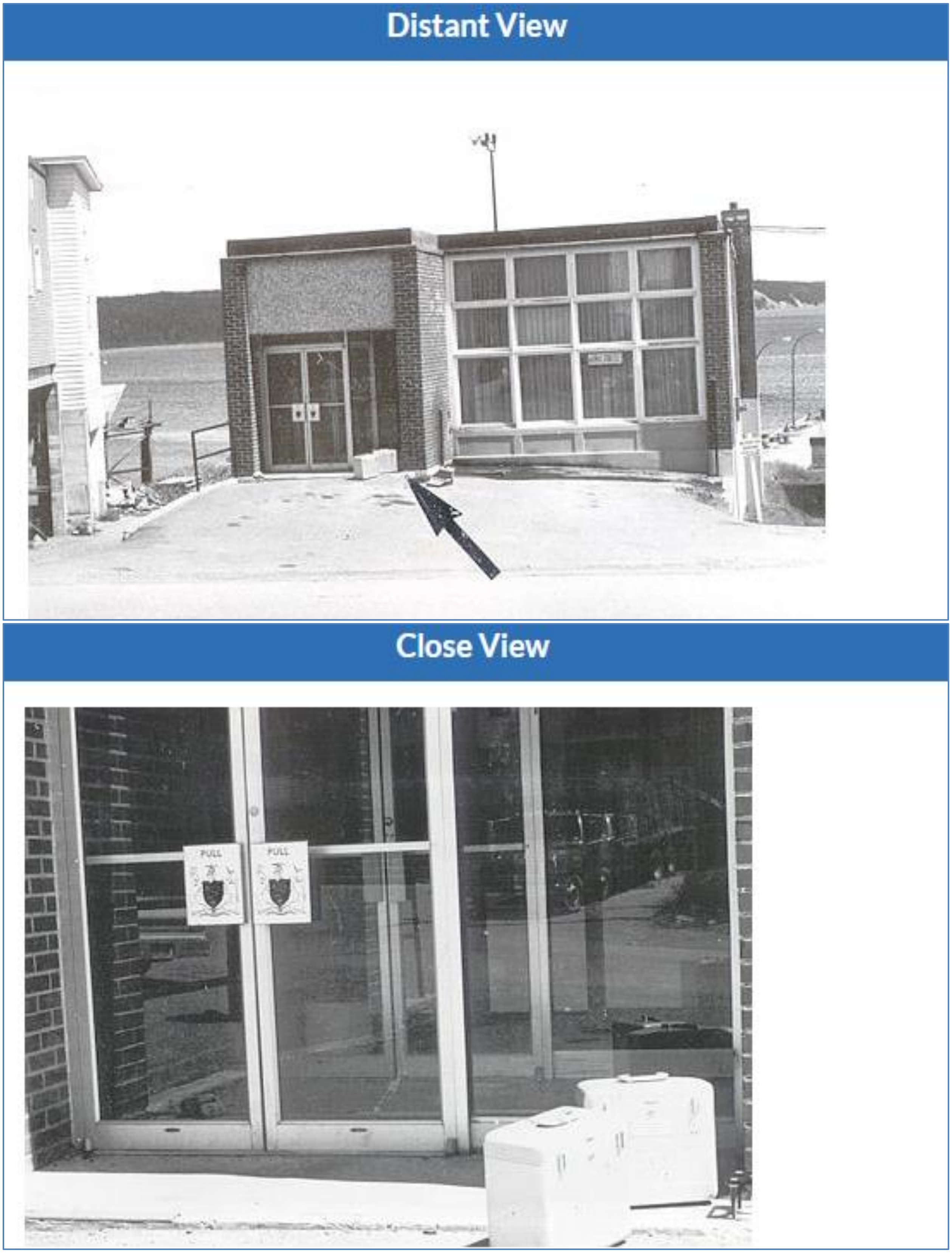

Figure B.2: Detailed description of the registered CGSN reference gravity station in Clarenville (retrieved from Government of Canada, 2020).

3. <u>CNA-GFW</u> (Tied-In)

- On the front step (concrete slab) of the College of the North Atlantic (CNA) Grand-Falls Windsor campus entrance to the left of the loading bay [Fig. B.3, top panel].
  - The exact location is **30cm** from the glass window and **30cm** from the brick wall, which is shown in the bottom panel of Figure B.3.

Figure B.3: <u>Top</u>: General location (orange "X") of the secondary reference station established in Grand-Falls Windsor for reader context (modified from Google Maps). <u>Bottom</u>: The exact base station location measured from the centre of the gravimeter tripod.

4. <u>MILLERTOWN</u> (Tied-In)

- In the gravel parking lot, to the left of C&S Variety convenience store in Millertown
  - The exact location is **1.5m** straight out from a metal electrical box on the left side of the building, just behind the wheelchair ramp [Fig. B.4].

Figure B.4: Location of the secondary reference station established in Millertown. Note that the arrow length is not to exact scale and the orange "X" is an approximate placement intended to help the reader understand the general location and surroundings (modified from Google Maps).

5. <u>LAUNDRY</u> (Local – Tied-In)

- In a gravel parking lot at the Valentine Gold Camp.
    - Exact location is **5.5m** from the right veranda railing of the female bunkhouse and directly across from the laundry room [Fig. B.5].

Figure B.5: <u>Right</u>: General location of the local base station LAUNDRY, established at the Valentine Gold camp. Note that the arrow length is not to exact scale and the orange "X" is an approximate placement for reader context. <u>Left</u>: Gravimeter sitting in the exact position, with a small amount of pink spray paint visible to the left of the front knob of the tripod.

APPENDIX C

LIDAR DATA, MAP GENERATION AND ANALYSIS

Lidar Data Overview and Map Creation: Valentine Gold Project, West-Central NL

By: Stephanie Abbott (M.Sc. Candidate)
and Marie Flanagan (Research Assistant)

FACULTY OF SCIENCE
Department of Earth Sciences

June 2020

This document provides an overview of LiDAR (Light Detection and Ranging) data acquired at *Marathon Gold Corporation's* Valentine Gold Project, by *Aethon Aerial Solutions* in partnership with *Newfoundland Helicopters*. The 63.8 km^2 project site is located in west-central Newfoundland, approximately 90 kilometres southeast of Deer Lake airport. The data summary and Oasis Montaj map generation workflow sections were written by Marie Flanagan, while the map itself was created by Stephanie Abbott, who also completed the LiDAR squares analysis.

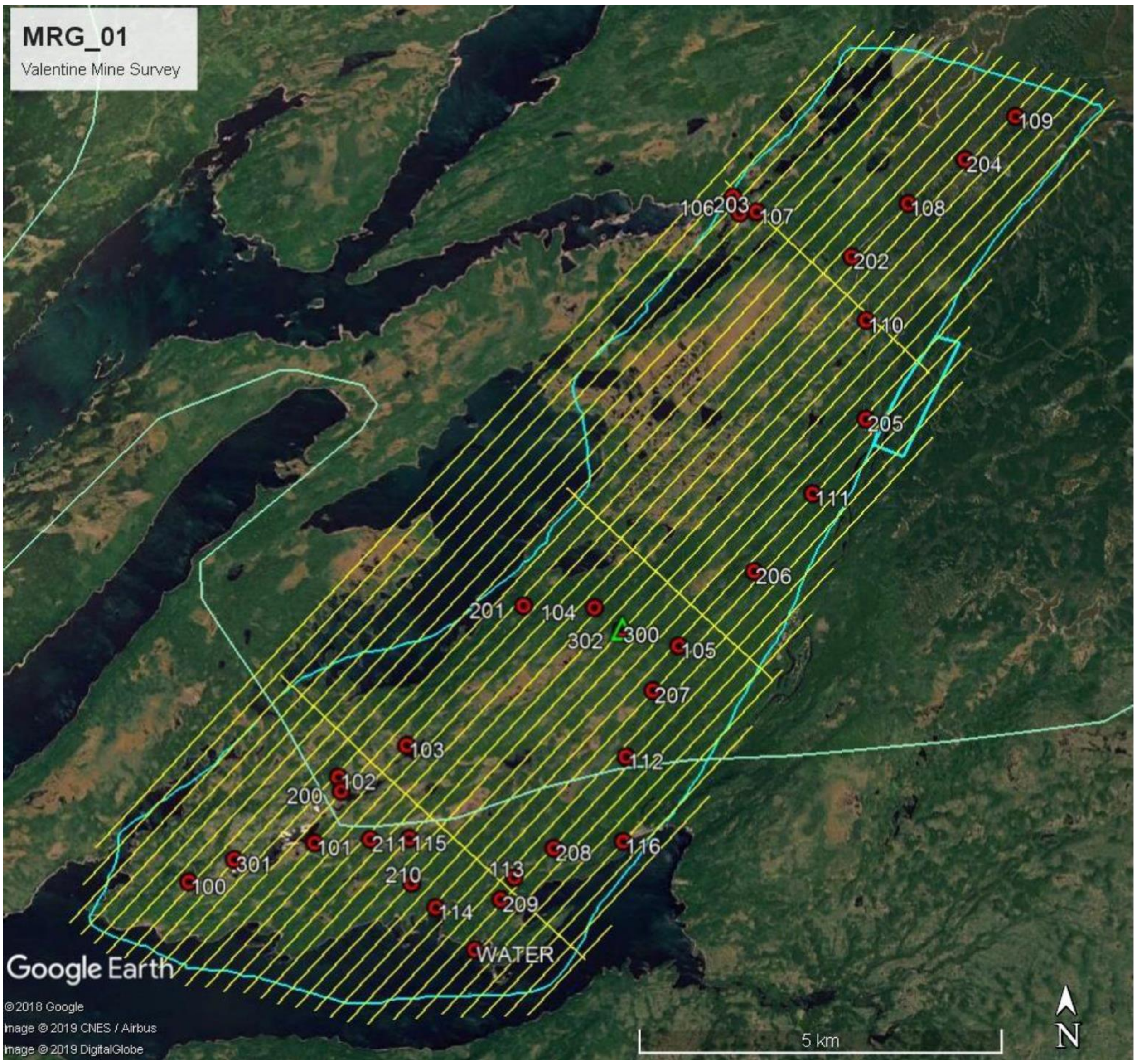

Figure C.1: Valentine Mine survey area flight lines (yellow), area of interest (light blue), GCPs (red markers) and base location (green triangle) overlain on Google Earth imagery (retrieved from Melanson and Parks, 2019).

The aerial survey was conducted on June 6th and 7th, 2019 using a Bell 206 helicopter, equipped with a Riegl VUX-1LR LiDAR scanner operating at 400kHz, for an overall ground point density of 20.3 points/m^3. The *Aethon* surveyors flew three, 31-line flights at 1000 ft AGL (above ground level), which are shown in Figure C.2. The helicopter flew at a ground speed of 40 knots while the Leica iCON GPS base station logged continuously at a 1 second interval (Melanson and Parks, 2019). Figure C.2 below displays the elevation over a priority section of the Valentine Lake Property, based on the acquired LiDAR data.

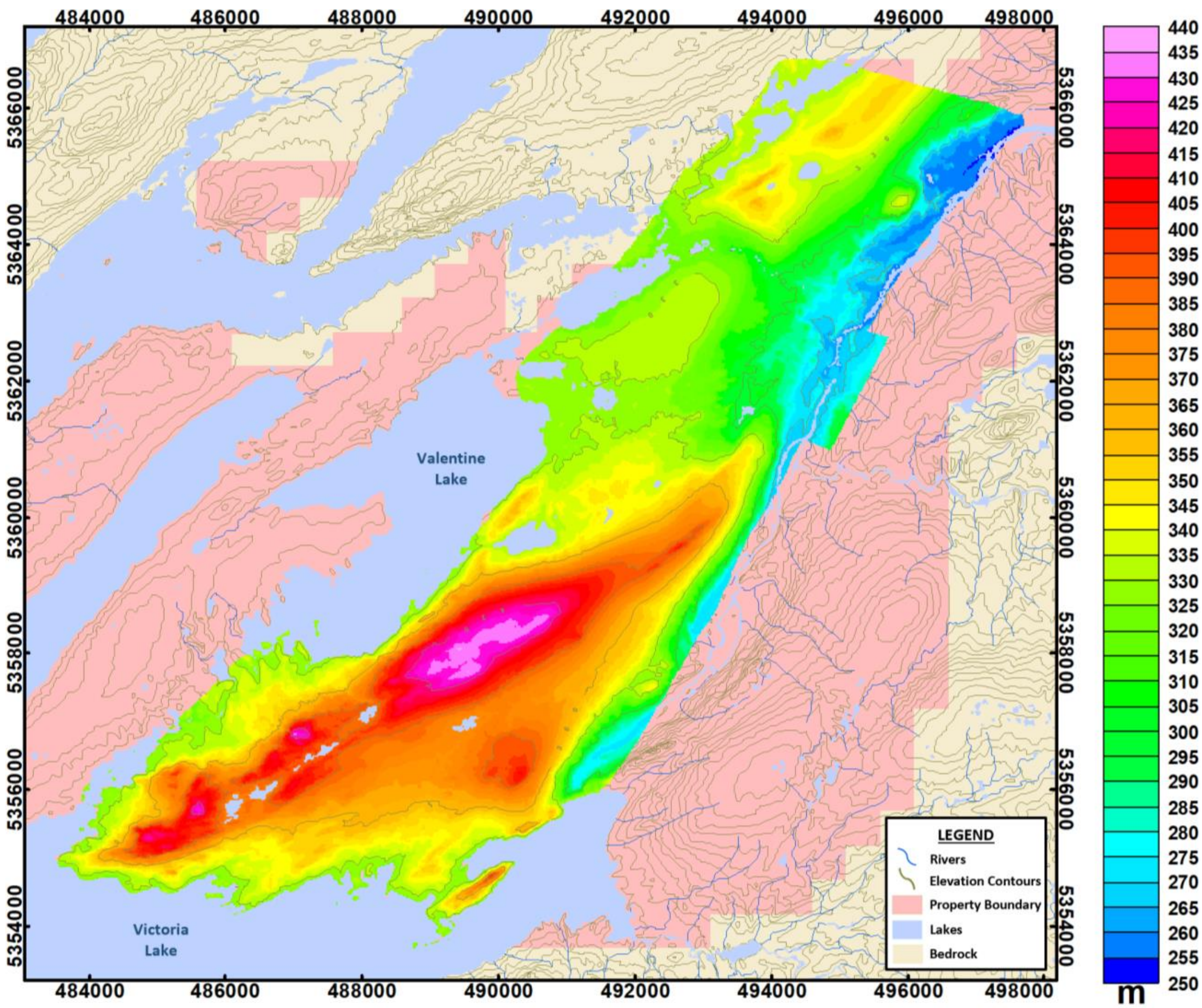

Figure C.2: LiDAR elevation map created using Oasis Montaj. The gridding method was minimum curvature, cell size was 5 metres, cells to extend beyond data was set to 0 and the colour method was linear. The contour interval within the LiDAR region was 30 metres, while outside was 10 metres.

The following section describes the source of the LiDAR data and a detailed explanation of the steps involved in the creation of the elevation map in Oasis Montaj.

DATA

Adam Wall, Senior Geologist at *Marathon Gold*, provided **306** individual **ASCII XYZ** files titled numerically from *"MRG_01 1m Grid Ground Tile–001"* to "*MRG_01 1m Grid Ground Tile–306*". Each file pertains to different contiguous area (tile) within the property, designed to represent a 500-metre x 500-metre square area sampled as 1 metre grids. Each XYZ file, which are Geosoft compatible, contained **Easting**, **Northing** and **Elevation** information with a vertical accuracy of 0.001 metres. To better evaluate the coverage and size of each LiDAR tile, the XYZ files were transferred into an Excel spreadsheet and a sample of these data are shown in Figure C.3. Through visual analysis, it was determined that the number of rows (*i.e.*, data points) in each range from 0 to 250000, with the 250000-point files corresponding to complete LiDAR tiles (*i.e.*, 500 metre x 500 metre squares) and any files containing less data points representing incomplete data "squares" (further discussed in the LiDAR "squares" analysis below).

Easting (m)	Northing (m)	Elevation (m)
493980.5	5366500.5	334.11
493981.5	5366500.5	333.97
493982.5	5366500.5	333.79
493983.5	5366500.5	333.72
493984.5	5366500.5	333.7
493985.5	5366500.5	333.55
493986.5	5366500.5	333.44
493987.5	5366500.5	333.22
493988.5	5366500.5	333.15
493989.5	5366500.5	333.01
493990.5	5366500.5	332.86
493991.5	5366500.5	332.68
493992.5	5366500.5	332.53
493993.5	5366500.5	332.32
493994.5	5366500.5	332.02

Table C.1: Sample data from LiDAR XYZ file "MRG_01 1m Grid Ground Tile – 001".

<u>GENERATING THE MAP</u>: OASIS MONTAJ

The following is a detailed list of instructions that describe how to create the LiDAR elevation map and export it in appropriate formats for further analysis:

1. **Create a folder to store the Oasis Project.**

2. **Open Oasis Montaj.**

<u>Note</u>: It is helpful to save (Click **Save Project** or **ctrl + S)** after each of the following steps.

3. Create a new project by clicking **File - New Project**. Assign it a distinguishable name and save it in the folder you have just created.

4. Create a new database by clicking **Database – New Database**. Give it an appropriate title. Make sure there are enough lines and channels available.

5. Import the data. Click **Database – Import – Geosoft XYZ…** Click **…** and select all sheets you would like to upload. Change '**Import Mode**' to Append. Click **OK**.

   Repeat this for every file you would like to add, when prompted '*Import data into the current database?*', select **Yes**.

6. Set coordinates. Click **Coordinates – Set Current X, Y, Z Coordinates**. Set **X** to *Easting*, **Y** to *Northing* and **Z** to *Elevation*.

7. Create the grid. Click **Grid and Image – Gridding – Minimum Curvature**. Pick **Elevation** for '*channel to grid*'. In the second line give it an appropriate name. Choose a reasonable cell size based on the size and sample interval of the dataset (in this case, 5m was chosen). Click **Advanced**. Select an appropriate '*Cells to extend beyond data*'. Here, this was set to 0, as this is ideal for such closely and evenly spaced data.

8. Create the map. Click **Grid and Image – Display on Map – Grid…**. For elevation maps, it is common to set the '*colour method*' as **linear**. Click **More** to adjust the contour interval, by assigning minimum and maximum values for the colour legend bar. You may have to come back to this after you have a better idea of these values.

If you are looking to re-open this map later in ArcMap, follow steps 9 to 11. If not, skip to step 12.

9. Duplicate Map. Click **Map – Duplicate Map…** assign an appropriate name (*i.e.*, '*Lidar Elevation for ArcMap*'). Select **Copy Current Contents**.

10. Create a new folder to save these files.

11. Export map. Click **Map** (tab at top of screen) > **Export…**

Select the *Output Format* as **GeoTIFF (*.tif)** and *Region to Export* as **Full Map**. Click **Screen** for best resolution. Click **OK**. Save it in the folder created in step 10.

Minimize or exit duplicated map and return to original.

12. Create a Base Map. Click **Map Tools – Base Map – Draw Base Map**. Set an appropriate map scale. In this case, 1:120000. This is to allow for legible UTM coordinates on the base map. Set appropriate margins (here, 1, 1, 1, 1, 1). Change '*Reference grid*' to **edge ticks**. Give map a title.

13. Move title to desired location.

14. Delete North Arrow and Scale Bar.

15. Add a legend. Click **Map Tools – Symbols – Colour Legend Bar…**. Make the title the unit (m). Click **Locate** and choose on the map where you would like it to be. Under **More**, click **Annotations**. Select **Post end values** (in this case, 250 and 430). Select **Location** to **'***At colour break'*. Adjust to desired size. Adjust to desired location.

Return to **Grid and Image – Display on Map – Grid… - More** to adjust the minimum and maximum contour interval values, if needed.

16. Add contours. Click **Map Tools – Contour – Contour…**. Select Multiples of levels. Pick appropriate smallest interval level (in this case, 30m). To label contours, click **Line Styles.** Select **Line weight-colour level 1** as *thin-black*. Click **Next**. Select **Line style level 1** as *solid*. Click **Next**. Select **Label level 1** as *Yes*. Click **Finish**. Click **OK**.

To change the contour line colour, click **Contour** under **Map Manager**. Double click the rectangle that appears. Right-click and click **Select All**. Right click again and click **Line Attributes…**

17. Adding background features to your map (optional). Click **ArcGIS Tools** (tab at top of screen) > **Import ArcGIS Shapefile(s)…**

Click Browse (…) to locate the desired shapefile. Under **Import data to** choose '*Do not import*' and **Plot map to** '*Current map*'. Select **OK**. Repeat for as many features as desired.

Note: There are too many data points in the LiDAR dataset to include location plot information.

18. Export map. Click **Map** (tab at top of screen) > **Export…**

Select Output Format as **JPEG High Quality (*.jpg**) and Region to Export as **Full Map**. Click **Screen** for best resolution. Click **OK**.

LiDAR SQUARES ANALYSIS

To quantify the local Digital Elevation Model (DEM) for the gravity terrain correction it was necessary to understand the full extent of each individual LiDAR tile and determine which of the 306 areas include the collected gravity stations. Initial effort to relate the datasets was executed using a *Python* code, which was designed to identify the LiDAR tiles where gravity stations exist and provide the LiDAR data point that is nearest to the gravity station within the associated tile [Tbl. C.2]. Subsequently, the difference in elevation measured by the LiDAR and the RTK GPS, used for the gravity surveys, was evaluated. Comparative analysis [Tbl. C.2] revealed that the elevation differences were, for the most part, reasonably small, with the expectation that the RTK elevations are likely more accurate.

Station	Station Easting	Station Northing	Station Elevation	Lidar File	Nearest Easting	Nearest Northing	Nearest Elevation	Lidar File Line #	dElev	dDist
VRB1	495924.532	5364723.372	331.1323	41	495924.5	5364723.5	331.18	111925	-0.0477	0.1319
VR1	495940.97	5364989.154	295.6373	41	495940.5	5364989.5	295.8	244941	-0.1627	0.5836
MVB1	495900.243	5365257.089	301.1453	30	495900.5	5365257.5	301.26	128901	-0.1147	0.4847
MVB2	496158.976	5365406.675	287.9195	31	496158.5	5365406.5	288.09	199132	-0.1705	0.5071
MVB3	496290.429	5365597.614	295.994	20	496290.5	5365597.5	296.12	48791	-0.126	0.1343
MVB4	496488.088	5365767.092	299.7638	20	496488.5	5365767.5	299.86	133989	-0.0962	0.5798
MVB5	496723.187	5365883.932	297.881	21	496723.5	5365883.5	298.09	191724	-0.209	0.5335
MVB1	495900.268	5365257.1	301.1167	30	495900.5	5365257.5	301.26	128901	-0.1433	0.4624
MVF1	495675.179	5365087.259	306.911	30	495675.5	5365087.5	307.07	43676	-0.159	0.4014
MVF2	495486.004	5364961.682	313.6162	40	495486.5	5364961.5	313.74	230987	-0.1238	0.5283
MVF3	495297.842	5364794.392	316.9434	40	495297.5	5364794.5	317.08	147298	-0.1366	0.3586
MVF4	495093.541	5364657.729	317.2367	40	495093.5	5364657.5	317.36	78594	-0.1233	0.2326
MVF5	494869.081	5364458.361	315.2733	51	494869.5	5364458.5	315.41	229370	-0.1367	0.4415
MVF6	494690.981	5364302.676	314.4179	51	494690.5	5364302.5	314.5	151191	-0.0821	0.5122
MVF7	494491.239	5364127.552	312.7704	50	494491.5	5364127.5	312.89	63992	-0.1196	0.2661
OMB1	493101.329	5360593.574	349.6559	126	493101.5	5360593.5	349.68	46602	-0.0241	0.1863
OM1	493266.542	5360754.979	345.2419	126	493266.5	5360754.5	345.27	127267	-0.0281	0.4808
MOF1	493753.365	5360846.926	334.3592	127	493753.5	5360846.5	334.41	173254	-0.0508	0.4469
MOV2A	493924.044	5361188.83	320.7819	116	493924.5	5361188.5	320.79	94425	-0.0081	0.5629

Table C.2: Sample of the LiDAR and gravity correlation data acquired using Python. Included are the differences in elevation and distance between the two datasets.

The results of this preliminary comparison were based on the understanding that the LiDAR tiles were all complete squares. However, upon further investigation it was suspected that some of the LiDAR files did not cover square areas as they had been cut off along lake boundaries, and consequently, some of the identified stations were outside of the identified LiDAR tile extent. Therefore, a map of the labelled LiDAR squares was created, to validate that the gravity stations were identified to be within the appropriate LiDAR tiles. This subsequent in-depth tile analysis involved examining each of the 306 individual **XYZ** files and plotting the data coverage to determine the extent of complete and incomplete squares. Initially, the tiles were sorted into three categories, "***actual full squares***" (*i.e.*, 500 metre x 500 metre tile with no gaps), "***essentially full squares***" (*i.e.*, corners missing, small gaps, etc.) and "***non squares***" (*i.e.*, incomplete tiles with significant gaps resulting in irregular shapes which identified some very small data files). It was determined that of the 306 tiles, **146** were full squares, **57** were essentially full squares and **102** were non squares [Tbl. C.3]. Tile 175 contained no data points, so it was omitted from the analysis.

LiDAR File #	Total # of Each Type of "Square"
1	146
2	57
3	102
4	TOTAL FILES = 305
5	
6	
7	
8	
9	
10	
11	
12	
13	
14	
15	
16	
17	
18	
19	
20	

Table C.3: Sorting of the LiDAR tiles. Shown are the first 20 files colour coded based on the type of square. Non squares are red, essentially full squares are blue and complete squares are black.

Thus, it was discovered that approximately 1/3 of the data are incomplete squares corresponding to the edges of the LiDAR data coverage. The LiDAR tile breakdown and relationship with the gravity stations were illustrated through a series of maps, which for ease, assumed that the "**essentially**" full squares were "**actual**" full squares. These maps are shown below as follows: all LiDAR tiles [Fig. C.3], full ("actual" and "essentially") tiles only [Fig. C.4], incomplete tiles only [Fig. C.6] and finally, the LiDAR tiles that contain gravity stations [Fig. C.6].

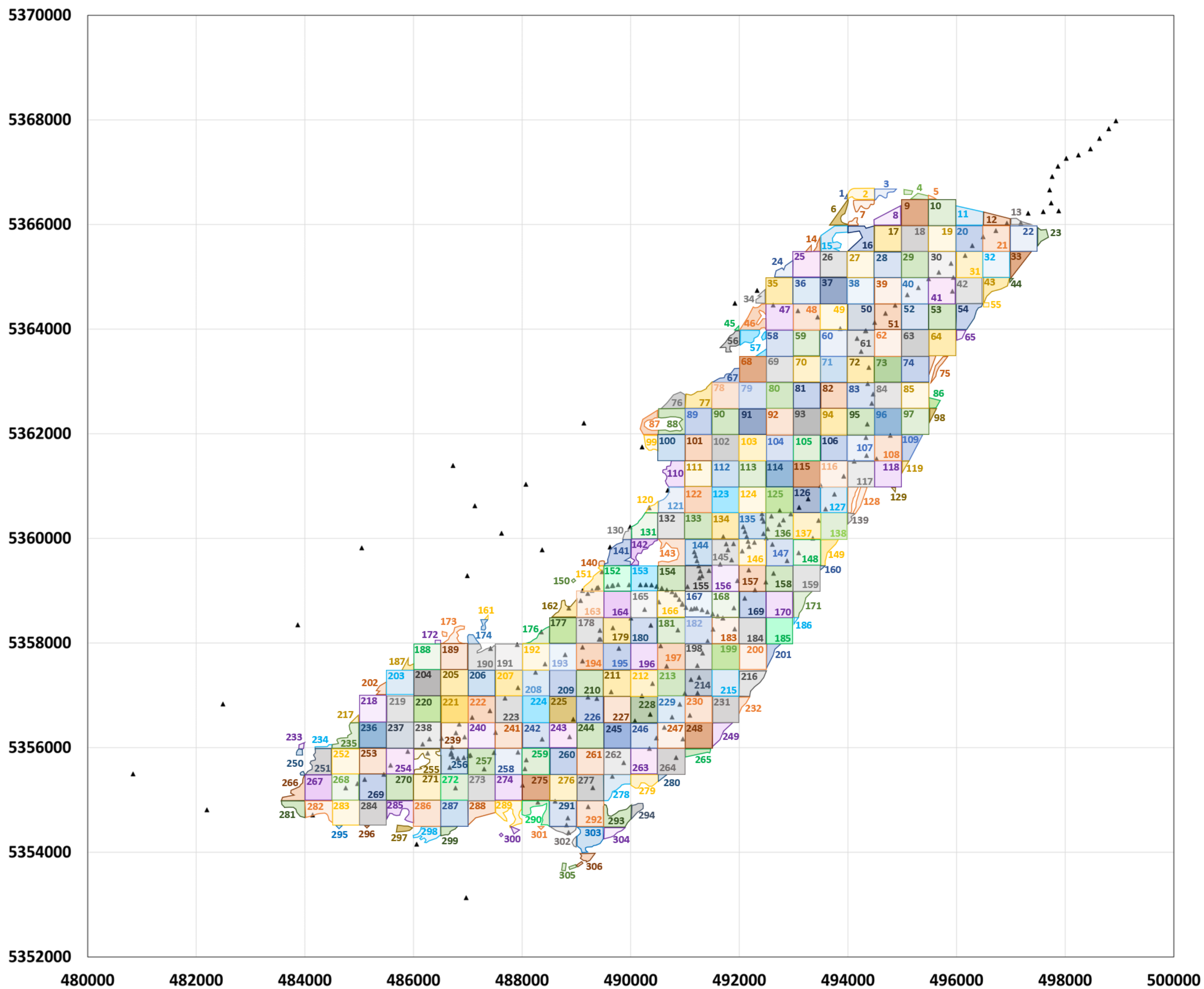

Figure C.3: Complete map of all 305 LiDAR tiles, labelled with their respective file number. Gravity station locations are denoted by the black triangles.

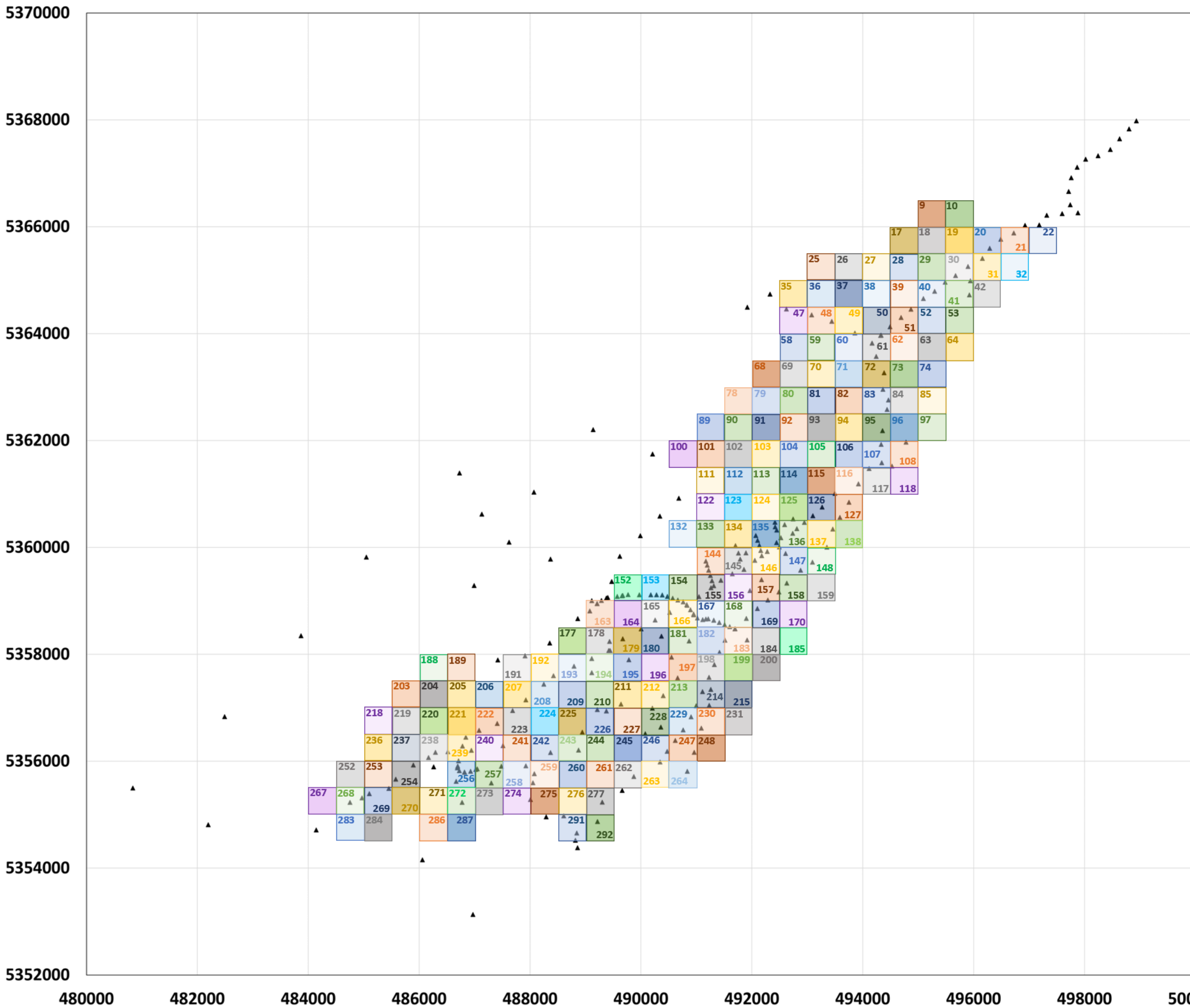

Figure C.4: Map of the 203 full ("actual" and "essentially") LiDAR tiles, labelled with their respective file number. Gravity station locations are denoted by the black triangles

Figure C.5: Map of the 102 incomplete LiDAR tiles, labelled with their respective file number. Gravity station locations are denoted by the black triangles.

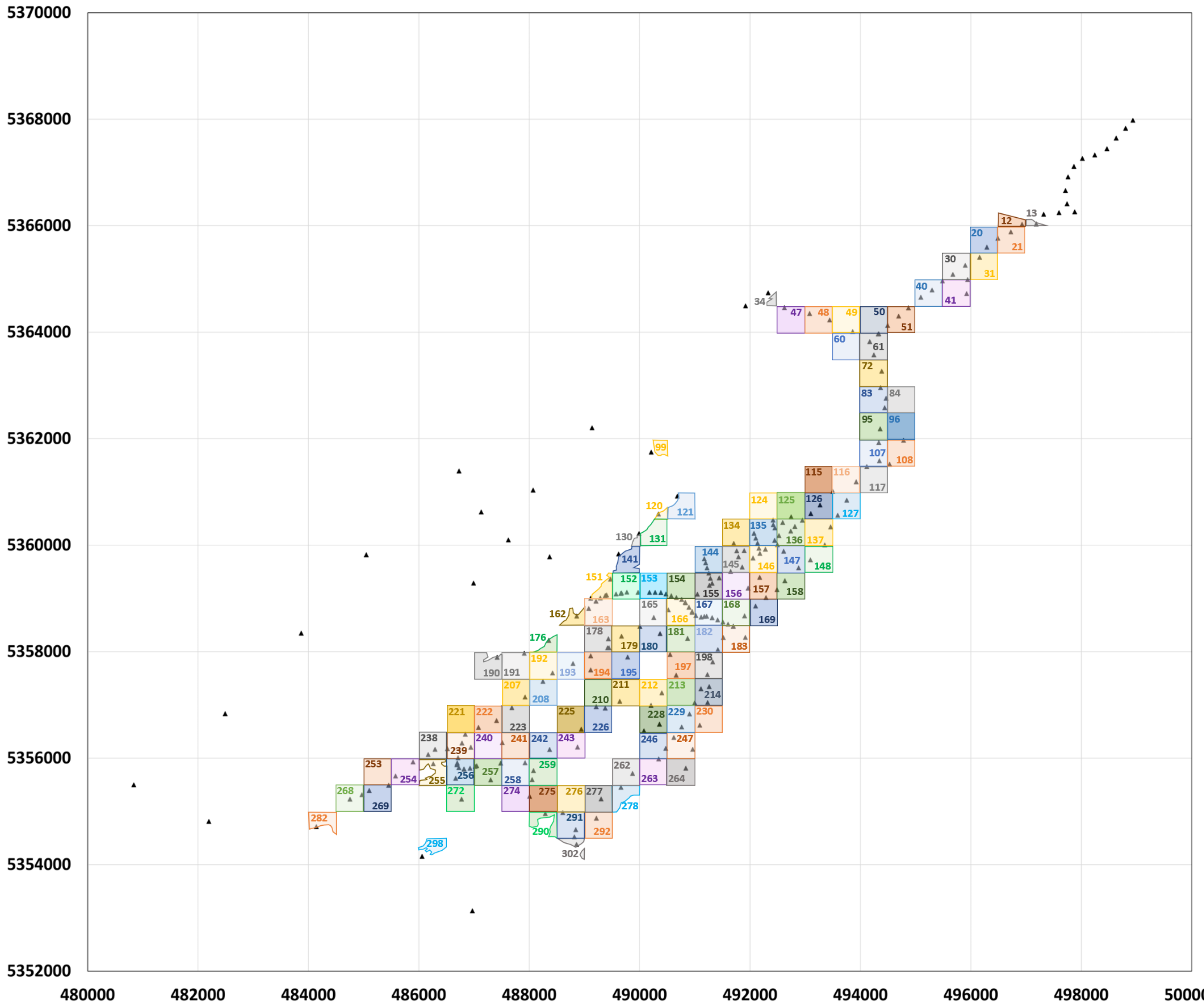

Figure C.6: Map of the 133 LiDAR tiles, labelled with their respective file number, that contain gravity stations (black triangles). They include a combination of full and incomplete squares.

With the LiDAR tiles sorted and the included gravity station locations verified, the data could now be reduced so that it could form the local DEM (along with the bathymetry data), while being small enough for Oasis Montaj to run in a reasonable computation time. Initial reduction involved maintaining the 1 metre data within a square of 20 metre side lengths, centred upon the gravity station and subsequently, reducing the remaining LiDAR squares to points every 10 metres. It is assumed that it would be excessive to maintain the 1 metre elevation sampling beyond 10 metres from the gravity station. While Oasis Montaj was able to handle this reduced, but still rather large (~ 5,000,000 data points) dataset, an additional terrain correction using forward modelling was carried out by PhD candidate Michael King (Section 4.4 and Appendix E). Expectedly, the code-based version ran exceedingly slow given the dense dataset and required that it be reduced even further. Therefore, the LiDAR was then reduced to 100th of the original size, for a manageable total of 558, 473 data points.

APPENDIX D

OASIS MONTAJ TERRAIN CORRECTION: METHODOLOGY AND WORKFLOW

METHODOLOGY

As previously stated, the terrain corrections executed through the Oasis Montaj *Gravity and Terrain Correction* extension are derived from a coalescence of methods depicted by Nagy (1966) and Kane (1962), which separate the survey extent into near, intermediate, and far zones. For a given gravity station, the influence of each zone on the terrain correction is evaluated using a specific algorithm. The near zone [Fig. D.1; Zone 0], comprising 0 to 1 cell from the gravity station, is subdivided into 4 triangular segments which define a plane between the gravity station and the elevation at each sloping corner (Geosoft Inc., 2015). The contributions of the triangular slopes are computed from the following equation:

$$\boldsymbol{g}_{z0} = \gamma\rho\boldsymbol{\theta}\left(-\sqrt{\boldsymbol{R}^2 + \boldsymbol{H}^2} + \frac{\boldsymbol{H}^2}{\sqrt{\boldsymbol{R}^2+\boldsymbol{H}^2}}\right) \tag{D.1}$$

where, respective variables, $\boldsymbol{R}$, $\boldsymbol{H}$ and $\boldsymbol{\theta}$ are illustrated in the right schematic of Figure D.1 below.

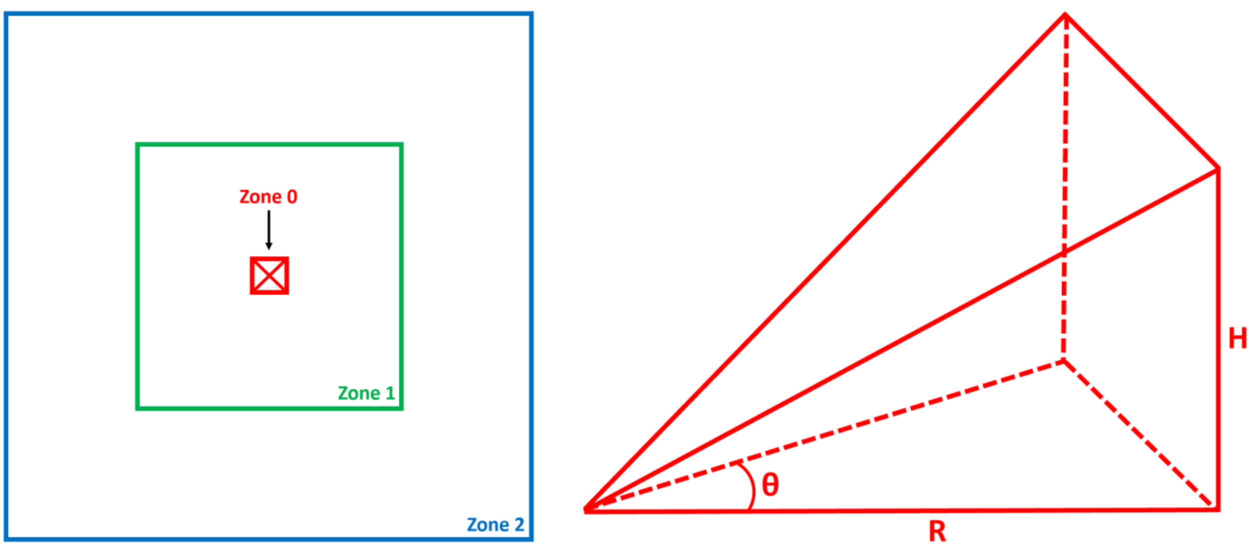

Figure D.1: Left: Schematic plan view diagram of the zonal breakdown used to calculate the terrain corrections. Right: The Zone 0 sloping triangular approach for computing the respective terrain contribution. Parameters R, H and θ are shown (recreated from Geosoft Inc., 2015).

To evaluate the terrain impact within the intermediate zone [Fig. D.1; Zone 1], which spans 1 to 8 cells from the station, the square prism method by Nagy (1966) is exploited. As expressed in Equation D.2, the gravitational effect on an observation point can be obtained by integrating over the volume of Zone 1:

$$\boldsymbol{g}_{z1} = -\gamma\rho \left|_{z_1}^{z_2} \left|_{y_1}^{y_2} \left|_{x_1}^{x_2} \boldsymbol{x}\cdot\ln(\boldsymbol{y}+\boldsymbol{r}) + \boldsymbol{y}\cdot\ln(\boldsymbol{x}+\boldsymbol{r}) + \boldsymbol{Z}\,arctan\frac{\boldsymbol{Z}\cdot\boldsymbol{r}}{\boldsymbol{x}\cdot\boldsymbol{y}}\right|\right|\right| \tag{D.2}$$

where, parameters, $\boldsymbol{x}$, $\boldsymbol{y}$, $\boldsymbol{Z}$ and $\boldsymbol{r}$ are defined in the left panel of the following Figure D.2.

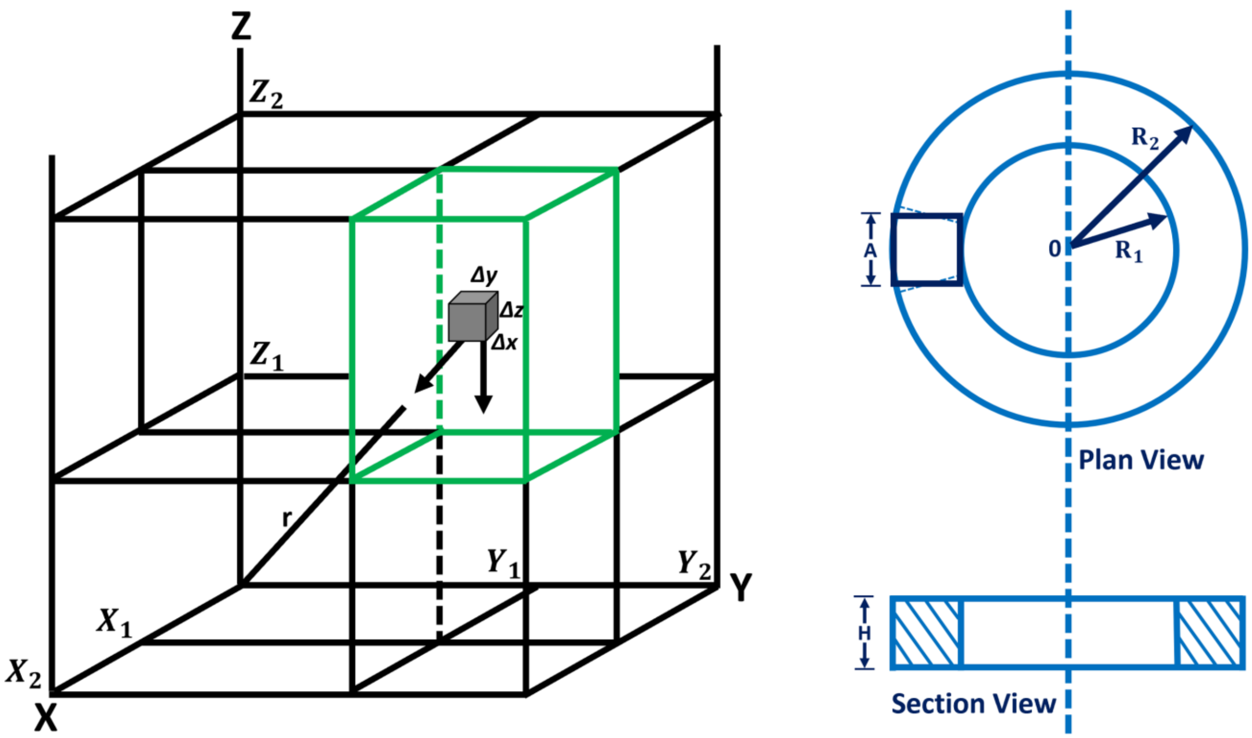

Figure D.2: Left: Schematic representation of the gravitational attraction of the right rectangular prism (green) method used to compute the terrain correction for Zone 1 (recreated from Nagy, 1966). Right: Conceptual diagram of the sectional ring used to obtain the terrain correction for Zone 2 (and beyond). Included are the variables specified in Eqns. D.2 and D.3 (recreated from Geosoft Inc., 2015).

In the far zone [Fig. D.1; Zone 2], which extends beyond 8 cells from the gravity station, the terrain contributions are based on the Kane (1962) square prism ring segment approximation. Kane reveals that integrating over a ring enhances computational feasibility as integration of a square prism is computationally exhaustive. The influence of each segment on a gravity reading is determined from Equation D.3:

$$\boldsymbol{g}_{z2} = 2\gamma\rho\boldsymbol{A}^2\left(\frac{\boldsymbol{R}_2-\boldsymbol{R}_1\sqrt{\boldsymbol{R}_1{}^2+\boldsymbol{H}^2}-\sqrt{\boldsymbol{R}_2{}^2+\boldsymbol{H}^2}}{(\boldsymbol{R}_2{}^2-\boldsymbol{R}_1{}^2)}\right) \tag{C.3}$$

where, variables, $\boldsymbol{A}$, $\boldsymbol{H}$, $\boldsymbol{R}_1$ and $\boldsymbol{R}_2$ are depicted in the right panel of the preceding Figure D.2.

OASIS MONTAJ WORKFLOW

The following workflow outlines the steps required to carry out a terrain correction using the *Gravity and Terrain Correction* extension of Oasis Montaj. The process is described for two different starting points, depending on the preference of the user. In the first scenario, all of the gravity survey corrections (*i.e.*, drift, latitude, free-air, etc.) are computed in Oasis Montaj, while the second situation executes the majority of the data reduction process manually in Microsoft Excel, prior to performing only the terrain correction in Oasis Montaj. Although this study exploited the latter technique, the former method is also commonly used, though the processing requirements are ambiguous, so they have been included here for future reference.

Required Input Files:

1. **Gravity Survey Files (Scenario 1 only)**
   - Separated by survey days
   - Compatible formats: *ASCII*, *.dmp*, *.dat*
2. **Base Station File (Scenario 1 only)**
   - Compatible formats: CSV (*.csv*) or Excel spreadsheet (*.xlsx*)
3. ***Location File* (Scenario 1 only)**
   - If available, but not obligatory (see details in step 3 below)

4. **Regional Digital Elevation Model (DEM) (Scenarios 1 and 2)**
    - Low resolution, extending far outside the survey area (*i.e.*, 10 to 30 kilometres)
    - Commonly extracted from *Natural Resources Canada* or the Oasis Montaj *Data Seeker*
5. **Local Digital Elevation Model (DEM) (Scenarios 1 and 2)**
    - High resolution, extending slightly outside the survey area (*i.e.*, up to 1 kilometre)
    - Data should be highly accurate (i.e., LiDAR) and correlate with the RTK GPS gravity station elevations.
6. **Excel Corrected "Master" Database (Scenario 2 only)**
    - All simple Bouguer corrected survey data with the base station information removed.
    - Survey stations are tagged as 1 and base stations, 0 (see details in step 7 below)

Processing Steps

The first 6 steps defined below are specific to scenario 1, where the entire process is completed in Oasis Montaj. If the "master" database has been compiled in Excel, then proceed directly to step 7 for how to properly format the database and subsequently perform the terrain correction.

Step 1: Import Gravity Data

- If using a CGX gravimeter, the data can be imported directly from the instrument as a *.dmp* or *.dat*. Otherwise, it can be imported as a CSV.
- Unfortunately, Oasis Montaj does not yet support bulk corrections, so the corrections are required to be computed individually for every survey data. Therefore, the data must be imported into separate databases, based on survey days.

Step 2: Import Base Station Database

- This ties the gravity survey readings to the absolute gravity on Earth (typically ~980000 mGal)

Step 3: Import Location Database (*if independently acquired*)

- This is an **optional** step.
- If precise station location measurements were acquired with a supplementary GPS (*e.g.*, RTK system) then they can be imported as a separate database and used in lieu of the GPS data collected from the gravimeter. Otherwise, omit this step.
- If a location database is not specified, Oasis Montaj will simply default to using the GPS data from the gravimeter.
- In either case, the projected XY and geographic latitude and longitude coordinates must be specified for the Oasis project (Coordinates → Set Current X, Y, Z).

Step 4: Run Gravity Corrections

- The *Gravity Corrections* dialog comprises basic corrections including *Drift*, *Tide* and *Base Station*; however, the gravimeter will likely output these calculations automatically.
- As a check, it is suggested to run the corrections on the raw (uncorrected) gravity channel.
- Running all corrections will result in a "*Grav_Corr*" channel with values tied into the base station (absolute gravity), somewhere near 980000 mGal.

Step 5: Run Latitude Correction

- This accounts for the ellipsoidal shape of the Earth (among other things), where gravity is stronger at the poles.
- Essentially, it removes regional effects, resulting in the residual, latitude corrected, gravity. Typical values are on the scale of 100's of mGal.

Step 6: Merge into Master Database (.gdb)

- This merges all the survey data into a master database and removes all base stations.
- The process recognizes the survey stations as 1s and the base stations as 0s.

In this study (scenario 2), the preceding correction steps 1 – 6 were completed manually in an Excel spreadsheet, which will serve as the "master" database

Step 7: Formatting Excel "Master" Database (Scenario 2 only)

- As the "master" database used to compute the terrain correction must contain station data only, the daily "loop" base station data (*i.e.*, *LAUNDRY*) in the simple Bouguer spreadsheet can be removed by doing the following:
- Import the spreadsheet into Oasis as a new database (.gdb) file.
- Create a new channel in the database called "**Mask**". Choose *Data Type* as **Double** and populate it with **1s**.
- Under **Database Utilities → Channel Math**, write the following math expression:
  Mask = (Station == "LAUNDRY") ? DUMMY:Mask;
  - This reads "*if Station equals LAUNDRY, then output a dummy, if not, then keep what is already in the mask*".
- Remove the base stations and the dummy days from the master database through **Database Tools → Window Data → Subset Database**. Window the database to the mask channel just created. This will generate a new database without the base station rows.
- Run the **Subset Database** tool again, this time using the *Easting* channel as your mask channel. This removes any dummies in the database.
- The end result is a database with only the relevant gravity survey stations.

The following steps 8 – 9 are specific to this research, therefore, if following method 1, skip ahead to step 10

The local digital elevation model was a combined grid of the high-resolution LiDAR (Appendix C) and bathymetry (Section 5.3.2) data acquired at the Valentine Gold Project. Given the data amalgamation, the resulting DEM contained data gaps and did not cover the full survey extent, omitting the 13 stations furthest to the northeast [Fig. D.3]. Therefore, to obtain an accurate terrain correction, the boundaries of the local DEM needed to be extended and the voids filled.

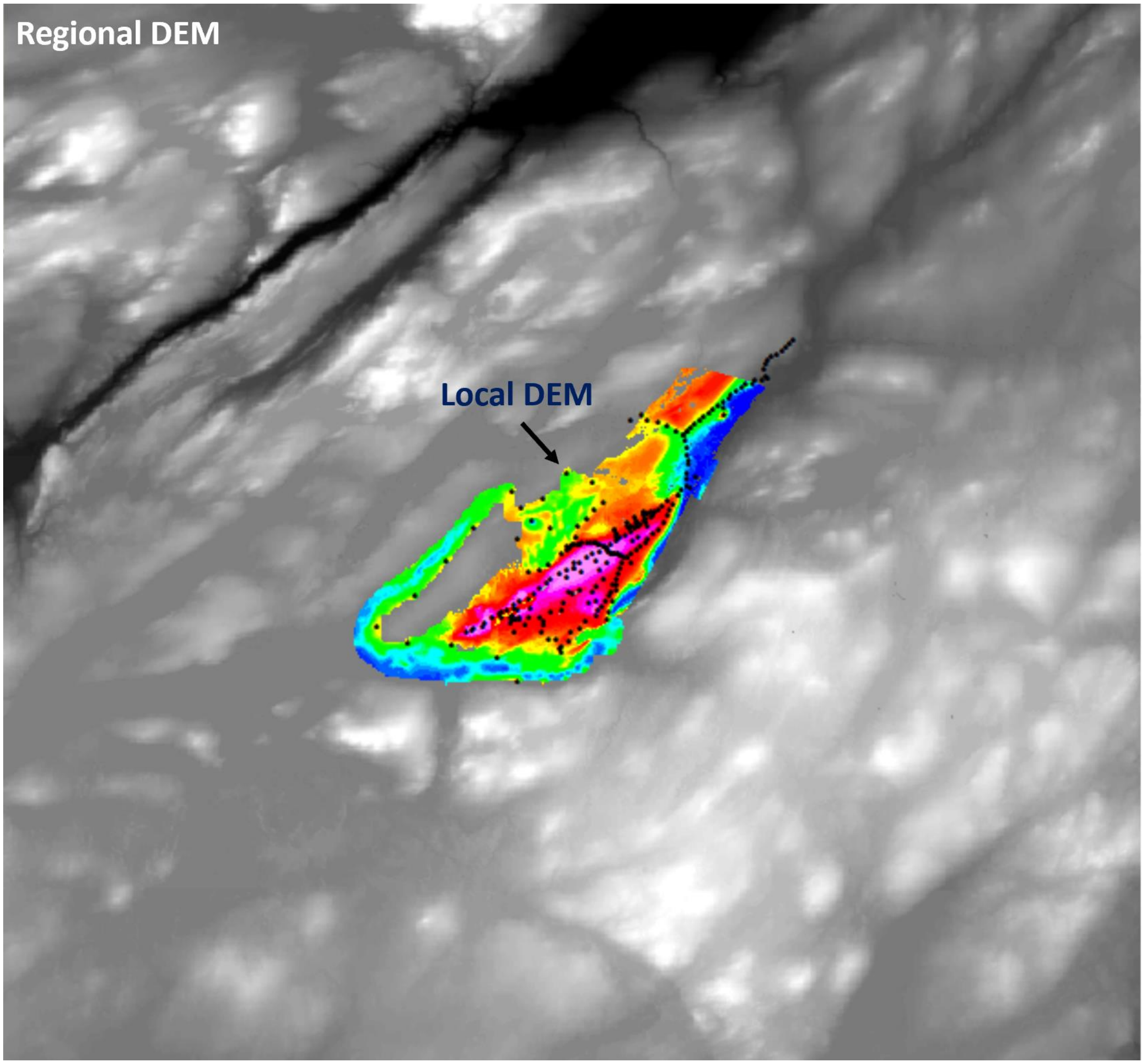

Figure D.3: The incomplete local DEM grid of combined LiDAR and bathymetry centred upon the regional DEM (grey scale: dark = low, light = high), which spans 15 kilometres in all directions around the gravity survey area. The regional DEM was obtained using the Government of Canada's Geospatial Data Extraction tool and the black dots are the acquired gravity station locations.

Step 8: Extend Size of Local DEM (specific to this study)

- To ensure complete data coverage, the local DEM was extended by **20%**:
  - **Grid and Image → Utilities → Expand Grid**

  The *Shape of the output grid* was set to **Square** and the *Expand X and Y dimension* were **0**.

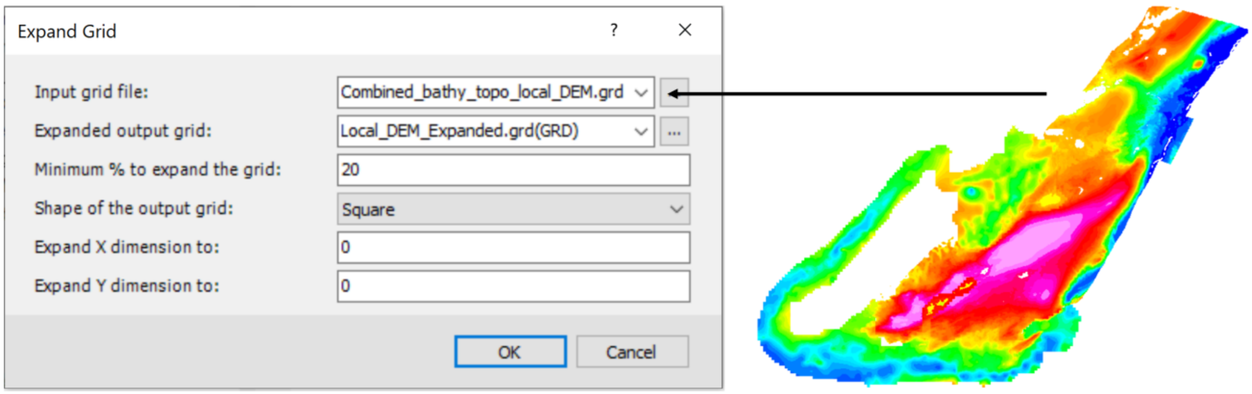

- Essentially, this expanded the white space around the local DEM, which could then be filled in with the regional DEM data (step 9 below) for complete coverage.

Step 9: Fill in Gaps in Local DEM (specific to this study)

- The extended region and gaps within the local DEM (i.e., any areas where local DEM data did not exist) were populated with data from the regional DEM:
  - **Grid and Image → Utilities → Boolean Operations**

  The *Input Grid File 1* was the **expanded local DEM**, *Input Grid File 2* was the **regional DEM**, the *Boolean Logic Option* was set to **OR**, *Size of Output Grid* was **Minimum** and the *Grid Values used in Overlap* areas was assigned **Grid 1 Only**.

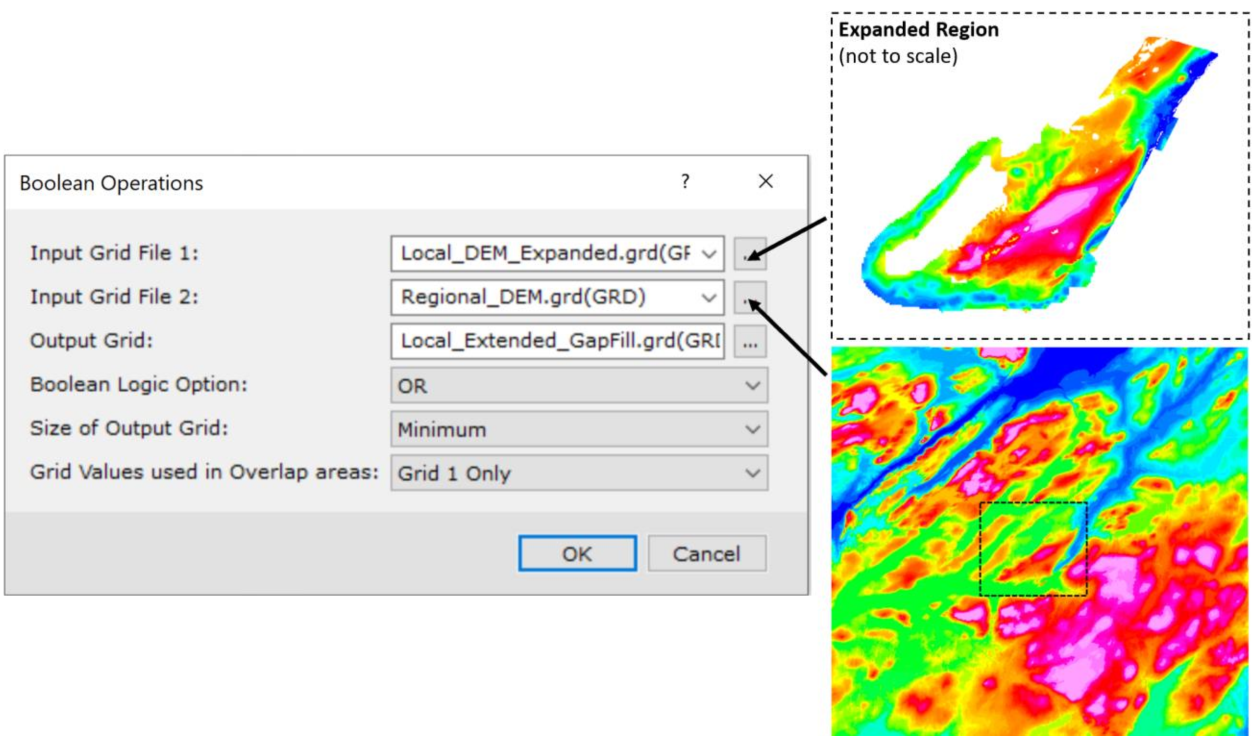

The resulting complete (*i.e.*, extended and gap-filled) local DEM is shown in comparison with the incomplete local DEM in Figure D.4 below.

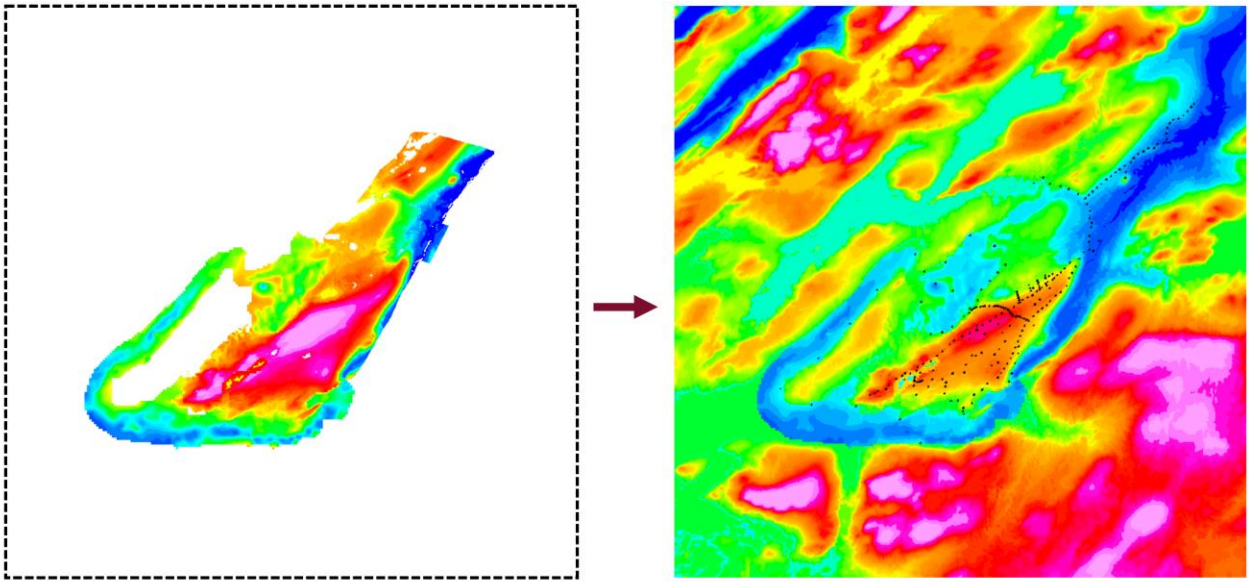

Figure D.4: The output of steps 8 and 9 are the complete local DEM (right) which, in comparison with the incomplete local DEM (left) has been expanded to include all gravity stations (black dots) and contains no data gaps.

<u>Step 10</u>: Create Regional Correction Grid

- This is an <u>**optional**</u> step, recommended for areas of <u>steep</u> topography. However, it serves as a good quality control check and was carried out in this study (chosen parameters shown below).
- Essentially, the regional correction grid computes a correction due to the topographic effects of the local and regional grid at every cell on the local grid.
- **Gravity → Terrain Corrections → Create Regional Correction Grid**:

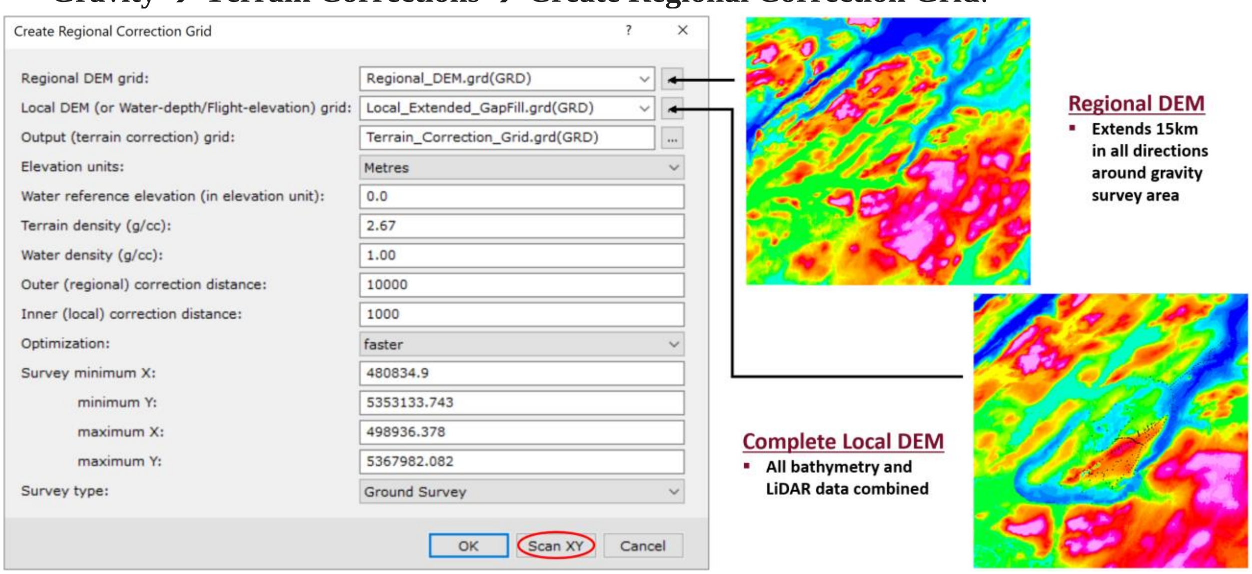

The output regional terrain correction grid, shown below in Figure D.5, is populated with the expected topographic contributions, resulting in small correction values (not elevations) which are added to the full terrain correction in the subsequent step 11.

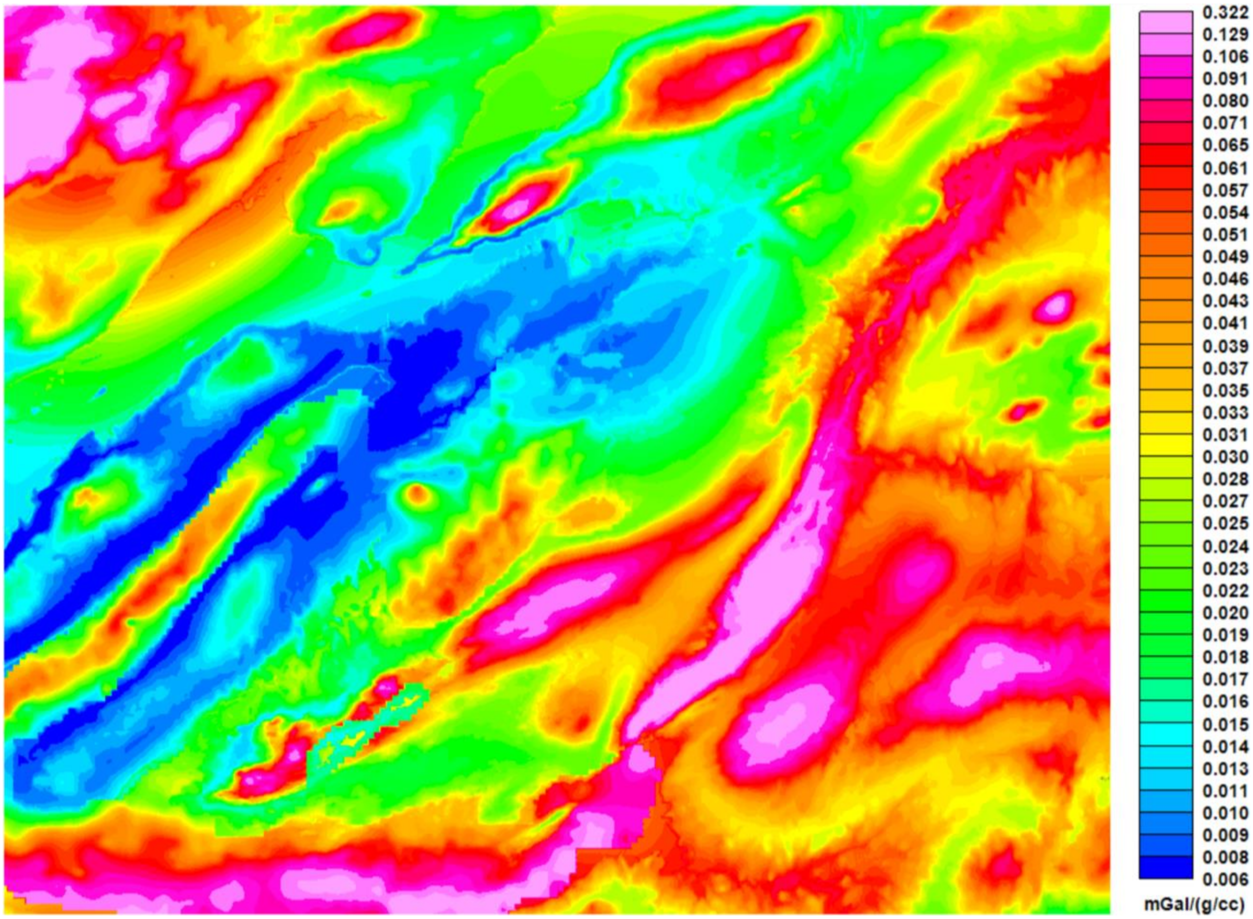

Figure D.5: The regional terrain correction grid computed in step 10. The grid units, mGal/(g/cm^3) are multiplied by the terrain density (2.67 g/cm^3) when the full terrain correction is calculated (step 11).

<u>Step 11</u>: Run Terrain Correction:

- The final processing step, which computes the full terrain correction values that are then **<u>added</u>** to the simple Bouguer gravity data to obtain the complete Bouguer anomaly [Fig. 4.7].
- The terrain correction can be computed using only the local DEM or, both the local DEM and the regional correction grid, provided it was generated in the optional step 10. If only the local DEM is used, then a *local correction distance* must be specified, otherwise it can be left blank.
- If the survey area includes any water bodies, the corresponding bathymetry data can be incorporated by providing a *grid* of the water depths, or if the water surface elevations are the same (approximately) then a *constant water reference elevation* can be specified.
- The parameters used in this study are specified in the *Terrain Correction* dialog window below.
- **Gravity → Terrain Corrections → Terrain Correction**:

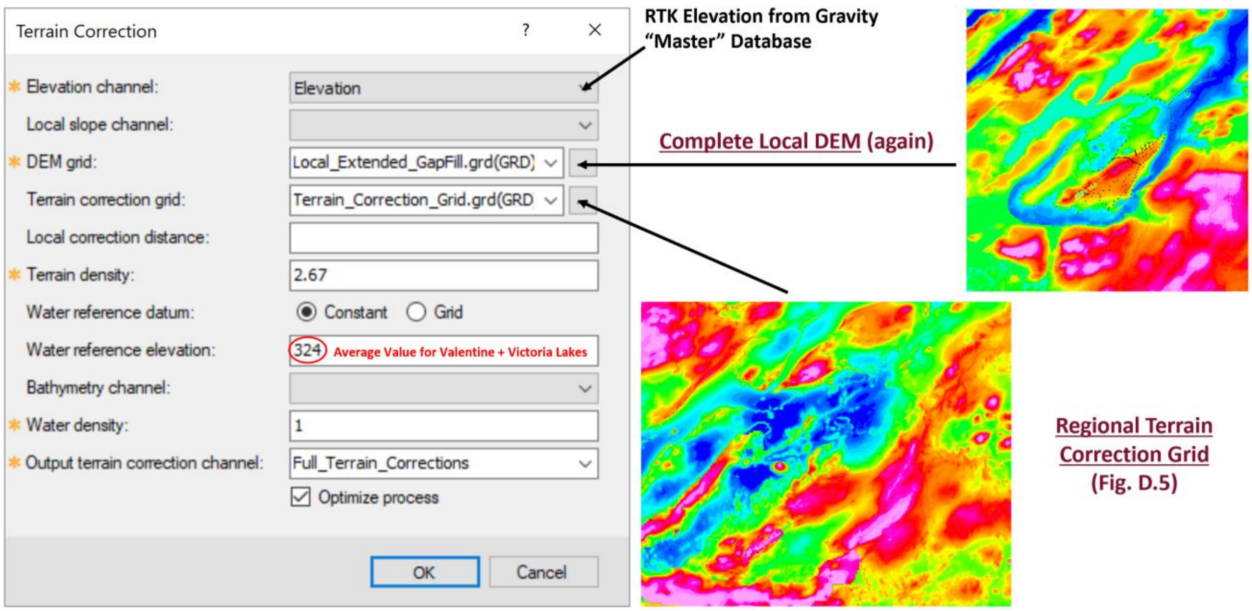

APPENDIX E

FORWARD MODELLING TERRAIN CORRECTION: METHODOLOGY

Complete Bouguer gravity anomaly calculations over the Valentine Lake, NL, gold property using a forward modelling approach

By: Michael King

Ph.D Candidate (Geophysics)

FACULTY OF SCIENCE
Department of Earth Sciences

April 2021

Methodology

Topography Model Building

To calculate terrain corrections using the forward modelling approach described in the preceding sections, a critical first step was to create a 3-D topography model for the Valentine Lake Property. In this study, several different topography models were constructed using a combination of topography and bathymetry data collected over the Valentine Lake vicinity. Considering the topography data, two topography datasets were considered in this study. One topography dataset was a regional digital elevation model (DEM) extracted from the *Natural Resources Canada* database (Fig. E.1) and the other was a higher resolution lidar dataset acquired over the Valentine Lake Property by *Marathon Gold* (Fig E.2). The bathymetry data (Fig. E.3) was acquired over various lakes and bogs throughout the Valentine Lake Property (e.g., Valentine and Victoria Lakes) using ground penetrating radar data acquired over the past couple years during the winter, and sonar data collected over Valentine Lake and Victoria Lake during the summer.

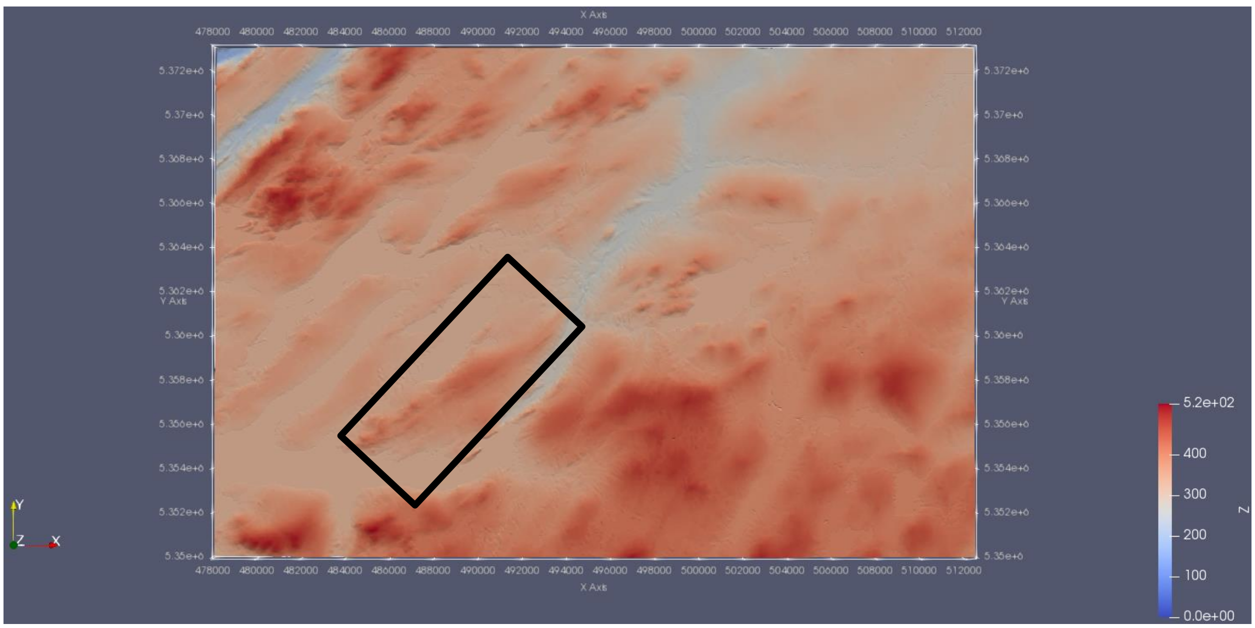

Figure E.1: Regional DEM extracted from *Natural Resources Canada* and the approximate extent of the Lidar data coverage (black rectangle).

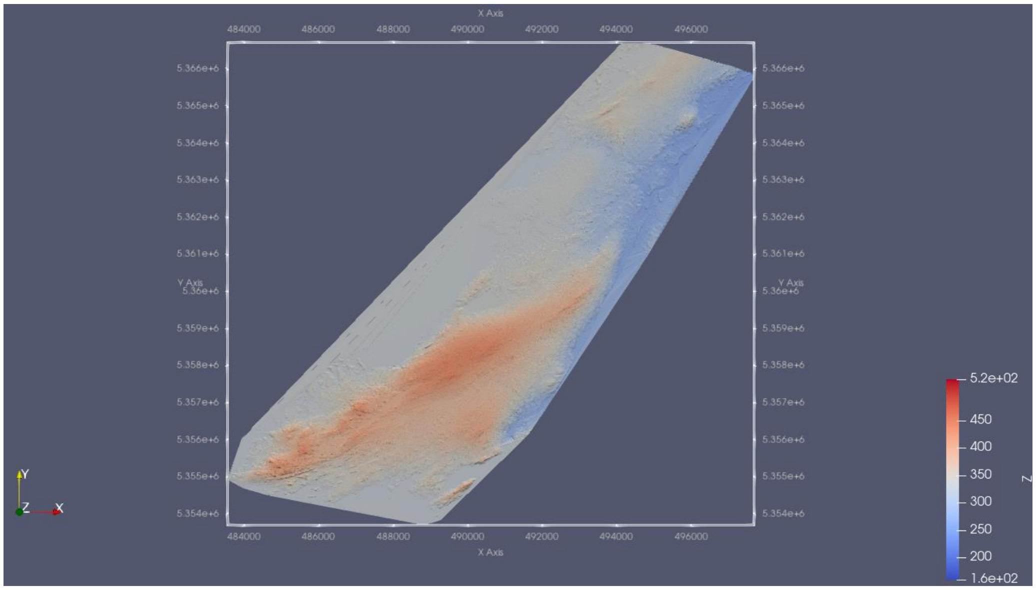

Figure E.2: Lidar data acquired over the Valentine Lake Property.

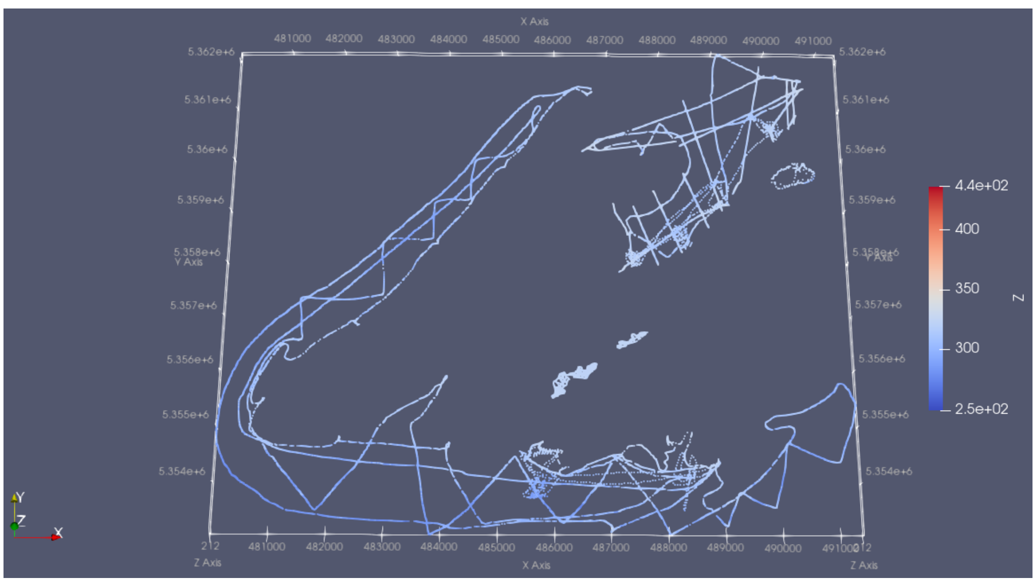

Figure E.3: Bathymetry data acquired over the Valentine Lake Property.

In this study, four 3-D topography models were considered using different combinations of topography and bathymetry datasets previously described (Table E.1). To create the topography models considered in this study, a suite of utility programs created by Peter Lelièvre were used to prepare the various files and data required to create 3-D models. Following the preparation of files and data, a program called Tetgen (Si, 2015) was used to construct 3-D models made up of tetrahedral cells with a user specified discretization and geometry. Each model was constructed by designing two separate regions (Fig E.4), a central region of interest (COI; blue rectangle in Figure E.4) and a padding region of interest (POI; red rectangle in Figure E.4). For each model, the COI is the region that includes the topography and/or bathymetry data of interest and was designed to encompass a much finer discretization of tetrahedral cells relative to the POI. In each model considered, the POI extends 230 km from the edges of the COI along the x-axis (easting direction) and 420 km from both edges of the COI along the y-axis (northing direction). The COI was designed to extend to a depth of 10 km, while the POI was designed using a depth extent of 20 km (Fig. E.5). Model 1 was constructed only using topography data from the regional DEM (Figure E.1). Model 2 included the regional DEM and lidar data (Fig. E.2) by cropping the regional DEM (removal of DEM data points) wherever there was lidar data coverage. Model 3 was the same as model 2 except for the addition of the bathymetry data (Fig. E.3) and model 4 only included lidar and bathymetry data (regional DEM excluded). In addition, each model considered was assigned a uniform density of 2.67g/cc.

Model #	DEM Included	Lidar Included	Bathymetry Included
1	Yes	No	No
2	Yes	Yes	No
3	Yes	Yes	Yes
4	No	Yes	Yes

Table E.1: Topography and bathymetry datasets used to create each model considered.

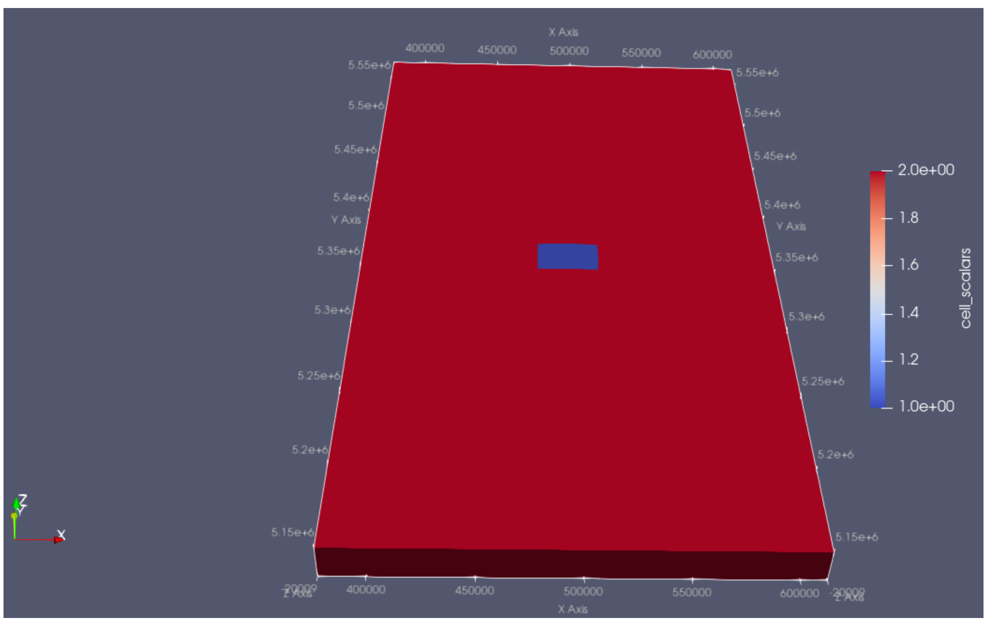

Figure E.4: Geometry of the 3-D topography model used for each model considered (identical geometry and depth extent for models 1, 2, 3 and 4). The blue rectangle (COI) contains the topography and/or bathymetry data of interest. The red rectangle (POI) represents a passing zone that extends outside the COI in order to avoid edge effects when conducting forward gravity modelling.

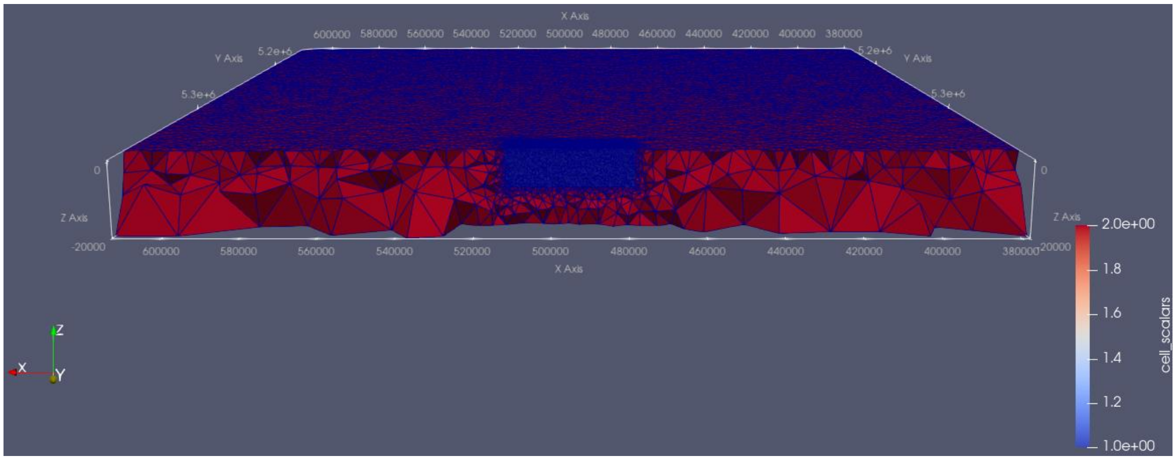

Figure E.5: Profile along the x-axis (easting direction) of the 3-D topography model (identical for models 1, 2, 3 and 4). Note the much finer discretization of cells within the COI (blue rectangle) in contrast to the POI (red rectangle).

Forward Modelling

Following the construction of 4 different topography models, forward gravity modelling was conducted in order to calculate the gravitational response of each uniform density (2.67 g/cc) topography model over the gravity station locations acquired within the Valentine Lake Property

Forward modelling of gravity data is a linear problem that is used to calculate gravity data for a given set of observation locations over a model of interest with user specified geometries and densities (Blakely, 1996). The vertical attraction of gravity (*g*), the component of gravity measured by most gravimeters, for a 3-D model in Cartesian coordinates (Equation E.2.1) is given by:

$$\begin{aligned} g(x,y,z) &= \frac{\partial U}{\partial z} \\ &= -\gamma \int_{z'}\int_{y'}\int_{x'} \rho(x',y',z')\,\frac{(z-z')}{r^3}\,dx'\,dy'\,dz' \end{aligned}$$

Equation E.2.1

where

$$r = \sqrt{(x-x')^2+(y-y')^2+(z-z')^2}$$

Equation E.2.2

ρ is density, *U* is gravitational potential, γ is the gravitational constant, (*x*, *y*, *z*) represents the position of an observation location given in Cartesian coordinates and (*x'*, *y'*, *z'*) is the location of a point mass given in Cartesian coordinates. More generally, Equation D.2.1 can be written as:

$$g(x,y,z) = \int_{z'}\int_{y'}\int_{x'} \rho(x',y',z')\,\psi(x-x',y-y',z-z')\,dx'\,dy'\,dz'$$

Equation E.2.3

where

$$\psi(x,y,z) = -\gamma \frac{z}{(x^2+y^2+z^2)^{3/2}}$$ *Equation E.2.4*

is the Green's function representing the gravitational attraction at a location (*x, y, z*) of a point mass located at (x', y', z') (Fig. E.6) (Blakely, 1996). Thus, forward gravity modelling entails the repeated calculation of Equation E.2.1 for a given set of observation locations. However, this calculation can become complicated and more computationally demanding for complex geological scenarios that are not easily represented using simple geometrical shapes such as rectangles or circles. More commonly, the gravitational sources can be discretized into *N* simpler cells, which can convert Equation E.2.1 into the form:

$$g_m = \sum_{n=1}^{N} \rho_n \psi_{mn}$$ *Equation E.2.5*

where g_m is the vertical attraction of gravity at the mth observation point, ρ_n represents the density of part *n,* and ψ_{mn} is the gravitational attraction at a point *m* due to a cell *n* with unit density.

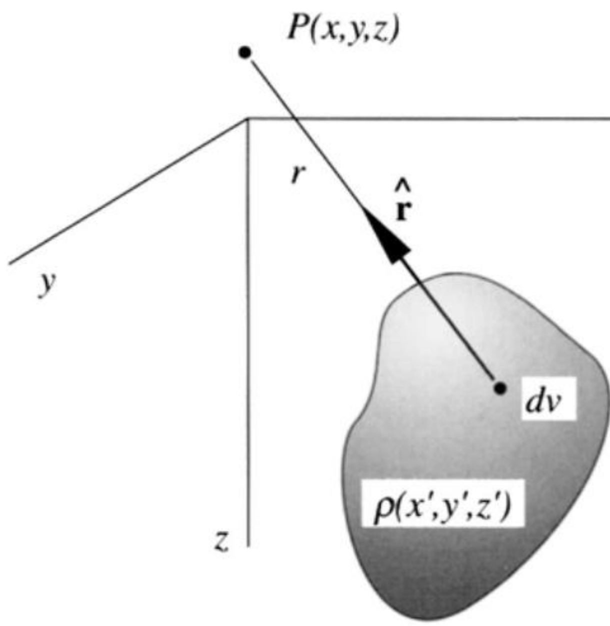

Figure E.6: An arbitrary 3-D body with density ρ(x', y', z') and shape observed at point P(x, y ,z). The unit vector $\hat{\boldsymbol{r}}$ points from a cell of the mass to point P (Blakely, 1996).

Herein, the gravity data calculated at each gravity station location within the topography models considered (Table E.1) are shown (Figs. E.7 – E.10). Overall, the gravity trends calculated using each topography model display very similar trends such as a gravity high over regions of higher topography within the gold bearing alteration zone and Victory SW (Figs. E.1 and E.2) and relative gravity lows within and surroundng Valentine Lake.

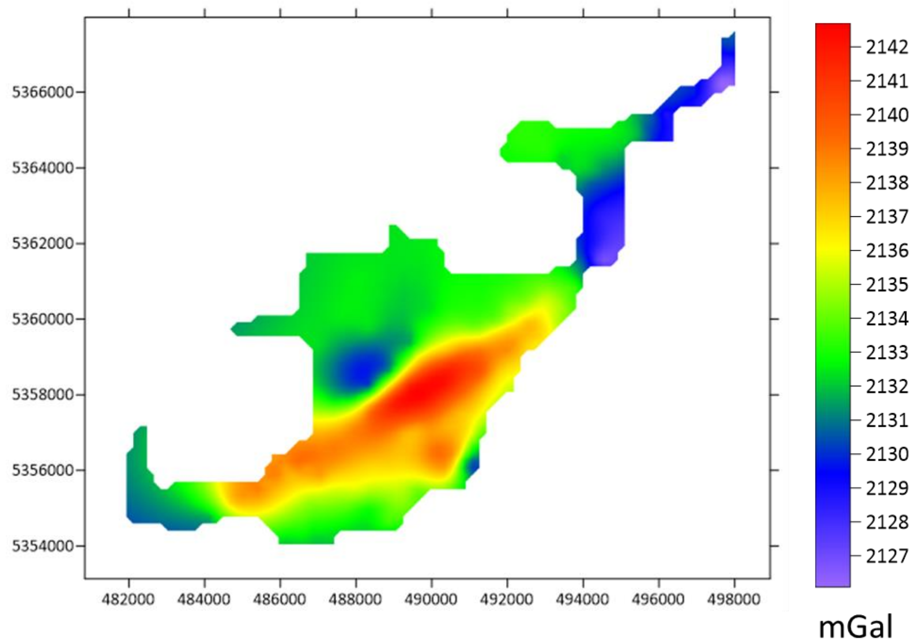

Figure E.7: Forward modelled gravity data calculated from model 1.

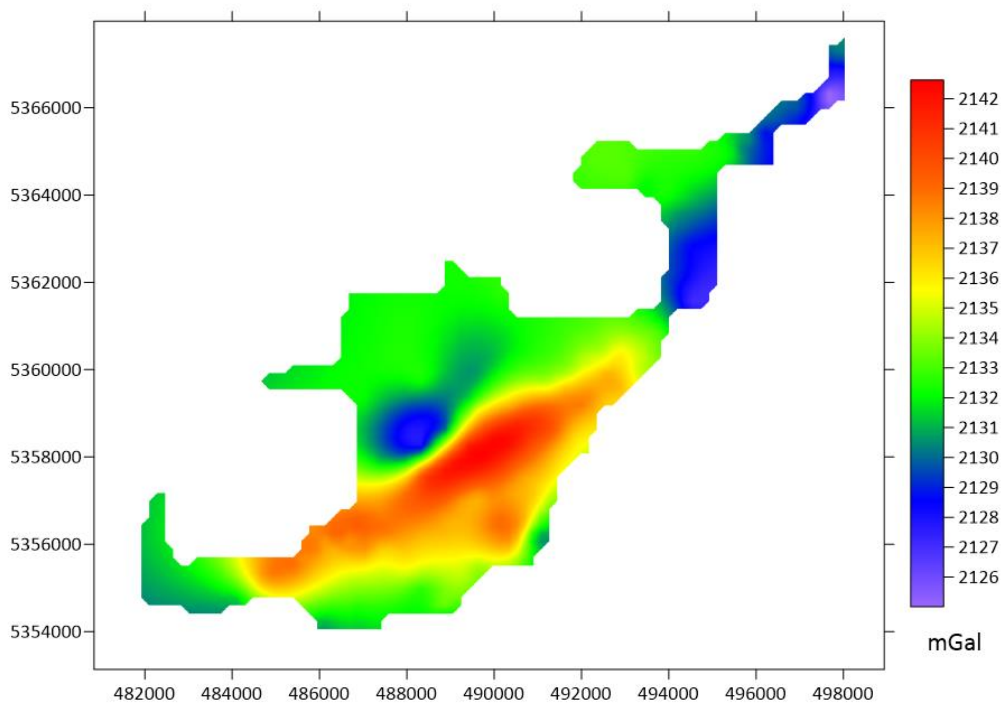

Figure E.8: Forward modelled gravity data calculated from model 2.

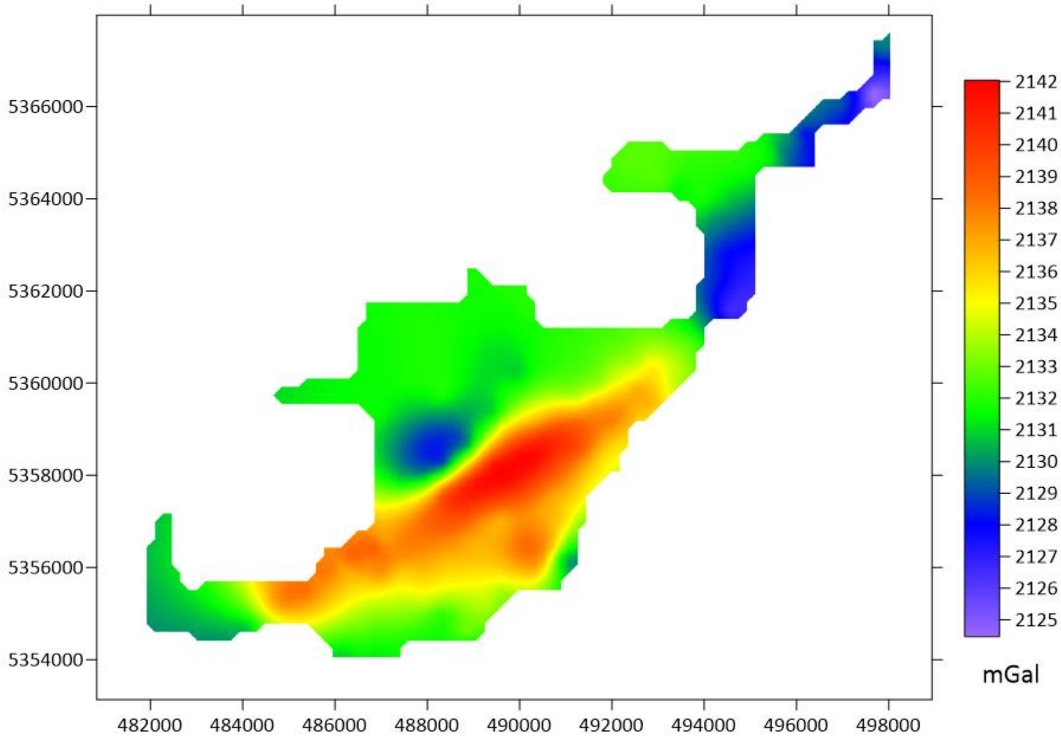

Figure E.9 Forward modelled gravity data calculated from model 3.

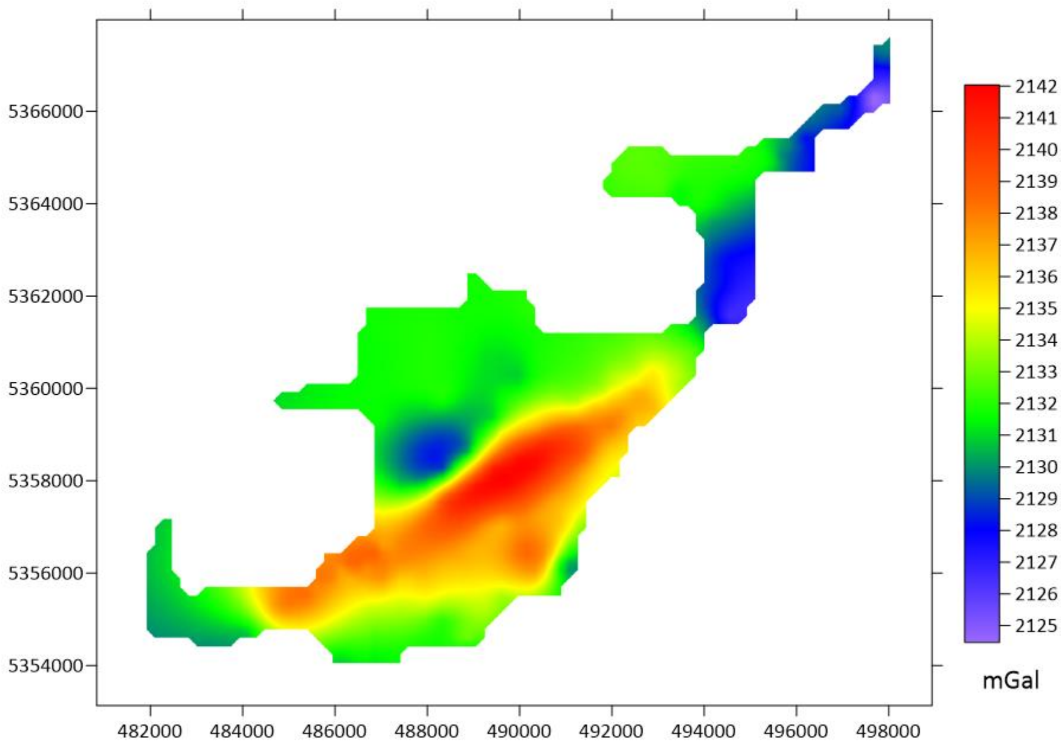

Figure E.10 Forward modelled gravity data calculated from model 4.

Terrain Corrections

The terrain correction is a crucial processing step to consider when interpreting gravity data that has acquired within an area with variable topography and bathymetry. Considering the simple Bouguer correction, this correction represents an approximate approach for removing the effect of topography and excess mass by using a Bouguer slab of constant density (Fig. E.11). However, the simple Bouguer correction often accompanies limitations due to the inability to account for topography and bathymetry surrounding the observation locations and the assumption of a Bouguer slab with a uniform density (Blakely, 1996).

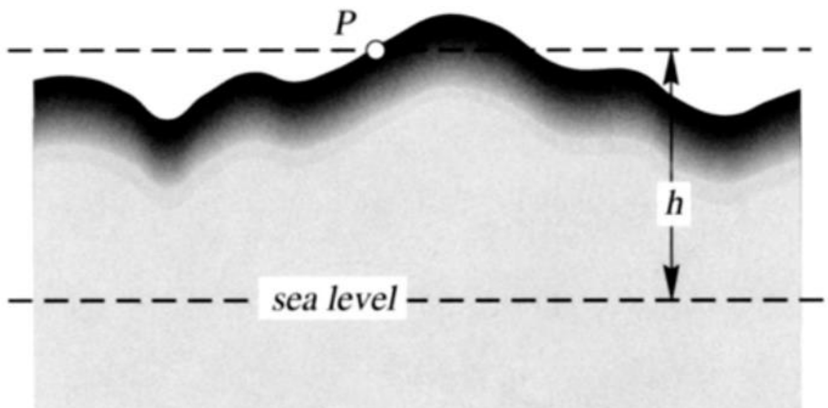

Figure E.11: Bouguer slab approximation from Blakely (1996). Point P (white circle) represents an observation location, and the dashed lines represent the height (h) of the Bouguer slab with constant density.

In this study, terrain corrections were calculated via a forward modelling approach using a terrain correction program created by Peter Lelievre. This terrain correction methodology involves removing the effect of topography, the Bouguer slab, and a linear regional trend using the following approach.

Gravity data after the free-air correction (d_{free}) (Equation E.3.1) can be given by:

$$\mathrm{d}_{free} = \mathrm{d}_{topo} + \mathrm{d}_{slab} + \mathrm{d}_{regional} + \mathrm{d}_{anom} \qquad \textit{Equation E.3.1}$$

where d_{topo} is the gravity response of a rock between a topography surface and some datum for some background density, d_{slab} is the gravity response of the Bouguer slab, $d_{regional}$ is some long wavelength component in the gravity data and d_{anom} is the response of any anomalous masses relative to the background density. The gravity response of a rock between a topography surface and some datum for some background density (d_{topo}) is equal to the product of the response of the rock between topography and some datum for unit density, which can be treated as a known quantity calculated from DEM information ($\hat{d}_{topo}$) and a background density (ρ) (Equation E.3.2).

$$\mathbf{d}_{topo} = \hat{\mathbf{d}}_{topo}\rho$$
Equation E.3.2

Additionally, the gravity response of the Bouguer slab (d_{slab}) and a linear regional trend ($d_{regional}$) (Equation E.3.3) can be given by:

$$\mathbf{d}_{slab} + \mathbf{d}_{regional} = \mathbf{e}c + \mathbf{x}u + \mathbf{y}v$$
Equation E.3.3

where e is a vector of ones of length N (number of data), x any y are the easting and northing locations, respectively, of the data observation locations and the scalars c, u and v represent the parameters of some regional linear trend. Using equations E.3.2 and E.3.3, equation E.3.1 can now be re-written (Equation E.3.4).

$$\mathbf{d}_{free} - \mathbf{d}_{anom} = \hat{\mathbf{d}}_{topo}\rho + \mathbf{e}c + \mathbf{x}u + \mathbf{y}v.$$
Equation E.3.4

The following equations (Equation E.3.5) can be used to simplify the subsequent set of equations (Equations E.3.6 – E.3.9):

$$\mathbf{d} \equiv \hat{\mathbf{d}}_{topo}$$
$$\mathbf{b} \equiv \mathbf{d}_{free} - \mathbf{d}_{anom}$$
Equation E.3.5

where d now represents the response of the rock between topography and some datum for unit density ($\hat{d}_{topo}$) and b now represents the difference between the free-air gravity data (d_{free}) and the gravity response of anomalous masses relative to a background density (d_{anom}). Using these relationships, equation 2.3.4 can be re-written (Equation E.3.6):

$$\mathbf{b} = \mathbf{d}\rho + \mathbf{e}c + \mathbf{x}u + \mathbf{y}v$$
Equation E.3.6

which can be treated as an overdetermined system with N equations and 4 unknowns (Equation E.3.7).

$$\mathbf{A}\mathbf{p} = \begin{pmatrix} \mathbf{d} & \mathbf{e} & \mathbf{x} & \mathbf{y} \end{pmatrix} \begin{pmatrix} \rho \\ c \\ u \\ v \end{pmatrix} = \mathbf{b}.$$
Equation E.3.7

The least squares solution (Equation E.3.8) is given as:

$$\mathbf{p} = \left(\mathbf{A}^{\mathrm{T}}\mathbf{A}\right)^{-1}\mathbf{A}^{\mathrm{T}}\mathbf{b}$$
Equation E.3.8

but can be re-written as:

$$\mathbf{p} = \mathbf{D}\mathbf{r}$$
Equation E.3.9

where

$$\mathbf{D} \equiv \left(\mathbf{A}^{\mathrm{T}}\mathbf{A}\right)^{-1}$$
$$\mathbf{r} \equiv \mathbf{A}^{\mathrm{T}}\mathbf{b}$$

Equation E.3.10

Thus, the re-written least squares solution (Equation E.3.9) involves the inverse of a 4 x 4 matrix. The program calculates a background density that provides the best fit to the free-air data and determines an additional linear trend to remove from the free-air anomaly. Thus, after solving Equation E.3.9 (Fig. E.12), the effect of the topography, Bouguer slab and a linear regional component can be removed, which results in the desired data response of anomalous masses (d_{anom}).

1. Initialize:
   - $\mathrm{d} = \mathrm{d}_{topo}$
   - calculate $\mathbf{D} \equiv \left(\mathbf{A}^{\mathrm{T}}\mathbf{A}\right)^{-1}$
   - $\mathrm{d}_{anom} = 0$
   - $\mathrm{b} = \mathrm{d}_{free}$
2. Solve:
   - calculate $\mathbf{r}$ for current b
   - $\mathrm{p} = \mathbf{D}\mathrm{r}$
3. Prepare for next iteration:
   - $\mathrm{d}_{anom} = \mathrm{d}_{free} - \mathrm{d}\rho - c$
   - $\mathrm{b} = \mathrm{d}_{free} - \mathrm{d}_{anom}$
4. If p has converged, stop, otherwise go to 2.

Figure E.12: Iterative scheme used to calculate terrain corrections via a forward modelling approach.

APPENDIX F

BOG HYPSOMETRY AND LAKE BATHYMETRY PRIORITIES OF MARATHON GOLD CORPORATION AND RESULTING SUPPLEMENTARY MAPS

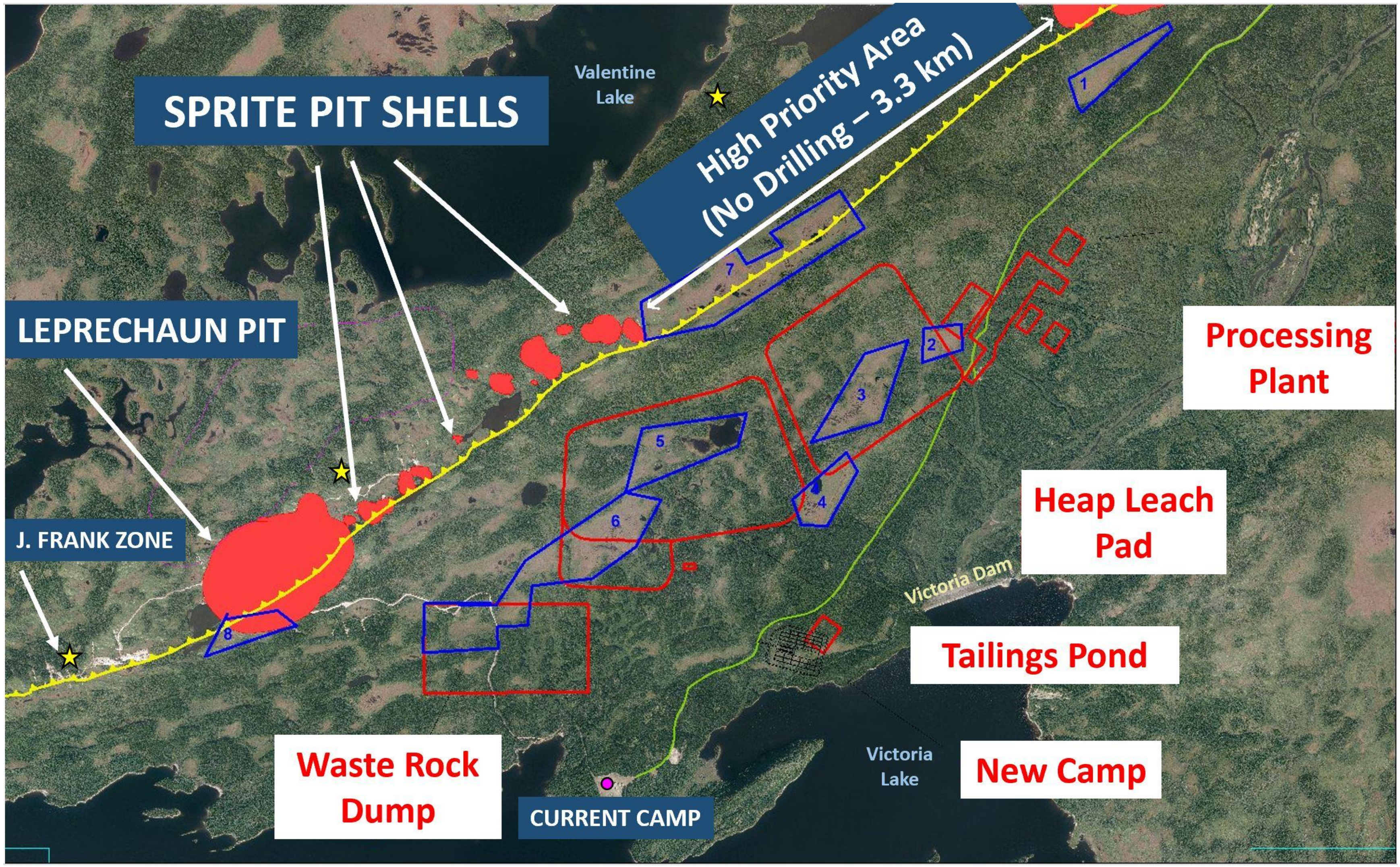

Figure F.1: Map of the 8 priority areas (blue) for GPR acquisition at the Valentine Gold Project, chosen by Marathon's engineering team. These areas consist of bogs and small ponds to which areas 2-6 underly future infrastructure.

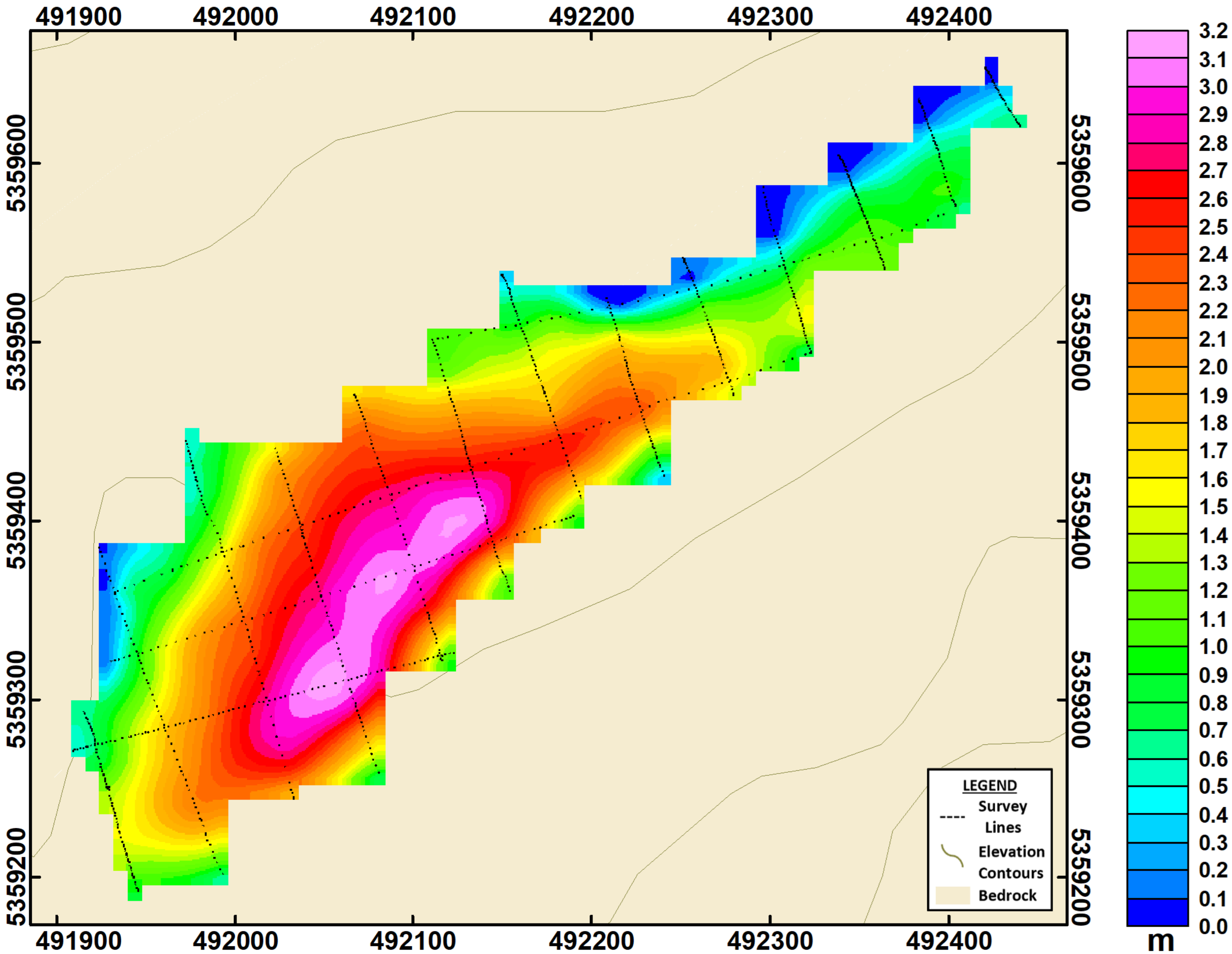

Figure F.2: Priority Area 1 (bog) hypsometry map showing qualitative variation with depth (see detailed analysis in Appendix H). It was gridded using minimum curvature, a cell size of 8 metres, cells to extend data beyond set to 0 and linear colour method.

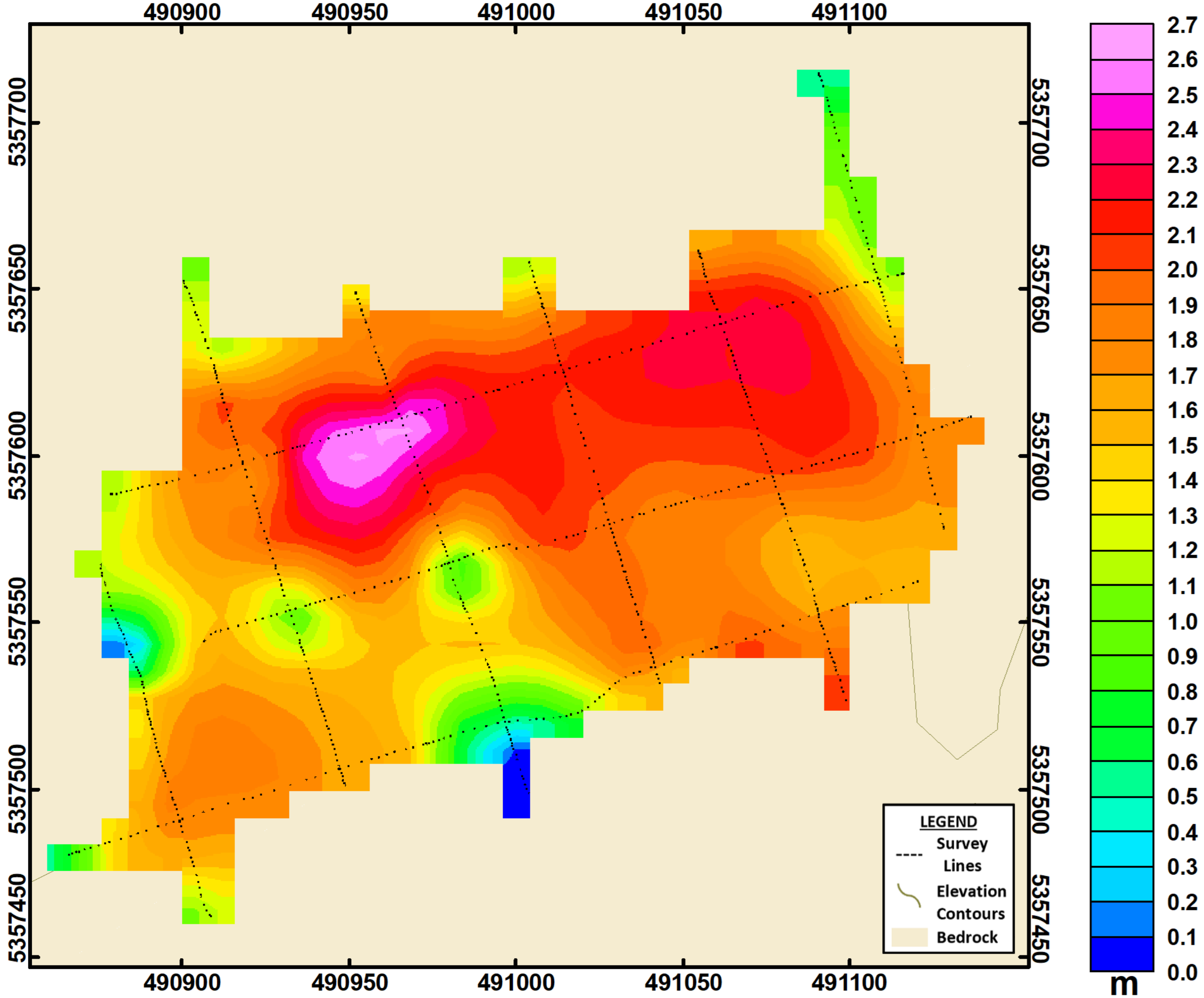

Figure F.3: Priority Area 2 (bog) hypsometry map showing qualitative variation with depth (see detailed analysis in Appendix H). It was gridded using minimum curvature, a cell size of 8 metres, cells to extend data beyond set to 0 and linear colour method.

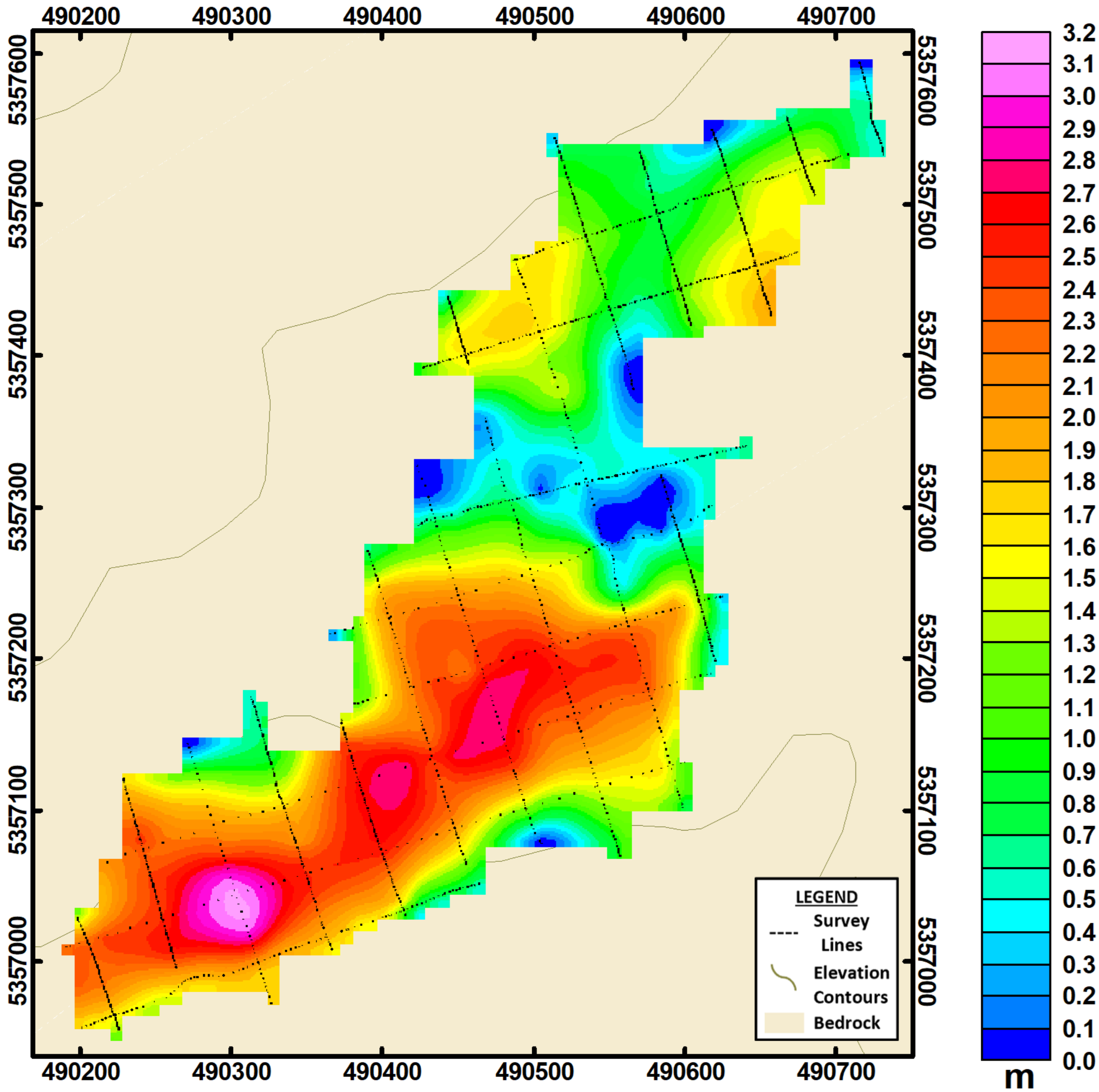

Figure F.4: Priority Area 3 (bog) hypsometry map showing qualitative variation with depth (see detailed analysis in Appendix H). It was gridded using minimum curvature, a cell size of 8 metres, cells to extend data beyond set to 0 and linear colour method.

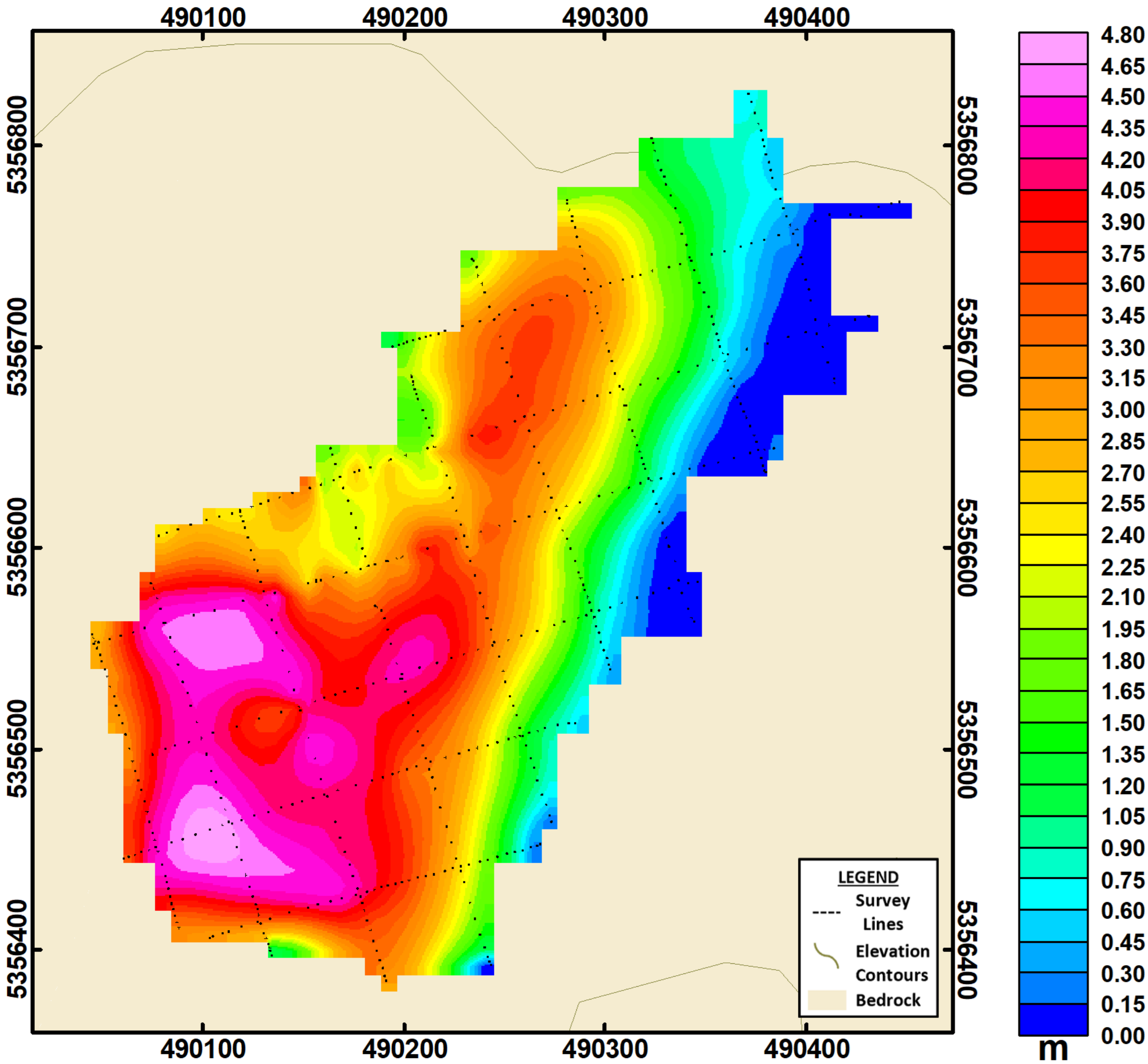

Figure F.5: Priority Area 4 (bog with small pond) hypsometry map showing qualitative variation with depth (see detailed analysis in Appendix H). It was gridded using minimum curvature, a cell size of 8 metres, cells to extend data beyond set to 0 and linear colour method.

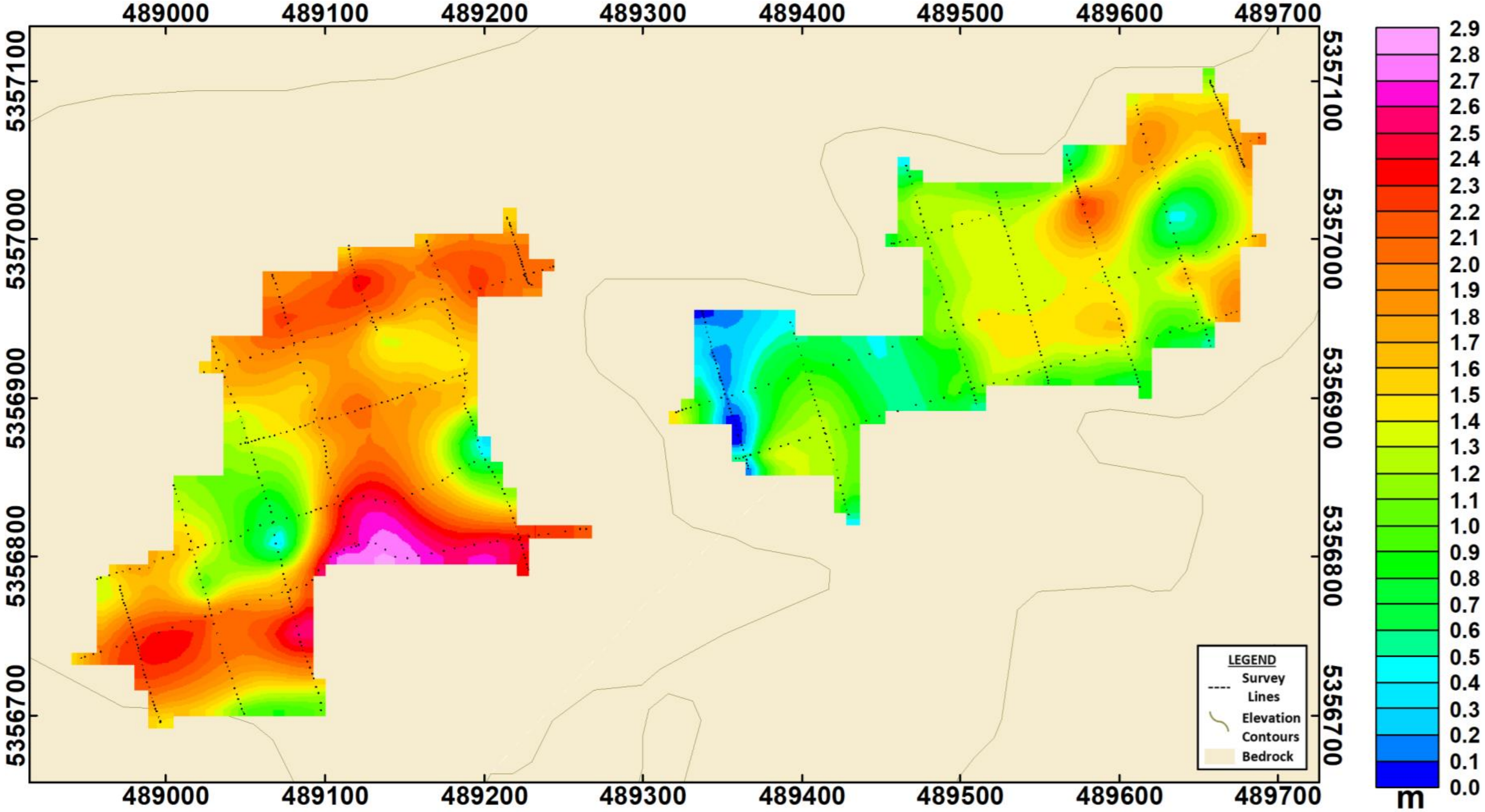

Figure F.6: Priority Area 5 (bog with small ponds) hypsometry map showing qualitative variation with depth (see detailed analysis in Appendix H). It was gridded using minimum curvature, a cell size of 8 metres, cells to extend data beyond set to 0 and linear colour method.

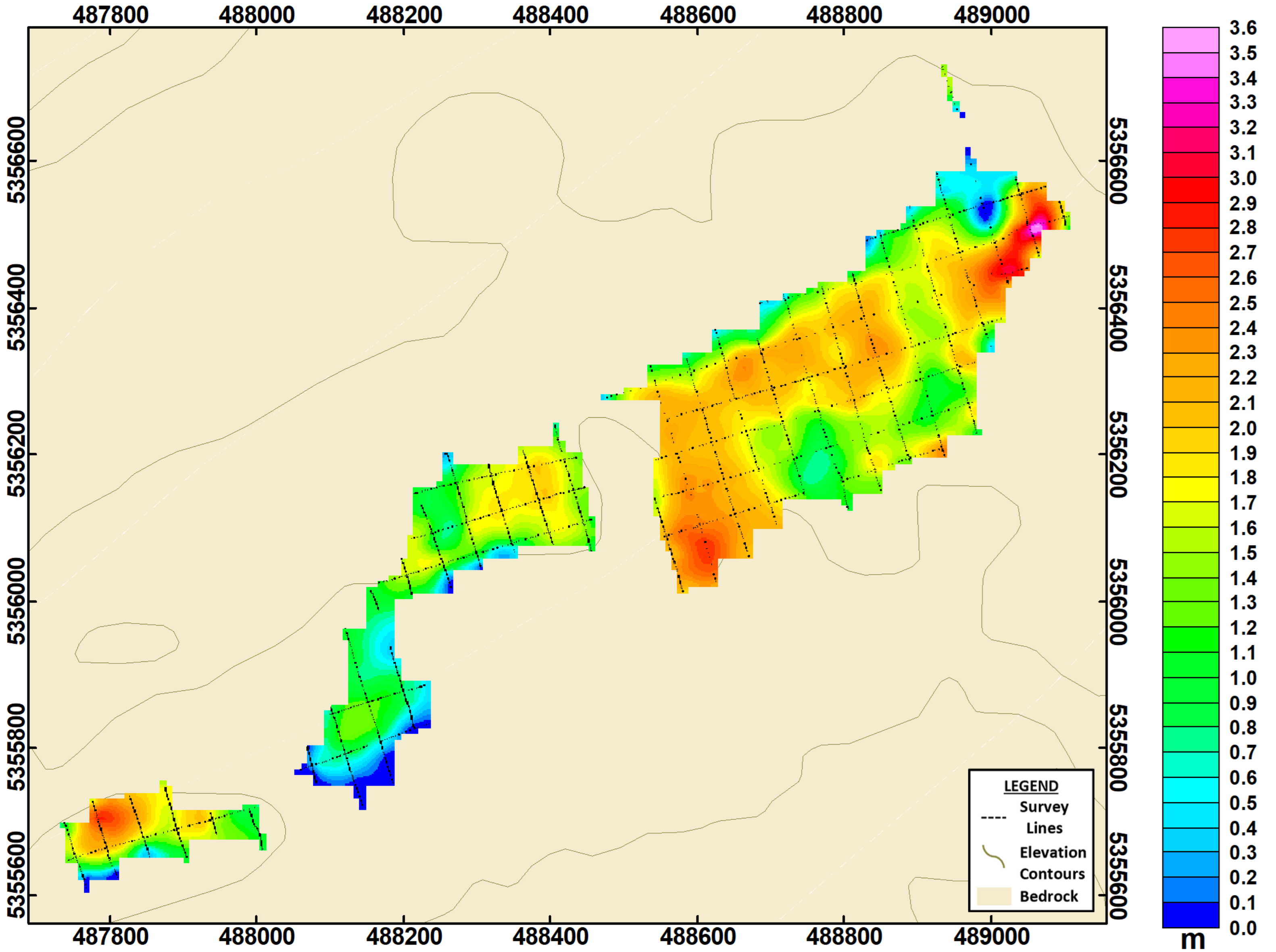

Figure F.7: Priority Area 6 (bog) hypsometry map showing qualitative variation with depth (see detailed analysis in Appendix H). It was gridded using minimum curvature, a cell size of 8 metres, cells to extend data beyond set to 0 and linear colour method.

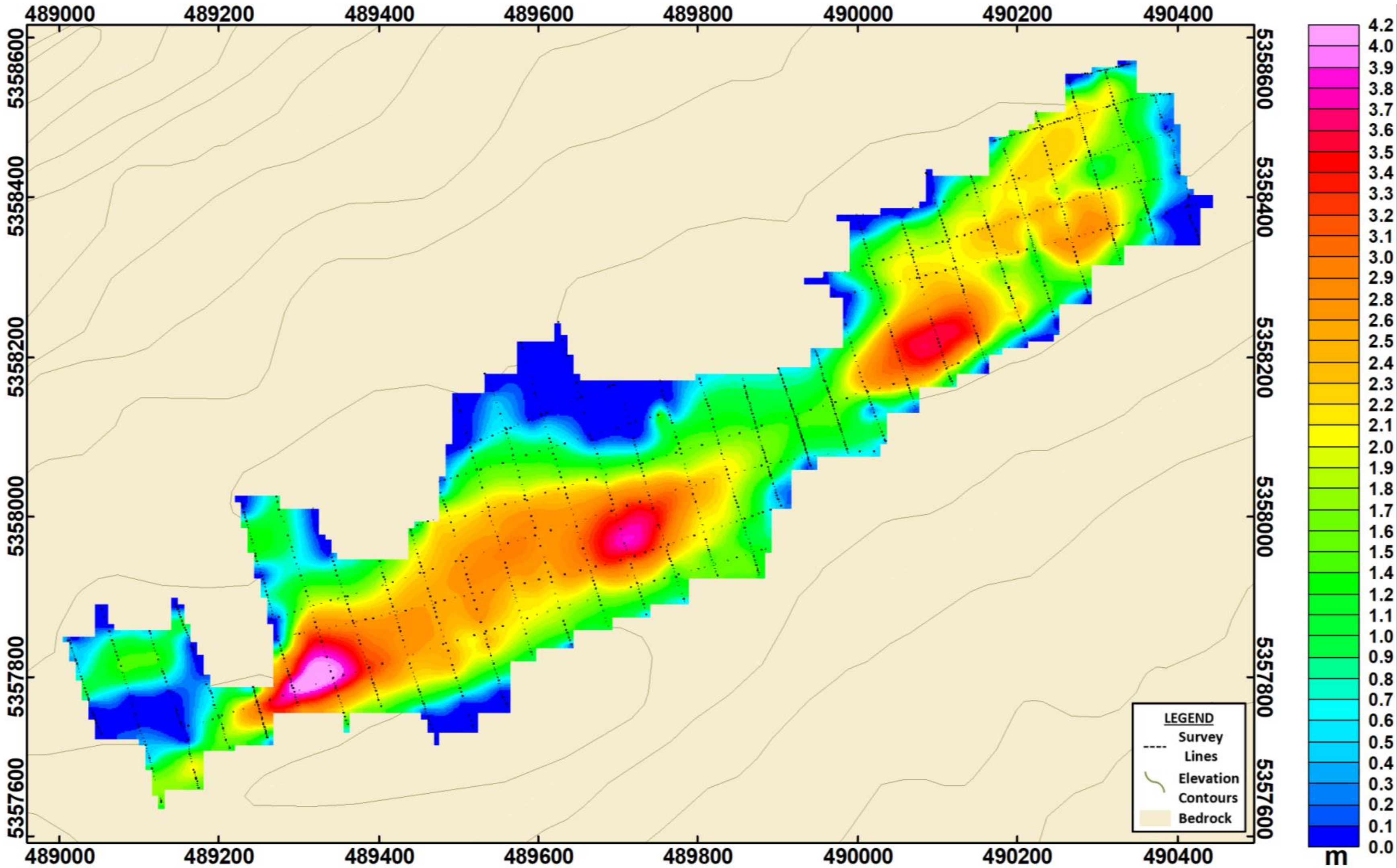

Figure F.8: Priority Area 7 (bog with small pond) hypsometry map showing qualitative variation with depth (see detailed analysis in Appendix H). It was gridded using minimum curvature, a cell size of 8 metres, cells to extend data beyond set to 0 and linear colour method.

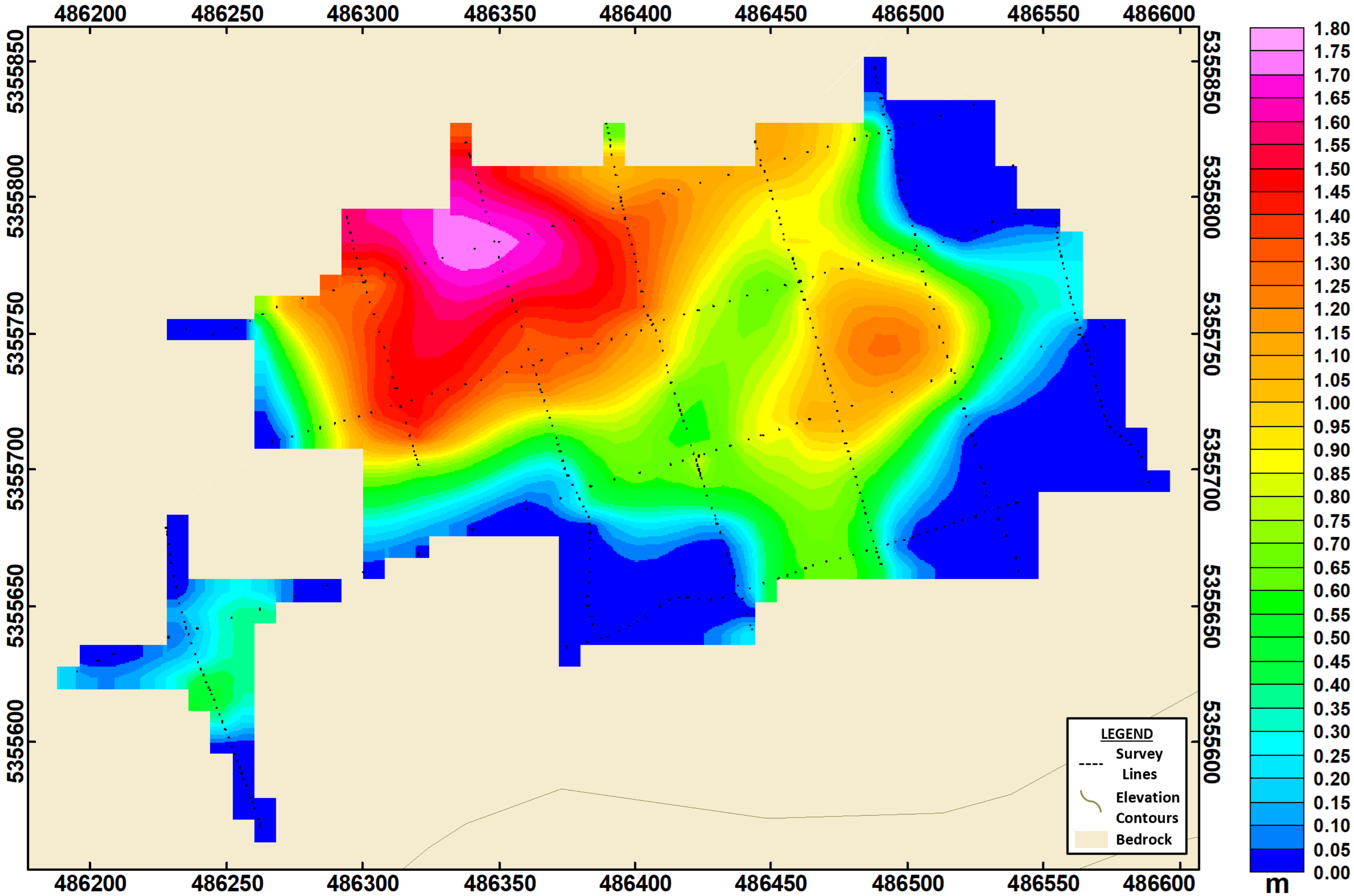

Figure F.9: Priority Area 8 (bog with small pond) hypsometry map showing qualitative variation with depth (see detailed analysis in Appendix H). It was gridded using minimum curvature, a cell size of 8 metres, cells to extend data beyond set to 0 and linear colour method.

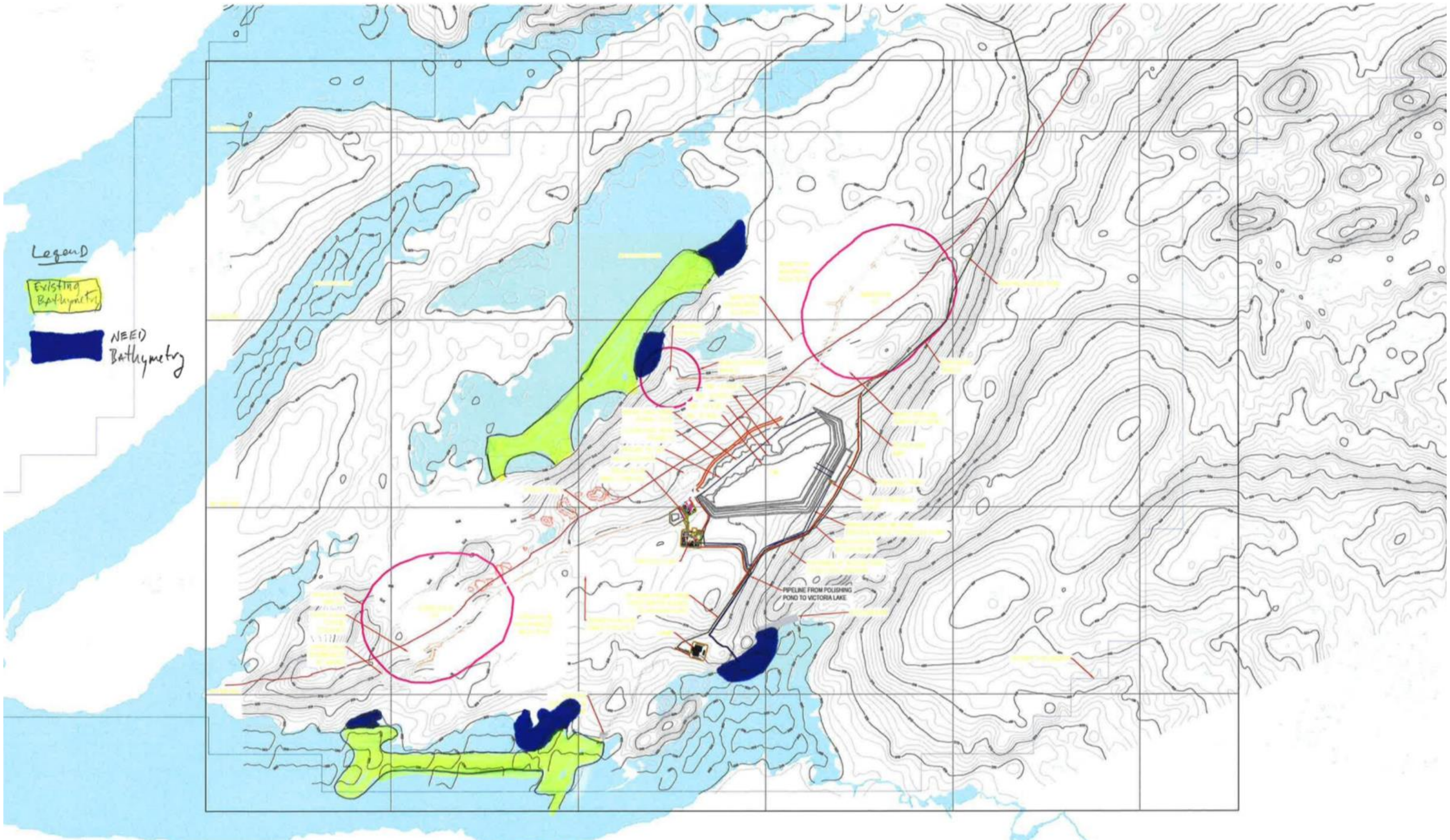

Figure F.10: Map provided by Marathon Gold Corporation indicating the outstanding bathymetry needs (dark blue) required for engineering purposes and the subsequent environmental and feasibility assessments. Existing bathymetry data (neon green) at the Valentine Gold Project is also shown.

APPENDIX G

SNOW AND ICE THICKNESS MEASUREMENTS AND BOG AND SOIL SAMPLE ANALYSIS

Table G.1: Ice and snow thickness measurements obtained from the small ponds within priority areas 4 and 5. Included are photos of the sample sites in area 4, additional depth to sediment and bedrock information for area 5 and noted observations from the measurement locations.

Pond Area	Line Type	DVL Line #	GPS Line #	Easting	Northing	Comments
4	X (TIE)	35	1450-3	490181	5356640	*all mud!! water fully frozen?*

Ice Thickness : **55cm**
Snow Thickness : **7.5-8.0cm**

Area 4: **pond** in foreground - **bog** in background (behind skidoo)

Hole 1: **Ice thickness** measurement

Hole 2: **Snow thickness** measurement

Pond Area	Line Type	DVL Line #	GPS Line #	Easting	Northing	Comments
5	Y	36	13250	489539	5356967	*contained some water*

Depth to Sediments : **1.05m** — *from top of snow to top of sediments/mud*
Ice Thickness : **55cm**
Snow Thickness : **15cm**
Depth of Boulders/Bedrock : **1.54m** — *hit solid on the bottom and had the "ping" of boulders or bedrock*

Table G.2: Ice and snow thickness measurements obtained from the small ponds within priority areas 7 and 8. Included are photos of the sample sites in area 7, additional depth to sediment and bedrock information for area 8 and noted observations from the measurement locations.

Pond Area	Line Type	DVL Line #	GPS Line #	Easting	Northing	Comments
7	Y	24	14250	490187	5358290	*all mud again!! water fully frozen?*

Ice Thickness : **79cm**
Snow Thickness : **23.4cm**

Area 7: **pond** in foreground **bog** in background (behind skidoo)

Hole 1: **Ice thickness** measurement - lots of mud!

Holes 1 + 2: **Snow Thickness** obtained from Hole 2

Pond Area	Line Type	DVL Line #	GPS Line #	Easting	Northing	Comments
8	X (TIE)	09	1650	486437	5355710	*contained some water*

Depth to Sediments : **65m** — *from top of snow to top of sediments/mud*
Ice Thickness : **48cm**
Snow Thickness : **13cm** — *pushed angle iron down to 2.11m, couldn't push any further but didn't get the "ping" of hitting bedrock, some sand at the end of the bar, so was likely in till*
Depth of Boulders/Bedrock : **???**

Table G.3: Water content analysis of 13 bog and 5 soil samples collected in the summer of 2019.

Start Date: August 27th, 2019 9:45 PM						Calibration							
					Weights (g)		Total Weight (g)						
					1000.2		4507.87						
					501.96								
	*Wgt = Weight				1003.7		Weight after Calibration (g)						
	*Wt = With				1001		4507.82						
	*W/O = Without				501								
					500.01								

Sample Name	Sealed Bag Wgt (g)	Sealed Bag Wgt Pre Bake (g)	Empty Jar (g)	Empty Jar Wt Cover (g)	Wet Sample in Jar W/O Cover (g)	Dry Sample W/O Cover (g)	Wet Sample in Jar Wt Cover (g)	Dry Sample Wt Cover (g)	Dirty Bag (g)	Stones Removed W/O Cover (g)	Wet Wgt (g)	Dry Wgt (g)	% Water
MA18346	903.04	901.9	403.97	417.77	1271.82	1155.45	1285.63	1169.26	33.67	970.59	682.99	566.62	17.03
Water Rd F6	856.99	855.96	404.85	418.7	1225.58	1065.63	1239.37	1079.45	34.27	784.09	539.19	379.38	29.64
Water Rd F23	964.09	963.01	406.47	420.42	1331.09	973	1345	986.99	33.89	No Stones	924.62	566.53	38.73
MA18346	865.8	864.76	404.41	417.91	1232.58	1108.59	1246.03	1122.11	33.4	947.83	667.41	543.42	18.5778
Drill Rd (CMP)	1492.93	1490.87	404.53	418.26	860.6	607.32	874.34	621.09	1021.34	597.03	445.78	192.5	56.8173
B6S1 Top	351.59	351.59	439.37	458.63	756.88	476.98	776.08	495.64	33.68	N/A	317.51	37.61	88.1547
B6S1 Middle	235.36	235.36	437.38	456.26	639.02	480.91	657.9	499.62	33.29	N/A	201.64	43.53	78.412
B6S1 Bottom	338.16	338.16	439.68	458.74	742.11	466.55	761.21	485.62	33.23	N/A	302.43	26.87	91.1153
B2S Top	264.96	264.96	438.79	457.62	667.02	460.95	685.81	479.38	35.06	N/A	228.23	22.16	90.2905
B2S Middle	301.93	301.93	438.29	457.85	704.41	479.56	723.89	498.96	34.82	N/A	266.12	41.27	84.492
B2S Bottom	313.48	312.36	444.6	463.65	724.4	471.33	743.35	490.28	32.33	N/A	279.8	26.73	90.4467
B8S2 All	231.78	231.19	403.97	417.57	603.39	429.8	617	443.42	31.64	N/A	199.42	25.83	87.0474
B7S1 Top	193.22	193.22	441.1	460.42	591.88	451.36	611.15	470.54	41.07	N/A	150.78	10.26	93.1954
B7S1 Middle	296.22	295.25	439.73	457.81	695.38	459.88	714.01	478.54	38.61	N/A	255.65	20.15	92.1181
B7S1 Bottom	290.78	290.1	440.43	459.8	659.01	462.37	714.31	481.54	35.3	N/A	218.58	21.94	89.9625
B7S2 Top	307.77	307.39	438.8	458.19	711.42	458.7	730.81	477.53	34.06	N/A	272.62	19.9	92.7005
B7S2 Middle	299.48	299.23	445.06	464.26	710.89	460.01	730.03	479.18	32.64	N/A	265.83	14.95	94.3761
B7S2 Bottom	313.3	313.14	444.63	463.65	719.7	464.8	738.71	483.81	37.48	N/A	275.07	20.17	92.6673

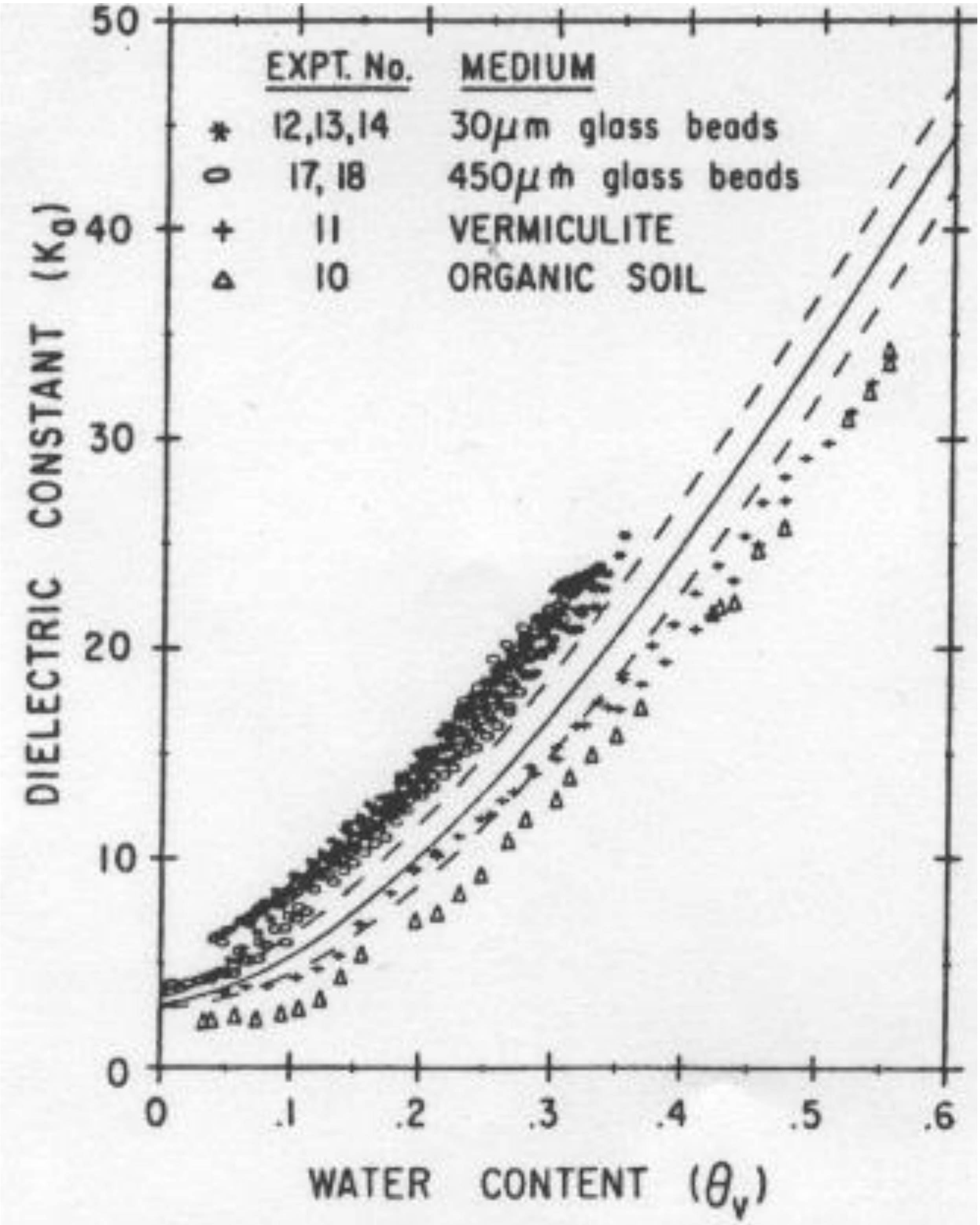

Figure G.1: Dielectric constant versus volumetric water content for glass beads, vermiculite and organic soil. The area between the dashed lines encompasses data for other soils (sandy loam to clays). Figure 6 of Topp et al. (1980).

Calculating Dielectric constant in wet bogs

A.M. Leitch July 2018

Topp et al. (1980) measured the dielectric constant (which determines the velocity of an EM wave) in various soils as a function of water content θ_v (Fig. G.1) and found best fit cubic polynomials to their data. For organic soil, their equation was:

$$\kappa = 1.74 - 0.34\,\theta_v + 135\,\theta_v^2 - 53.3\,\theta_v^3 \qquad \text{(G.1)}$$

The data for these experiments extended to $\theta_v = 0.55$. For $\theta_v = 1$, Equation (G.1) gives $\kappa = 81.78$. In the experiments, they measured κ for water at 20°C as 81.5 (Topp et al., 1980). The dielectric constant for water is a function of temperature (Fig. G.2), with an established value of 80.1 at 20°C (e.g., Moldoveanu and David, 2013).

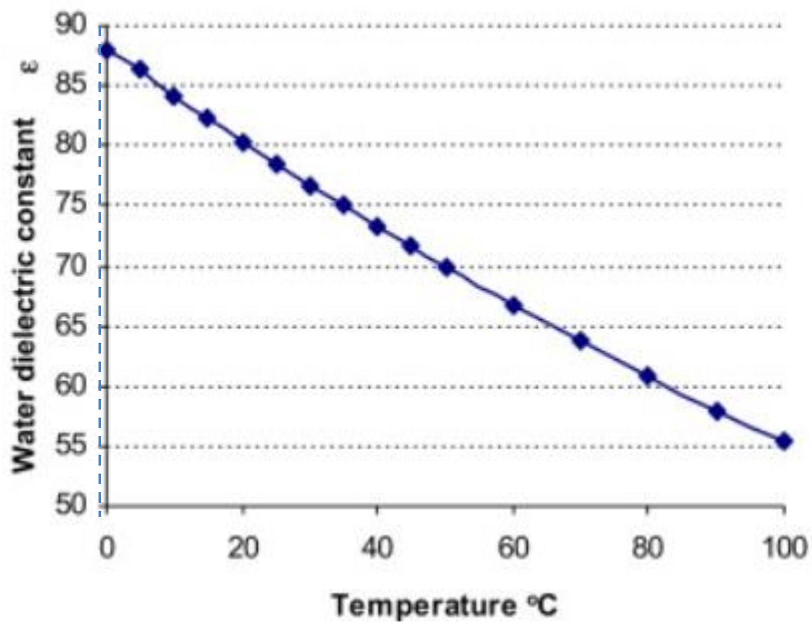

Figure G.2: Dielectric constant as a function of temperature for water (Figure 7.2.3. from Moldoveanu and David, 2013).

Given that the water content of wet bogs is very high, often more than 90%, it is desirable to find a fit to the data that is most accurate at high values of θ_v. To achieve this, the data in Figure G.1 were carefully read off the figure using an overlain grid and entered into an Excel spreadsheet. A value of $\kappa = 80.1$ for $\theta_v = 1$ was added to the data (Fig. G.3). A cubic fit best was found to be:

$$\kappa = 1.63 + 2.76\,\theta_v + 130\,\theta_v^2 - 54.4\,\theta_v^3 \qquad \text{(G.2)}$$

This equation produces $\kappa = 80.0$ for $\theta_v = 1$, and over the range 0 to 0.55 in θ_v, κ differs from the result of Eqn. (G.1) by at most 0.20.

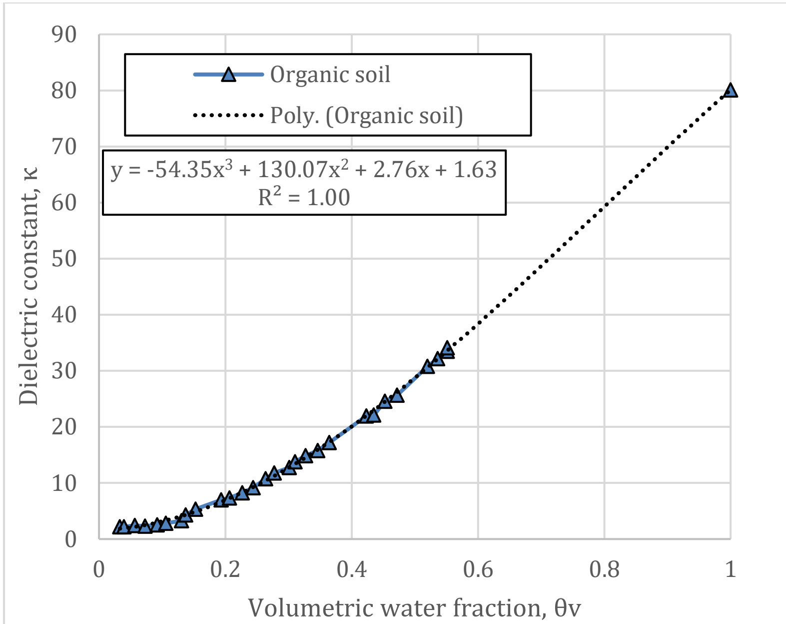

Figure G.3: Dielectric constant versus water content for organic soil (from Topp et al., 1980) with the addition of data point κ = 80.1 for θ_v =1, and best fit cubic polynomial.

For values of θ_v between 0.85 and 0.95, the wave velocity (v = c/√κ) based on these relations is between 0.037 and 0.035.

Topp et al. (1980) investigated the effect of temperatures between 10 and 30°C, for a soil with dielectric constant of about 20, and did not observe a significant change. In fact, their data suggests a slight increase in κ with increasing temperature, opposite the change for water in Figure G.2. The effect of temperature on velocities in wet bogs is unclear. If the velocities change as they do in water at high water content, then for values of θ_v between 0.85 and 0.95, the wave velocity is between 0.036 and 0.033.

An appropriate wave velocity for wet bogs can be taken as v ~ 0.035 ± 0.002 m/ns.

Note that our measurements of water content gave % by weight not volume, however the density of organic matter in bogs is very close to that of water, so there is a good correspondence between these two measures of water content.

References:

Topp, G.C., Davis, J.L. and Annan, A.P. 1980. Electromagnetic Determination of Soil Water Content: Measurements in Coaxial Transmission Lines, Water Resources Research. **16** (3): 574 – 582.

Moldoveanu, S.C., and David, V. 2013. Essentials in Modern HPLC Separations, Chapter 3, Mobile Phases and their Properties. pp. 532, Elsevier. https://doi.org/10.1016/B978-0-12-385013-3.00007-0.

APPENDIX H

GPR TWO-LAYER SYSTEM ANALYSIS

Allowing for ice/snow cover in GPR depth analysis over bogs and lakes

A.M. Leitch May 2021

Preamble

The *Sensors and Software* package EKKO_Project 5 displays wave reflection traces in a profile with the two-way travel time (TWT) on one vertical axis and a calculated depth on the other vertical axis (Fig. H.1). The left, depth axis is calculated based on two parameters provided by the user: the antenna separation and the subsurface velocity, which is assumed to be constant. The right, time axis starts at zero at the top of the profile and is linear. Inspection of the depth axis will reveal that there is an offset between zero time and zero depth, and that the axis is not quite linear at shallow depths. These are consequences of the antenna separation. The zero-depth offset in particular will be incorrect if the GPR is travelling over ice or snow. This document explains how to allow for this, to obtain more accurate estimates of depth in lakes and bogs beneath such a layer.

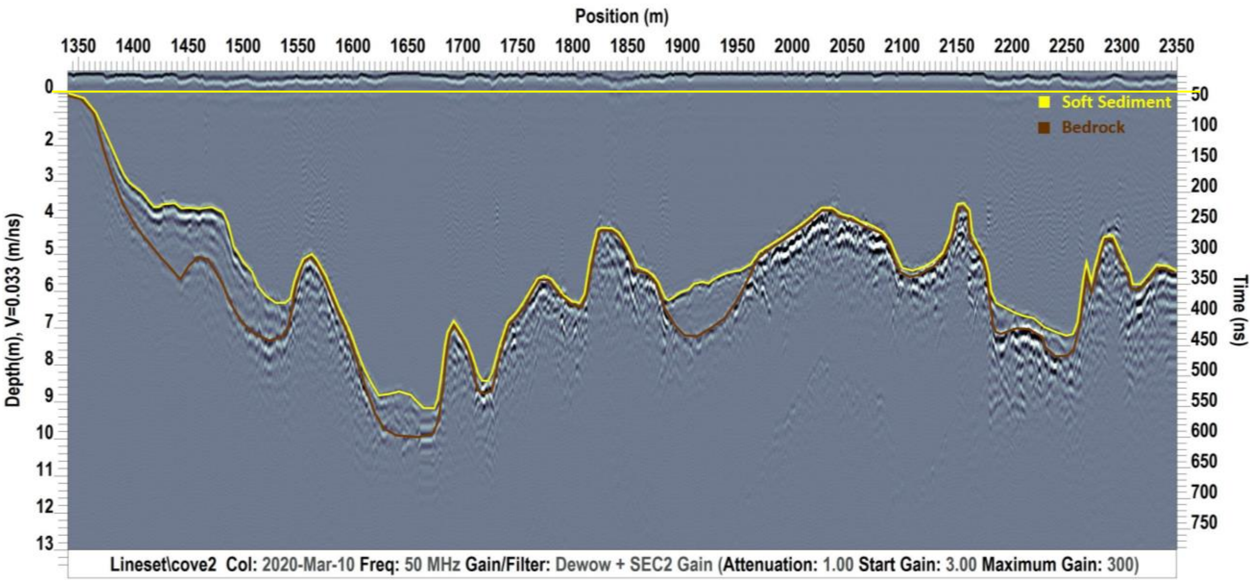

Figure H.1: Example GPR profile over a freshwater lake (Valentine Lake). The horizontal yellow line connects the zero on the depth axis to a finite offset on the time axis.

1. EKKO Project calculation of depth vs TWT

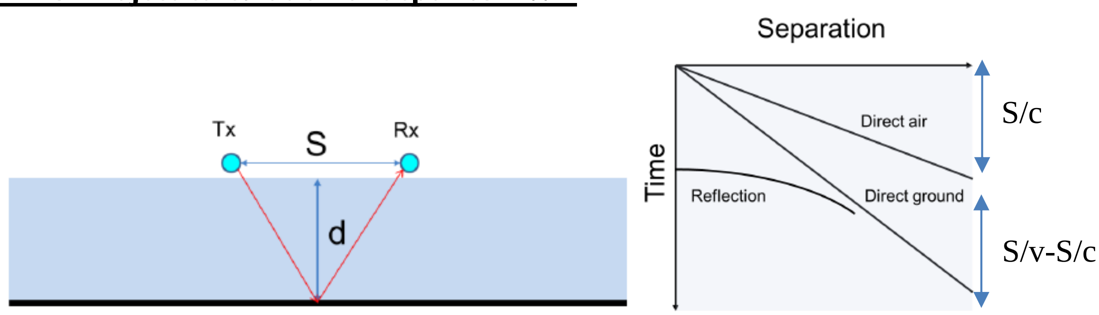

Figure H.2: Left: Common offset GPR geometry. Right: Three primary events observed on a GPR record, as a function of the separation between the transmitter (Tx) and receiver (Rx) antennas (Annan, 2015).

As illustrated in Figure H.2, for a survey over a uniform layer of depth d, underlain by a reflective boundary, a pulse emitted from the transmitter Tx produces three responses at the receiver Rx: from the pulse travelling through the air (‘*Direct air*’), from the pulse travelling horizontally through the ground (‘*Direct ground*’), and the reflection from the lower interface. If there is no separation between the antennas, the air and ground waves are coincident at time zero, and the TWT for the reflection is simply given by:

$$T_{rS0} = \frac{2d}{v} \;\; ; \quad d = \frac{1}{2} v T_{rS0} \tag{H.1}$$

where *v* is the (uniform) wave velocity in the subsurface.

For a finite separation, *S*, the time taken for the three waves to arrive after leaving the transmitter are:

$$T_a = \frac{S}{c} \;\; ; \;\; T_g = \frac{S}{v} \;\; ; \;\; T_r = \frac{2}{v}\sqrt{d^2 + (S/2)^2} \tag{H.2}$$

where *c* is the speed of light in air/vacuum. Now, the time axis at the receiver starts when the air wave arrives at the receiver, not when it leaves the transmitter, therefore, in ‘receiver time’ TWT the air wave travel time is subtracted. Thus:

$$TWT = \frac{2}{v}\sqrt{d^2 + (S/2)^2} - {}^{S}\!/_{c} \;\; ; \;\; d = \frac{1}{2}\left(v^2 (TWT + S/c)^2 - S^2\right)^{1/2} \tag{H.3}$$

Thus we can see that the relationship between d and TWT is not linear, and there is a zero offset. From Eqn. 3, the time offset at d=0 is (see Fig. 2):

$$TWT_{d0} = S\left(\frac{1}{v} - \frac{1}{c}\right) \;\; ; \;\; (d = 0) \tag{H.4}$$

For the example in Figure. H.1, for $v = 0.033$, $c = 0.3$ and $S = 1.4$, $TWT_{d0} = 1.4(1/0.033-1/0.3) = 38\ ns$. Plots of *d* from equations (H.1) and (H.3) are shown in Figure. H.3. Note the non-linearity for small *d* and the decreasing offset. This offset decreases as $TWT >> S/c$ and $vTWT >> S$.

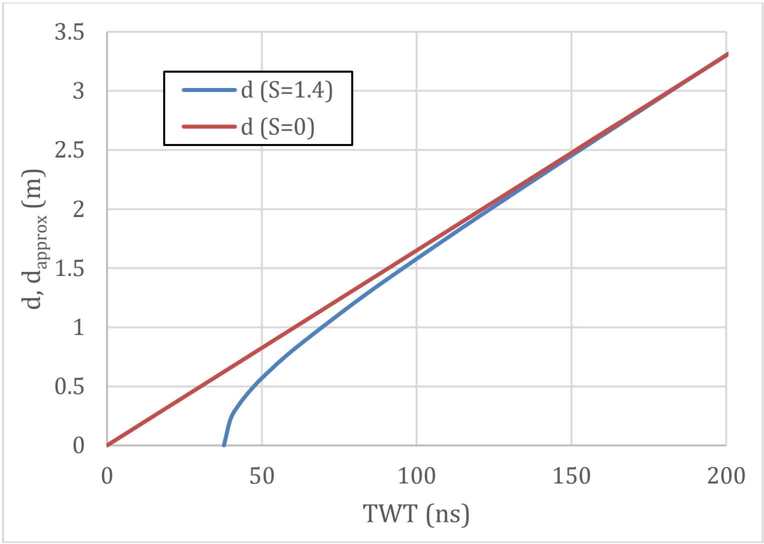

Figure H.3: The relationship between interface depth and TWT for two values of antenna separation, S.

2. A two-layer system

A general diagram of a two-layer system, where the wave velocity in the top layer is greater than that in the bottom layer (*v1* > *v2*) is shown in Figure A.4. This is the situation when the top layer is ice or snow, and the bottom layer is water or bog (or indeed most surficial materials).

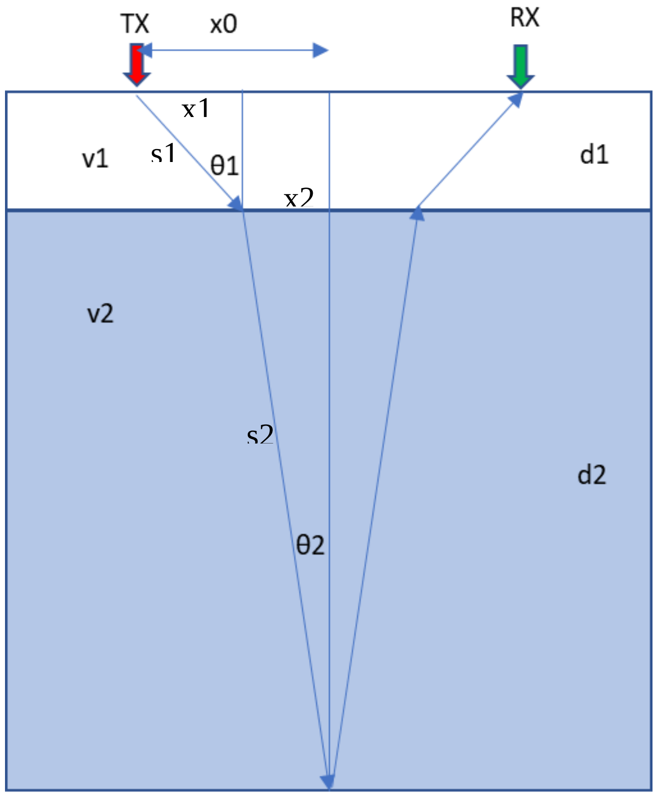

Figure H.4: Sketch of a 2-layer system, showing variables. Note that $x_0 = S/2$.

It is possible to derive general expressions relating the lower layer depth d_2 to TWT, if d_1 and the velocities and x_0 are known, however the expressions are very complex (Section 4). From Pythagoras (with receiver time starting when the air wave arrives) we have:

$$TWT = 2\left(\frac{\sqrt{x_1^2+d_1^2}}{v_1} + \frac{\sqrt{(x_0-x_1)^2+d_2^2}}{v_2} - \frac{x_0}{c}\right) \tag{H.5}$$

where $x_1 = x{*}x_0$ and x is the solution of the quartic equation:

$$x^4 - 2x^3 + [1 + d_1^2F + d_2^2(1-F)]x^2 - 2d_1^2Fx + d_1^2F = 0 \tag{H.6}$$

F is a function of the velocities:

$$F = \frac{v_1^2}{(v_1^2 - v_2^2)} \tag{H.7}$$

The quartic is not easy to solve analytically. It is easier to 'forward model' the system of equations, as is done in the Excel spreadsheet "*GPRonSnow+Ice*" which is presented in Section 5 as Tables H.4 and H.5.

2.1. <u>Valentine Lake Example</u>

Given values v_1, v_2, d_1 and x_0 (all known in a typical survey), it is straight forward to assign a range of values of θ_1, and then from the equations in Section 4 below, calculate TWT and d_2. This exercise was performed, using the spreadsheets shown in Tables H.4 and H.5, for the values in Table H.1.

Table H.1: Parameter values for bathymetry surveys over Valentine and Victoria Lakes.

Variable	Value	Units
$\boldsymbol{v_1}$ (ice)	0.16	m/ns
$\boldsymbol{v_2}$ (water)	0.033	m/ns
$\boldsymbol{d_1}$ (ice thickness)	0.65	m
$\boldsymbol{x_0}$ (half antenna separation = $S/2$)	0.7	m

Figure H.5 shows the difference between the actual depth of the 2-layer system ($d_1 + d_2$), and the calculated assuming a 1-layer system (d_{EKKO} from Eqn. H.3), versus the calculated depth d_{EKKO}. Thus, the graph shows the amount that should be *added* to the interpretations of bathymetry. The graph asymptote to 0.48 for higher values of d. It is seen that the 1-layer solution (provided by EKKO_project for $v = 0.033$) always underestimates the depth. (Basically, because the wave travels much faster in ice than in water, so the contribution of the ice layer to the total depth is underestimated.) The discrepancy is about 0.5 m for $d_{EKKO} > 3m$ and given the resolution of the 50

MHz antennas (0.165 m in water), it is valid to add 0.5 m to EKKO_project's values for all values of $d_{EKKO} \geq 1\ m$. For apparent depths less than this, the depths are more seriously underestimated. For $d_{EKKO} \approx 0.5\ m$, the discrepancy is about 0.8 m (so actual depth is 1.3 m), and for an apparent depth of 0, the actual depth is about 1.1 m.

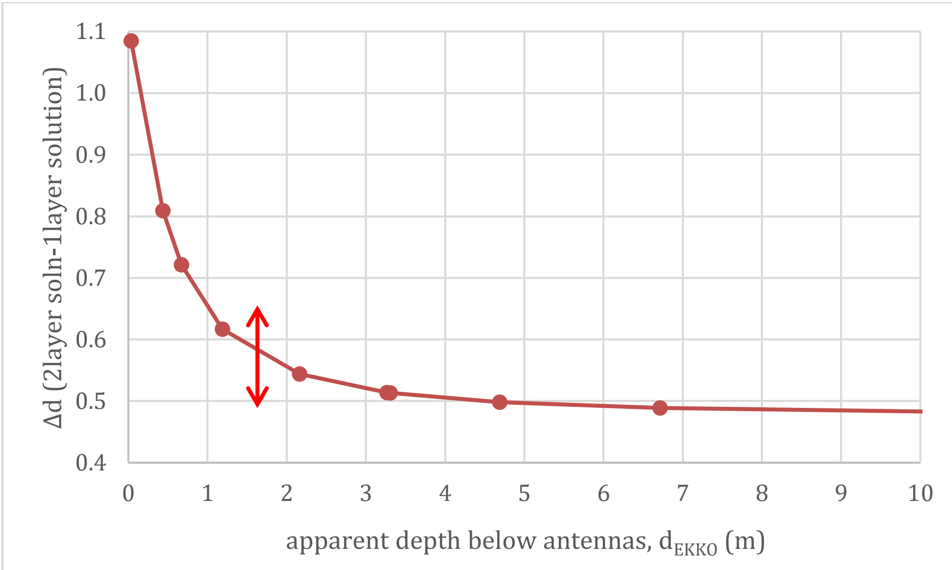

Figure H.5: $\Delta d = d_{actual}$ (2-layer solution) – d_{EKKO} (1 layer solution) versus d_{EKKO}. For the two-layer solution, $d = d_1+d_2$ (i.e., including ice and water layers). Double ended arrow gives the resolution for 50 MHz antennas in water. Calculated for survey parameters in Table H.1.

It should be noted that, for bathymetry surveys over the Valentine and Victoria lakes, the desired information is the elevation (above sea level) of the bottom of the lake. Therefore, the distance between the known elevation of the ice surface and the bottom of the lake is to be measured. This is a different situation than the hypsometry surveys of the bogs, where bog thickness is the desired measure.

2.2. Bog Example

For surveys over the bogs, the desired measurement is d_2, not the total depth beneath the antennas $d_2 + d_1$, and the cover is typically snow. There may be a layer of frozen ground beneath the snow (though this was not observed in *Marathon* bogs in winter 2020). This is not considered here.

Dry snow is a mix of ice and air, so the wave velocity depends on the ratio, varying between 0.3 m/ns for air and 0.16 m/ns for ice. Figure H.6 illustrates the variation between these limits.

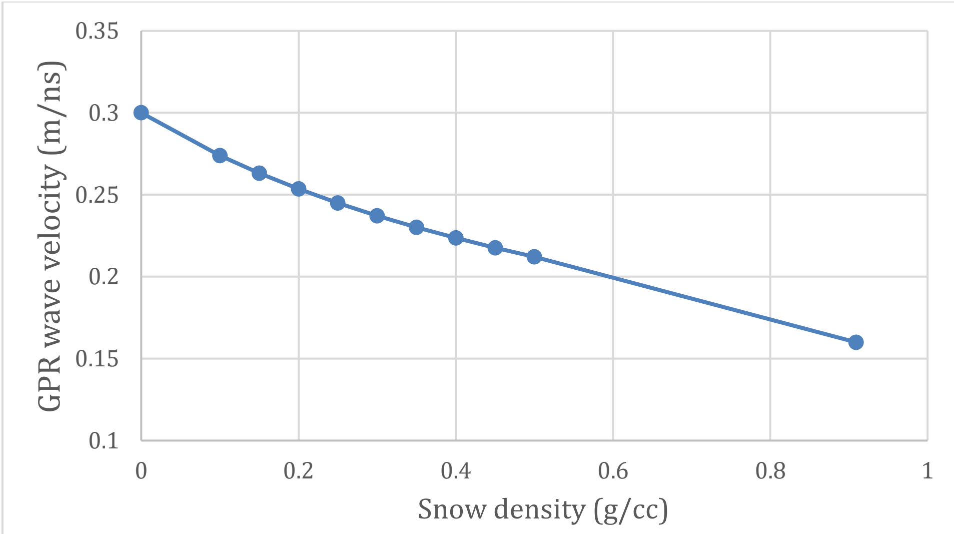

Figure H.6: GPR wave velocity versus snow density.

In the following, an intermediate value of snow compaction is assumed. For a snow density of 0.42 g/cm^3, the wave velocity is 0.22 m/ns. Snow thicknesses measured in the winter of 2020 were mostly between 0.5 and 1 m.

Table H.2: Parameter values for hypsometry surveys over bogs.

Variable	**Value**	**Units**
$\boldsymbol{v_1}$ (snow)	0.22	m/ns
$\boldsymbol{v_2}$ (bog)	0.035	m/ns
$\boldsymbol{d_1}$ (snow thickness)	0.5-1.0	m
$\boldsymbol{x_0}$ (half antenna separation=S/2)	0.7	m

For an overlying layer of snow, as for the case of an overlying layer of ice, estimates of the distance between the antennas and the bottom of the bog from Equation H.3 (assuming constant velocity) are always less than the actual distance (because the wave travels faster in the snow – even faster than in ice).

However, if we compare the results of Equation H.3 (d_{EKKO}) with the depth of the second (bog) layer only, then the difference can be positive or negative (Figure H.7).

For apparent depths > 1.5 m (for 0.5 m snow cover) or > 1 m (for 1 m snow cover), the measured depth is more than the actual depth, so up to ~10 cm (~20 cm for 1 m of snow) should be *subtracted* from the measured bog depth d_{EKKO}. This is because the wave spends some time traversing the snow layer. It is much shorter than the time it would spend traversing an equivalent layer of bog, because the wave speed in snow is more than 6x faster than it is in bog, but it still adds to the time. (The extra time is not exactly $d_{snow} \times v_{snow}/v_{bog}$ because of the zero offset time being calculated for bog rather than snow.) Note that for snow depth less than about 1 m, the correction to the bog depth is comparable to the resolution of the 50 MHz antennas, so arguably insignificant.

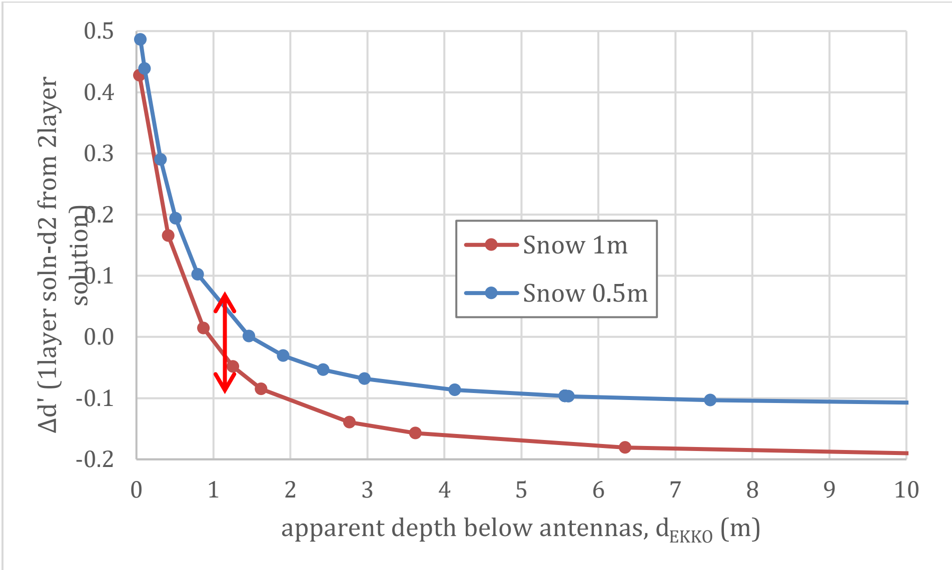

Figure H.7: $\Delta d' = d_{2actual}$ (2-layer solution) – d_{EKKO} (1-layer solution) versus d_{EKKO}. For the two-layer solution, d_2 corresponds to the bog layer only. Double ended arrow gives the resolution for 50 MHz antennas in water. Calculated for survey parameters in Table H.2.

For small apparent depths, the actual bog depth is deeper by up to 40 or 50 cm. This is due mainly to the incorrect zero offset for depth. TWT_{d0} in Equation H.4 should have v for snow rather than v for the bog.

$$TWT_{d0}(bog) = 1.4\left(\frac{1}{0.035} - \frac{1}{0.3}\right) = 35.3\,ns;\;\; (d = 0) \qquad \text{(H.8a)}$$

$$TWT_{d0}(snow) = 1.4\left(\frac{1}{0.22} - \frac{1}{0.3}\right) = 1.70\,ns;\;\; (d = 0) \qquad \text{(H.8b)}$$

This difference of 33.6 ns corresponds to a thickness of *33.6 x 0.035 = 0.6 m* of bog. The other factor, which partially offsets this effect, is that for small depths the angle θ_1 (Figure H.4) is relatively large, so the path through the bog layer is more nearly vertical (the wave spends less time in the bog than it would if it followed the path illustrated in the left panel of Figure H.2).

3. <u>Suggested corrections</u>

For the lake, the purposes of the bathymetry survey were: 1) to make terrain gravity corrections; 2) estimates of unfrozen water in winter (to see whether fish would survive). For both these purposes, estimates of water depths in shallow areas (< 1 m) are unimportant, so a general correction of adding ~0.5 m to all bathymetric measurements is adequate (see Section 5.2.1.3).

For the bogs, a similar argument might be made. In this case, one could say that the existing maps show the qualitative variation with depth; that for apparent depths > 1m, the real depth is a little shallower but only by 10 or 20 cm, similar to the resolution of the GPR; and that for apparent depths of < 1m, the bog depths are greater by a few decimeters (up to 50 cm).

If this is not good enough, we can make an estimated correction. The maximum (apparent) bog depth is 4.8 m. An empirical correction for bog depth, assuming snow cover between 0.5 and 1 m, is (within 3cm):

$$d_2 = d_{EKKO} + \frac{A}{d_{EKKO}^{1.5} + B} + C \quad \text{(H.9)}$$

where the values of A, B and C are given in Table H.3. An example of the fit is shown in Figure H.8. The main difference the snow depth makes in the fit is in the offset C.

Table H.3: Parameter values for Equation (9), for bog depths up to 5 m.

Snow cover (m)	A	B	C	Max error (m)
0.5	0.19	0.3	-0.12	0.03
0.75	0.19	0.31	-0.15	0.03
1.0	0.18	0.3	-0.18	0.03

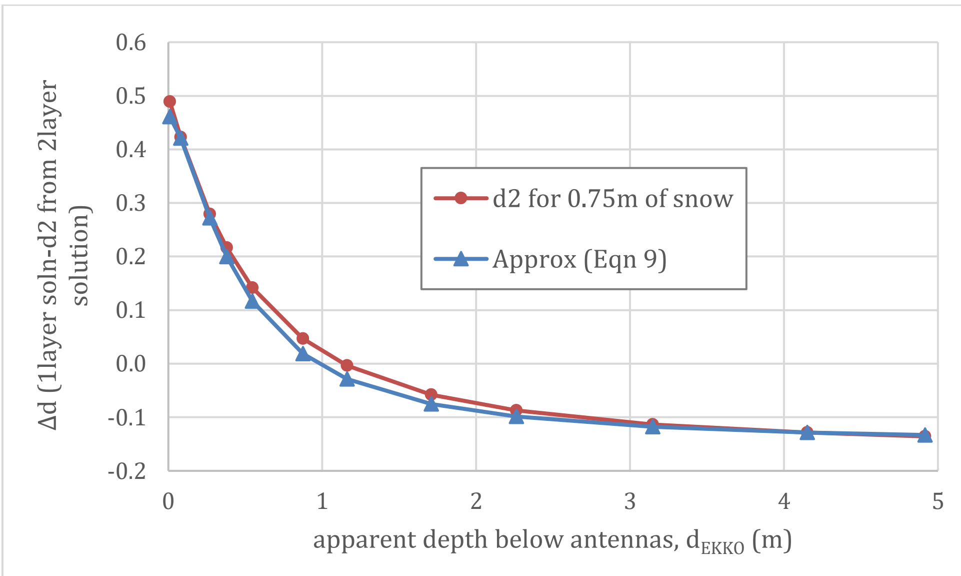

Figure H.8: The amount Δd to be added to apparent depth (d_{EKKO}) of bog to allow for 75 cm of overlying snow, and approximation (empirical fit) given by Equation H.9.

4. General Solution for an EM wave travelling through a 2-layer system

'Known' Variables:

- $\boldsymbol{v_1, v_2}$ (velocities in layers 1 and 2)
- $\boldsymbol{d_1, d_2}$ (thicknesses of layers 1 and 2)
- $\boldsymbol{x_0}$ (half-separation of Tx and Rx)

'Unknown' Variables:

$\boldsymbol{x_1, x_2}$ (half horizontal distances travelled in layers 1 and 2)

$\boldsymbol{s_1, s_2}$ (half total distances travelled in layers 1 and 2)

$\boldsymbol{\theta_1, \theta_2}$ (angles taken by rays, measured from the vertical)

TWT (two-way travel time of rays, measured from when the air wave reaches the receiver)

Equations:

$$v_2 \sin\theta_1 = v_1 \sin\theta_2 \qquad \textit{Snell's Law} \qquad \text{(H.10)}$$

$$s_1^2 = x_1^2 + d_1^2 \qquad \textit{Pythagoras} \qquad \text{(H.11)}$$

$$s_2^2 = x_2^2 + d_2^2 \qquad \text{(H.12)}$$

$$TWT = 2\left(\frac{s_1}{v_1} + \frac{s_2}{v_2} - \frac{x_0}{c}\right) \qquad \text{(H.13)}$$

$$x_0 = x_1 + x_2 \qquad \text{(H.14)}$$

$$\sin\theta_1 = \frac{x_1}{s_1} \qquad \text{(H.15)}$$

$$\sin\theta_2 = \frac{x_2}{s_2} \qquad \text{(H.16)}$$

7 equations for 7 unknowns, therefore have a unique solution. We want *TWT* as function of *d*'s and *v*'s.

So, eliminate angles, s's and x's. There are 3 key distances, d_1, d_2 and x_0.

First, eliminate the angles. Substitute (H.15) and (H.16) into (H.10)

$$v_2 \frac{x_1}{s_1} = v_1 \frac{x_2}{s_2}; \quad \frac{x_1}{v_1 s_1} = \frac{x_2}{v_2 s_2} \qquad \text{(H.17)}$$

Scale distances by $\boldsymbol{x_0}$ (i.e. $x_0 \rightarrow 1$, $x_1 \rightarrow x_1/x_0 = x$, $s_1 \rightarrow s_1/x_0$, etc.) This eliminates x_2.

$$x_2{}' = 1 - x \tag{H.18}$$

$$\frac{x}{v_1 s_1} = \frac{(1-x)}{v_2 s_2} \tag{H.19}$$

$$s_1^2 = x^2 + d_1^2 \tag{H.20}$$

$$s_2^2 = (1-x)^2 + d_2^2 \tag{H.21}$$

3 Equations, 3 remaining unknowns: x, s_1, and s_2 (*TWT* is a function of the others).

From (H.19)

$$\frac{s_1}{s_2} = \frac{x}{(1-x)}\frac{v_2}{v_1} \quad ; \quad \frac{s_1^2}{s_2^2} = \frac{x^2}{(1-x)^2}R^2 \tag{H.22}$$

where $R = v_2/v_1$

Dividing (H.20) by (H.21):

$$\frac{s_1^2}{s_2^2} = \frac{x^2 + d_1^2}{(1-x)^2 + d_2^2} = \frac{x^2}{(1-x)^2}R^2 \tag{H.23}$$

Multiplying through:

$$(x^2 + d_1^2)(1-x)^2 = x^2\ ((1-x)^2 + d_2^2)R^2 \tag{H.24}$$

Expanding:

$$(x^2 + d_1^2)(1 - 2x + x^2) = x^2\ (1 - 2x + x^2 + d_2^2)R^2 \tag{H.25a}$$

$$x^2 + d_1^2 - 2x^3 - 2xd_1^2 + x^4 + x^2 d_1^2 = R^2x^2\ - 2R^2x^3 + R^2x^4 + d_2^2R^2x^2 \tag{H.25b}$$

Gathering terms:

$$(1-R^2)x^4 - 2(1-R^2)x^3 + (1 - R^2 + d_1^2 - d_2^2R^2)x^2 - 2xd_1^2 + d_1^2 = 0$$

Divide by (1-R^2):

$$x^4 - 2x^3 + \left(1 + \frac{d_1^2 - d_2^2R^2}{(1-R^2)}\right)x^2 - \frac{2xd_1^2}{(1-R^2)} + \frac{d_1^2}{(1-R^2)} = 0$$

Let $F = 1/(1-R^2)$, $R^2/(1-R^2) = F-1$

$$F = \left(1 - \frac{v_2^2}{v_1^2}\right)^{-1} = \frac{v_1^2}{v_1^2 - v_2^2} \tag{H.26}$$

$$x^4 - 2x^3 + (1 + Fd_1^2 - (F-1)d_2^2)x^2 - 2Fd_1^2 x + Fd_1^2 = 0 \tag{H.27}$$

The two-way travel time is:

$$TWT = 2\left(\frac{s_1}{v_1} + \frac{s_2}{v_2} - \frac{x_0}{c}\right) \tag{H.13}$$

In terms of d_1, d_2 and x, *TWT'* (normalized wrt x_0) is:

$$TWT' = 2\left(\frac{\sqrt{x^2 + d_1^2}}{v_1} + \frac{\sqrt{(1-x)^2 + d_2^2}}{v_2} - \frac{1}{c}\right) \tag{H.28}$$

TWT' is scaled time. NOTE: if distances are scaled with x_0 and velocities are not, then times *TWT'=x'/v* (scaled x). Actual *TWT* = x' x x_0/*v*, so times need to be multiplied by x_0.

NOTE THAT DISTANCES ARE ALL SCALED WRT x_0

5. GPR on Snow and Ice Spreadsheets

Table H.4: GPR two-layer ice analysis spreadsheet.

These calculations make use of the analysis in Section 4
Given the velocities v1 and v2, the antenna separation 2x0, and the depth of the top layer d1
For a range of theta1, we calculate theta2 from Snell's Law, then x1 and x2 from trigonometry
If x2<0, then theta1 is too large to penetrate into the lower layer (no solution)
d2 is then calculated (trigonometry), and s1 and s2 from Pythagoras
TWT1 and TWT2 are the two way travel times in the two layers, TWT is the sum of these times and TWT1/TWT2 the ratio

Eqn. H.27 is a check on the equations. It should be zero.
The distance variables are normalized wrt x0 (this does not affect angles). To return to normalized time, TWT is multiplied by x0.

th1max=atan(1/d1)
theta2=atan(x2/d2)
d2=x2/tan(th2)
Note what happens when v2>v1

Example:			m	norm.			norm.			norm.
v1=	0.16	d1=	0.65	0.9286	R=	0.2063		s1(diag)=	0.9552	1.3646409
v2=	0.033	d2=			F=	1.0444		s1(diag)/v1=	5.9703	8.5290059
x0=	0.7	th1max=	47.12		x0/c=	2.3333	3.333	d1/v1=	4.0625	5.8035714

											Normalized	norm.				
theta1	theta2	x1	x2	d2(m)	s1	s2	TWT1	TWT2	TWT(ns)	TWT1/TWT2	x	Eqn. H.27	x0/d2	d1+d2	d1lay (m)	d2lay-d1lay
5	1.03	0.057	0.643	35.772	0.65	35.78	8.2	2168.3	2174.2	0.0038	0.081	-2.1094E-15	0.020	36.422	35.94379	0.48
8	1.64	0.091	0.609	21.195	0.66	21.20	8.2	1285.1	1291.0	0.0064	0.131	-2.1094E-15	0.033	21.845	21.36639	0.48
10	2.05	0.115	0.585	16.334	0.66	16.34	8.3	990.6	996.5	0.0083	0.164	-1.3323E-15	0.043	16.984	16.50458	0.48
15	3.06	0.174	0.526	9.836	0.67	9.85	8.4	597.0	603.1	0.0141	0.249	-1.6653E-15	0.071	10.486	10.00332	0.48
20	4.05	0.237	0.463	6.553	0.69	6.57	8.6	398.1	404.5	0.0217	0.338	-1.4433E-15	0.107	7.203	6.714218	0.49
25	5.00	0.303	0.397	4.536	0.72	4.55	9.0	276.0	282.6	0.0325	0.433	-8.8818E-16	0.154	5.186	4.68788	0.50
29.85	5.89	0.373	0.327	3.168	0.75	3.19	9.4	193.0	200.1	0.0485	0.533	-8.8818E-16	0.221	3.818	3.304998	0.51
30	5.92	0.375	0.325	3.132	0.75	3.15	9.4	190.8	197.9	0.0492	0.536	0	0.223	3.782	3.267996	0.51
35	6.79	0.455	0.245	2.055	0.79	2.07	9.9	125.4	133.0	0.0791	0.650	0	0.341	2.705	2.161502	0.54
40	7.62	0.545	0.155	1.156	0.85	1.17	10.6	70.7	78.9	0.1501	0.779	0	0.606	1.806	1.188737	0.62
42.5	8.01	0.596	0.104	0.742	0.88	0.75	11.0	45.4	54.1	0.2427	0.851	0	0.944	1.392	0.670723	0.72
43.4	8.15	0.615	0.085	0.596	0.89	0.60	11.2	36.5	45.3	0.3064	0.878	0	1.174	1.246	0.436832	0.81
44.18	8.26	0.632	0.068	0.471	0.91	0.48	11.3	28.8	37.8	0.3932	0.902	0	1.488	1.121	0.035711	1.08
47.1	8.69	0.699	0.001	0.003	0.95	0.00	11.9	0.2	9.8	57.5880	0.999	0	207.065	0.653		
50	9.09	0.775	-0.075	-0.466	1.01	0.47	12.6	28.6	38.9	0.4415	1.107	0	-1.501			
55	9.73	0.928	-0.228	-1.332	1.13	1.35	14.2	81.9	93.7	0.1730	1.326	0	-0.526			
60	10.29	1.126	-0.426	-2.346	1.30	2.38	16.3	144.5	158.4	0.1125	1.608	-4.3299E-15	-0.298			
65	10.77	1.394	-0.694	-3.647	1.54	3.71	19.2	225.0	241.9	0.0855	1.991	-1.3212E-14	-0.192			
70	11.18	1.786	-1.086	-5.496	1.90	5.60	23.8	339.6	361.0	0.0700	2.551	-3.5416E-14	-0.127			
75	11.49	2.426	-1.726	-8.489	2.51	8.66	31.4	525.0	554.1	0.0598	3.465	-2.3703E-13	-0.082			
80	11.72	3.686	-2.986	-14.396	3.74	14.70	46.8	891.1	935.5	0.0525	5.266	-1.5551E-12	-0.049			
85	11.86	7.430	-6.730	-32.054	7.46	32.75	93.2	1985.0	2075.9	0.0470	10.614	-3.6205E-11	-0.022			

Table H.5: GPR two-layer snow (approximation) analysis spreadsheet.

Here, we are after an empirical formula to correct bog depths up to 4.8 m, using an average snow thickness of 75cm.
These calculations make use of the analysis in Section 4
Given the velocities v1 and v2, the antenna separation 2*x0, and the depth of the top layer d1

For a range of theta1, we calculate theta2 from Snell's Law, then x1 and x2 from trigonometry
If x2<0, then theta1 is too large to penetrate into the lower layer (no solution)
d2 is then calculated (trigonometry), and s1 and s2 from Pythagoras
TWT1 and TWT2 are the two way travel times in the two layers, TWT is the sum of these times and TWT1/TWT2 the ratio
(H.27) is a check. It should be zero.

th1max=atan(1/d1)
theta2=atan(x2/d2)
d2=x2/tan(th2)
Note what happens when v2>v1

							norm.														
Example:			m	**norm.**				**s1(diag)=**	1.0259142	**norm.**											
v1=	0.22	**d1=**	0.75	1.0714286	**R=**	0.1590909		**s1(diag)/v1=**	4.6632465	1.46559175											
v2=	0.035	**d2=**			**F=**	1.0259671				6.66178069											
x0=	0.7	**th1max=**	43.03		**x0/c=**	2.3333333	3.3333333	**d1/v1=**	3.4090909	4.87012987										-0.15	
																				1.5	
																				1/x^n	**error**
		normalized	**normalized**	**normalized**	**normalized**	**normalized**	**normalized**	**normalized**	**normalized**			**normalized**	**normalized**	**normalized**				d1=0.75	0	0.19	
theta1	**theta2**	**x1**	**x2**	**d2**	**s1**	**s2**	**TWT1**	**TWT2**	**TWT (ns)**	**TWT1/TWT2**	**x**	**Eqn. H.27**	**x0/d2**	**d1+d2**	**d1lay (m)**	**d1l-d2lay**	**d2-d1layer**	**off**	0.31		
26	4.00	0.366	0.334	4.780	0.83	4.79	7.6	273.8	279.1	0.0277	0.5226	0	0.209	5.530	4.916034	-0.61	-0.136	-0.14	-0.13305	0.003	
28	4.28	0.399	0.301	4.022	0.85	4.03	7.7	230.5	235.8	0.0335	0.5697	0	0.249	4.772	4.150333	-0.62	-0.129	-0.13	-0.12832	0.000	
31	4.70	0.451	0.249	3.033	0.87	3.04	8.0	173.9	179.5	0.0457	0.6438	0	0.330	3.783	3.14632	-0.64	-0.113	-0.11	-0.11775	-0.004	
34	5.10	0.506	0.194	2.173	0.90	2.18	8.2	124.7	130.6	0.0660	0.7227	0	0.460	2.923	2.2609	-0.66	-0.088	-0.09	-0.09878	-0.011	
36	5.37	0.545	0.155	1.651	0.93	1.66	8.4	94.8	100.9	0.0889	0.7784	0	0.606	2.401	1.709071	-0.69	-0.058	-0.06	-0.07532	-0.018	
38	5.62	0.586	0.114	1.159	0.95	1.16	8.7	66.5	72.8	0.1301	0.8371	0	0.863	1.909	1.161959	-0.75	-0.003	0.00	-0.0284	-0.025	
39	5.75	0.607	0.093	0.921	0.97	0.93	8.8	52.9	59.3	0.1659	0.8676	0	1.086	1.671	0.874151	-0.80	0.047	0.05	0.018545	-0.028	
40	5.87	0.629	0.071	0.687	0.98	0.69	8.9	39.5	46.1	0.2254	0.8990	0	1.455	1.437	0.545927	-0.89	0.142	0.14	0.116342	-0.025	
40.4	5.92	0.638	0.062	0.595	0.98	0.60	9.0	34.2	40.8	0.2618	0.9119	0	1.680	1.345	0.378765	-0.97	0.216	0.22	0.199839	-0.017	
40.6	5.94	0.643	0.057	0.549	0.99	0.55	9.0	31.6	38.2	0.2846	0.9183	0	1.821	1.299	0.26981	-1.03	0.279	0.28	0.272083	-0.007	
40.8	5.97	0.647	0.053	0.503	0.99	0.51	9.0	28.9	35.6	0.3114	0.9248	0	1.986	1.253	0.080537	-1.17	0.423	0.42	0.420818	-0.002	
40.82	5.97	0.648	0.052	0.499	0.99	0.50	9.0	28.7	35.3	0.3144	0.9255	0	2.005	1.249	0.009634	-1.24	0.489	0.49	0.461039	-0.028	
42.5	6.17	0.687	0.013	0.118	1.02	0.12	9.2	6.8	13.7	1.3641	0.9818	0	8.478	0.868						0.010	**Stdev**

APPENDIX I

STANTEC BATHYMETRY DATA AND DEPTH COMPARISON ANALYSIS

Table I.1: Sample of the additional bathymetry data acquired by Stantec Inc. in 2010 and 2018.

Valentine Lake				Victoria Lake			
Latitude	Longitude	Temperature	Depth_m	Latitude	Longitude	Temperature	Depth_m
48.3853584	-57.14627535	25.75938225	1.95619202	48.341283	-57.16017866	19.05344582	14.48724747
48.38517115	-57.14689167	24.998106	1.94642639	48.34092685	-57.16130561	19.04225349	13.16870117
48.38495758	-57.14747907	24.47192955	3.11846161	48.3407935	-57.1626561	19.01986122	12.21153641
48.38525908	-57.14733675	24.1472683	2.27850342	48.34076576	-57.16305607	19.01986122	10.41440964
48.38569426	-57.14696224	24.01292992	2.67895126	48.34076325	-57.16309866	19.01986122	10.61951447
48.38652097	-57.14627744	23.80021858	5.89228821	48.34076081	-57.16313998	19.01986122	10.41440964
48.38692548	-57.14596597	23.65468025	8.03126144	48.34075804	-57.16318189	19.01986122	10.48277664
48.38722522	-57.1454711	23.40838432	6.20483398	48.34075486	-57.1632238	19.01986122	10.61951447
48.38768564	-57.14538795	23.13969994	2.62034607	48.34075109	-57.16326379	19.01986122	10.55114746
48.38814362	-57.14533506	22.89340782	6.47830963	48.34074774	-57.16330393	19.01986122	10.89299011
48.38860019	-57.14517061	22.75906181	7.44524384	48.34074505	-57.16334349	19.00866508	10.61951447
48.38903755	-57.14491077	22.66950417	5.86298752	48.34074238	-57.16338491	19.00866508	11.10786438
48.38935162	-57.14444147	22.4791851	8.45124435	48.34073868	-57.16342521	19.00866508	10.55114746
48.38976133	-57.14416017	22.38962364	11.0297279	48.3407365	-57.16346529	19.00866508	10.68788528
48.39018202	-57.14384133	22.3112545	12.4166451	48.34073482	-57.16350526	19.00866508	10.61951447
48.39056323	-57.14346204	22.27766991	13.3835716	48.3407313	-57.16354516	19.00866508	10.61951447
48.39096179	-57.14303608	22.27766991	13.7254219	48.34072728	-57.16358497	18.99746895	9.72095108
48.39138591	-57.14267901	22.36723137	12.2799034	48.34072436	-57.16362319	18.99746895	8.822387695
48.39181439	-57.14232596	23.31882286	11.8599205	48.34071932	-57.16366277	18.99746895	8.968894958
48.39220357	-57.14196822	22.70308876	11.5864487	48.34071505	-57.16370366	18.99746895	8.275436401
48.39261503	-57.14170637	22.38962364	11.9966621	48.3407112	-57.16374322	18.98627663	7.621047974
48.39304343	-57.14139331	22.22169304	12.1333962	48.34069719	-57.16442299	18.94149208	12.41664505
48.39347854	-57.14110237	22.33364677	11.5864487	48.34070884	-57.16510495	18.91910744	12.55337906
48.39389176	-57.14069174	22.04257011	12.6217461	48.34071513	-57.16579377	18.89671516	13.58868027
48.39428177	-57.14022697	22.2440815	11.9282951	48.34073834	-57.16648126	18.89671516	13.38357162

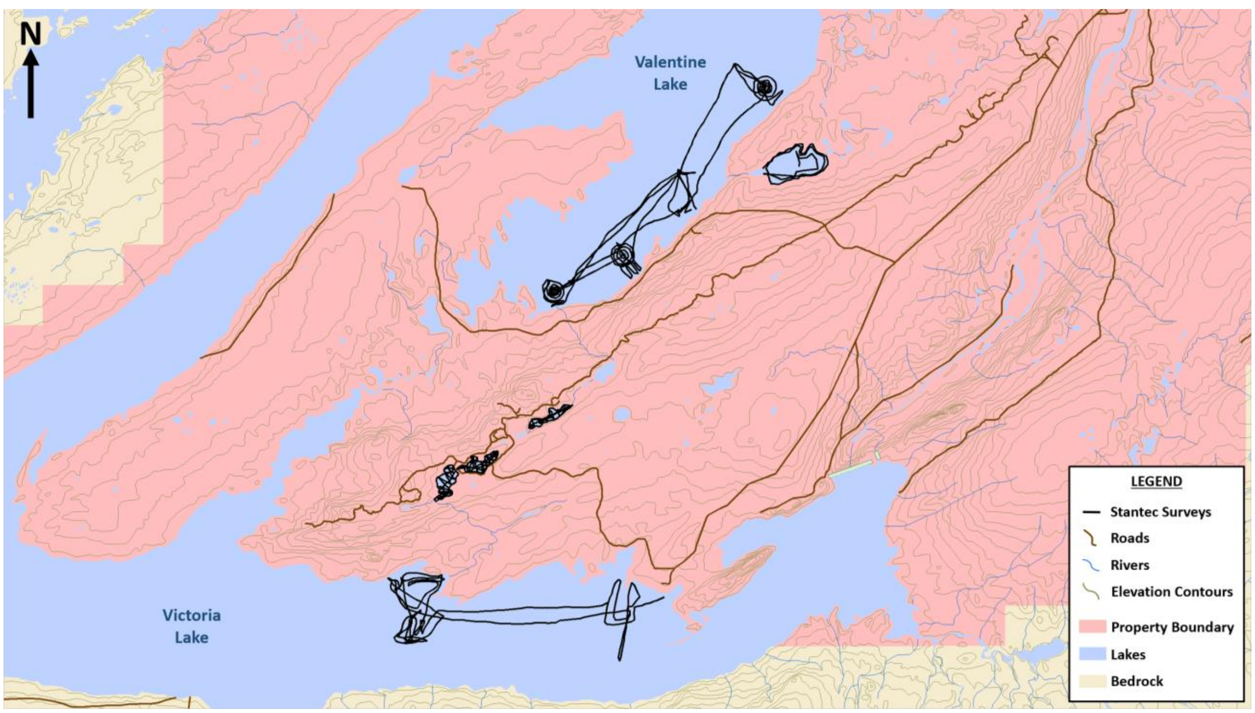

Figure I.1: Map showing the Stantec data measurement locations. The Valentine and Victoria Lake data surveys were conducted in 2018, while the smaller inner ponds were surveyed in 2010.

Memorial University and Stantec Bathymetry: Data Intersection Analysis

By: Marie Flanagan

(Research Assistant)

MEMORIAL UNIVERSITY

FACULTY OF SCIENCE
Department of Earth Sciences

July 2020

The purpose of this report is to determine the water surface elevation offset between *Stantec Inc.'s* recorded lake depths and *Memorial University's* (*MUN*) recorded lake depths. Victoria Lake is a hydroelectric reservoir with a dam therefore, the water level can have significant variation in time. The offset in water surface elevation must be corrected before combining the data to make a more accurate bathymetry map.

An Excel file "*Intersection_Depths_MUN+Stantec*" was provided by Stephanie Abbott (M.Sc. Candidate, *Memorial University*), which contained the following information columns:

- **Easting_S** – the original *Stantec* Easting value that is closest to the intersection Easting value
- **Northing_S** – the original *Stantec* Northing value closest to the intersection Northing value
- **Distance_S** – how far the closest original *Stantec* data point is from the intersection point
- **Depth_S** – the original depth value from the closest original *Stantec* point
- **Intersect_X** – the intersecting Easting value of the two datasets
- **Intersect_Y** – the intersecting Northing value of the two datasets
- **Depth_M** – the original depth value from the closest original *MUN* point
- **Distance_M** – how far the closest original *MUN* data point is from the intersection point
- **Easting_M** – the original *MUN* Easting value that is closest to the intersection Easting value
- **Northing_M** – the original *MUN* Northing value closest to the intersection Northing value

The data found within the above Excel spreadsheet originated from *Stantec Inc.* and *Memorial University*. A preview of the acquired data can be seen below in Table I.2.

Easting_S	Northing_S	Distance_S	Depth_S	Intersect_X	Intersect_Y	Depth_M	Distance_M	Easting_M	Northing_M
489709	5360962.2	1.4676464	12.964	489710.27	5360961.5	13.499	0.6383626	489709.7	5360961.26
489709	5360962.2	1.233911	12.964	489709.19	5360961	13.499	0.5826693	489709.7	5360961.26
489697	5360955.8	1.5146038	11.86	489697.34	5360954.4	12.143	0.6169398	489696.8	5360954.14
489697	5360955.8	2.3544457	11.86	489695.89	5360953.6	12.143	1.0392009	489696.8	5360954.14
489750	5360942.4	12.649573	13.794	489738.69	5360947.9	14.233	3.7493779	489739.4	5360951.54
489725	5360891.4	6.1550077	12.69	489728.59	5360886.2	12.671	5.0450702	489727.8	5360881.19
489731	5360876	7.9208997	12.28	489728.11	5360883.2	12.671	2.0752493	489727.8	5360881.19
489555	5360044.9	22.621873	11.586	489567.21	5360063.7	12.383	1.0632761	489567	5360062.65
490172	5360768.6	0.6902563	8.549	490172.74	5360768.1	8.719	1.9143004	490171.6	5360766.52
490129	5360709.2	17.760964	5.863	490139.85	5360722.9	6.091	1.7561209	490140.8	5360724.38

Table I.2: Sample of the data within the "Intersection_Depths_MUN+Stantec" spreadsheet.

Originally there were **72** intersections of *Stantec* and *MUN* bathymetry data at Valentine Lake and **60** intersections at Victoria Lake.

The data was sorted by the *Stantec* distance from the intersection and all data more than **10 metres** from the intersection point was removed. Next, the data was sorted by the *MUN* distance from the intersection and all data more than **5 metres** from the intersection point was removed.

To sort data, highlight the column you would like to sort by, then click the data tab, then select Sort Z-A (highest to lowest).

This left **33** intersections at Valentine Lake and **18** intersections at Victoria Lake.

A column of the depth differences between *MUN* and *Stantec's* data was created and the average, as well as standard deviation were calculated.

Stantec Depth - MUN Depth		
-0.17		
-0.157		
1.888		
-0.776		
-1.214		
-0.604		
1.94		

Table I.3: Sample of the calculated depth difference (in metres) between Stantec and MUN depth data.

The mean average of the Valentine Lake depth differences (*Stantec* recorded depth subtract *MUN* depth) is **-0.201091 m** and the standard deviation is **1.01378**. The mean average of the Victoria Lake depth differences is **0.26828 m**, while the standard deviation is **2.584539**.

As can be seen for both lakes, the standard deviation is significantly higher than the lake depth differences, so <u>no adjustments</u> will be made to correct the depth data before compiling.